Isogeometric Finite Element Analysis of Nonlinear Structural Vibrations

Oliver Weeger

Vom Fachbereich Mathematik der Technischen Universität Kaiserslautern
zur Verleihung des akademischen Grades

Doktor der Naturwissenschaften
(Doctor rerum naturalium, Dr. rer. nat.)

genehmigte Dissertation.

1. Gutachter: Prof. Dr. Bernd Simeon (Technische Universität Kaiserslautern)
2. Gutachter: Prof. Dr. Carlo Lovadina (Università degli studi di Pavia)
Datum der Disputation: 17. April 2015

D 386

Zusammenfassung

In dieser Arbeit stellen wir eine neuartige Methode für die nichtlineare Frequenzanalyse von angeregten mechanischen Schwingungen vor. Zur effizienten Ortsdiskretisierung der partiellen Differentialgleichungen der nichtlinearen Kontinuumsmechanik wenden wir das Prinzip der isogeometrischen Analyse an. Die isogeometrische Finite Elemente Methode bietet im Vergleich zu klassischen Finiten Elemente-Diskretisierungen zahlreiche Vorteile, insbesondere eine exakte Geometriedarstellung und höhere Genauigkeit der numerischen Approximationen mittels Spline-Funktionen. Anschließend verwenden wir die Harmonic Balance Methode zur Berechnung der nichtlinearen Schwingungsantwort bei periodischen externen Anregungen. Dabei wird die Lösung des aus der Ortsdiskretisierung resultierenden, nichtlinearen gewöhnlichen Differentialgleichungssystems im Frequenzraum als abgeschnittene Fourierreihe entwickelt. Um eine effektive Anwendung der Methode auf große Systeme im Rahmen von industriellen Problemen zu ermöglichen, ist eine Modellreduktion der Ortsdiskretisierung der Bewegungsgleichung notwendig. Dazu schlagen wir eine modale Projektionsmethode vor, die mit modalen Ableitungen und damit Informationen zweiter Ordnung erweitert wird. Wir untersuchen das Prinzip der modalen Ableitungen theoretisch und demonstrieren anhand numerischer Beispiele die Anwendbarkeit und Genauigkeit der Reduktionsmethode bei der nichtlinearen Frequenzanalyse. Außerdem erweitern wir die nichtlineare Vibrationsanalyse mittels gemischter isogeometrischer Methoden auf inkompressible Elastizität.

Abstract

In this thesis we present a new method for nonlinear frequency response analysis of mechanical vibrations. For an efficient spatial discretization of nonlinear partial differential equations of continuum mechanics we employ the concept of isogeometric analysis. Isogeometric finite element methods have already been shown to possess advantages over classical finite element discretizations in terms of exact geometry representation and higher accuracy of numerical approximations using spline functions. For computing nonlinear frequency response to periodic external excitations, we rely on the well-established harmonic balance method. It expands the solution of the nonlinear ordinary differential equation system resulting from spatial discretization as a truncated Fourier series in the frequency domain. A fundamental aspect for enabling large-scale and industrial application of the method is model order reduction of the spatial discretization of the equation of motion. Therefore we propose the utilization of a modal projection method enhanced with modal derivatives, providing second-order information. We investigate the concept of modal derivatives theoretically and using computational examples we demonstrate the applicability and accuracy of the reduction method for nonlinear static computations and vibration analysis. Furthermore, we extend nonlinear vibration analysis to incompressible elasticity using isogeometric mixed finite element methods.

Acknowledgements

Over the last years many people have been supporting me in the course of preparing this thesis and I would like to acknowledge their kind efforts and assistance.

First of all, I would like to express my gratitude towards my supervisor Prof Dr Bernd Simeon for guiding my research over the last five years, first a as diploma student at TU München and then as a PhD candidate at TU Kaiserslautern. I appreciate that he left a lot of freedom for me to pursue my own ideas, set the right direction when it was necessary and contributed valuable advice.

I am also very grateful to Dr Utz Wever, who has been my advisor at Siemens for many years. He supported my work in various ways and was always available for fruitful discussions. Furthermore I want to thank Dr Stefan Boschert for leading our *TERRIFIC* project activities at Siemens and his profound advice.

I also want to thank the research group heads at Siemens Corporate Technology, Dr Efrossini Tsouchnika and Roland Rosen, who gave me the chance to pursue my PhD project in an industrial environment and contributed the funding for my research activities. For the pleasant and inspiring working environment, I would like to thank all my colleagues at Siemens, in particular Dr Meinhard Paffrath, Dr Dominic Kohler and Dr Yayun Zhou for their company and support. My thanks also goes to all other PhD students at Siemens CT and StuNet for discussions, lunches and leisure activities.

I am indebted to Prof Dr Carlo Lovadina for giving me the chance to spend a two-month research visit at the University of Pavia and the excellent cooperation we had there. Dr Nicola Cavallini deserves my special thanks for the great collaboration, his dedication to our work and his manifold support. I also want to thank all the colleagues and friends I met in Pavia for the joyful time we had together.

For the close collaboration, fruitful discussions and her support, I deeply want to express my gratitude towards my colleague Daniela Fußeder. At TU Kaiserslautern I furthermore want to thank Dr Anh-Vu Vuong and Anmol Goyal for their cooperation.

It was a great pleasure to work with many colleagues from all over Europe, who were involved in the "TERRIFIC" EU project. I want to thank them for the collaboration and enjoyable project meetings. Special thanks goes to the group of Prof Dr Bert Jüttler at JKU Linz and Dr Vibeke Skytt from SINTEF in Oslo, who supported my work with their multi-patch parameterizations.

For the balancing distraction, relaxation and fun we had together in the last years, I am very thankful to all my friends.

In the end I would also like to thank the most important person in my life, my girlfriend Serene, who has been giving me so much encouragement and joy over all the years. Deepest thank also goes to my family, who has always unconditionally supported my path through life.

Financial funding of my work by Siemens AG, TU Kaiserslautern, and the European Union within the 7th framework project "TERRIFIC" is gratefully acknowledged.

Kaiserslautern, April 2015 Oliver Weeger

Contents

1 Introduction

Within the industrial engineering and product development process, numerical simulation plays a very important role as it allows the investigation of the behavior of a product or system while it is still in the development stage. These simulations very often rely on the mathematical modeling of physical phenomena in electromagnetics, fluid and solid mechanics, or thermal conduction as partial differential equations, a numerical solution scheme for these equations and its algorithmic computer implementation.

Even though computing powers have manifolded over the past decades [37], there is still need for the development of more efficient methods and algorithms, since demands on accuracy and complexity of numerical simulations have evolved to the same degree. Furthermore, the integration of the computer-aided product development stages, i.e. design (CAD), analysis, redesign or optimization, and manufacturing (CAM), into a seamless computer-aided engineering (CAE) process is rather difficult. As these fields all have evolved separately, different types of geometry representations and descriptions are employed in each of them.

1.1 Scope and context

This thesis addresses the simulation of mechanical vibrations with large amplitudes and nonlinear material behavior, which is particularly important when rubber components are involved. The aim is to develop a numerical method for the computation of nonlinear steady-state response of forced vibrations, which is accurate, efficient and easy to be integrated into the CAE process.

Mechanical motion of a body can be modeled mathematically using a nonlinear partial differential equation (PDE). This equation of motion of elastodynamics has to be discretized in space and time in order to be solved numerically, since analytical solutions can not be found in general.

For the spatial semi-discretization of the structural vibration problem we rely on the isogeometric finite element method. In order to overcome the gap between computer-aided design, numerical simulation and manufacturing, isogeometric analysis (IGA) was introduced by Hughes et al. in 2005 [63]. The substantial idea behind isogeometric methods is the use of the same geometry representation throughout the whole engineering process. This is showcased in Figure 1.1, using the so-called “TERRIFIC Demonstrator”, a mechanical part which we use as application for the methods we develop.

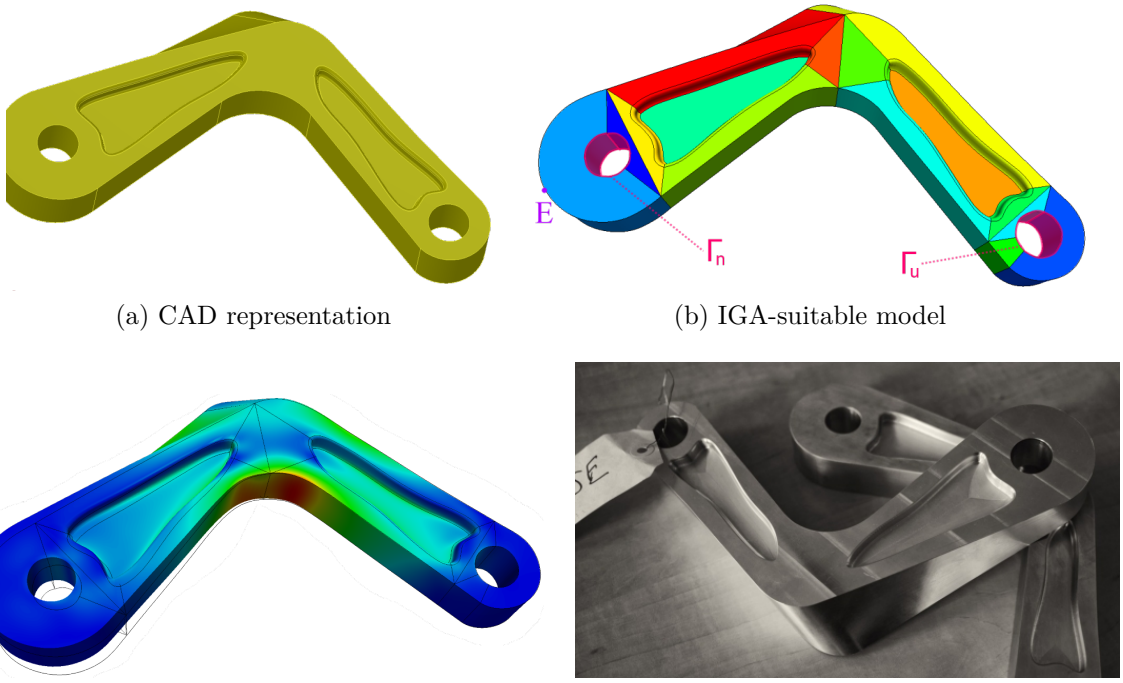

(a) CAD representation

(b) IGA-suitable model

(c) Stress analysis output

(d) Manufactured part

Figure 1.1: Illustration of an integrated isogeometric engineering process, using the TERRIFIC Demonstrator part as example: a CAD model (a) has to be translated into an IGA-suitable multi-patch model (b). Then computational analysis can be carried out (c) and the approved design can finally be manufactured (d)

As spline functions, such as B-Splines and non-uniform rational B-Splines (NURBS) [93], are typically employed for geometric design in CAD software, in IGA these functions are also used for the discretization of geometry and numerical solution in an isoparametric fashion. This concept has already been implemented into several numerical discretization methods, such as boundary elements [110], collocation [5], finite volumes [59], and, of course, isogeometric finite elements [63]. These isogeometric methods have been successfully applied for the solution of many kinds of engineering problems, for instance electromagnetics [88], mechanical analysis of solids [48, 49, 63] and structures [21, 24, 42, 73], and also coupled problems like fluid-structure interaction [16, 59] or thermomechanics [43]. A detailed introduction into IGA and summary of properties and applications of isogeometric methods can be found in the monograph [39].

Many mathematical properties of isogeometric finite element discretizations have already been thoroughly investigated, especially focusing on higher continuity of spline basis functions in comparison with Lagrangian elements [14, 19, 40, 50, 64]. In particular, it has been shown that spline-based finite elements have substantial advantages over classical Lagrangian finite elements in the context of linear vibration analysis. In eigenvalue problems so-called optical and acoustical branches are avoided, which leads to a much higher accuracy especially in higher eigenfrequencies [42]. IGA is more accurate per degree of freedom (DOF) for numerical solutions of linear elliptic, parabolic and hyperbolic PDEs than standard finite element methods due to higher continuity of splines, whereas rates of convergence are the same [39, 64].

Isogeometric analysis has also been applied in nonlinear continuum mechanics and incompressible elasticity, where the above-mentioned advantages of the approach could also be verified [6, 48, 84, 118]. The special treatment of incompressible and near incompressible problems using mixed elements [84, 118], reduced integration [24], or strain projection methods [48] is especially important for the simulation of rubber and elastomer materials. Here, we employ a mixed formulation based on [6, 7, 23, 109] for the isogeometric finite element discretization of (near) incompressible materials and then also include it in nonlinear frequency analysis. A special focus lies on comparison of different kinds of isogeometric mixed elements, namely Taylor-Hood and subgrid elements, which were so far used and investigated only for the linear Stokes problem [28].

As outlined above, isogeometric finite element methods (IGA-FEM) offer many advantages over classical finite element discretizations, in particular a better integration into the CAE process, higher accuracy per DOF, especially in frequency analysis, and a simple and flexible implementation of mixed formulations. Consequently, they are our method of choice and we use IGA-FEM in this thesis for the spatial semi-discretization of the equation of motion.

After the spatial semi-discretization of nonlinear elastodynamics equation, which yields a system of nonlinear ordinary differential equations (ODEs), we employ the harmonic balance method (HBM) for time domain discretization [86, 87, 117]. In general, HBM can be applied for frequency and steady-state vibration analysis of periodic systems of nonlinear ODEs, and is based on Fourier transformation and solution of the ODE in the frequency domain.

Though harmonic balance is a well-established method for nonlinear frequency analysis, for example in the context of integrated circuit simulations [31, 106], it is so far hardly used in mechanics, only for lower dimensional structural models such as beams and plates [80, 81, 98, 99, 100]. Within commercial finite element analysis (FEA) software, nonlinear frequency response analysis has to be carried out as transient analysis using time integration methods, either integrating until steady state is reached or using shooting methods.

Having studied the use of isogeometric finite elements in combination with harmonic balance for the nonlinear Euler-Bernoulli beam model already in [126, 127], we extend the method to 3-dimensional continuum mechanics and elastodynamics [128]. As HBM uses a truncated Fourier expansion of length m for frequency domain approximation of each DOF of the spatial discretization, it produces a blow-up of total DOFs: the sparse linear system to be solved in the end is not only m-times larger, but also with m-times as many nonzero entries per row than the matrix arising from spatial discretization.

Therefore model order reduction (MOR) of the spatial discretization is needed to reduce the size of the linear system significantly and make an efficient numerical solution of the system arising from HBM possible. In linear FEA and vibration analysis, modal reduction is a well-established technique [62]. There, the equation of motion is projected onto a subspace spanned by a subset of eigenmodes. However, for nonlinear problems more advanced methods are needed [94, 130]. For example, nonlinear normal modes (NNMs) [77, 119] or Proper Orthogonal Decomposition (POD) [17, 60, 112] can be used.

We propose to use a projection with eigenmodes and additionally modal derivatives [68, 111], which are a second-order enhancement of linear eigenmodes, for the use in nonlinear frequency analysis [128]. In contrast to most other common reduction methods so

far used in nonlinear dynamics, it does not require a current state of deformation of the system and continuous basis updates, thus the projection basis can be fully precomputed based on the linearized system. Furthermore, there are also similar well-established techniques of second-order enhancements in other fields of computational engineering such as uncertainty quantification [101].

The reduction method using eigenmodes and modal derivatives has been successfully applied in nonlinear dynamic analysis by time integration before [11, 12, 96, 112], and we show that it is especially suitable in our nonlinear vibration framework with harmonic balance and makes a large-scale application of nonlinear frequency analysis possible.

1.2 Publications and software

Within the course of preparing this thesis, the author has already published intermediate results and achievements in scientific journals and conference proceedings. Isogeometric finite elements and harmonic balance with application to the nonlinear Euler-Bernoulli beam structural model were investigated in the diploma thesis [126] and published in [127]. The application to 3-dimensional nonlinear elasticity with large deformations and hyperelastic constitutive laws, as well as the use of reduction with modal derivatives were published in [128]. Implementation of isogeometric mixed Taylor-Hood elements and their performance in static nonlinear incompressible elasticity were investigated as part of [33]. Linear elasticity computations for evaluation of an isogeometric segmentation pipeline for the generation of analysis-suitable multi-patch models from CAD models were contributed to [89].

We have implemented the methods and tested the computational examples presented in this thesis in different software packages. The results related to the linear and nonlinear beam were obtained using a `MATLAB` implementation. All methods for 3-dimensional elasticity are related to the development of `IGAsolvers` `C++`-library within the TERRIFIC EU-project [53]. They are partially available for download and use under GNU Lesser General Public License (LGPL) at [121]. Mixed methods for static nonlinear incompressible elasticity were also implemented in `C++` using `igatools` library [91].

1.3 Outline

This thesis is structured in 7 chapters. After this introductory chapter we give a summary of the main ideas behind *isogeometric analysis* and isogeometric finite element discretizations in Chapter 2. As it is an important aspect of the simulation of complex real-life geometries, we set a focus on the treatment and implementation of multi-patch problems.

In Chapter 3 we review the theory of *nonlinear continuum mechanics*, including large deformation kinematics and visco-hyperelastic constitutive relations, and apply the isogeometric finite element method for the spatial discretization. We also present theory and discretization of linear elasticity and the nonlinear Euler-Bernoulli beam, and show computational applications for validation of our implementations.

Then we treat *nonlinear vibration analysis* in Chapter 4, introduce the harmonic balance method and apply it to nonlinear continuum mechanics and dynamics. We use computational applications to validate the approach and to examine convergence of the isogeometric discretization and truncated Fourier series.

Chapter 5 is dedicated to *model order reduction* and its application to nonlinear vibration analysis. We motivate the use of a novel projection method with modal derivatives, explain it in detail, and study it analytically and numerically.

We introduce *isogeometric mixed methods* for near incompressible elasticity problems in Chapter 6. We outline their integration into harmonic balance method and study their performance in numerical examples for static nonlinear deformation and nonlinear frequency analysis problems.

Finally, Chapter 7 concludes this thesis with a summary and an outlook on future research directions.

2 Isogeometric analysis and finite elements

This chapter provides a basic introduction into the concepts of isogeometric analysis and isogeometric finite elements, which we use for the spatial discretization of the vibration problem.

Spline functions have been an essential foundation of CAD over the past decades and thus we briefly review their definition and properties in Section 2.1. The idea behind isogeometric analysis is to employ splines also for the numerical solution of PDEs, for example in a finite element method. Since much research has been done on the field of isogeometric methods in the past years, we present only the basic ideas and properties relevant in this work in Section 2.2. We lay a special focus on the treatment of multi-patch problems, where the computational domain is decomposed into several spline geometries. In Section 2.3 we present and compare two strategies for the implementation of constraints for multi-patch problems.

2.1 B-Splines and NURBS

B-Splines and *Non-Uniform Rational B-Splines* (NURBS) are the tools that are typically used for describing geometries in computer-aided design and also for representing the numerical solution in isogeometric analysis [39, 51, 63, 93]. Detailed definitions and introductions, including proofs and computer implementations can be found in [93], while [102] also includes an historical perspective on the topic. Here a brief review of the main definitions and properties is given.

2.1.1 B-Spline and NURBS basis functions

Starting point is the definition of a *knot vector* $\Xi = (\xi_1, \ldots, \xi_m)$ as a non-decreasing sequence of *knots* $\xi_i \in \mathbb{R}$ $(i = 1, \ldots, m)$, $\xi_i \leq \xi_{i+1}$ $(i = 1, \ldots, m-1)$ on the *parameter space* $\Omega_0 = [\xi_1, \xi_m] \subset \mathbb{R}$.

In the following, some terminology associated with the knot vectors will be useful. If Ξ is a knot vector we use Ξ^0 to refer to the corresponding *distinct knot vector* where all knots of Ξ^0 have multiplicity one. The half-open interval $[\xi_i, \xi_{i+1})$ is called the *i-th knot span* or *element*. The total number of nonzero knot spans or elements in Ξ is ℓ. The

length of a knot span is $h_i = \xi_{i+1} - \xi_i$ $(i = 1, \ldots, \ell)$ and $h = \min_{i=1,\ldots,\ell} h_i$ is the *mesh parameter*. If the knots ξ_i are uniformly distributed over Ξ, then we call the knot vector *uniform*, and if the first and last knot have multiplicity $p+1$, i.e. $\xi_1 = \ldots = \xi_{p+1}$ and $\xi_{m-p} = \ldots = \xi_m$, the knot vector is called *open*.

Definition 2.1 (B-Spline basis functions)**.** *The* B-Spline basis functions $B_i^p(\xi) : \Omega_0 \to [0,1]$ *of degree p (order $p+1$) are defined for $i = 1, \ldots, n$ ($n = m - p - 1$) by the Cox-de Boor recursion:*

$$\begin{aligned} B_i^0(\xi) &= \begin{cases} 1 & \xi_i \leq \xi < \xi_{i+1} \\ 0 & else \end{cases}, \\ B_i^p(\xi) &= \frac{\xi - \xi_i}{\xi_{i+p} - \xi_i} B_i^{p-1}(\xi) + \frac{\xi_{i+p+1} - \xi}{\xi_{i+p+1} - \xi_{i+1}} B_{i+1}^{p-1}(\xi). \end{aligned} \tag{2.1}$$

Here it is assumed that the quotient $0/0$ is 0.

There are many useful properties of B-Spline basis functions B_i^p, $i = 1, \ldots, n$, and among them we point out that they

- are piecewise polynomials of degree p,
- have compact support, i.e. $\text{supp}(B_i^p) = [\xi_i, \xi_{i+p+1})$,
- are non-negative, i.e. $B_i^p(\xi) \geq 0 \; \forall \xi \in [\xi_1, \xi_m]$,
- form a partition of unity for an open knot vector, i.e. $\sum_{i=1}^n B_i^p(\xi) \equiv 1 \; \forall \xi \in [\xi_1, \xi_m]$,
- are smooth, i.e. they are p-times continuously differentiable (C^p-continuous) inside a knot span and at inner knots of multiplicity k ($k \leq p$) only C^{p-k}.

Here we only use B-Spline basis functions on open knot vectors with inner knots of multiplicity $1 \leq k \leq p$.

Example 2.1 (Different types of B-Spline basis functions on the same distinct knot vector)**.** *An example of B-Spline basis functions with different degrees and continuities based on the same distinct knot vector $\Xi^0 = (0, 0.2, 0.4, 0.6, 0.8, 1)$ can be found in Figure 2.1:*

(a) $\Xi = (0, 0, 0.2, 0.4, 0.6, 0.8, 1, 1)$, $p = 1$, $m = 8$, $n = 6$*:*
linear with C^0-continuity at all inner knots

(b) $\Xi = (0, 0, 0.2, 0.4, 0.6, 0.8, 1, 1)$, $p = 2$, $m = 10$, $n = 7$*:*
quadratic with C^1-continuity at all inner knots

(c) $\Xi = (0, 0, 0, 0.2, 0.4, 0.6, 0.8, 1, 1, 1)$, $p = 3$, $m = 12$, $n = 8$*:*
cubic with C^2-continuity at all inner knots

(d) $\Xi = (0, 0, 0, 0.2, 0.4, 0.4, 0.6, 0.8, 0.8, 1, 1, 1)$, $p = 3$, $m = 15$, $n = 11$*:*
cubic with C^1-continuity at $\xi = 0.4$, C^0-continuity at $\xi = 0.8$ and C^2-continuity at all other knots

Definition 2.2 (Non-Uniform Rational B-Spline basis functions)**.** *The definition of* Non-Uniform Rational B-Spline *(NURBS) basis functions N_i^p is based on B-Spline basis functions B_i^p on a knot vector Ξ and additional* weights $w_i > 0$ $(i = 1, \ldots, n)$*:*

$$N_i^p(\xi) = \frac{B_i^p(\xi)\, w_i}{\sum_{j=1}^n B_j^p(\xi)\, w_j}. \tag{2.2}$$

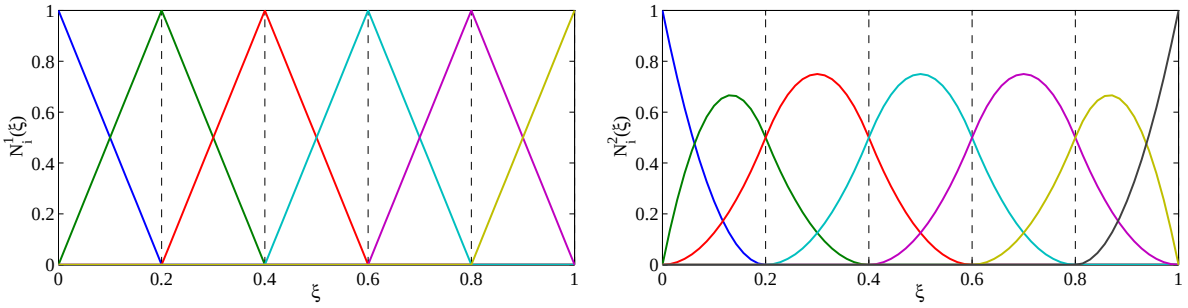

(a) Linear C^0 B-Spline basis functions

(b) Quadratic C^1 B-Spline basis functions

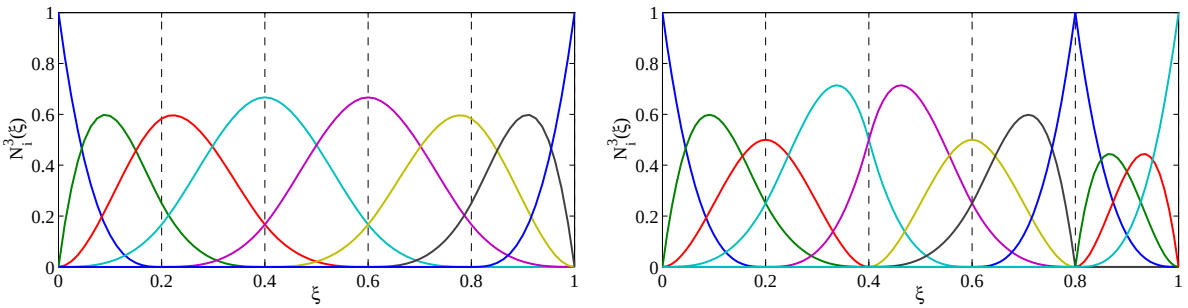

(c) Cubic C^2 B-Spline basis functions

(d) Cubic B-Splines with mixed continuities

Figure 2.1: Different types of B-Spline basis functions on the same distinct knot vector

Efficient algorithms for the evaluation of B-Spline and NURBS basis functions and their derivatives are described in detail in [93].

NURBS are piecewise rational functions and the essential properties of B-Splines given above hold for NURBS as well. For equal weights, i.e. $w_i = const.\ \forall i = 1, \ldots, n$, NURBS reduce to B-Spline basis functions and thus in the following we are only using the term NURBS.

Definition 2.3 (Spline spaces)**.** *The vector space of NURBS basis functions of degree p and minimum continuity $k \leq p-1$ on the open knot vector Ξ is denoted by*

$$\mathcal{S}_p^k(\Xi) = \text{span}\{N_i^p\}_{i=1,\ldots,n}. \tag{2.3}$$

Note that $\dim(\mathcal{S}_p^k(\Xi)) = m - p - 1 = n$ and N_i^p actually are a basis of $\mathcal{S}_p^k(\Xi)$, since they are linearly independent.

2.1.2 Spline geometries

In CAD programs geometry is typically represented by spline curves and surfaces. The additional benefit of NURBS over B-Splines is the possibility to represent conic intersections exactly, which is very important for designing engineering shapes. Here we introduce spline curves and volumes, since we need to have a solid representation for our 3-dimensional applications.

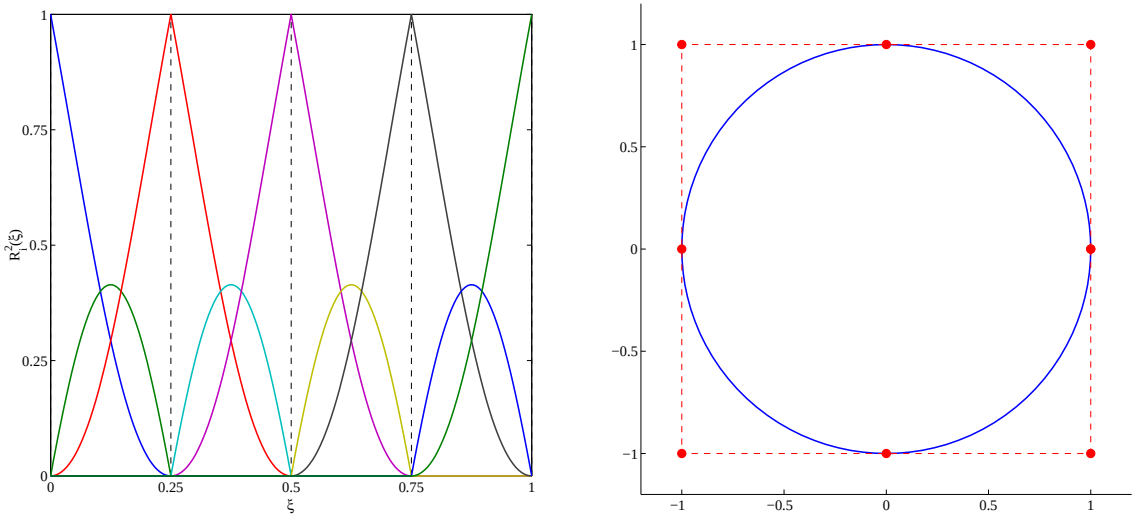

(a) Quadratic NURBS basis functions of the circle

(b) Circle (blue) with control points (red) and control polygon (dashed red)

Figure 2.2: A circle as a NURBS curve

Definition 2.4 (Spline curve)**.** *A* spline curve $\boldsymbol{c} : \Omega_0 \to \mathbb{R}^d$ *is defined by a spline space* $\mathcal{S}_p^k(\Xi)$ *and* control points $\boldsymbol{c}_i \in \mathbb{R}^d$ $(i = 1, \ldots, n)$*:*

$$\boldsymbol{c}(\xi) = \sum_{i=1}^{\ell} N_i^p(\xi)\ \boldsymbol{c}_i. \tag{2.4}$$

Spline curves as defined above have the following properties:

- The polygon formed by the control points $\{\mathbf{c}_i\}_{i=1,\ldots,n}$ is called *control polygon*.
- Convex hull property, i.e. the curve is completely contained in its control polygon.
- Interpolation of start and end points, i.e. $\mathbf{c}(\xi_1) = \mathbf{c}_1$, $\mathbf{c}(\xi_m) = \mathbf{c}_n$.
- Affine invariance, i.e. affine transformations of the curve can be performed on its control points.
- Displacing a control point $\mathbf{c}_i$ only influences the curve locally in the knot interval $[\xi_i, \xi_{i+p+1})$.
- The continuity properties of the curve correspond to the ones of B-Spline/NURBS functions.

Example 2.2 (A circle as a NURBS curve)**.** *A typical example used to illustrate the capabilities of NURBS is the exact representation of a circle. In Figure 2.2 a circle of radius 1 around the origin is shown. The knot vector of the quadratic NURBS basis functions is* $\Xi = (0, 0, 0, \frac{1}{4}, \frac{1}{4}, \frac{1}{2}, \frac{1}{2}, \frac{3}{4}, \frac{3}{4}, 1, 1, 1)$*, i.e.* $p = 2$*,* $m = 12$*,* $n = 9$*, weights are* $w = (1, \frac{1}{2}\sqrt{2}, 1, \frac{1}{2}\sqrt{2}, 1, \frac{1}{2}\sqrt{2}, 1, \frac{1}{2}\sqrt{2}, 1)$ *and control points of the curve are* $\binom{1}{0}, \binom{1}{1}, \binom{0}{1}, \binom{-1}{1}, \binom{-1}{0}, \binom{-1}{-1}, \binom{0}{-1}, \binom{1}{-1}, \binom{1}{0}$*.*

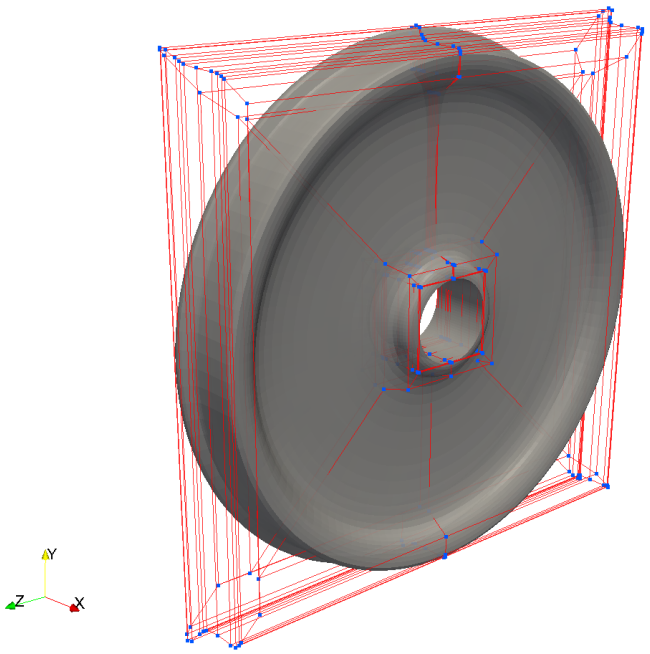

Figure 2.3: A train wheel as a NURBS volume. Showing the control points (blue), the control point mesh (red) and the volume itself (gray)

It is possible to define multivariate NURBS functions, for example in 3D, as product of univariate NURBS:

$$N_{i_1 i_2 i_3}^{p_1 p_2 p_3}(\xi_1, \xi_2, \xi_3) = \frac{w_{i_1} w_{i_2} w_{i_3} B_{i_1}^{p_1}(\xi_1) B_{i_2}^{p_2}(\xi_2) B_{i_3}^{p_3}(\xi_3)}{\sum_{j_1=1}^{n_1} \sum_{j_2=1}^{n_2} \sum_{j_3=1}^{n_3} w_{j_1} w_{j_2} w_{j_3} B_{j_1}^{p_1}(\xi_1) B_{j_2}^{p_2}(\xi_2) B_{j_3}^{p_3}(\xi_3)}, \tag{2.5}$$

where $N_{i_1 i_2 i_3}^{p_1 p_2 p_3} : \Omega_0^1 \times \Omega_0^2 \times \Omega_0^3 \to \mathbb{R}$.

Since this notation is very laborious and we are going to deal with trivariate NURBS many more times in this work, in the following n, p, i should be understood as 3-dimensional multi-indices $n = (n_1, n_2, n_3)$, $p = (p_1, p_2, p_3)$ and $i = (i_1, i_2, i_3)$, giving the number, degree and index of trivariate NURBS functions $N_i^p(\boldsymbol{\xi})$ with parameters $\boldsymbol{\xi} = (\xi_1, \xi_2, \xi_3)$. The reference domain $\Omega_0 = \Omega_0^1 \times \Omega_0^2 \times \Omega_0^3$ and *mesh* or *triangulation* $\boldsymbol{\Xi} = \Xi^1 \times \Xi^2 \times \Xi^3$ are defined using the Cartesian product of domains resp. knot vectors of each parameter direction.

Definition 2.5 (Spline volume)**.** *A* spline volume $\boldsymbol{v} : \boldsymbol{\Omega}_0 \to \mathbb{R}^3$ *is defined by a trivariate spline space* $\mathcal{S}_p^k(\boldsymbol{\Xi})$ *and a mesh of control points* $\boldsymbol{v}_i \in \mathbb{R}^3$*:*

$$\boldsymbol{v}(\boldsymbol{\xi}) = \sum_{i=1}^{n} N_i^p(\boldsymbol{\xi})\ \boldsymbol{v}_i. \tag{2.6}$$

Example 2.3 (A train wheel as a NURBS volume)**.** *Figure 2.3 shows a simplified model of a train wheel as a NURBS volume. The volume itself is displayed in gray, the control points in blue and the control mesh in red. The NURBS basis functions are quadratic in all three directions and the volume has 504 basis functions and control points in total.*

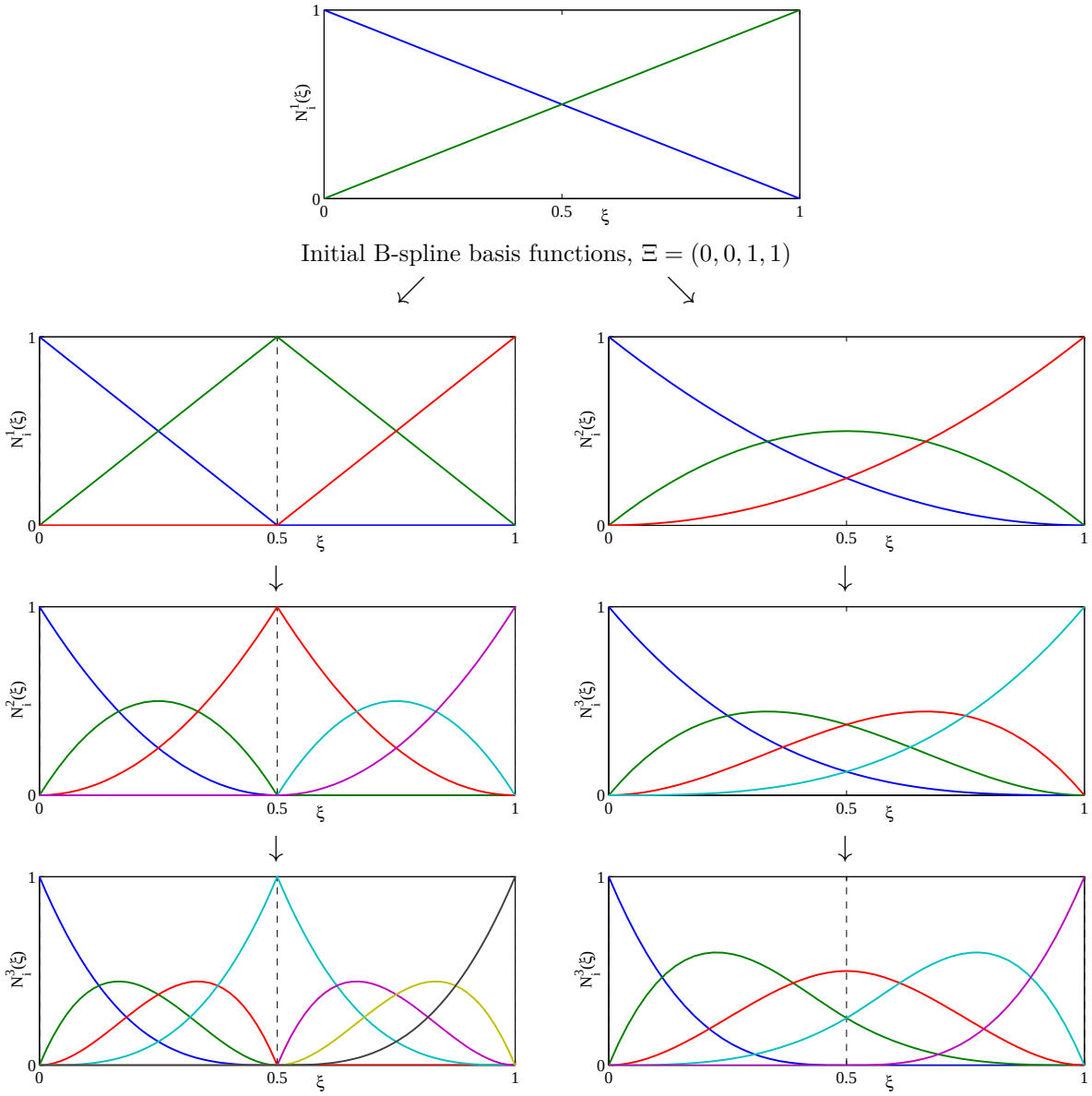

(a) p-method: knot insertion, then twice order elevation, $\Xi_a^* = (0, 0, 0, 0, 0.5, 0.5, 0.5, 1, 1, 1, 1)$

(b) k-method: two order elevations, then knot insertion, $\Xi_b^* = (0, 0, 0, 0, 0.5, 1, 1, 1, 1)$

Figure 2.4: Comparison of refinement strategies: p-method and k-method

2.1.3 Refinement

An important feature of B-Spline and NURBS geometries is the possibility to refine a spline geometry without changing its shape. There exist three basic types of refinement, which are described in the following when applied to a univariate spline space (Def. 2.3) resp. a spline curve (Def. 2.4). For more details see [39].

h-refinement

h-refinement or *knot insertion* means that a given knot vector Ξ is extended to Ξ^* by introducing an additional knot $\xi^* \in \Omega_0$ such that $\Xi \subset \Xi^*$. This provides a new set of $n+1$ basis functions and a new set of $n+1$ control points $\mathbf{c}_i^*$ has to be computed as linear

combinations of the original control points $\mathbf{c}_i$.

A knot insertion step can be used to split an element into two by adding a new distinct knot, similar to the h-refinement process in classical finite element analysis. But here the continuity at the new knot is C^{p-1}, while it is C^0 in FEA. It is also possible to decrease continuity of basis functions at an existing knot by increasing its multiplicity.

In this work usually h-refinement refers to a uniform refinement of the knot vector. This means that in every nonempty knot interval $[\xi_i, \xi_{i+1})$ a new knot $\xi_i^* = (\xi_{i+1} + \xi_i)/2$ is inserted. Thus the number of knots increases to $m^* = m + \ell$, the number of elements to $\ell^* = 2\ell$ and $n^* = n + \ell$. The mesh parameter of the refined knot vector Ξ^* is $h^* = h/2$.

p-refinement

p-refinement or *order/degree elevation* is used to increase the polynomial degree of the spline space to $p^* = p + 1$. The multiplicity of all distinct knots has to be increased by one for the new knot vector Ξ^*, in order to maintain C^{p-1} continuity at inner knots, i.e. $\mathcal{S}_p^k(\Xi^0)$ is refined to $\mathcal{S}_{p+1}^k(\Xi^0)$.

This strategy is similar to p-refinement in FEA resp. p-FEM, where higher degree polynomials are used on element level. However, in IGA continuity at inner knots is maintained and not reduced to C^0.

After p-refinement it is $m^* = m + \ell + 1$, $\ell^* = \ell$, $n^* = n + \ell$ and $h^* = h$.

k-refinement

When a series of h- and p-refinements is performed, its order influences the result, i.e. the refinement strategies do not commute. *k-refinement* means that p-refinements are carried out before any h-refinement steps, since this leads to a minimal multiplicity resp. maximal continuity of inner knots. The differences between refinement strategies are illustrated with the following example.

Example 2.4 (Comparison of refinement strategies)**.** *As simple example for the comparison of different refinement strategies is presented in Figure 2.4. We start from the knot vector $\Xi = (0, 0, 1, 1)$, $\Xi^0 = (0, 1)$, defining the linear B-Spline space $\mathcal{S}_1^0(\Xi^0)$. We want to add the knot $\xi^* = 0.5$ and degree-elevate twice to $p^* = 3$:*

(a) p-method: first h-refinement and then two p-refinements lead to $\Xi_a^* = (0, 0, 0, 0, 0.5, 0.5, 0.5, 1, 1, 1, 1)$. The final spline space has $p_a^* = 3$, $m_a^* = 11$, $n_a^* = 7$ with C^0-continuity at $\xi = 0.5$.

(b) k-method: first two p-refinements and then h-refinement, i.e. k-refinement, lead to $\Xi_b^* = (0, 0, 0, 0, 0.5, 1, 1, 1, 1)$. The final spline space has $p_b^* = 3$, $m_b^* = 9$, $n_b^* = 5$ with C^2-continuity at $\xi = 0.5$.

Remark 2.1. *In numerical studies for the comparison of performance of isogeometric vs. classical finite elements, the k-method is typically, and also in this thesis, associated with IGA and the p-method with FEM [42].*

Local refinement

Due to the tensor product structure of spline meshes, the above presented $p/h/k$-refinement strategies have a global impact on the meshes. Degree elevation can of course only

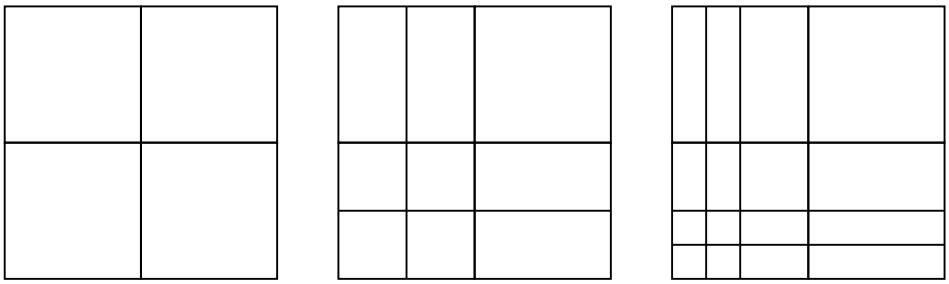

(a) Original mesh (b) after one h-ref. (c) after two h-ref.

Figure 2.5: Tensor product refinement with knot insertion

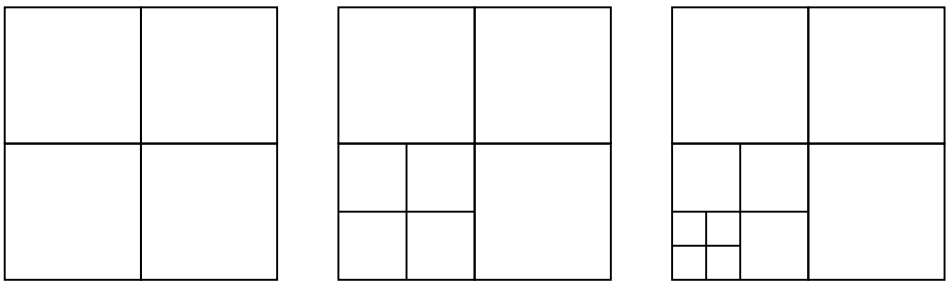

(a) Original mesh (b) after one local ref. (c) after two local ref.

Figure 2.6: True local refinement

be applied to a complete knot vector and also knot insertion in the knot vector of one parameter dimension has a global effect on the tensor product mesh, see Example 2.5.

For a true local refinement of spline meshes the tensor product structure must be circumvented or avoided. Several attempts have been developed, such as hierarchical B-Splines (HB-Splines) [52], splines on T-meshes (T-Splines) [107] and locally refined B-Splines (LR B-Splines) [44]. They have all been successfully applied also in the context of isogeometric analysis and isogeometric finite element methods [15, 69, 125], but are beyond the scope of this thesis.

Example 2.5 (Visualization of global vs. local refinement strategies)**.** *The effect of global refinement is visualized in Figure 2.5, where one would like to refine around the bottom left corner of the initial 2-dimensional mesh (a). In both knot insertion steps (b) and (c) one knot in inserted in each knot vector, but this carries on in the tensor product mesh to the top left and bottom right corners.*

Instead, one would like to do a true local refinement of only the bottom left area, as it is shown in Figure 2.6 and as it is possible for classical finite element meshes or advanced refinement methods such as hierarchical splines or T-splines.

2.2 Isogeometric finite element method

As discussed in the introductory chapter, the main idea behind *isogeometric analysis* (IGA) is to bridge the gap between CAD and FEM. Based on [39, 63] we summarize now the major properties and discuss the relation to classical finite elements.

The key ingredients of IGA are spline basis functions and geometries, as introduced in the previous Section 2.1, which are used for both representing the geometry and spanning the solution spaces in the Galerkin method. The *isoparametric concept* of classical FEM employs also the same function spaces for representation of geometry and solution, but there a conversion step is applied, where the CAD geometry is approximated by these piecewise polynomials. On the other hand, IGA with NURBS makes it possible to bypass this conversion and mesh generation step, and moreover offers higher continuity of the numerical approximation.

2.2.1 Isogeometric Galerkin discretization

We introduce the concept of an isogeometric finite element discretization of a linear partial differential equation in a general setting:

Definition 2.6 (Variational formulation of PDE problem)**.** *We seek a solution $\boldsymbol{u} \in \mathcal{S}$ of the* variational *or* weak formulation *of a partial differential equation on a domain $\Omega \subset \mathbb{R}^d$ using test functions $\boldsymbol{v} \in \mathcal{V}$, where $\mathcal{S} = \{\boldsymbol{u} : \boldsymbol{u} \in (H^1(\Omega))^r, \boldsymbol{u}|_{\delta\Omega} = \boldsymbol{h}\}$, $\mathcal{V} = \{\boldsymbol{v} : \boldsymbol{v} \in (H^1(\Omega))^r,\ \boldsymbol{v}|_{\delta\Omega} = \boldsymbol{0}\}$, $a(\cdot,\cdot)$ is a bilinear form, $l(\boldsymbol{v}) = \langle \boldsymbol{v}, \boldsymbol{f} \rangle$ a linear form, $\boldsymbol{f}$ the right hand side function, $\langle \cdot,\cdot \rangle$ the standard L^2-scalar product, and r the range of the solution space:*

$$\boldsymbol{u} \in \mathcal{S}: \quad a(\boldsymbol{v}, \boldsymbol{u}) = l(\boldsymbol{v}) \ \ \forall\ \boldsymbol{v} \in \mathcal{V}. \tag{2.7}$$

Existence and uniqueness of the solution are guaranteed by the theorem of Lax-Milgram if $a(\cdot,\cdot)$ is continuous and coercive and $l(\cdot)$ is coercive.

The idea behind isogeometric analysis is that the domain Ω of problem (2.7) is given in terms of a *geometry function* $\mathbf{g}$, which maps a reference domain $\Omega_0 \subset \mathbb{R}^{d_0}$, $1 \leq d_0 \leq d$, onto the physical domain of the problem:

$$\mathbf{g} : \Omega_0 \to \Omega,\ \mathbf{x} = \mathbf{g}(\boldsymbol{\xi}). \tag{2.8}$$

This geometry function or *parameterization* can be expressed in terms of a spline geometry, here a NURBS volume, see (2.6):

$$\mathbf{x} = \mathbf{g}(\boldsymbol{\xi}) = \sum_{i=1}^{n} N_i^p(\boldsymbol{\xi}) \mathbf{v}_i. \tag{2.9}$$

Then Galerkin's method is applied, i.e., the infinite-dimensional function spaces $\mathcal{S}$ and $\mathcal{V}$ are approximated by finite-dimensional subspaces $\mathcal{S}^h \subset \mathcal{S}$ and $\mathcal{V}^h \subset \mathcal{V}$. Following the isoparametric paradigm, these spaces are spanned by the push-forward of the NURBS basis functions of the geometry function $\mathbf{g}$ onto the physical domain Ω (or a refinement thereof):

$$\begin{aligned} \mathcal{S}^h &\subset \operatorname{span}\left\{ N_i^p \circ \mathbf{g}^{-1} \right\}^r, \qquad \mathbf{u}^h(\mathbf{x}) = \sum_{i=1}^{n} N_i^p \left(\mathbf{g}^{-1}(\mathbf{x}) \right) \mathbf{d}_i \\ \mathcal{V}^h &\subset \operatorname{span}\left\{ N_i^p \circ \mathbf{g}^{-1} \right\}^r, \qquad \mathbf{v}^h(\mathbf{x}) = \sum_{i=1}^{n} N_i^p \left(\mathbf{g}^{-1}(\mathbf{x}) \right) \delta\mathbf{d}_i, \end{aligned} \tag{2.10}$$

where $\mathbf{d}_i,\ \delta\mathbf{d}_i \in \mathbb{R}^r$ are the control points of displacements and virtual displacements.

Substituting $\mathbf{u}^h$ and $\mathbf{v}^h$ from (2.10) into the weak form (2.7) and making use of the bilinearity of $a(\cdot,\cdot)$ and linearity of $l(\cdot)$ yields

$$\delta\mathbf{d}^T\,\mathbf{K}\,\mathbf{d} = \delta\mathbf{d}^T\,\mathbf{b} \quad \forall\delta\mathbf{d}\in\mathbb{R}^N, \tag{2.11}$$

with $N = rn$, *stiffness matrix* $\mathbf{K}\in\mathbb{R}^{N\times N}$ and *load vector* $\mathbf{b}\in\mathbb{R}^N$,

$$\begin{aligned} K_{ij}^{kl} &= a(N_i^p\,\mathbf{1}_k, N_j^p\,\mathbf{1}_l) \quad , \; i=1,\dots,n,\; j=1,\dots,n, \quad k=1,\dots,r,\; l=1,\dots,r \\ b_i^k &= l(N_i^p\,\mathbf{1}_k) \qquad\qquad\quad , \; i=1,\dots,n, \qquad\qquad\quad k=1,\dots,r, \end{aligned} \tag{2.12}$$

where $\mathbf{1}_k$ is the r-dimensional unit vector with a 1 in direction k.
The *displacement vector* $\mathbf{d} = (\mathbf{d}_1^T,\dots,\mathbf{d}_n^T)^T$ is then computed by solving a linear system

$$\mathbf{K}\,\mathbf{d} = \mathbf{b}, \tag{2.13}$$

which results in the approximate displacement $\mathbf{u}^h$ in the form of a spline geometry.

For the evaluation of (2.12) integrals over the physical domain Ω in $a(\cdot,\cdot)$ and $l(\cdot)$ are transformed and computed on the parameter domain Ω_0 using $\boldsymbol{\xi} = \mathbf{g}^{-1}(\mathbf{x})$. In the same fashion, derivatives of $\mathbf{u}^h(\mathbf{x})$ with respect to $\mathbf{x}$ can be transformed to derivatives with respect to $\boldsymbol{\xi}$ using the chain rule. Thus it is necessary to compute the Jacobian of the geometry function $\mathbf{Dg}(\boldsymbol{\xi}) = (\partial g_i/\partial\xi_j)_{ij}$ and its inverse, which requires that the parameterization is invertible and the inverse is also continuous.

The entries of $\mathbf{K}$ and $\mathbf{b}$ are computed by quadrature rules at the element level and then assembled into the global stiffness matrix and load vector. A Gaussian quadrature rule is used with $p+1$ quadrature points on each knot span, very similar to classical FEM, with knot spans playing the role of elements, see [62, 66] for more details.

2.2.2 Properties of isogeometric finite elements

As the isogeometric finite element discretization is a Galerkin method, just as the classical finite element method, many mathematical properties of FE discretizations can be carried over to isogeometric finite elements [14, 64, 114]. A summary of numerical analysis properties of isogeometric finite element methods can be found in [19].

In the following we use some abbreviations for standard norms

$$\|\cdot\| := \|\cdot\|_{L^2(\Omega)^r}\,, \qquad \|\cdot\|_p := \|\cdot\|_{H^p(\Omega)^r}\,, \qquad \|\cdot\|_E := \sqrt{a(\cdot,\cdot)} \tag{2.14}$$

and $\sigma = \min\{p+1,\; 2(p+1-m)\}$, where $2m$ is the order of the differential operator from which $a(\cdot,\cdot)$ is derived.

A-priori error estimates

For linear elliptic boundary value problems such as (2.7) with sufficiently regular exact solution and data, standard error estimates from FEM are also valid for isogeometric FE [64, 114]:

$$\begin{aligned} \|\mathbf{u}-\mathbf{u}^h\|_E &\le Ch^{p+1-m}\,\|\mathbf{u}\|_{p+1}, \\ \|\mathbf{u}-\mathbf{u}^h\| &\le Ch^{\sigma}\,\|\mathbf{u}\|_{p+1}. \end{aligned} \tag{2.15}$$

The major difference between classical finite elements and IGA is the continuity of basis functions: while a FE discretizations consists of many small elements with polynomials as element-wise basis functions and C^0-continuity over element boundaries, isogeometric spline discretizations have a higher continuity of maximum C^{p-1} over knots, i.e. element boundaries. But this advantage of IGA, which usually becomes obvious in numerical results, is not reflected in the standard error estimates (2.15).

However, in [50] it was shown that higher degree spline spaces with maximal continuity are optimal for the approximation of many function spaces such as L^2- and H^1-spaces. In numerical studies the k-method provided much better results than the p-method, thus suggesting that IGA can be more accurate than FEM per DOF.

Eigenvalue problems

In [41, 42, 65] the properties of IGA in wave propagation and eigenvalue problems, i.e. modal or linear vibration analysis, were investigated and compared to standard FEM. In the same fashion of (2.7), we can write the eigenvalue problem as follows:

$$\mathbf{u}_i \in \mathcal{S}, \omega_i \in \mathbb{R}: \quad \omega_i^2 \langle \mathbf{v}, \mathbf{u}_i \rangle + a(\mathbf{v}, \mathbf{u}_i) = 0 \ \ \forall\, \mathbf{v} \in \mathcal{V}. \tag{2.16}$$

The discrete spectra of numerical approximations vs. analytical eigenfrequencies ω_i^h/ω_i were analyzed for one-, two- and three-dimensional cases. As shown with the example in Figure 2.7, higher continuity of splines is very beneficial for the accuracy of eigenfrequency approximations. While the p-method leads to optical and acoustical branches in the spectra for higher degrees of $p \geq 3$ and a very low accuracy with divergent behavior for $i \to n$, the spectra for the isogeometric k-method are smooth with a much higher accuracy over the whole domain. Only at the end of the spectrum a few outliers occur, which are discussed in detail in [42]. In the 1D cases of linear string and beam vibrations, where $a(u,v) = \int_\Omega v'\, u' dx$ resp. $a(u,v) = -\int_\Omega v''\, u'' dx$, it is even possible to compute the spectra analytically and verify the numerical results [42].

In [64, 114] the following relations and error bounds for FEM and IGA approximation for eigenfunctions $\mathbf{u}_i$ and eigenvalues $\lambda_i = \omega_i^2$ were established, when the smallness condition $h\lambda_i^{1/(2m)} \leq \epsilon$ is fulfilled:

$$\begin{aligned}
\|\mathbf{u}_i^h - \mathbf{u}_i\|^2 + \frac{\lambda_i^h - \lambda_i}{\lambda_i} &= \frac{\|\mathbf{u}_i^h - \mathbf{u}_i\|_E^2}{\lambda_i}, \\
\frac{\lambda_i^h - \lambda_i}{\lambda_i} &\leq C \left(h\lambda_i^{1/(2m)}\right)^{2(p+1-m)}, \\
\frac{\|\mathbf{u}_i^h - \mathbf{u}_i\|_E}{\lambda_i^{1/2}} &\leq C \left(h\lambda_i^{1/(2m)}\right)^{p+1-m}, \\
\|\mathbf{u}_i^h - \mathbf{u}_i\| &\leq C \left(h\lambda_i^{1/(2m)}\right)^{\sigma}.
\end{aligned} \tag{2.17}$$

Due to the smallness condition, these approximation estimates only hold for the lower part of the spectrum up to some wave number $i \ll n$. Nevertheless, in [64] it could be shown numerically that the whole spectrum of eigenfunctions can be approximated much more accurately with smooth splines than with C^0 finite elements.

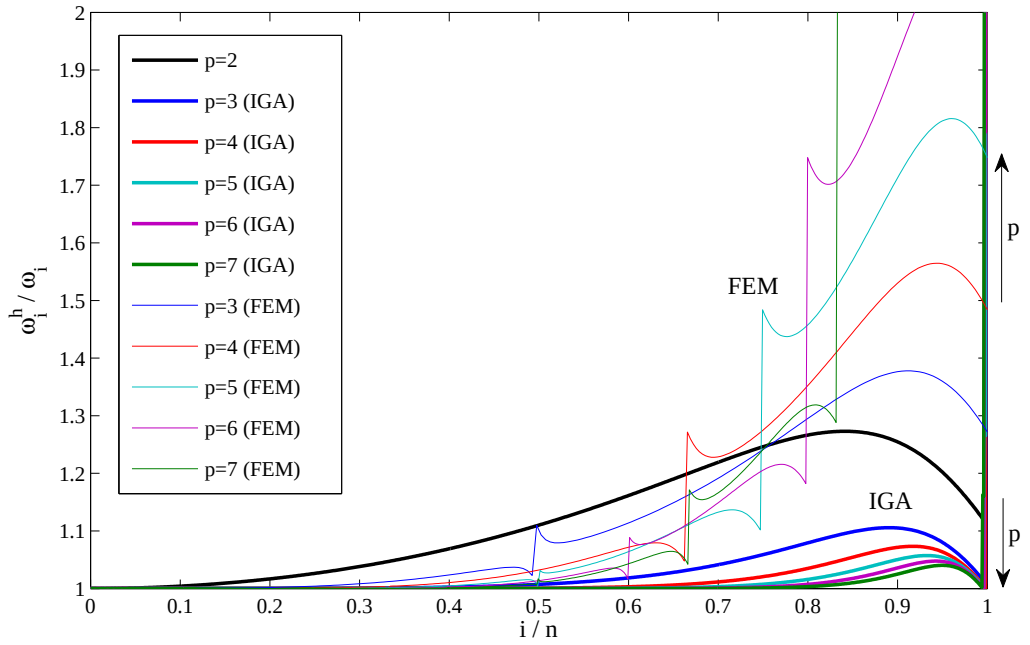

Figure 2.7: Comparison of discrete spectra of eigenfrequencies ω_i^h/ω_i for a linear beam for C^1-continuous p-method (FEM) and C^{p-1}-continuous k-method (IGA)

Time-dependent problems

The impact of approximation accuracy of eigenvalues and eigenfunctions on time-dependent problems, such as parabolic and hyperbolic linear PDEs, was also investigated in [64]. In the error estimates of parabolic problems, the influence of poorly approximated higher modes is damped out by an exponentially decaying factor $e^{\lambda_i t}$. In contrast to that, for hyperblic problems, as they are treated in this thesis, the errors in higher modes and in the modal projection of the initial data persist for all time. Thus significant errors in eigenfunctions, as they occur for standard FEM already in the mid and higher spectrum, can also significantly contribute to the error of the time-dependent solution, especially in nonlinear applications. In these situations much more accurate results can be expected from IGA, since approximation quality of higher modes is much better.

Computational costs

An important argument for the use of IGA or FEM in practical applications are the computational costs, which mainly consist of the assembly of the stiffness matrix (2.12) and solution of the linear system (2.13). [19, 105] feature comparisons of the influence of continuity of basis functions, C^0 (FEM) or C^{p-1} (IGA), on computational costs:

Assuming periodicity boundary conditions of maximal continuity and $r = d$, the number of DOFs is $N = p^d \ell$ for C^0 and $N = \ell$ for C^{p-1} basis functions. In both cases the local, element-wise contributions to the stiffness matrix have to be computed using numerical quadrature with a cost of $\mathcal{O}(p^{2d})$ operations per quadrature point, independent of the continuity. Using Gaussian quadrature with $(p+1)^d$ points per element, we have $\ell(p+1)^d$ points in total. In terms of N, this means $\mathcal{O}(Np^{3d})$ operations in the C^0 case and $\mathcal{O}(Np^{3(d+1)})$ in the C^{p-1} case. Thus assembly is more costly for the same number of DOFs in IGA than in FEM. To alleviate this disadvantage of IGA and reduce the quadrature

effort, advanced quadrature [8, 66] and assembly strategies have been developed [71, 82].

Higher continuity also influences the number of nonzeros of the stiffness matrix and its sparsity pattern. In the C^0 case the total number of nonzeros is $\text{nnz} = (p+2)^d p^d \ell = (p+2)^d N$, while it is $\text{nnz} = (2p+1)^d \ell = (2p+1)^d N$ for C^{p-1} basis functions [19]. So for same N there are more nonzeros in the IGA stiffness matrix, i.e. it is more densely-populated than a FEM matrix. This has a severe impact on the performance of linear algebra solvers used to solve the system (2.13). Direct solvers consume more memory for IGA then for FEM and solution times are longer. The performance of iterative solvers mainly depends on the number of iterations, the cost of one iteration, and preconditioning and was investigated in [36]. Preconditioning techniques have been adapted to IGA to make iterative solution of large systems more efficient, where a summary of methods, including Overlapping Schwarz, BPX, BDDC, multigrid, and FETI, is presented in [19].

In a competitive isogeometric finite element analysis software library, which could keep up with established and commercial finite element analysis codes and software regarding computational times, the above-mentioned quadrature strategies and solution techniques should be implemented. However, due to limited time and resources, they could not be considered in the `IGAsolvers` software developed within the course of this thesis [121].

2.3 Multi-patch parameterizations

So far we have assumed that the physical domain Ω can be represented by a geometry function in terms of a single spline geometry, see (2.8) and (2.9). However, complex engineering designs available as CAD models can usually not be represented as a single, tensor product spline geometry, since the topology of the object differs from a rectangle in 2D or a cube in 3D [40]. Then an isogeometric analysis suitable parameterization has to be generated by splitting the object into several parts (patches), with geometry functions mapping reference domains onto the physical domains for each patch. In the following we describe the treatment of multi-patch domains in isogeometric finite element analysis.

2.3.1 Formulation of multi-patch problems

In a multi-patch problem we have a partition of the initial domain Ω into b subdomains (patches):

$$\overline{\Omega} = \bigcup_{i=1}^{b} \overline{\Omega^i}, \quad \Omega^i \cap \Omega^j = \emptyset. \tag{2.18}$$

If two patches Ω_i and Ω_j are adjacent, i.e.

$$\overline{\Omega^i} \cap \overline{\Omega^j} = \Gamma^{ij} \neq \emptyset, \tag{2.19}$$

we call Γ^{ij} the interface between Ω^i and Ω^j.

To find the solution $\mathbf{u} \in \mathcal{S}$ of the general PDE problem, see (2.7), we have to solve it on each patch for $\mathbf{u}^i = \mathbf{u}|_{\Omega^i}$ and need to add constraints for the displacements to be continuous on the interfaces of the patches:

$$i = 1, \dots, b: \ \mathbf{u}^i \in \mathcal{S}^i = \mathcal{S}|_{\Omega^i} : \begin{cases} a(\mathbf{v}^i, \mathbf{u}^i) &= l(\mathbf{v}^i) & \forall\, \mathbf{v}^i \in \mathcal{V}^i = \mathcal{V}|_{\Omega^i}, \\ \mathbf{u}^i &= \mathbf{u}^j & \text{on } \Gamma^{ij}. \end{cases} \tag{2.20}$$

Parameterization of the geometry of the object is now given by a set of geometry functions $\mathbf{g}^i : \Omega_0^i \to \Omega^i$ as spline geometries for each patch, compare (2.8) and (2.9).

Even though IGA claims to bridge the gap between design and analysis, multi-patch parameterizations of real-life objects as spline volumes are not trivially found. Typically in CAD only the boundary surfaces of an object are represented and multi-patch spline volume parameterizations have to be generated based on these surface descriptions. These parameterizations may only approximate the original CAD geometries and do not necessarily represent them exactly. Automated methods for segmentation into patches and parameterization of patches are still under development [70, 74, 89]. In fact, for a smooth and lossless *isogeometric* design through analysis process, the incorporation of spline functions into numerical methods is not enough, it also requires a change in the product design approach [45].

An example can be found in Figure 3.8 in Section 3.5.2, which shows the geometry of the "TERRIFIC Demonstrator" as CAD model and an analysis-suitable multi-patch parameterization consisting of 15 volume patches.

2.3.2 Enforcement of continuity constraints

For the solution of the multi-patch PDE problem (2.20), discrete isogeometric finite element solution spaces $\mathcal{S}^{h^i} \subset \mathcal{S}^i$ and test function space $\mathcal{V}^{h^i} \subset \mathcal{V}^i$ have to be generated based on the patch-wise geometry functions $\mathbf{g}_i$, as in (2.10). Then stiffness matrices $\mathbf{K}^i$ and force vectors $\mathbf{b}^i$ can be assembled for each patch as in (2.12).

Furthermore, the continuity constraints $\mathbf{u}^i = \mathbf{u}^j$ on Γ^{ij} have to be discretized and enforced. Thereby in general two cases can be distinguished: conforming and non-conforming parameterizations.

Conforming parameterizations

A multi-patch model has conforming parameterizations, when

$$\mathbf{g}_i|_{\Gamma_{ij}} \equiv \mathbf{g}_j|_{\Gamma_{ij}} \; \forall \, \Gamma_{ij}. \tag{2.21}$$

In a 3D model this means that the two spline surfaces $\mathbf{g}_i|_{\Gamma_{ij}}$ and $\mathbf{g}_j|_{\Gamma_{ij}}$ of the neighboring patches i and j of the interface Γ_{ij} must be identical, i.e. degrees, knot vectors, weights and control points of the geometry functions coincide. Then the continuity constraint for the discretized solutions $\mathbf{u}^{h^i}$ and $\mathbf{u}^{h^j}$ is simply that corresponding displacement control points $\mathbf{d}_k^i$ and $\mathbf{d}_l^j$ have to be equal whenever the associated geometry control points $\mathbf{v}_k^i$ and $\mathbf{v}_l^j$ are equal, i.e.

$$\mathbf{d}_k^i = \mathbf{d}_l^j \quad \forall \, \mathbf{d}_k^i, \; \mathbf{d}_l^j \text{ with } \mathbf{v}_k^i = \mathbf{v}_l^j. \tag{2.22}$$

For the enforcement of these constraints basically two implementation strategies exist:

(a) ***Elimination***: If $\mathbf{d}_k^i$ and $\mathbf{d}_l^j$ are two corresponding displacement control points in patches i and j, the l-th row and column from $\mathbf{K}^j$ are removed and added to the k-th row and column of $\mathbf{K}^i$, same for the right hand side vectors $\mathbf{b}^i$ and $\mathbf{b}^j$. Assembly of

the global stiffness matrix looks like this:

$$\hat{\mathbf{K}} = \begin{pmatrix} \hat{\mathbf{K}}^1 & * & * & \cdots & * \\ * & \hat{\mathbf{K}}^2 & * & \cdots & * \\ * & * & \ddots & \ddots & \vdots \\ \vdots & \vdots & \ddots & \ddots & * \\ * & * & \cdots & * & \hat{\mathbf{K}}^b \end{pmatrix}, \quad \hat{\mathbf{d}} = \begin{pmatrix} \hat{\mathbf{d}}^1 \\ \hat{\mathbf{d}}^2 \\ \vdots \\ \vdots \\ \hat{\mathbf{d}}^b \end{pmatrix}, \quad \hat{\mathbf{b}} = \begin{pmatrix} \hat{\mathbf{b}}^1 \\ \hat{\mathbf{b}}^2 \\ \vdots \\ \vdots \\ \hat{\mathbf{b}}^b \end{pmatrix} \tag{2.23}$$

Here $\hat{\mathbf{K}}^i$ denotes that some DOFs, i.e. rows and columns, might have been removed from $\mathbf{K}^i$ and $*$ denotes that these blocks might be zero, or contain some contributions from other blocks in terms of added rows and columns. The size of the global stiffness matrix $\mathbf{K}$ is then Nr minus the number of constraints and the block structure is broken up.

(b) ***Lagrangian multipliers***: It is also possible to assemble the patch stiffness matrices $\mathbf{K}^i$ into one big block-structured matrix and then add the constraints $\mathbf{d}_k^i = \mathbf{d}_l^j$ by a Lagrangian multiplier approach as $\boldsymbol{\lambda}_{kl}^{ij}(\mathbf{d}_k^i - \mathbf{d}_l^j) = 0$:

$$\mathbf{K}^* = \begin{pmatrix} \mathbf{K}^1 & \mathbf{0} & \cdots & \mathbf{0} & \mathbf{B}^{12T} & \mathbf{0} \\ \mathbf{0} & \mathbf{K}^2 & \cdots & \mathbf{0} & & \\ \vdots & \vdots & \ddots & \vdots & \mathbf{0} & \mathbf{B}^{ijT} \\ \mathbf{0} & \mathbf{0} & \cdots & \mathbf{K}^b & \vdots & \mathbf{0} \\ \mathbf{B}^{12} & & \mathbf{0} & \cdots & \mathbf{0} & \mathbf{0} \\ \mathbf{0} & & \mathbf{B}^{ij} & \mathbf{0} & \mathbf{0} & \mathbf{0} \end{pmatrix}, \quad \mathbf{d}^* = \begin{pmatrix} \mathbf{d}^1 \\ \mathbf{d}^2 \\ \vdots \\ \mathbf{d}^b \\ \boldsymbol{\lambda}^{12} \\ \boldsymbol{\lambda}^{ij} \end{pmatrix}, \quad \mathbf{b}^* = \begin{pmatrix} \mathbf{b}^1 \\ \mathbf{b}^2 \\ \vdots \\ \mathbf{b}^b \\ \mathbf{0} \\ \mathbf{0} \end{pmatrix} \tag{2.24}$$

Each row of the matrices $\mathbf{B}^{ij}$ contains a 1 at the location of column k of block $\mathbf{K}^i$ and a -1 at column l of block $\mathbf{K}^j$. The linear system described by (2.24) has a saddle point structure, which is discussed further in Section (2.3.3).

Theorem 2.1. *The displacement vector* $\boldsymbol{d}$ *of a multi-patch problem obtained using Lagrangian multipliers is equal the one obtained using elimination.*

Proof. We use the following notations:

$$\mathbf{K} = \operatorname{diag}(\mathbf{K}^1, \ldots, \mathbf{K}^b) \in \mathbb{R}^{n \times n},$$
$$\mathbf{d} = ({\mathbf{d}^1}^T, \ldots, {\mathbf{d}^b}^T)^T \in \mathbb{R}^n, \quad \mathbf{b} = ({\mathbf{b}^1}^T, \ldots, {\mathbf{b}^b}^T)^T \in \mathbb{R}^n,$$

for the stiffness matrix, displacement and load vector of the multi-patch system before elimination of DOFs or application of constraints and it holds $\operatorname{rg}(\mathbf{K}) = r < n$.

Equation (2.24) with Lagrangian multipliers is now written more compactly as

$$\begin{aligned} \mathbf{K}\,\mathbf{d} + \mathbf{B}^T\,\boldsymbol{\lambda} &= \mathbf{b}, \\ \mathbf{B}\,\mathbf{d} &= \mathbf{0}, \end{aligned}$$

where $\mathbf{B} \in \mathbb{R}^{m \times n}$, $m = n - r$, is the constraint matrix of rank m with exactly one 1 and one -1 in each row and $\boldsymbol{\lambda} \in \mathbb{R}^m$ is the vector of Lagrangian multipliers.

Assuming that there exists a projection matrix $\mathbf{C} \in \mathbb{R}^{n \times r}$ of rank r and a vector of reduced DOFs $\hat{\mathbf{d}} \in \mathbb{R}^r$ such that

$$\mathbf{d} = \mathbf{C}\,\hat{\mathbf{d}},$$

it follows:

$$\begin{aligned} \mathbf{K}\mathbf{C}\,\hat{\mathbf{d}} + \mathbf{B}^T\,\boldsymbol{\lambda} &= \mathbf{b}, \\ \mathbf{B}\mathbf{C}\,\hat{\mathbf{d}} &= \mathbf{0}. \end{aligned}$$

Left-multiplication of the first equation with $\mathbf{C}^T$, which is a rank-conserving transformation on $\mathbb{R}^r$, yields

$$\begin{aligned} \mathbf{C}^T\mathbf{K}\mathbf{C}\,\hat{\mathbf{d}} + \mathbf{C}^T\mathbf{B}^T\,\boldsymbol{\lambda} &= \mathbf{C}^T\mathbf{b}, \\ \mathbf{B}\mathbf{C}\,\hat{\mathbf{d}} &= \mathbf{0}. \end{aligned}$$

If we showed that $\mathbf{BC} = \mathbf{O}$, where $\mathbf{O} \in \mathbb{R}^{m \times r}$ is the $m \times r$ null matrix, it would only remain the equation

$$\mathbf{C}^T\mathbf{K}\mathbf{C}\,\hat{\mathbf{d}} = \mathbf{C}^T\mathbf{b},$$

and using $\hat{\mathbf{K}} = \mathbf{C}^T\mathbf{K}\mathbf{C}$ and $\hat{\mathbf{b}} = \mathbf{C}^T\mathbf{b}$, it would be the same system as in (2.23), i.e.

$$\hat{\mathbf{K}}\,\hat{\mathbf{d}} = \hat{\mathbf{b}}.$$

A matrix $\mathbf{C}$ which yields $\mathbf{BC} = \mathbf{O}$ can easily be found: it is a boolean matrix with exactly one 1 in each row and at least one 1 in each column, where the total number of 1s is n. This matrix is exactly the one which assigns each of the displacement control points in $\mathbf{d}$ to one of the DOFs in $\hat{\mathbf{d}}$ after elimination and adds the stiffness matrix contributions of an eliminated DOF from $\mathbf{K}$ to the row and column of the matrix after elimination $\hat{\mathbf{K}}$. □

Remark 2.2. *Implementation strategies for conforming parameterizations can also be extended to situations where one geometry function is an h-refinement of the other, as described in [40]. This allows a simple kind of "local" refinement using multiple patches.*

Remark 2.3. *The Lagrangian multiplier strategy can also be used to implement general Dirichlet-type boundary conditions such as*

- *prescription of displacements:* $\boldsymbol{u}|_{\Gamma_D} = \boldsymbol{h}$,
- *symmetry of displacements w.r.t. normal direction:* $(\boldsymbol{u} \cdot \boldsymbol{n})|_{\Gamma_D} = \boldsymbol{0}$,
- *periodicity of displacements at faces of one parameter direction:* $\boldsymbol{u}|_{\Gamma_{\xi^i=0}} = \boldsymbol{u}|_{\Gamma_{\xi^i=1}}$,

where the boundary $\Gamma_D \subset \Gamma$ *can be a face of the topological cube (or a iso-subface), an isoline on a face (or a subline) or a point on a face.* $\Gamma_{\xi^i=0}$ *and* $\Gamma_{\xi^i=1}$ *refer to the faces of the topological cube, where the parameter direction* i *is fixed at the minimal resp. maximal value.*

Non-conforming parameterizations

This is the most general case, as parameterizations of the patches can be chosen arbitrarily, i.e. degrees, knot vectors and number of control points may be different. Continuity constraints have to be enforced weakly by methods such as Nitsche's method [3, 104], penalty methods, mortar or Lagrangian multiplier methods [29, 61] and augmented Lagrangian multiplier methods. These methods mostly have its origins in domain decomposition

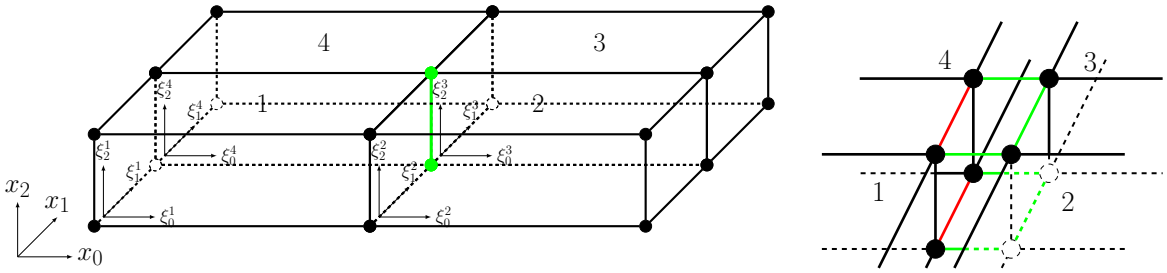

(a) Geometry with the common edge in green. Constraints on two control points of each patch have to be enforced

(b) Constraints in red are not enforced to avoid redundancies

Figure 2.8: Four cubes joining in one edge

of classical FEM and a summary of application in isogeometric multi-patch analysis is provided in [3].

Due to the design of libraries used for the implementation of software developed in the course of this thesis, the methods and applications presented here are restricted to conforming parameterizations. Both presented approaches for treatment of continuity constraints, Lagrangian multipliers and elimination, have been implemented [121].

2.3.3 Saddle point problems

As described above by (2.24), the Lagrangian multiplier approach for implementation of multi-patch coupling constraints and Dirichlet-type boundary conditions leads to the solution of a saddle point problem, i.e. a linear equation system of the form

$$\mathbf{K}^* \, \mathbf{d}^* = \mathbf{b}^* \quad \Leftrightarrow \quad \begin{pmatrix} \mathbf{K} & \mathbf{B}^T \\ \mathbf{B} & \mathbf{0} \end{pmatrix} \begin{pmatrix} \mathbf{d} \\ \boldsymbol{\lambda} \end{pmatrix} = \begin{pmatrix} \mathbf{b} \\ \mathbf{c} \end{pmatrix}, \tag{2.25}$$

where $\mathbf{K} \in \mathbb{R}^{n \times n}$, $\mathbf{B} \in \mathbb{R}^{m \times n}$, $n > m$. The entries of $\mathbf{c}$ are zero and may contain nonzeros only when inhomogeneous Dirichlet conditions are included, see Remark 2.3.

Saddle point problems arise in many engineering and scientific applications, especially also in mixed formulations [20, 23], which we address in the isogeometric context later on in Chapter 6. Thus we want to take a closer look at their properties and numerical solution methods, where [22] serves as a main reference.

Solvability conditions

In our case the matrix $\mathbf{K}$ arising from (2.24) is symmetric and positive semi-definite. If Dirichlet boundary conditions had been incorporated into the patch-wise matrices, which is usually not the case for all patches, it would be symmetric positive definite. For $\mathbf{K}$ to be non-singular and (2.25) to have a unique solution a necessary and sufficient condition is that $\mathbf{B}$ has full rank and $\ker(\mathbf{K}) \cap \ker(\mathbf{B}) = \{0\}$ [22].

The full rank condition $\mathrm{rg}(\mathbf{B}) = m$ is not trivially fulfilled for the multi-patch coupling matrix arising from (2.24). This can be demonstrated by a simple example of four cubes joining in one edge, see Figure 2.8(a), or even simpler in 2D by four squares joining in one vertex. The constraint matrix for the common edge highlighted in green resp. one of

the common control points would look like this:

$$\mathbf{B} = \begin{pmatrix} \cdots & 1 & \cdots & -1 & \cdots & 0 & \cdots & 0 & \cdots \\ \cdots & 0 & \cdots & 1 & \cdots & -1 & \cdots & 0 & \cdots \\ \cdots & 0 & \cdots & 0 & \cdots & 1 & \cdots & -1 & \cdots \\ \cdots & -1 & \cdots & 0 & \cdots & 0 & \cdots & 1 & \cdots \end{pmatrix}. \tag{2.26}$$

By summing up all rows it can be easily seen that this matrix is singular and that $\mathrm{rg}(\mathbf{B}) = 3$. This means that one of the constraints is redundant and not to be enforced, as shown in Figure 2.8(b).

To avoid such redundancies and set up the global constraint matrix, an approach from graph theory can be used: every control point located on an interface is a vertex and every constraint is an edge of a directed graph. Then the constraint matrix $\mathbf{B}$ can be interpreted as incidence matrix of that directed graph with vertices in columns and edges in rows. Finding a full rank sub-matrix of $\mathbf{B}$ is then equivalent to finding a forest or spanning tree of the (undirected) graph, which can be done by a breadth-first or depth-first search algorithm [129]. In other words, we only include the constraints resp. rows in $\mathbf{B}$ which correspond to the edges contained in the forest of the graph.

We do not explicitly check if the condition $\ker(\mathbf{K}) \cap \ker(\mathbf{B}) = \{0\}$ is fulfilled, but we expect it due to the following considerations. In a 3-dimensional elasticity problem, one needs to restrict 6 degrees of freedom (3 translations and 3 rotations) of the structure for the stiffness matrix to be non-singular. When no Dirichlet boundary conditions are applied to each of the patch-wise stiffness matrices, we can expect that $\mathrm{rg}(\mathbf{K}) = n - 6b$. However, since the patch-wise matrices defining $\mathbf{K}$ are not coupled, a basis of $\ker(\mathbf{K})$ must be partitioned by patches, i.e. there are 6 basis vectors which are nonzero for the DOFs corresponding to a certain patch and are zero for all other DOFs. In contrast to that, a basis of $\ker(\mathbf{B})$ must involve nonzero DOFs for at least two patches due to the structure of $\mathbf{B}$.

Remark 2.4. *For the numerical examples presented in this thesis a breadth-first search algorithm was implemented to determine a full rank constraint matrix of interface and Dirichlet-type constraints.*

Solution methods

Having guaranteed that a unique solution of the saddle point problem (2.25) exist, a numerical algorithm must be selected to actually solve it. However, saddle point problems may be ill-conditioned, especially when $\mathbf{K}$ is only positive semi-definite and the underlying (isogeometric) finite element spaces are h-refined, which is deteriorating the rate of convergence of iterative solvers and increasing the need of preconditioning [22]. A summary of different coupled and segregated solution methods for saddle point problems in general is also given in [22], including direct and iterative solvers with suitable preconditioners. For isogeometric multi-patch problems the so-called IETI method (Isogeometric Tearing and Interconnecting) as an adaption of FETI method was proposed in [75].

Remark 2.5. *In our computational applications for the solution of the saddle point problem* (2.25) *usually a sparse direct linear solver is used. Preconditioning for iterative solvers as described above was not implemented due to a different focus set in this work.*

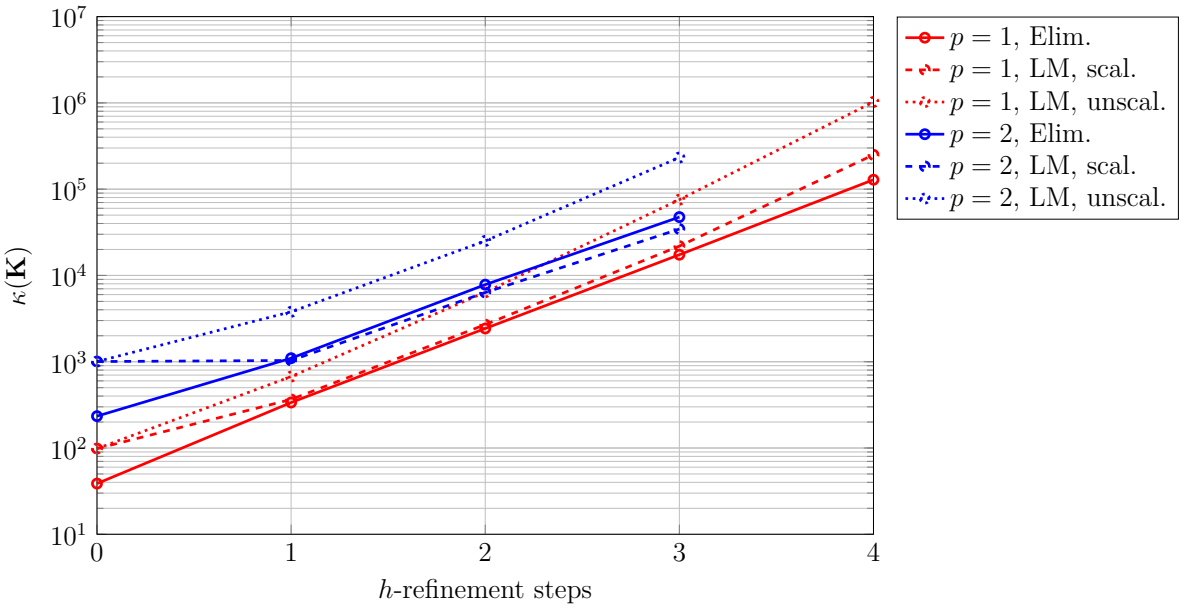

Figure 2.9: Comparison of condition numbers κ of stiffness matrix $\mathbf{K}$ from multi-patch implementations using elimination (Elim.) and Lagrangian multipliers (LM) with and without scaling (scal., unscal.). h- and k-refinement are performed for degree $p = 1, 2$.

2.3.4 Numerical study of multi-patch implementations

In the following we compare the two implementation strategies *elimination* and *Lagrangian multipliers* for conforming multi-patch parameterizations presented in Section 2.3.2 regarding condition number of the stiffness matrix of the linear system.

The problem discretized with isogeometric finite elements is a simplification of 3-dimensional linear elasticity, see later Section 3.3, with bilinear form

$$a(\mathbf{v}, \mathbf{u}) = \frac{\mu}{2} \int_{\Omega} \left(\nabla \mathbf{v} + \nabla \mathbf{v}^T \right) : \left(\nabla \mathbf{u} + \nabla \mathbf{u}^T \right) \, d\mathbf{x}. \tag{2.27}$$

The domain $\Omega \subset \mathbb{R}^3$ consists of four patches as unit cubes sharing one common edge, see Figure 2.8. The patch domains Ω^i are parameterized with linear B-Splines with knot vectors $(0, 0, 1, 1)^3$. Of course, it is also possible to represent this domain with a single patch of width and depth 2 and height 1, even with an equivalent parameterization using knot vectors $(0, 0, 1, 2, 2) \times (0, 0, 1, 2, 2) \times (0, 0, 1, 1)$.

For this problem the stiffness matrix $\mathbf{K}$ is assembled for different uniform refinements of degree p and mesh parameter h. Then the condition number

$$\kappa(\mathbf{K}) = \left| \frac{\lambda_{\max}(\mathbf{K})}{\lambda_{\min}(\mathbf{K})} \right|, \tag{2.28}$$

i.e. the ratio of maximal to minimal eigenvalue of the matrix, is computed as a measure of the accuracy of the numerical solution of the linear system to be solved.

Figure 2.9 shows the development of the condition number $\kappa(\mathbf{K})$ over several h-refinement steps for $p = 1, 2$ with $\mathbf{K}$ either coming from a multi-patch implementation with

p	h-steps	0	1	2	3	4
1	$N_{Elim.}$	54	225	1,215	7,803	55,539
1	N_{LM}	150	435	1,797	9,705	62,385
1	N-ratio	36%	52%	68%	80%	89%
2	$N_{Elim.}$	225	588	2,178	10,830	66,150
2	N_{LM}	423	948	3,006	13,170	73,818
2	N-ratio	53%	62%	72%	82%	90%

Table 2.1: Comparison of number of degrees of freedom N and DOF-ratios for multi-patch constraint implementations using elimination (Elim.) and Lagrangian multipliers (LM)

elimination (*Elim.*), i.e. $\hat{\mathbf{K}}$ from (2.23), or Lagrangian multipliers (*LM*), i.e. $\mathbf{K}^*$ from (2.24). Elimination is (except for sorting of degrees of freedom) equivalent to the single-patch parameterization and thus gives the same condition number of the matrix. When Lagrangian multipliers are used, scaling of the constraints is an important factor: in the case *unscal.* the constraints are implemented using 1 and -1, see (2.26), while in the case *scal.* a scaling factor f_{ij} for each constraint on Γ_{ij} was introduced as

$$f_{ij} = \frac{1}{2}\left(\mu^i + \mu^j\right) \cdot \frac{1}{2} \cdot \frac{\mathrm{vol}(\Omega^i) + \mathrm{vol}(\Omega^j)}{\sqrt{\ell^i \cdot \ell^j}}, \tag{2.29}$$

which averages the material parameters μ, volume of patches $\mathrm{vol}(\Omega)$ and mesh refinement as number of elements ℓ of both patches involved. This scaling factor is then of similar magnitude as the entries of the stiffness matrix.

As expected, the condition number of the unscaled Lagrangian multiplier approach is the worst, almost an order of magnitude above the elimination approach. However, with an appropriate scaling of constraints the condition number of the scaled LM approach stays on the same level as elimination.

We can conclude that scaling of constraints is important factor in improving the condition number of the stiffness matrix of a multi-patch implementation with Lagrangian multipliers. However, elimination still provides two major advantages: $\mathbf{K}$ is not only symmetric, but also positive definite, which allows the use of iterative solvers for large problems, and the total number of DOFs is smaller, see Table 2.1, which reduces solution time for any linear solution method used, but especially for direct solvers.

2.4 Summary

Isogeometric analysis and isogeometric finite element discretizations are essential foundations of the methods we develop and present in this thesis.

Since CAD and IGA both heavily rely on spline functions and spline geometries, we have recapitulated the fundamental definitions and properties of B-Splines and NURBS basis functions and geometries.

Then we have introduced the isogeometric finite element discretization of a general PDE problem and reviewed its main properties. Especially relevant in this work are the advantages over classical FE in modal analysis and higher accuracy per DOF, which are a result of the higher inter-element continuity of the spline-based k-method (IGA) compared to piecewise polynomial formulations with C^0-continuity, i.e. the p-method or FEM.

Isogeometric analysis of complex 3D geometries very often requires a multi-patch decomposition of the domain into several spline volumes. Thus we have outlined two methods for enforcement of coupling constraints of conforming multi-patch parameterizations, namely elimination and Lagrangian multipliers (LM). We have shown analytically and numerically that both methods lead to the same result. As the Lagrangian multiplier approach requires the solution of a saddle point problem, we have also discussed properties and solution methods of those. Furthermore, we have shown that scaling of coupling constraints is important when LM are used and has a great impact on the condition number of the linear system to be solved.

The theory on saddle point problems is going to become relevant again in Chapter 6, when incompressible problems are going to be treated with mixed methods.

3 Isogeometric finite elements in nonlinear elasticity

As a first step towards nonlinear frequency analysis, we now apply the isogeometric finite element method, which we have already introduced in preceding Chapter 2, for the spatial semi-discretization of nonlinear continuum mechanics and dynamics.

First, we give a basic introduction to the 3-dimensional continuum mechanics background, i.e. kinematics, constitutive laws for hyperelasticity and visco-hyperelasticity, and governing partial differential equations in Section 3.1. Then we apply the isogeometric finite element discretization to nonlinear elasticity, present solution methods for the arising nonlinear equation system of elastostatics and review its properties in Section 3.2. Furthermore, we include brief descriptions of linear elasticity (Section 3.3) and of the nonlinear Euler-Bernoulli beam model (Section 3.4), since these problems are also relevant for feasibility, validation and benchmarking of nonlinear methods. Finally, in Section 3.5, we use computational examples to demonstrate the properties of the isogeometric approach and validate the implementations.

3.1 Continuum mechanics introduction

An introduction into continuum mechanics is given based on the monographs [20, 35, 83, 130]. The focus lies on ingredients necessary for the (isogeometric) finite element formulation of nonlinear elasticity, which is then introduced in Section 3.2.

3.1.1 Kinematics

Motion and deformation of a solid body over time can be described with respect to its *initial* or *reference configuration* given by the domain $\bar{\Omega}$, the closure of an open, bounded and connected set $\Omega \in \mathbb{R}^3$. At every time $t \in \mathbb{R}^+$, the *current* position $\mathbf{y} \in \Omega_t \subset \mathbb{R}^3$ of each *material* point $\mathbf{x} \in \Omega$ can be expressed in terms of its initial position and a *displacement* vector field $\mathbf{u} : \Omega \times \mathbb{R}^+ \to \mathbb{R}^3$ (see also Figure 3.1):

$$\mathbf{y}(\mathbf{x}, t) = \mathbf{x} + \mathbf{u}(\mathbf{x}, t). \tag{3.1}$$

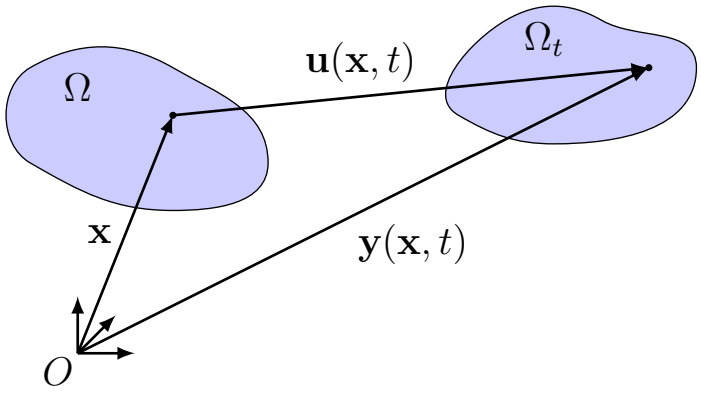

Figure 3.1: Motion of a solid body with domain Ω. At time t the current position $\mathbf{y}$ of a material point is given in terms of its initial position $\mathbf{x}$ and displacement $\mathbf{u}$

The term *Lagrangian configuration* is used when deformation is described with respect to the initial, reference or material coordinates $\mathbf{x}$. It is also possible to use the *Eulerian description*, where deformation is expressed with respect to the current or spatial coordinates $\mathbf{y}$. In the following all kinematic and other quantities are only referring to the Lagrangian configuration.

Deformation gradient

For the description of the deformation process we need a tensor, which maps material line elements $d\mathbf{x}$ onto spatial line elements $d\mathbf{y}$:

$$d\mathbf{y} = \mathbf{F}\, d\mathbf{x}. \tag{3.2}$$

This *deformation gradient* $\mathbf{F} : \Omega \times \mathbb{R}^+ \to \mathbb{R}^{3\times 3}$ can be expressed as the gradient of current position with respect to initial position of each material point:

$$\mathbf{F}(\mathbf{x},t) = \frac{d\mathbf{y}}{d\mathbf{x}}(\mathbf{x},t) = \mathbf{I} + \frac{d\mathbf{u}}{d\mathbf{x}}(\mathbf{x},t) = \mathbf{I} + \nabla\mathbf{u}(\mathbf{x},t). \tag{3.3}$$

Since the mapping in (3.2) must be bijective and self-penetration of the body is excluded, the Jacobian determinant $J = \det\mathbf{F}$ must not be singular and $J > 0$. J is a measure of the volume change of the body and for incompressible materials, which are addressed separately in Chapter 6, it must hold $J \equiv 1$.

Strain measures

Furthermore we need strain measures defined in the initial configuration, such as the *Green-Lagrange strain tensor*:

$$\mathbf{E}(\mathbf{x},t) = \frac{1}{2}\Big(\mathbf{C}(\mathbf{x},t) - \mathbf{I}\Big). \tag{3.4}$$

It is defined using the *right Cauchy-Green tensor*

$$\mathbf{C}(\mathbf{x},t) = \mathbf{F}^T\mathbf{F} = \mathbf{I} + \nabla\mathbf{u}^T + \nabla\mathbf{u} + \nabla\mathbf{u}^T\nabla\mathbf{u}, \tag{3.5}$$

which is a quadratic expression in terms of the deformation gradient $\mathbf{F}$ resp. the displacement gradient $\nabla\mathbf{u}$.

Time derivatives

For time-dependent problems and in the case of history resp. time-dependent constitutive laws the time-derivatives of kinematic quantities also need to be considered. The velocity and acceleration of a material point in the reference configuration read as:

$$\begin{aligned} \mathbf{v}(\mathbf{x},t) &= \frac{d\mathbf{y}}{dt} = \dot{\mathbf{y}}(\mathbf{x},t) = \dot{\mathbf{u}}(\mathbf{x},t), \\ \mathbf{a}(\mathbf{x},t) &= \frac{d^2\mathbf{y}}{dt^2} = \ddot{\mathbf{y}}(\mathbf{x},t) = \ddot{\mathbf{u}}(\mathbf{x},t). \end{aligned} \tag{3.6}$$

The time-derivative of the deformation gradient is

$$\dot{\mathbf{F}}(\mathbf{x},t) = \nabla\dot{\mathbf{u}} = \nabla\mathbf{v}, \tag{3.7}$$

and of the Green-Lagrange and Cauchy-Green strain tensor it is

$$\dot{\mathbf{E}}(\mathbf{x},t) = \frac{1}{2}\dot{\mathbf{C}}(\mathbf{x},t) = \frac{1}{2}\left(\mathbf{F}^T\dot{\mathbf{F}} + \dot{\mathbf{F}}^T\mathbf{F}\right). \tag{3.8}$$

3.1.2 Balance equations

With the kinematic quantities introduced in the preceding Section 3.1.1, we can follow [20, 130] in formulating the strong form of local balance differential equations in the Lagrangian configuration. These must hold for all material points $\mathbf{x} \in \Omega$ at times $t \in \mathbb{R}^+$.

ρ_0 being the initial and ρ the current mass density of the object, the *conservation of mass* reads as

$$\int_{\Omega_t} \rho(\mathbf{y},t)d\mathbf{y} = \int_{\Omega} \rho_0(\mathbf{x})d\mathbf{x}, \tag{3.9}$$

which can be simplified to:

$$\rho J = \rho_0. \tag{3.10}$$

From the *conservation of linear momentum* the main partial differential equation describing motion of a body subject to volume forces $\rho_0\mathbf{b}$ is derived, *Cauchy's equation of motion*:

$$\operatorname{div}\mathbf{F}\,\mathbf{S} + \rho_0\mathbf{b} = \rho_0\ddot{\mathbf{u}}. \tag{3.11}$$

Local *balance of angular momentum* yields the symmetry of the second Piola-Kirchhoff (PK2) stress tensor

$$\mathbf{S} = \mathbf{S}^T, \tag{3.12}$$

and the *first law of thermodynamics*, i.e. conservation of energy, reads:

$$\rho_0\dot{u} = \mathbf{S}\cdot\dot{\mathbf{E}} - \operatorname{div}\mathbf{Q} + \rho_0 R, \tag{3.13}$$

where u is the specific internal energy, R the heat source and $\mathbf{Q}$ heat flux.

In addition to these equilibrium equations we need *boundary conditions* for displacements and tractions for the elastostatic problem:

$$\begin{aligned} \mathbf{u} &= \mathbf{h} \text{ on } \Gamma_u, \\ \mathbf{F}\,\mathbf{S}\,\mathbf{n} &= \mathbf{t} \text{ on } \Gamma_n, \end{aligned} \tag{3.14}$$

where $\Gamma_u, \Gamma_n \subset \partial\Omega$ are the parts of the boundary of the domain Ω where prescribed displacements $\mathbf{h}$ and $\mathbf{t}$ tractions act, and $\mathbf{n}$ is the outer surface normal of a boundary point.

Furthermore, for time-dependent elastodynamic problems also *initial conditions* for displacements $\mathbf{u}$ and velocities $\mathbf{v}$ are needed:

$$\mathbf{u}(\mathbf{x}, 0) = \hat{\mathbf{u}}, \quad \mathbf{v}(\mathbf{x}, 0) = \hat{\mathbf{v}} \quad \forall \mathbf{x} \in \Omega. \tag{3.15}$$

3.1.3 Hyperelastic constitutive laws

The local balance equations as introduced in Section 3.1.2 feature a stress measure, namely the *second Piola-Kirchhoff stress tensor* $\mathbf{S}$, which is also defined in the material configuration. It is related to the true Cauchy stress $\boldsymbol{\sigma}$ in the current configuration by the following equation:

$$\mathbf{S} = J\mathbf{F}^{-1}\boldsymbol{\sigma}\mathbf{F}^{-T}. \tag{3.16}$$

For many materials, such as steel, aluminum or rubber, the assumption of Green elasticity or *hyperelasticity* is valid, which means that the constitutive relation of strain and stress is defined by a potential ψ, the so-called *strain energy function*. We only deal with *isotropic* materials, which means that the response of the material is indifferent from the directions. The 2nd Piola-Kirchhoff stress can then be expressed as derivative of the strain energy function w.r.t. the Green-Lagrange or right Cauchy-Green strain tensors:

$$\mathbf{S} = \frac{d\psi}{d\mathbf{E}} = 2\frac{d\psi}{d\mathbf{C}}. \tag{3.17}$$

General hyperelastic materials

For isotropic materials it is possible to express the strain energy function in a very general way in terms of the invariants of the Cauchy-Green tensor:

$$\psi(\mathbf{C}) = \psi(I_C, II_C, III_C), \tag{3.18}$$

where the invariants can be expressed of the principal stretches, i.e. the roots λ_1, λ_2 and λ_3 of the eigenvalues of $\mathbf{C}$ ($\mathbf{C}$ is symmetric positive-definite):

$$\begin{aligned} I_C &= \lambda_1^2 + \lambda_2^2 + \lambda_3^2 = \operatorname{tr}(\mathbf{C}), \\ II_C &= \lambda_1^2\lambda_2^2 + \lambda_2^2\lambda_3^2 + \lambda_3^2\lambda_1^2 = \frac{1}{2}\left(\operatorname{tr}(\mathbf{C})^2 + \operatorname{tr}(\mathbf{C}^2)\right), \\ III_C &= \lambda_1^2\lambda_2^2\lambda_3^2 = \det \mathbf{C}. \end{aligned} \tag{3.19}$$

Then it follows for the 2nd Piola-Kirchhoff stress:

$$\mathbf{S} = 2\left[\left(\frac{\partial\psi}{\partial I_C} + I_C\frac{\partial\psi}{\partial II_C}\right)\mathbf{I} - \frac{\partial\psi}{\partial II_C}\mathbf{C} + III_C\frac{\partial\psi}{\partial III_C}\mathbf{C}^{-1}\right]. \tag{3.20}$$

Since the choice of ψ is still arbitrary and material parameters have to be fitted by experiments, in practice a few choices of strain-energy functions are commonly used, including Mooney-Rivlin, Ogden and Neo-Hookean laws [130].

Material laws used in this thesis

In this work we utilize to two commonly used choices of isotropic strain energy functions. The first is the linear *St. Venant-Kirchhoff* material law, which is also used in linear elasticity and restricted to large displacements and finite rotations but small strains:

$$\begin{aligned}\psi(\mathbf{E}) &= \frac{\lambda}{2}\,\mathrm{tr}(\mathbf{E})^2 + \mu\,\mathrm{tr}(\mathbf{E}^2),\\ \mathbf{S} &= \lambda\,\mathrm{tr}(\mathbf{E})\mathbf{I} + 2\mu\,\mathbf{E},\end{aligned} \tag{3.21}$$

The second is a particular choice of a nonlinear *Neo-Hookean* material law:

$$\begin{aligned}\psi(\mathbf{C}) &= \frac{\lambda}{2}\,(\ln J)^2 - \mu\,\ln J + \frac{\mu}{2}\,(\mathrm{tr}(\mathbf{C}) - 3)\,,\\ \mathbf{S} &= \lambda \ln J\,\mathbf{C}^{-1} + \mu\,(\mathbf{I} - \mathbf{C}^{-1}).\end{aligned} \tag{3.22}$$

Both material laws include two constitutive parameters, the so-called *Lamé constants* λ and μ, which can be computed from the modulus of elasticity E (Young's modulus) and Poisson's ratio ν:

$$\lambda = \frac{\nu E}{(1+\nu)(1-2\nu)}, \qquad \mu = \frac{E}{2(1+\nu)}. \tag{3.23}$$

The case of $\nu \to 0.5$ and $\lambda \to \infty$, i.e. (almost) incompressible material behavior, is addressed in Chapter 6.

Linearization

For linearization within the later described solution process the incremental constitutive 4th order tensor, or *elasticity tensor* is needed:

$$\mathbb{C} = \frac{d\mathbf{S}}{d\mathbf{E}} = \frac{d^2\psi}{d\mathbf{E}^2} = 2\frac{d\mathbf{S}}{d\mathbf{C}} = 4\frac{d^2\psi}{d\mathbf{C}^2} \tag{3.24}$$

For the St. Venant-Kirchhoff material it is

$$\mathbb{C}_{ijkl} = \lambda\,\delta_{ij}\delta_{kl} + \mu\,(\delta_{ik}\delta_{jl} + \delta_{il}\delta_{kj})\,, \quad i,j,k,l = 1,2,3, \tag{3.25}$$

and for the Neo-Hookean material

$$\mathbb{C}_{ijkl} = \lambda\,\mathbf{C}^{-1}_{ij}\mathbf{C}^{-1}_{kl} + (\mu - \lambda\ln J)\left(\mathbf{C}^{-1}_{ik}\mathbf{C}^{-1}_{jl} + \mathbf{C}^{-1}_{il}\mathbf{C}^{-1}_{kj}\right), \quad i,j,k,l = 1,2,3. \tag{3.26}$$

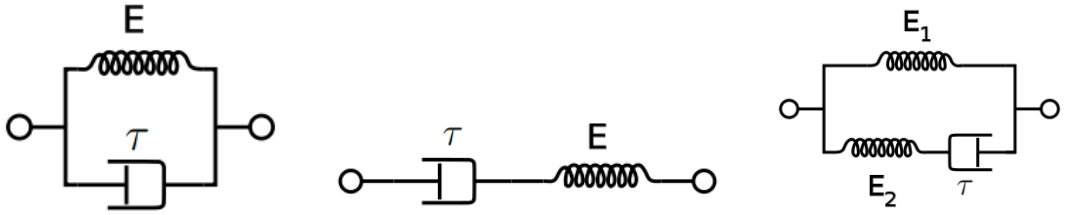

(a) Kelvin-Voigt (b) Maxwell (c) Standard linear solid

Figure 3.2: Spring-dashpot models for linear viscoelastic material behavior (source: wikipedia.org). E resp. E_1 and E_2 are the stiffnesses of linear springs and τ is the relxation time of a damper element

3.1.4 Visco-hyperelasticity

While the static or quasi-static behavior of materials such as rubber or elastomers can be described by (almost incompressible) hyperelastic materials laws, they show viscoelastic, time- resp. frequency- (and temperature-) dependent material properties when subject to harmonic loading [25, 46, 78, 130].

In one dimension several rheological models, i.e. spring-dashpot constitutive models, exist for describing viscoelastic behavior and among them are (see also Figure 3.2):

- Kelvin-Voigt:
$$\sigma = E\varepsilon + \tau\dot{\varepsilon} \tag{3.27}$$
- Maxwell:
$$E\sigma + \tau\dot{\sigma} = E\tau\varepsilon \tag{3.28}$$
- Standard linear solid / generalized Maxwell:
$$E_2\sigma + \tau\dot{\sigma} = E_1E_2\varepsilon + (E_1 + E_2)\tau\dot{\varepsilon} \tag{3.29}$$

Here τ is called *relaxation time* and $\eta = \tau/E = \tan(\delta)$ is the *loss factor*.

We extend 3-dimensional hyperelasticity to time-dependent visco-hyperelasticity by the following enhancement of the PK2 stress tensor based on the Kelvin-Voigt model [46, 130]:

$$\mathbf{S} = \mathbf{S}_e + \mathbf{S}_v. \tag{3.30}$$

Here, $\mathbf{S}_e$ represents the hyperelastic stress contribution and $\mathbf{S}_v$ the viscous stress contribution, which depends on the rate of the Green-Lagrange strain $\dot{\mathbf{E}}$. $\mathbf{S}_e$ is selected from one of the hyperelastic constitutive laws and possible examples for $\mathbf{S}_v$ are

$$\mathbf{S}_v = 2\eta\mu\dot{\mathbf{E}}. \tag{3.31}$$

in analogy to linear viscoelasticity, or from [130]:

$$\mathbf{S}_v = J\tau\mathbf{C}^{-1}\dot{\mathbf{E}}\mathbf{C}^{-1}. \tag{3.32}$$

In harmonic motion the material parameters such as Young's modulus E, loss factor η and eventually Poisson's ratio ν are typically not constant, but depend on the frequency f resp. angular frequency $\omega = 2\pi f$. An example for a material with strongly frequency-

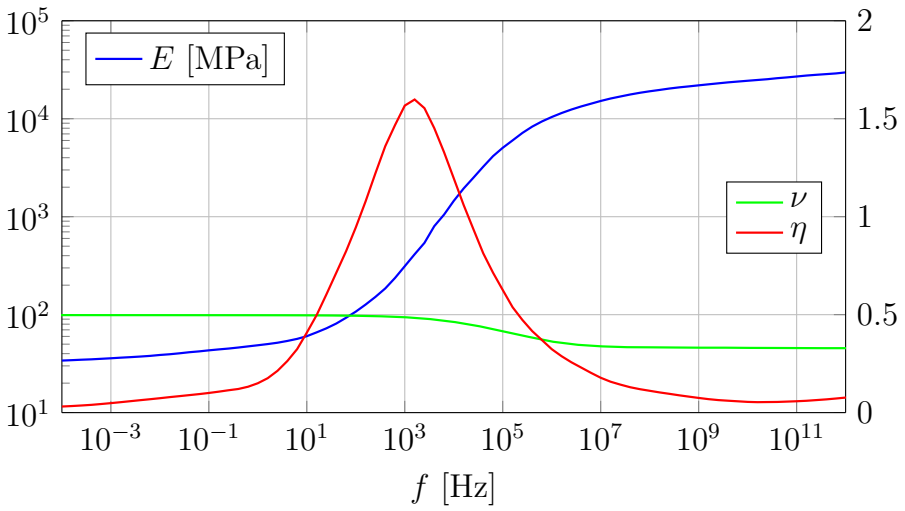

Figure 3.3: Example of frequency-dependent material properties: Young's modulus E, Poisson's ratio ν and loss factor η over excitation frequency f for polymer material Viton® 50°ShA

dependent material properties is Viton® 50°ShA, a polymer which is frequently used for sealing rings and gaskets. Measurements of material properties have been obtained at Siemens and are shown in Figure 3.3.

However, realistic modeling of materials with viscoelastic properties in general is a wide field of scientific research by itself and thus beyond the scope of this work. As material properties are very characteristic for a specific material used, we take the frequency-dependent properties of Viton® 50°ShA, as given in Figure 3.3, as an example to test the methods developed in this thesis.

3.2 Nonlinear isogeometric finite element analysis

Since an analytical solution of problems in nonlinear mechanics is usually not possible for complicated domains and material laws, we seek a numerical approximation using an isogeometric finite element discretization of continuum mechanics equations. It is based on the weak form of the equation of motion (Section 3.2.1) and isogeometric spline discretizations of geometry and displacement field (Section 3.2.2). The resulting nonlinear system of equations, which needs to be solved in order to determine the unknown control point displacements of a static deformation, is solved by a Newton's method (Section 3.2.3).

3.2.1 Weak form of the equation of motion

To find an approximate solution $\mathbf{u}^h$ of the exact displacement $\mathbf{u}$ of the nonlinear continuum mechanics problem governed by balance equations introduced in Section 3.1.2, we only demand that the equation of motion (3.11) is fulfilled in a weak sense [130]. Thus the residual remaining from (3.11) is multiplied with a test function $\delta\mathbf{u}$, the so-called virtual displacement fulfilling the boundary condition $\delta\mathbf{u} = \mathbf{0}$ on Γ_u, and then integrated over

the domain Ω:

$$\int_\Omega \left\{ \rho_0 \, \delta\mathbf{u}^T \ddot{\mathbf{u}}^h - \delta\mathbf{u}^T \mathrm{div} \left(\mathbf{F}(\mathbf{u}^h) \, \mathbf{S}(\mathbf{u}^h) \right) - \rho_0 \, \delta\mathbf{u}^T \mathbf{b} \right\} d\mathbf{x} = 0 \quad \forall \delta\mathbf{u}. \tag{3.33}$$

Integration by parts of this *principle of virtual work* and application of divergence theorem yield:

$$\int_\Omega \rho_0 \, \delta\mathbf{u}^T \ddot{\mathbf{u}}^h \, d\mathbf{x} + \int_\Omega \nabla(\delta\mathbf{u}) \cdot \left(\mathbf{F}(\mathbf{u}^h) \, \mathbf{S}(\mathbf{u}^h) \right) \, d\mathbf{x} = \int_\Omega \rho_0 \, \delta\mathbf{u}^T \mathbf{b} \, d\mathbf{x} + \int_{\Gamma_n} \delta\mathbf{u}^T \, \mathbf{t} \, d\Gamma. \tag{3.34}$$

This can be rewritten using the variation of the Green-Lagrange strain tensor

$$\delta\mathbf{E} = \frac{1}{2} \left(\nabla(\delta\mathbf{u})^T \mathbf{F} + \mathbf{F}^T \nabla(\delta\mathbf{u}) \right) \tag{3.35}$$

as the weak form of the equation of motion:

$$\int_\Omega \rho_0 \, \delta\mathbf{u}^T \ddot{\mathbf{u}}^h \, d\mathbf{x} + \int_\Omega \delta\boldsymbol{E} \cdot \mathbf{S}(\mathbf{u}^h) \, d\mathbf{x} = \int_\Omega \rho_0 \, \delta\mathbf{u}^T \mathbf{b} \, d\mathbf{x} + \int_{\Gamma_n} \delta\mathbf{u}^T \, \mathbf{t} \, d\Gamma \quad \forall \delta\mathbf{u}. \tag{3.36}$$

The first term on the left of the equality sign refers to the virtual change in kinetic energy, the second to the internal virtual work and the terms on the right to the external virtual work from applied body forces and surface tractions.

In the case of compressible hyperelastic materials, a displacement-based strain energy function ψ exists, describing the elastic energy stored in the solid. Then the *virtual work equation* (3.36) of the static problem, where $\ddot{\mathbf{u}} = \mathbf{0}$, can also be derived by minimizing an elastic energy functional [7, 130]:

$$\Pi_d(\mathbf{u}) = \int_\Omega \psi(\mathbf{C}) \, d\mathbf{x} - \int_\Omega \rho_0 \, \mathbf{b} \, d\mathbf{x} + \int_{\Gamma_n} \mathbf{t} \, d\Gamma \; \rightarrow \; \min. \tag{3.37}$$

An approximation of the minimizer $\mathbf{u}^h$ can then be found by setting the first variation of (3.37) to zero, i.e. $d\Pi_d(\mathbf{u}^h)[\delta\mathbf{u}] = 0$, which leads to the virtual work equation (3.36) (without the kinetic energy term).

3.2.2 Isogeometric finite element discretization

For the spatial discretization and solution of the virtual work equation (3.36) we use the isogeometric finite element method as introduced in Section 2.2.1.

Starting point is a trivariate spline volume parameterization of material coordinates, i.e. the geometry function mapping a parameter domain $\Omega_0 \subset \mathbb{R}^3$ onto the material coordinates $\mathbf{x} \in \Omega \subset \mathbb{R}^3$:

$$\mathbf{x} = \mathbf{g}(\boldsymbol{\xi}) = \sum_{i=1}^{n} N_i^p(\boldsymbol{\xi}) \, \mathbf{v}_i \, , \quad \boldsymbol{\xi} \in \Omega_0. \tag{3.38}$$

As already mentioned in Section 2.1.2, degree p, number of basis functions n and index i should be understood as 3-dimensional vectors resp. multi-indices.

The discretized spaces for displacements $\mathbf{u}^h \in \mathcal{S}^h \subset \mathcal{S}$ and virtual displacements $\delta\mathbf{u}^h \in \mathcal{V}^h \subset \mathcal{V}$ are selected as push-forward of the spline spaces defining the geometry onto the material coordinates, see (2.10):

$$\begin{aligned} \mathbf{u}^h(\mathbf{x},t) &= \sum_{i=1}^{n} N_i^p \left(\mathbf{g}^{-1}(\mathbf{x})\right) \mathbf{d}_i(t), \\ \delta\mathbf{u}^h(\mathbf{x}) &= \sum_{i=1}^{n} N_i^p \left(\mathbf{g}^{-1}(\mathbf{x})\right) \delta\mathbf{d}_i. \end{aligned} \tag{3.39}$$

The kinematic quantities described in Section 3.1.1 have to be evaluated depending on the discretized displacements. For the deformation gradient this means:

$$\begin{aligned} \mathbf{F}(\mathbf{x},t) &= \mathbf{I} + \nabla\mathbf{u}^h(\mathbf{x},t) = \mathbf{I} + \sum_{i=1}^{n} \mathbf{d}_i(t)\, \nabla N_i^p(\mathbf{x}) \\ &= \mathbf{I} + \sum_{i=1}^{n} \mathbf{d}_i(t)\, \frac{dN_i^p}{d\boldsymbol{\xi}} \left(\mathbf{g}^{-1}(\mathbf{x})\right) \cdot \left(\frac{d\mathbf{g}}{d\boldsymbol{\xi}}\right)^{-1}. \end{aligned} \tag{3.40}$$

Cauchy-Green and Green-Lagrange strain tensors can then be computed from $\mathbf{F}$ and the 2nd Piola-Kirchhoff stress can be evaluated. Switching to the Voigt vector notation for matrices $\mathbf{E}$ and $\mathbf{S}$ (see [130])

$$\begin{aligned} \vec{\mathbf{E}} &= (E_{11},\ E_{22},\ E_{33},\ 2E_{12},\ 2E_{23},\ 2E_{13})^T, \\ \vec{\mathbf{S}} &= (S_{11},\ S_{22},\ S_{33},\ S_{12},\ S_{23},\ S_{13})^T, \end{aligned} \tag{3.41}$$

the virtual Green-Lagrange strain tensor can be written as

$$\delta\vec{\mathbf{E}}_i(\mathbf{x}) = \mathbf{B}_i(\mathbf{x})\, \delta\mathbf{d}_i, \tag{3.42}$$

with virtual displacement control points $\delta\mathbf{d}_i$ and the matrix $\mathbf{B}_i \in \mathbb{R}^{6\times 3}$ as:

$$\begin{aligned} \mathbf{B}_i(\mathbf{x}) &= \begin{pmatrix} F_{11}N_{i,1}^p & F_{21}N_{i,1}^p & F_{31}N_{i,1}^p \\ F_{12}N_{i,2}^p & F_{22}N_{i,2}^p & F_{32}N_{i,2}^p \\ F_{13}N_{i,3}^p & F_{23}N_{i,3}^p & F_{33}N_{i,3}^p \\ F_{11}N_{i,2}^p + F_{12}N_{i,1}^p & F_{21}N_{i,2}^p + F_{22}N_{i,1}^p & F_{31}N_{i,2}^p + F_{32}N_{i,1}^p \\ F_{12}N_{i,3}^p + F_{13}N_{i,2}^p & F_{22}N_{i,3}^p + F_{23}N_{i,2}^p & F_{32}N_{i,3}^p + F_{33}N_{i,2}^p \\ F_{11}N_{i,3}^p + F_{13}N_{i,1}^p & F_{21}N_{i,3}^p + F_{23}N_{i,1}^p & F_{31}N_{i,3}^p + F_{33}N_{i,1}^p \end{pmatrix} \\ &\hat{=} \frac{1}{2}\left(\nabla N_i^p(\mathbf{x})^T\, \mathbf{F}(\mathbf{x}) + \mathbf{F}(\mathbf{x})^T\, \nabla N_i^p(\mathbf{x})\right). \end{aligned} \tag{3.43}$$

Inserting all the discretized kinematic quantities into the weak form of the equation of motion (3.36) then yields:

$$\begin{aligned} &\delta\mathbf{d}_i^T \int_\Omega \rho_0\, N_i^p\, \mathbf{I}\, N_j^p\, d\mathbf{x}\, \ddot{\mathbf{d}}_j \;+\; \delta\mathbf{d}_i^T \int_\Omega \mathbf{B}_i^T\, \vec{\mathbf{S}}(\mathbf{d})\, d\mathbf{x} \\ &\qquad = \delta\mathbf{d}_i^T \int_\Omega \rho_0\, N_i^p\, \mathbf{b}\, d\mathbf{x} \;+\; \delta\mathbf{d}_i^T \int_{\Gamma_n} N_i^p\, \mathbf{t}\, d\Gamma \quad i,j = 1,\ldots,n. \end{aligned} \tag{3.44}$$

Since this equation has to be fulfilled for all admissible $\delta\mathbf{d}_i$, we finally arrive at the

discretized equation of motion, just as in standard finite element methods [62, 130]:

$$\mathbf{M}\,\ddot{\mathbf{d}}(t) + \mathbf{f}\,(\mathbf{d}(t)) = \mathbf{b}(t), \tag{3.45}$$

which needs to be solved for the unknown vector of control point displacements $\mathbf{d}$. Therefor the entries of the *internal force vector* $\mathbf{f} \in \mathbb{R}^N$,

$$\mathbf{f}_i = \int_\Omega \mathbf{B}_i^T\, \vec{\mathbf{S}}(\mathbf{d})\, d\mathbf{x} \quad i = 1, \ldots, n, \tag{3.46}$$

the *external force vector* $\mathbf{b} \in \mathbb{R}^N$,

$$\mathbf{b}_i = \int_\Omega \rho_0\, N_i^p\, \mathbf{b}\, d\mathbf{x} + \int_{\Gamma_n} N_i^p\, \mathbf{t}\, d\Gamma \quad i = 1, \ldots, n, \tag{3.47}$$

and the consistent *mass matrix* $\mathbf{M} \in \mathbb{R}^{N\times N}$,

$$\mathbf{M}_{ij} = \mathbf{I} \int_\Omega \rho_0\, N_i^p\, N_j^p\, d\mathbf{x} \quad i, j = 1, \ldots, n, \tag{3.48}$$

have to be assembled.

3.2.3 Solution of the static problem

In the elastostatic problem the time-dependence of external force and internal variables is neglected and the equation of motion (3.11) is

$$-\mathrm{div}\,\mathbf{F}\,\mathbf{S}(\mathbf{u}) = \rho_0 \mathbf{b}, \tag{3.49}$$

and its discretized form, compare (3.45), reads:

$$\mathbf{f}(\mathbf{d}) = \mathbf{b}. \tag{3.50}$$

Existence of a solution

As in detail discussed in [35, 83], a number of constitutive assumptions has to be made in order to show the existence of a solution of the continuous problem of elasticity (3.49). These include:

- Isotropy and the existence of a stored energy function ψ, see Section 3.1.3
- For small strains the stored energy function must take the form

$$\psi(\mathbf{E}) = \frac{\lambda}{2}\,\mathrm{tr}(\mathbf{E})^2 + \mu\,\mathrm{tr}(\mathbf{E}^2) + \mathcal{O}(\|\mathbf{E}\|^2) \tag{3.51}$$

- Large strains must result in large stresses, i.e.

$$\lim_{\det \mathbf{F}\to+0} \psi(\mathbf{F}) = +\infty \quad \wedge \quad \lim_{\det \mathbf{F}\to+\infty} \psi(\mathbf{F}) = +\infty \tag{3.52}$$

- Poly- or quasi-convexity of the strain energy function

Algorithm 1 Newton's method for nonlinear elasticity

Initial guess: $\mathbf{d}^0$
Tolerances: $\varepsilon_d,\ \varepsilon_r > 0$
Initialization: $s \leftarrow 0$
repeat
  Assembly: $\mathbf{f}^s \leftarrow \mathbf{f}(\mathbf{d}^s)$, $\mathbf{K}_T^s \leftarrow \mathbf{K}_T(\mathbf{d}^s)$
  Evaluate residual: $\mathbf{r}^s \leftarrow \mathbf{f}^s - \mathbf{b}$
  Compute update: $\Delta\mathbf{d}^s \leftarrow$ Solve $\mathbf{K}_T^s\, \Delta\mathbf{d}^s = -\mathbf{r}^s$
  Evaluate error: $e_d \leftarrow \frac{\|\Delta\mathbf{d}^s\|}{\|\mathbf{d}^s\|}$, $e_r \leftarrow \frac{\|\mathbf{r}^s\|}{\|\mathbf{b}\|}$
  Update: $\mathbf{d}^{s+1} \leftarrow \mathbf{d}^s + \Delta\mathbf{d}^s$
  $s \leftarrow s + 1$
until $e_d < \varepsilon_d \ \wedge\ e_r < \varepsilon_r$
Return value: $\mathbf{d} \leftarrow \mathbf{d}^s$

- The Legendre-Hadamard condition, i.e. ellipticity or positive definiteness of the elasticity tensor $\mathbb{C}(\mathbf{F})$ (3.24)

Under these constitutive and further assumptions, such as smoothness of the boundary of Ω, it is shown in [35, 83] that a nonlinear elasticity problem has a solution in the neighborhood of the solution of the linearized problem (Section 3.3). However, in practical applications some of these conditions might be violated and in general several (or even infinite) solutions may exist and bifurcation of solution paths can occur.

Numerical solution using Newton's method

To solve the nonlinear system of equations (3.50) for the unknown control point displacements $\mathbf{d}$, it is rewritten in residual form:

$$\mathbf{r}(\mathbf{d}) = \mathbf{f}(\mathbf{d}) - \mathbf{b} = \mathbf{0}. \tag{3.53}$$

Typically, iterative procedures are used to find an approximate solution of the residual equation, such as fixed-point methods, Newton-Raphson methods, modified or quasi-Newton methods, and arc-length continuation methods [130].

In Algorithm 1 we describe the use of a classical Newton-Raphson method for the solution of the static nonlinear elasticity problem (3.53).

As initial guess typically $\mathbf{d}^0 = \mathbf{0}$ is used, which yields the solution of the linear problem as $\mathbf{d}^1$ in the first iteration. In case Algorithm 1 is part of a loop with increasing load factor $\lambda = 1, 2, \ldots$ for the right-hand side $\mathbf{b}(\lambda) = \lambda\mathbf{b}$, the result of the previous load step is used. Since the solution of (3.50) is not necessarily unique and Newton's method can only find a solution in the neighborhood of the initial guess, $\mathbf{d}^0$ is a crucial input quantity.

The matrix $\mathbf{K}_T(\mathbf{d})$ is the so-called *tangential stiffness matrix*. It is the derivative of the residual $\mathbf{r}$, resp. the internal force vector $\mathbf{f}$, w.r.t. the displacement vector $\mathbf{d}$:

$$\mathbf{K}_T(\mathbf{d}) = \frac{d\mathbf{r}}{d\mathbf{d}}(\mathbf{d}) = \frac{d\mathbf{f}}{d\mathbf{d}}(\mathbf{d}). \tag{3.54}$$

It can be computed and assembled as a sum of two matrices:

$$\mathbf{K}(\mathbf{d}) = \mathbf{K}^{geo}(\mathbf{d}) + \mathbf{K}^{mat}(\mathbf{d}), \tag{3.55}$$

with the geometric tangent matrix

$$\mathbf{K}_{ij}^{geo}(\mathbf{d}) = \sum_{e=1}^{\ell} \left\{ \mathbf{I} \int_{\Omega_e} \nabla N_i^{p\,T}\, \mathbf{S}(\mathbf{d})\, \nabla N_j^p \, d\mathbf{x} \right\} \tag{3.56}$$

and the material tangent matrix

$$\mathbf{K}_{ij}^{mat}(\mathbf{d}) = \sum_{e=1}^{\ell} \left\{ \int_{\Omega_e} \mathbf{B}_i^T\, \mathbb{C}(\mathbf{d})\, \mathbf{B}_j \, d\mathbf{x} \right\}. \tag{3.57}$$

Here $\mathbb{C} = \frac{d\vec{\mathbf{S}}}{d\vec{\mathbf{E}}} \in \mathbb{R}^{6\times 6}$ is the matrix form of the constitutive 4th order tensor (3.24).

The internal force vector $\mathbf{f}^s$ and tangential stiffness matrix $\mathbf{K}_T^s$ have to be reassembled in every step s of the iteration, since they depend on the current displacement $\mathbf{d}^s$, while the right-hand side vector $\mathbf{b}$ stays constant, as we do not consider right-hand sides dependent on $\mathbf{d}$.

The structure and solution procedure of the system $\mathbf{K}_T^s \Delta\mathbf{d}^s = -\mathbf{r}^s$ for the displacement update $\Delta\mathbf{d}^s$ is also completely analogous to the general linear case, see Sections 2.2.2.

Two convergence criteria are checked: e_d is measuring the relative size of the increment in the s-th step and e_r is the norm of the residual, normalized by the norm of the right-hand side. Once the convergence criteria are met, the displacement from the last iteration step $\mathbf{d}^s$ is returned and can be used to to compute the current configuration $\mathbf{y} = \mathbf{x} + \mathbf{u}(\mathbf{x})$ as displaced NURBS volume and other postprocessing results such as evaluation of stresses and strains.

Remark 3.1. *As discussed for general linear problems in Section 2.3, an extension of the isogeometric finite element discretization of nonlinear elasticity to multi-patch parameterizations is possible in a straight-forward manner. It was also implemented for the numerical examples discussed in this thesis.*

3.3 Brief note on linear elasticity

Linear elasticity theory can be interpreted as a linearization of nonlinear theory around the undeformed and stress-free initial state [83]. It is only valid for small displacements and strains, i.e. when $\|\nabla\mathbf{u}\| \ll 1$. Here we briefly review the equations and IGA discretization of linear elasticity, since we are going to compare results of linear and nonlinear analysis for validation of methods and implementations, for instance in Section 3.5.

The equation of motion of linear elasticity, compare (3.11), reads

$$\rho\ddot{\mathbf{u}} - \operatorname{div}\boldsymbol{\sigma}(\mathbf{u}) = \rho\mathbf{b}, \tag{3.58}$$

where the Cauchy stress $\boldsymbol{\sigma}$ is expressed by the linear St. Venant-Kirchhoff constitutive

law, see (3.21),

$$\boldsymbol{\sigma}(\mathbf{u}) = 2\mu\, \boldsymbol{\varepsilon}(\mathbf{u}) + \lambda\, \mathrm{tr}(\boldsymbol{\varepsilon}(\mathbf{u}))\mathbf{I} = \mathbb{C} : \boldsymbol{\varepsilon}(\mathbf{u}), \tag{3.59}$$

using the *linear strain tensor*, which is a linearization of the Green-Lagrange strain tensor (3.4),

$$\boldsymbol{\varepsilon}(\mathbf{u}) = \frac{1}{2}\left(\nabla \mathbf{u}^T + \nabla \mathbf{u}\right), \tag{3.60}$$

and the 4th order *linear elasticity tensor*, see (3.25),

$$\mathbb{C}_{ijkl} = \lambda\, \delta_{ij}\delta_{kl} + \mu\left(\delta_{ik}\delta_{jl} + \delta_{il}\delta_{kj}\right), \quad i,j,k,l = 1,2,3. \tag{3.61}$$

The corresponding stored energy function can be written as

$$\psi(\boldsymbol{\varepsilon}) = \frac{1}{2}\boldsymbol{\varepsilon} : \mathbb{C} : \boldsymbol{\varepsilon} = \mu\, \mathrm{tr}(\boldsymbol{\varepsilon}^2) + \frac{\lambda}{2}\, \mathrm{tr}(\boldsymbol{\varepsilon})^2. \tag{3.62}$$

For the weak form of the boundary value problem associated with (3.58) it follows:

$$\int_\Omega \rho_0\, \delta\mathbf{u}^T \ddot{\mathbf{u}}^h\, d\mathbf{x} + \int_\Omega \delta\boldsymbol{\varepsilon} \cdot \boldsymbol{\sigma}(\mathbf{u}^h)\, d\mathbf{x} = \int_\Omega \rho_0\, \delta\mathbf{u}^T \mathbf{b}\, d\mathbf{x} + \int_{\Gamma_n} \delta\mathbf{u}^T\, \mathbf{t}\, d\Gamma \quad \forall \delta\mathbf{u}, \tag{3.63}$$

with $\delta\boldsymbol{\varepsilon} = \frac{1}{2}(\nabla(\delta\mathbf{u}) + \nabla(\delta\mathbf{u})^T)$. Taking advantage of the symmetries of $\boldsymbol{\sigma}$ and $\mathbb{C}$ this can be rewritten as

$$\int_\Omega \rho_0\, \delta\mathbf{u}^T \ddot{\mathbf{u}}^h\, d\mathbf{x} + \int_\Omega \nabla(\delta\mathbf{u}) \cdot \mathbb{C} \cdot \nabla\mathbf{u}^h\, d\mathbf{x} = \int_\Omega \rho_0\, \delta\mathbf{u}^T \mathbf{b}\, d\mathbf{x} + \int_{\Gamma_n} \delta\mathbf{u}^T\, \mathbf{t}\, d\Gamma \quad \forall \delta\mathbf{u}. \tag{3.64}$$

Note that the linear elastostatic problem

$$\int_\Omega \nabla(\delta\mathbf{u}) \cdot \mathbb{C} \cdot \nabla\mathbf{u}^h\, d\mathbf{x} = \int_\Omega \rho_0\, \delta\mathbf{u}^T \mathbf{b}\, d\mathbf{x} + \int_{\Gamma_n} \delta\mathbf{u}^T\, \mathbf{t}\, d\Gamma \quad \forall \delta\mathbf{u}. \tag{3.65}$$

has exactly the same form as the abstract linear PDE problem (2.7) used for the introduction of isogeometric finite element methods in Section 2.2.1, where

$$a(\mathbf{v},\mathbf{u}) = \int_\Omega \nabla\mathbf{v} \cdot \mathbb{C} \cdot \nabla\mathbf{u}\, d\mathbf{x}. \tag{3.66}$$

An isogeometric finite element discretization of the form $\mathbf{u}^h(\mathbf{x}) = \sum_{i=1}^n N_i^p(\mathbf{x})\mathbf{d}_i$ then leads to the solution of a linear equation system $\mathbf{K}\,\mathbf{d} = \mathbf{b}$, as discussed in detail in Section 2.2.

3.4 Nonlinear Euler-Bernoulli beam

As a proof of concept, in [126, 127] we have already investigated isogeometric finite element discretizations and nonlinear frequency analysis for a simpler nonlinear structural mechanical model, the nonlinear Euler-Bernoulli beam model. Since we also use it for validation of methods and convergence analysis in this thesis, see Section 4.4.1, we include here a brief review of nonlinear Euler-Bernoulli beam theory and its discretization, too.

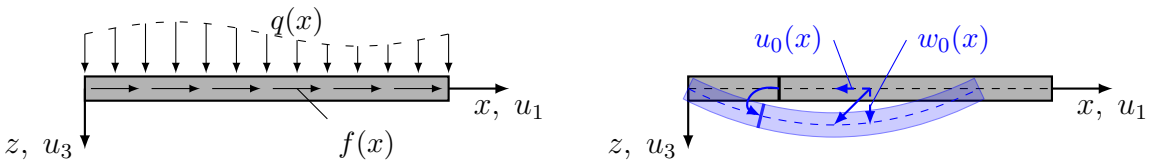

Figure 3.4: Unsupported beam under external forces line load q and line-edge load f with transverse deformation w_0 and longitudinal deformation u_0 of neutral axis

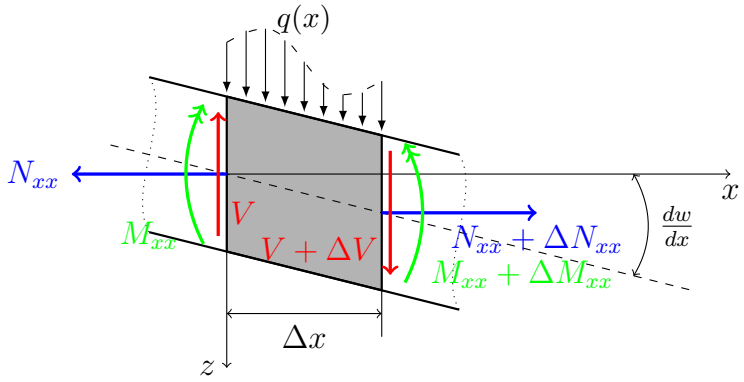

Figure 3.5: Internal forces and moments on an infinitesimal beam segment

3.4.1 Nonlinear Euler-Bernoulli beam model

A nonlinear beam model based on *Euler-Bernoulli hypothesis* and *von Kármán strains* is presented in detail in [20, 87, 95]. This theory, which is suitable for transverse deformations with small strains and moderate rotations, will be briefly summarized using [95] as main reference.

The displacement field (u_1, u_2, u_3) along coordinate axis (x, y, z) is expressed by the axial and transversal displacements of the neutral axis $u_0(x)$ and $w_0(x)$, see Figure 3.4:

$$u_1 = u_0(x) - z\, w_0'(x), \quad u_2 = 0, \quad u_3 = w_0(x). \tag{3.67}$$

From the general definition of strains

$$\varepsilon_{ij} = \frac{1}{2}\left(\frac{\partial u_i}{\partial x_j} + \frac{\partial u_j}{\partial x_i}\right) + \frac{1}{2}\sum_{k=1}^{3} \frac{\partial u_k}{\partial x_i}\frac{\partial u_k}{\partial x_j}, \tag{3.68}$$

only the 00- resp. xx-component of the moderately nonlinear *von Kármán strain* is considered

$$\varepsilon_{xx} = u_0' + \frac{1}{2}{w_0'}^2 - z\, w_0'' = \varepsilon_{xx}^0 + z\, \varepsilon_{xx}^1, \tag{3.69}$$

with the axial strain ε_{xx}^0 and curvature ε_{xx}^1:

$$\varepsilon_{xx}^0 = u_0' + \frac{1}{2}{w_0'}^2, \quad \varepsilon_{xx}^1 = -w_0''. \tag{3.70}$$

From the *linear constitutive law*, i.e. Hooke's law, for the stress $\sigma_{xx} = E\varepsilon_{xx}$ of an isotropic beam with Young's modulus E, cross section area A and second moment of

area I, we obtain the internal force in x-direction N_{xx} and the internal bending moment around y-axis M_{xx},

$$N_{xx} = EA\,\varepsilon^0_{xx}, \quad M_{xx} = EI\,\varepsilon^1_{xx}. \tag{3.71}$$

The equilibrium of internal forces and moments with axial and transversal external forces $f(x)$ and $q(x)$ applied on an infinitesimal beam segment Δx (see Figure 3.5) and taking the limit $\Delta x \to 0$ leads to the governing equations

$$\begin{aligned} -N'_{xx} &= f(x), \\ -\left(N_{xx}\, w'_0\right)' - M''_{xx} &= q(x). \end{aligned} \tag{3.72}$$

Inserting equations (3.70) and (3.71) into (3.72) then results in the differential equations for the bending of a nonlinear Euler-Bernoulli beam, depending on axial and transversal deformations u_0 and w_0:

$$\begin{aligned} -\left[EA\,\left(u'_0 + \frac{1}{2}{w'_0}^2\right)\right]' &= f(x), \\ -\left[EA\,\left(u'_0 + \frac{1}{2}{w'_0}^2\right)\,w'_0\right]' - \left[-EI\,w''_0\right]'' &= q(x). \end{aligned} \tag{3.73}$$

3.4.2 Isogeometric finite element discretization

For a finite element discretization of the nonlinear beam formulation we need the weak form of governing equations (3.72) resp. (3.73). According to [95] these will be derived directly from the strong form (3.72) using the method of weighted residuals, i.e. multiplying the equations with test functions v_1 resp. v_2, taking the integral over the length L of the beam and applying integration by parts once resp. twice:

$$\begin{aligned} \int_0^L N_{xx} \cdot v'_1 \, dx &= \int_0^L f \cdot v_1 \, dx + \left[N_{xx} \cdot v_1\right]_0^L, \\ \int_0^L -M_{xx} \cdot v''_2 + w'_0 \cdot N_{xx} \cdot v'_2 \;\; dx &= \\ \int_0^L q \cdot v_2 \, dx &+ \left[(M'_{xx} + w'_0 \cdot N_{xx}) \cdot v_2\right]_0^L + \left[M_{xx} \cdot v'_2\right]_0^L. \end{aligned} \tag{3.74}$$

The deformations u_0 and w_0, as well as test functions v_1 and v_2 must be included in appropriate function spaces $\mathcal{S}_u, \mathcal{S}_w, \mathcal{V}_u, \mathcal{V}_w$ and satisfy prescribed deformation boundary conditions [62].

To solve the weak equations (3.74), Galerkin discretization is applied, i.e., the problem is solved on a mesh Ω_h with finite-dimensional function spaces $\mathcal{S}^h_u \subset \mathcal{S}_u$, $\mathcal{S}^h_w \subset \mathcal{S}_w$, $\mathcal{V}^h_u \subset \mathcal{V}_u$, $\mathcal{V}^h_w \subset \mathcal{V}_w$ defined on Ω_h. Then u_0 and w_0 can be expressed as

$$u_0(x) = \sum_{i=1}^n u_i N^p_i(x), \qquad w_0(x) = \sum_{i=1}^n w_i N^p_i(x) \tag{3.75}$$

with $\{N^p_i\}_{i=1,\dots,n}$ being a spline basis of $\mathcal{S}^h_u$ and $\mathcal{S}^h_w$.

Inserting these representations into (3.74) leads to the nonlinear system

$$\begin{aligned} \sum_{j=1}^{n} K_{ij}^{11}\, u_j \quad &+ \sum_{J=1}^{n} K_{iJ}^{12}(w_0)\, w_J \;= b_i^1, \quad i = 1, \dots, n, \\ \sum_{j=1}^{n} K_{Ij}^{21}(w_0)\, u_j \quad &+ \sum_{J=1}^{n} K_{IJ}^{22}(w_0)\, w_J \;= b_I^2, \quad I = 1, \dots, n, \end{aligned} \tag{3.76}$$

with stiffness matrices and force vectors

$$\begin{aligned} K_{ij}^{11} &= \int_0^L EA\; N_i^{p\prime}\; N_j^{p\prime}\; dx, \\ K_{iJ}^{12}(w_0) &= \frac{1}{2} \int_0^L EA\; w_0'\; N_i^{p\prime}\; N_J^{p\prime}\; dx, \\ K_{Ij}^{21}(w_0) &= \int_0^L EA\; w_0'\; N_I^{p\prime}\; N_j^{p\prime}\; dx \;=\; 2\, \mathbf{K}_{jI}^{12}, \\ K_{IJ}^{22}(w_0) &= \int_0^L EI\; N_I^{p\prime\prime}\; N_J^{p\prime\prime}\; dx + \frac{1}{2} \int_0^L EA\; w_0''\; N_I^{p\prime}\; N_J^{p\prime}\; dx, \\ b_i^1 &= \int_0^L f(x)\; N_i^p\; dx \;+\; \hat{Q}_i, \\ b_I^2 &= \int_0^L q(x)\; N_I^p\; dx \;+\; \bar{Q}_I. \end{aligned} \tag{3.77}$$

and $\hat{Q}_i$, $\bar{Q}_I$ being boundary terms derived from (3.74). More details can be found in [95]. Now (3.77) can be condensed to the following nonlinear equation system for control point deformations $\mathbf{d}$, with deformation-dependent stiffness matrix $\mathbf{K} = \mathbf{K}(\mathbf{d})$ and force vector $\mathbf{b}$:

$$\mathbf{d} = \begin{pmatrix} \mathbf{u} \\ \mathbf{w} \end{pmatrix}, \; \mathbf{K}(\mathbf{d}) = \begin{pmatrix} \mathbf{K}^{11} & \mathbf{K}^{12} \\ \mathbf{K}^{21} & \mathbf{K}^{22} \end{pmatrix}, \; \mathbf{b} = \begin{pmatrix} \mathbf{b}^1 \\ \mathbf{b}^2 \end{pmatrix}, \tag{3.78}$$

$$\mathbf{f}(\mathbf{d}) = \mathbf{K}(\mathbf{d})\, \mathbf{d} = \mathbf{b}. \tag{3.79}$$

This nonlinear system of equations has the same structure as (3.53) and can be solved using Newton's method as in Algorithm 1 to compute the static displacement of the beam.

Computational applications and convergence studies for static displacements of the nonlinear Euler-Bernoulli beam with isogeometric finite element discretization, i.e. examples for the solution of (3.79) were computed and discussed in [126, 127]. Results and numerical convergence analysis for nonlinear frequency analysis were also obtained in the scope of [126, 127] and are presented here in Section 4.4.1.

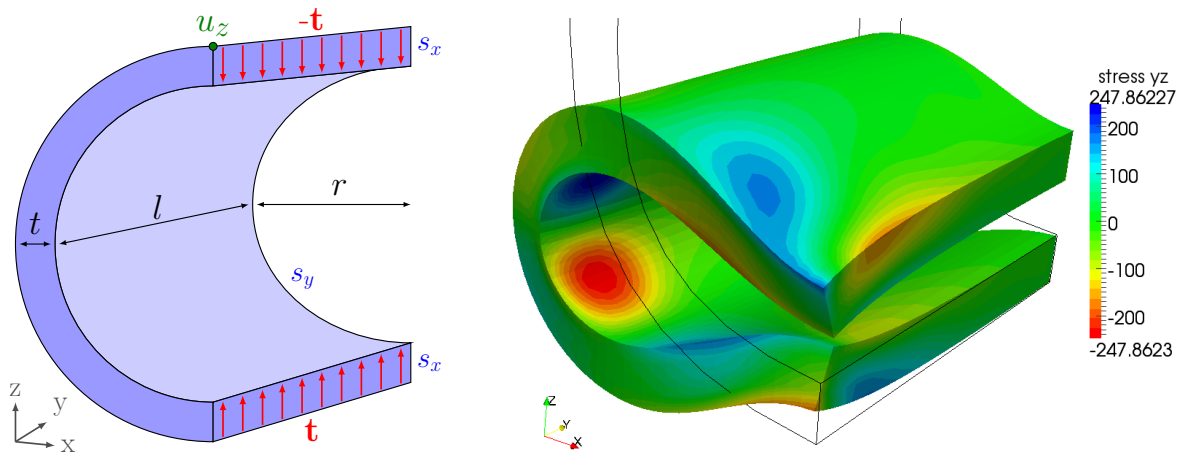

(a) Geometry and dimensions of cylinder

(b) Deformed cylinder colored by Cauchy stress σ_{yz}

Figure 3.6: Geometry and deformation of thick cylinder

3.5 Computational applications

With the computational examples presented in this section we want to validate the implementation of our isogeometric finite element discretization of 3-dimensional static nonlinear elasticity with large deformations and nonlinear constitutive laws.

3.5.1 Large deformation of thick cylinder

As a first benchmark for the validation of the solution of the nonlinear elastostatic problem using isogeometric finite elements we take the large deformation of a thick cylinder. This problem was already investigated in [84] to show the advantages of isogeometric compared to Lagrangian finite elements.

Due to symmetry, the cylinder can be modeled as a quarter cylinder, which is displayed in Figure 3.6(a). The geometrical parameters of the quarter cylinder are inner radius $r = 0.08$ m, thickness $t = 0.02$ m and length $l = 0.15$ m. This geometry can be parameterized exactly as a NURBS volume, using quadratic NURBS in circumferential direction (u) and linear B-Splines in thickness (v) and length direction (w).

For the analysis, parameters of Neo-Hookean material are chosen the same as in [84]: $E = 16.8$ kPa, $\nu = 0.4$ and $\rho = 470.0$ kg/m^3. Opposing surface loads are applied with $\mathbf{t} = (0, 0, 235.0)^T$ Pa (Figure 3.6(a)) and cause a very large compression of the quarter cylinder, as can be seen in Figure 3.6(b).

For the validation of our implementation we refine the spline parameterization of geometry for the analysis and obtain a mesh with $p = (4, 4, 3)$, $\ell = (16, 8, 1)$, $n = 3168$. Then we compute the deformation field and evaluate stresses. In Figure 3.6(b) the deformed cylinder is visualized and colored by the values of Cauchy stress σ_{yz}. These results correspond optically very well with the ones obtained in [84].

Furthermore, we carry out a small convergence study for k-refinement of the isogeometric analysis mesh. The load is decreased on 100 instead of 235 Pa in order to ensure convergence of Newton iterations and guarantee a realistic deformation without self-penetration of the cylinder. k-refinement is performed to obtain degree $p = 2, 3$ in all three parameter

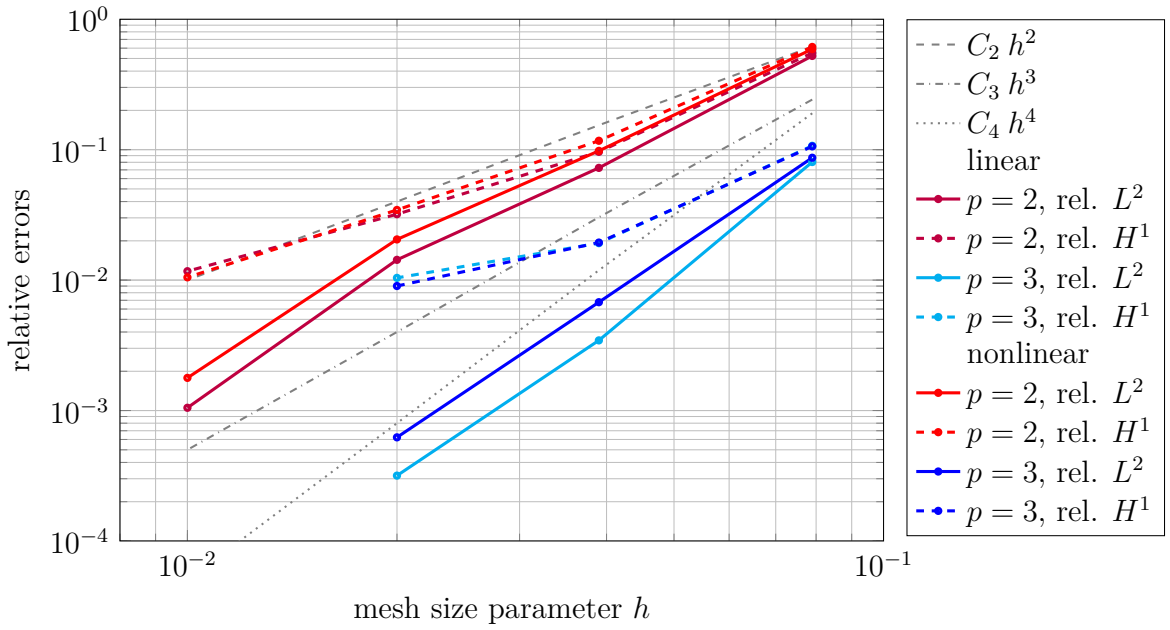

Figure 3.7: Convergence of relative errors in L^2- and H^1-norm for linear and nonlinear large deformation analysis of thick cylinder. k-refinement was performed to obtain degree $p = 2, 3$ and mesh size h of the parameterization

directions of the mesh. For h-refinement the mesh size parameter depends on the number of elements and the geometry. It is computed as:

$$h = \max\left\{\frac{\pi}{2}\frac{r+t}{\ell_u}, \frac{l}{\ell_v}, \frac{t}{\ell_w}\right\}. \tag{3.80}$$

For the comparison we evaluate the relative errors of numerical solutions $\mathbf{u}^h$ in L^2- and H^1-norm:

$$\text{rel. } L^2: \frac{\|\mathbf{u}^* - \mathbf{u}^h\|_{L^2(\Omega)}}{\|\mathbf{u}^*\|_{L^2(\Omega)}}, \qquad \text{rel. } H^1: \frac{\|\mathbf{u}^* - \mathbf{u}^h\|_{H^1(\Omega)}}{\|\mathbf{u}^*\|_{H^1(\Omega)}}, \tag{3.81}$$

where we take numerical solution for the maximally refined mesh with $p = (3, 3, 3)$, $\ell = (16, 16, 2)$, $n = 10830$ as reference solution $\mathbf{u}^*$.

Results of the convergence study are shown in Figure 3.7. We can observe roughly the expected convergence rates of order $p + 1$ for the L^2- and order p for the H^1-norm for both linear and nonlinear analysis. Until convergence criteria of the Newton's method are met in the nonlinear case, i.e. a relative error of residual of 10^{-5} and relative error of displacement update of 10^{-6}, 7-9 iterations are needed.

With this cylinder example we have validated the implementation of our isogeometric finite element discretization of nonlinear elasticity by a comparison with the results of [84] and a convergence study.

3.5.2 TERRIFIC Demonstrator as multi-patch example

The so-called "TERRIFIC Demonstrator" is a mechanical part which was introduced within the European project "TERRIFIC" [53] to show an isogeometric CAE workflow

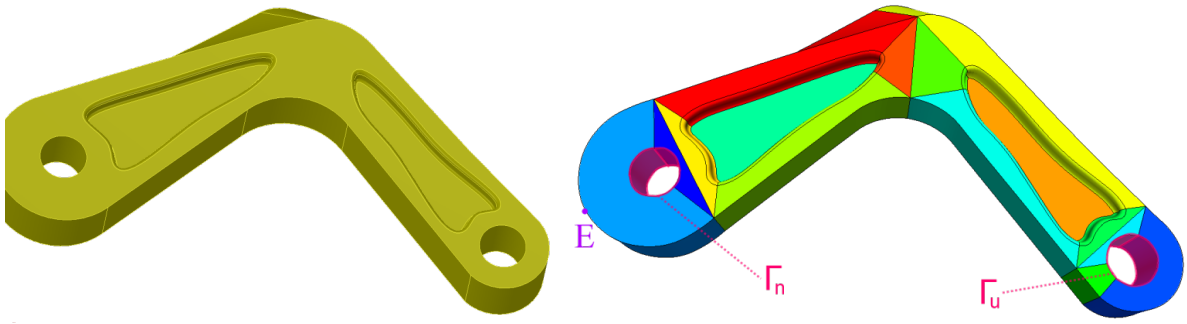

(a) geometry in CAD system (b) IGA-suitable multi-patch parameterization

Figure 3.8: Geometry of the TERRIFIC Demonstrator as design in a CAD system (a) and as an analysis-suitable multi-patch volume model (b). Patches are highlighted in different colors; boundaries Γ_u and Γ_n, as well as evaluation point E, are also shown in (b)

from design, over analysis to manufacturing. It was designed in a CAD system (Figure 3.8(a)), an IGA-suitable NURBS volume parameterization was generated for mechanical simulation (Figure 3.8(b)), and also other models for dip-paint simulation and computer-aided manufacturing were derived. Acknowledgement for the design goes to Stefan Boschert from Siemens Corporate Technology in Munich and for the multi-patch parameterization to Vibeke Skytt from SINTEF in Oslo.

The TERRIFIC Demonstrator serves also as a realistic, industrial-scale application of the methods developed within this thesis. The isogeometric volume parameterization consists of 15 patches of quadratic B-Spline volumes, with a total of 6,474 control points and 19,422 DOFs. When multi-patch coupling with Lagrangian multipliers is used, the isogeometric finite element discretization of the model has 22,914 DOFs, otherwise when elimination is used, it is only 15,930 DOFs.

Now we want to compare the results of both types of multi-patch constraint implementations for static linear and nonlinear analysis. We choose St. Venant-Kirchhoff material law with the following material parameters:

$$E = 74.0 \text{ GPa}, \quad \nu = 0.33, \quad \rho = 2800 \text{ kg/m}^3. \tag{3.82}$$

As boundary conditions we take a clamping of the right bore hole in Figure 3.8(a) by a zero Dirichlet condition at Γ_u and a surface traction on the left bore hole as a Neumann boundary condition on Γ_n:

$$\begin{aligned} \mathbf{u} &= \mathbf{0} \quad \text{on } \Gamma_u, \\ \mathbf{t} &= (60.0,\ -42.0,\ 0.0)^T \text{ MPa} \quad \text{on } \Gamma_n. \end{aligned} \tag{3.83}$$

Running the isogeometric finite element simulations, we find that the results of both multi-patch implementations are equal up to at least 12 significant digits for linear and nonlinear analysis for all quantities observed, which are displacement at evaluation point E in Figure 3.8(b), L^2- and H^1-norms of displacement field, and potential energy. The different constraint implementation strategies do not have an influence on assembly times, but of course on the solution time of the linear system. Here it is around 3-times faster

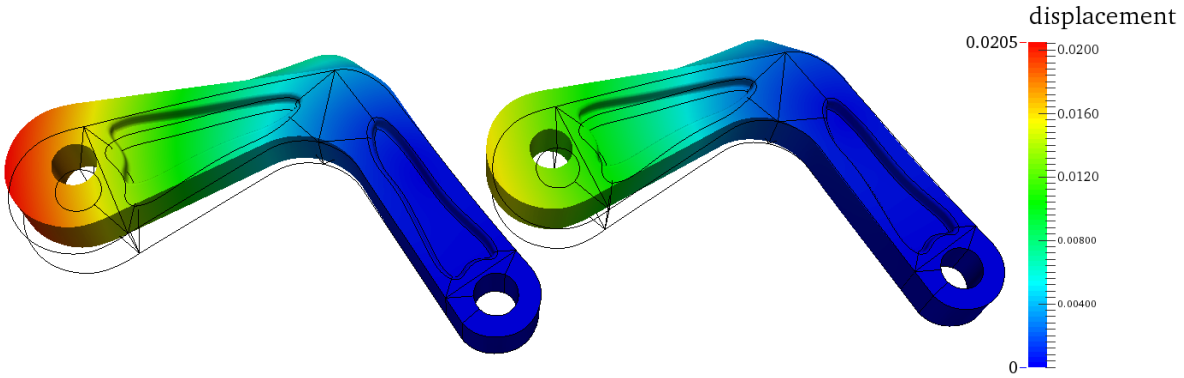

(a) Colored by displacement magnitude in m

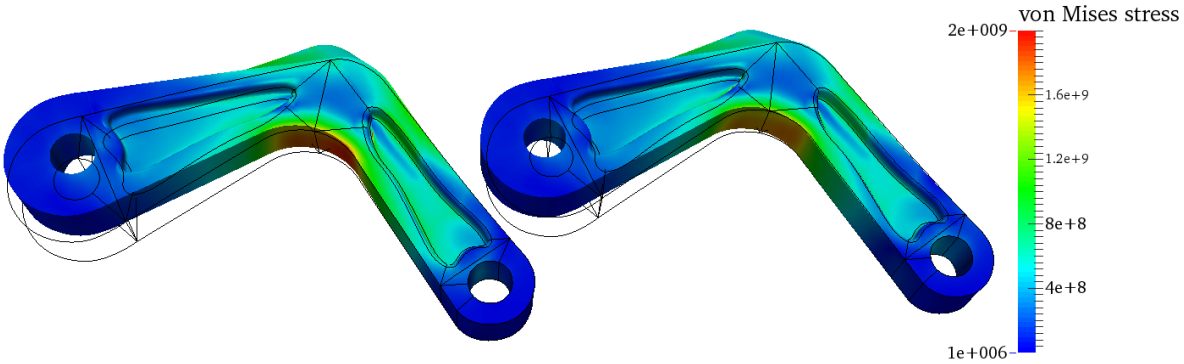

(b) Colored by von Mises stress in Pa

Figure 3.9: Linear (left) and nonlinear (right) deformation of TERRIFIC Demonstrator. Linear analysis over-estimates displacements (a) and stresses (b) more than 20% compared to nonlinear results

for elimination than for Lagrangian multipliers, since the linear system is smaller and has better properties, i.e. it is not a saddle-point problem.

Simulation results for the static linear and nonlinear elasticity computations are visualized in Figure 3.9, where the deformed structure is plotted and colored by values of deformation magnitude 3.9a and von Mises stress 3.9b. Even though the difference between linear and nonlinear analysis might not look significant, the comparison in Table 3.1 shows that quantities such as deformation at evaluation point E, L^2- and H^1-norms of displacement, and potential energy deviate more than 20% and thus justify the use of nonlinear analysis methods.

In Figure 3.10 it can be noticed that unphysical high stress peaks occur at indentations in the bending area of the part. These peaks appear for linear and nonlinear analysis, and are caused by a bad parameterization, which is near-singular at the highlighted positions on the boundaries, i.e. $\det(d\mathbf{x}/d\boldsymbol{\xi}) \approx 0$. This is not so much a problem for the analysis itself, since quadrature points are located off the boundaries, but for the postprocessing with strain and stress evaluation. However, it shows both the difficulty of obtaining parameterizations for realistic geometries and the need for development of sophisticated methods (see Section 2.3.1).

Altogether, with this computational example we have validated the two alternative implementations of multi-patch constraints also for nonlinear elasticity. Furthermore we have seen that near-singular parameterizations may cause problems for stress evaluation

	u_x [m]	u_y [m]	u_z [m]	E_{pot} [J]	$\|u\|_{L^2}$	$\|u\|_{H^1}$
linear	0.0183	0.0086	0.0018	$1.23{\cdot}10^{3}$	$2.03{\cdot}10^{-4}$	$1.89{\cdot}10^{-3}$
nonlinear	0.0142	0.0066	0.0011	$9.80{\cdot}10^{2}$	$1.53{\cdot}10^{-4}$	$1.47{\cdot}10^{-3}$
nonl./lin.	77.4%	76.0%	57.3%	79.4%	75.3%	77.8%

Table 3.1: Comparison of simulation results for linear and nonlinear deformation analysis of TERRIFIC Demonstrator. Deviations of more than 20% show that linearization is not accurate and justify the use of nonlinear analysis

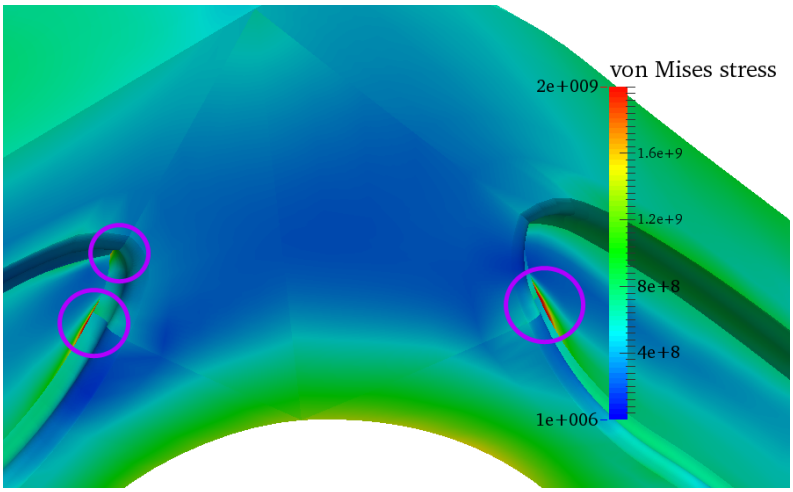

Figure 3.10: Unphysical high stress peaks, which occur at indentations in the bending area of the part, are highlighted in purple circles. They are caused by a bad, near-singular geometry parameterization

and should be avoided. However, this is an issue of the generation of analysis-suitable parameterizations and beyond the scope of this work.

3.6 Summary

We have dedicated this chapter to the spatial discretization of nonlinear elasticity problems using the isogeometric finite element method, which was already introduced in Chapter 2.

We have started with an introduction to fundamentals of 3-dimensional continuum mechanics. As we aim at the simulation of vibrations of rubber components, also visco-hyperelastic constitutive laws with frequency-dependent material parameters need to be considered.

Then we have explained the application of the isogeometric finite element method to the discretization of the nonlinear continuum mechanics problem. The displacements of static deformations can then be computed using a Newton's method.

For the evaluation of nonlinear analysis, we need to compare the results with linear elasticity, which is only valid for small displacements. Furthermore, we have introduced the simpler structural model of the nonlinear Euler-Bernoulli beam, which also serves for validation and benchmarking of our methods.

Finally, we have used computational applications to validate the implementation of isogeometric finite elements for nonlinear elasticity and confirmed the convergence properties. With the TERRIFIC Demonstrator example, we have proven the ability to simulate realistic geometries as isogeometric multi-patch models.

4 Nonlinear frequency analysis

Having introduced the problem formulation of nonlinear structural dynamics and the spatial discretization using isogeometric finite elements in preceding Chapter 3, we now target the topic of frequency analysis.

We start with a brief review of methods for linear frequency analysis, i.e. modal analysis of eigenfrequencies and eigenmodes, and direct frequency response to harmonic excitations in Section 4.1. Thereafter we give a general survey of methods for nonlinear frequency analysis in Section 4.2. Then we introduce in detail the method of harmonic balance for nonlinear steady-state frequency response analysis for periodic excitations, its application in nonlinear mechanics and its properties in Section 4.3. Finally, in Section 4.4 we discuss computational examples for nonlinear frequency analysis using harmonic balance and isogeometric finite element discretizations.

4.1 Overview of linear frequency analysis methods

In Section 3.3 we have introduced the linear elasticity problem, which reads, see (3.58),

$$\rho\ddot{\mathbf{u}} - \operatorname{div}\boldsymbol{\sigma}(\mathbf{u}) = \rho\mathbf{b} \quad \forall\mathbf{x}\in\Omega,\ t\in[0,T], \tag{4.1}$$

in the strong form. After (isogeometric) finite element discretization we have a system of N coupled linear ordinary differential equations for control point displacements $\mathbf{d}$:

$$\mathbf{M}\,\ddot{\mathbf{d}}(t) + \mathbf{K}\,\mathbf{d}(t) = \mathbf{b}(t) \quad \forall t\in[0,T]. \tag{4.2}$$

Furthermore, in vibration problems we have periodicity conditions for the displacement vectors in time:

$$\mathbf{d}(0) = \mathbf{d}(T) \quad \wedge \quad \dot{\mathbf{d}}(0) = \dot{\mathbf{d}}(T). \tag{4.3}$$

In structural dynamics very often velocity-dependent damping is introduced in the discretized equation of motion:

$$\mathbf{M}\,\ddot{\mathbf{d}}(t) + \mathbf{C}\,\dot{\mathbf{d}}(t) + \mathbf{K}\,\mathbf{d}(t) = \mathbf{b}(t) \quad \forall t\in[0,T]. \tag{4.4}$$

The damping term $\mathbf{C}\,\dot{\mathbf{d}}$ can relate to viscose effects in the material, internal or external friction and leads to dissipation of energy [130]. Using $\dot{\mathbf{d}} = \mathbf{v}$, (4.4) can also be rewritten

as a first order linear symmetric ODE system:

$$\begin{pmatrix} \mathbf{M} & \mathbf{0} \\ \mathbf{0} & -\mathbf{K} \end{pmatrix} \begin{pmatrix} \dot{\mathbf{v}} \\ \dot{\mathbf{d}} \end{pmatrix} + \begin{pmatrix} \mathbf{C} & \mathbf{K} \\ \mathbf{K} & \mathbf{0} \end{pmatrix} \begin{pmatrix} \mathbf{v} \\ \mathbf{d} \end{pmatrix} = \begin{pmatrix} \mathbf{b} \\ \mathbf{0} \end{pmatrix}. \tag{4.5}$$

A typical choice of the damping matrix is so-called *Rayleigh or modal damping*, where $\mathbf{C} = \alpha\mathbf{M} + \beta\mathbf{K}$. The Rayleigh coefficients $\alpha, \beta > 0$ have to be chosen carefully and fit to the material used and also to a frequency range where they are valid [62].

When linear viscoelastic materials are employed, and can be described using the Kelvin-Voigt model, see Section 3.1.4, the damping matrix takes the form $\mathbf{C} = \eta\mathbf{K}$, where η is the loss factor.

4.1.1 Modal analysis and eigenfrequencies

Modal analysis plays an important role in structural and mechanical engineering, since eigenfrequencies and eigenforms are important characteristics of the dynamical behavior of structures. Solutions of the generalized eigenvalue problem indicate resonance frequencies that should be avoided for forced vibrations [62].

Linear eigenvalue problem

From the equation of motion (4.2) with $\mathbf{b}(t) \equiv \mathbf{0}$ and periodicity conditions (4.3) by making the ansatz $\mathbf{d}(t) = \boldsymbol{\phi}_k \, e^{i\omega_k t}$ one can derive the well-known eigenvalue problem

$$\omega_k^2 \, \mathbf{M} \, \boldsymbol{\phi}_k = \mathbf{K} \, \boldsymbol{\phi}_k, \; k = 1, \ldots, N, \tag{4.6}$$

for the N linear natural frequencies $\omega_k > 0$, resp. eigenfrequencies $\lambda_k = \omega_k^2$, and corresponding eigenvectors or eigenmodes $\boldsymbol{\phi}_k \neq \mathbf{0}$ [39, 62]. Using $\boldsymbol{\Lambda} = \operatorname{diag}(\omega_1^2, \ldots, \omega_N^2)$ and $\boldsymbol{\Phi} = (\boldsymbol{\phi}_1, \ldots, \boldsymbol{\phi}_N)$, the eigenvalue problem can be written as:

$$\boldsymbol{\Lambda} \, \mathbf{M} \, \boldsymbol{\Phi} = \mathbf{K} \, \boldsymbol{\Phi}. \tag{4.7}$$

Typically the eigenmodes are normalized such that

$$\boldsymbol{\Phi}^T \, \mathbf{M} \, \boldsymbol{\Phi} = \mathbf{I} \quad \text{and} \quad \boldsymbol{\Phi}^T \, \mathbf{K} \, \boldsymbol{\Phi} = \boldsymbol{\Lambda}. \tag{4.8}$$

As we have already outlined in Section 2.2.2, higher smoothness of isogeometric spline discretizations is particularly advantageous compared to standard C^0 finite elements for the solution of eigenvalue problems [42, 76].

Complex eigenvalue problem

When damping is included, the ansatz $\mathbf{d}(t) = \boldsymbol{\phi}_k \, e^{\lambda_k t}$ is made with complex λ_k and it follows that $\mathbf{v}(t) = \lambda_k \, \boldsymbol{\phi}_k \, e^{\lambda_k t} =: \boldsymbol{\psi}_k \, e^{\lambda_k t}$ and thus

$$\lambda_k \begin{pmatrix} -\mathbf{M} & \mathbf{0} \\ \mathbf{0} & \mathbf{K} \end{pmatrix} \begin{pmatrix} \boldsymbol{\psi}_k \\ \boldsymbol{\phi}_k \end{pmatrix} = \begin{pmatrix} \mathbf{C} & \mathbf{K} \\ \mathbf{K} & \mathbf{0} \end{pmatrix} \begin{pmatrix} \boldsymbol{\psi}_k \\ \boldsymbol{\phi}_k \end{pmatrix}, \; k = 1, \ldots, 2N. \tag{4.9}$$

Algorithm 2 Iterative eigenvalue problem for frequency-dependent materials

1: **for** $k = 1, 2, \ldots$ **do**
2: Solve: $\omega_k^{0\,2}\,\mathbf{M}\,\boldsymbol{\phi}_k^0 = \mathbf{K}(0)\,\boldsymbol{\phi}_k^0$
3: Initialization: $s \leftarrow 0$
4: **repeat**
5: $s \leftarrow s + 1$
6: Assembly: $\mathbf{K}^s \leftarrow \mathbf{K}(\omega_k^{s-1})$
7: Solve: $\omega_k^{s\,2}\,\mathbf{M}\,\boldsymbol{\phi}_k^s = \mathbf{K}^s\,\boldsymbol{\phi}_k^s$
8: **until** $|(\omega_k^s - \omega_k^{s-1})/\omega_k^s| < \varepsilon$
9: Return values: $\hat{\omega}_k = \omega_k^s,\ \hat{\boldsymbol{\phi}}_k = \boldsymbol{\phi}_k^s$
10: **end for**

This gives N pairs of complex-conjugate eigenvalues of the form

$$k = 1, \ldots, N: \quad \begin{cases} \lambda_{2k-1} &= -\zeta_k\omega_k - i\omega_k\sqrt{1-\zeta_k^2}, \\ \lambda_{2k} &= -\zeta_k\omega_k + i\omega_k\sqrt{1-\zeta_k^2}. \end{cases} \tag{4.10}$$

where ω_k are again the natural frequencies and ζ_k the modal damping ratios, which can be computed from $\lambda_{2k-1} = \alpha_k - i\beta_k$ and $\lambda_{2k} = \alpha_k + i\beta_k$:

$$\omega_k = \sqrt{\alpha_k^2 + \beta_k^2}, \qquad \zeta_k = -\alpha_k/\omega_k, \qquad k = 1, \ldots, N. \tag{4.11}$$

The damped and undamped natural frequencies are equal when the matrix $\mathbf{K}\mathbf{M}^{-1}\mathbf{C}$ is symmetric [79], which is the case for Rayleigh and viscoelastic Kelvin-Voigt damping:

$$\begin{aligned} \mathbf{C} = \alpha\mathbf{M} + \beta\mathbf{K} \quad &\Rightarrow\ \mathbf{K}\mathbf{M}^{-1}\mathbf{C} = \alpha\mathbf{K} + \beta\mathbf{K}\mathbf{M}^{-1}\mathbf{K}, \\ \mathbf{C} = \eta\mathbf{K} \quad &\Rightarrow\ \mathbf{K}\mathbf{M}^{-1}\mathbf{C} = \eta\mathbf{K}\mathbf{M}^{-1}\mathbf{K}. \end{aligned} \tag{4.12}$$

Here symmetry is obvious since $\mathbf{K}$ and $\mathbf{M}$ are symmetric.

Frequency-dependent eigenvalue problem

Viscoelastic materials, as introduced in Section 3.1.4, may have strongly frequency-dependent properties constants that should be taken into account also for the solution of eigenvalue problems:

$$\hat{\omega}_k^2\,\mathbf{M}\,\hat{\boldsymbol{\phi}}_k = \mathbf{K}(\omega_k)\,\hat{\boldsymbol{\phi}}_k,\ k = 1, \ldots, N. \tag{4.13}$$

In [123] an iterative approach for the solution of the linear eigenvalue problem with $\mathbf{K} = \mathbf{K}(\omega)$ was suggested to determine the frequency-dependent natural frequencies $\hat{\omega}_k$ and eigenmodes $\hat{\boldsymbol{\phi}}_k$, which is presented here in Algorithm 2.

In general the stiffness matrix $\mathbf{K}(\omega)$ depends on two frequency-dependent parameters, Young's modulus $E(\omega)$ and Poisson's ratio $\nu(\omega)$. If ν is assumed as constant, only $E(\omega)$ remains as a linear parameter:

$$\mathbf{K}(\omega) = \frac{E(\omega)}{E(0)}\mathbf{K}(0). \tag{4.14}$$

In this case it is not necessary to reassemble $\mathbf{K}(\omega)$ in every iteration step, it can just be obtained by scaling of $\mathbf{K}(0)$. Furthermore, as it is shown in Appendix A.1, the frequency-dependent eigenvalue problem even reduces to $\hat{\boldsymbol{\phi}}_k = \boldsymbol{\phi}_k$ and the solution of the following scalar nonlinear equation for $\hat{\omega}_k$:

$$\hat{\omega}_k = \omega_k \sqrt{\frac{E(\hat{\omega}_k)}{E_0}}. \tag{4.15}$$

However, in situations where $\mathbf{K}$ is obtained from an isogeometric multi-patch finite element discretization, see Section 2.3.1, $\mathbf{K}(\omega) = \frac{E(\omega)}{E(0)}\mathbf{K}(0)$ is not necessarily true for the global stiffness matrix, but maybe only for a patch submatrix with frequency-dependent material it is $\mathbf{K}^i(\omega) = \frac{E^i(\omega)}{E^i(0)}\mathbf{K}^i(0)$. Then the above-mentioned simplification as scalar nonlinear equation for $\hat{\omega}_k$ cannot be used anymore, but at least in Algorithm 2 the submatrix can be scaled and need not be reassembled.

Also the complex eigenvalue problem with damping from (4.9) can be formulated for frequency-dependent materials and an iteration similar to Algorithm 2 can be carried out to compute natural frequencies and damping ratios.

Modal participation factors

For systems with several hundreds of thousands or even millions of degrees of freedom it is very costly to compute numerical solutions of the generalized eigenvalue problem, see subsequent Section 4.1.1. Thus typically only a fraction of the smallest eigenfrequencies and corresponding modes is computed [62].

Effective modal masses or *modal participation factors* are a measure of the significance of modes for the vibration of a system and may provide a guideline for how many and which modes should be computed to accurately capture the vibrational behavior of a system, or which modes should be included in a reduction basis when a system is reduced onto its modes, see Chapter 5.

Modal participation factors are computed with respect to an influence vector $\mathbf{r} \in \mathbb{R}^N$. Typically, it is $\mathbf{r} \equiv \mathbf{1}$, or to differentiate among spatial directions it can be chosen $\mathbf{r}_x = (1,0,0,1,0,0,\ldots,1,0,0)^T$ and $\mathbf{r}_y$, $\mathbf{r}_z$ analogous.

Then for a mass-normalized eigenmode $\boldsymbol{\phi}_k$ with $\boldsymbol{\phi}_k^T \mathbf{M} \boldsymbol{\phi}_k = 1$, the modal participation factor Γ_k and effective modal mass $m_{\text{eff},k}$ are defined as

$$\Gamma_k = \boldsymbol{\phi}_k^T \, \mathbf{M} \, \mathbf{r}, \quad m_{\text{eff},k} = \Gamma_k^2. \tag{4.16}$$

When $\mathbf{r} \equiv \mathbf{1}$ it holds for the effective modal masses and the total mass of the system m_{tot}:

$$\sum_{k=1}^{N} m_{\text{eff},k} = 3 m_{\text{tot}}. \tag{4.17}$$

Numerical solution of generalized eigenvalue problems

Typically generalized eigenvalue problems like (4.6) are rewritten as standard eigenvalue problems [13, 124]:

$$\lambda_k \boldsymbol{\phi}_k = \mathbf{M}^{-1}\mathbf{K} \, \boldsymbol{\phi}_k, \quad k = 1, \ldots, N, \tag{4.18}$$

which requires $\mathbf{M}$ to be positive definite, i.e. invertible. Then, an iterative numerical algorithm for the approximate solution of the symmetric standard eigenvalue problem for some k has to be chosen from a wide range of methods, including Householder-QR-inverse, generalized Jacobi, Krylov subspace or determinant search methods [13, 113].

In multi-patch problems with Lagrangian multipliers, see Section 2.3.2, the generalized eigenvalue problem (4.6) takes the form

$$\begin{aligned} & \lambda_k \, \mathbf{M}^* \, \boldsymbol{\phi}_k^* = \mathbf{K}^* \, \boldsymbol{\phi}_k^*, && k = 1, \dots, N, \\ \Leftrightarrow \quad & \lambda_k \begin{pmatrix} \mathbf{M} & \mathbf{0} \\ \mathbf{0} & \mathbf{0} \end{pmatrix} \begin{pmatrix} \boldsymbol{\phi}_k \\ \boldsymbol{\psi}_k \end{pmatrix} = \begin{pmatrix} \mathbf{K} & \mathbf{B}^T \\ \mathbf{B} & \mathbf{0} \end{pmatrix} \begin{pmatrix} \boldsymbol{\phi}_k \\ \boldsymbol{\psi}_k \end{pmatrix}, && k = 1, \dots, N, \end{aligned} \tag{4.19}$$

where the matrix $\mathbf{M}^*$ is only positive semi-definite. A static condensation, as for example used for lumped mass matrices with zero diagonal entries, is not possible here, since the (2,2)-block of $\mathbf{K}^*$ is also zero. Instead, it must be reformulated as a standard eigenvalue problem by inverting $\mathbf{K}^*$:

$$\frac{1}{\lambda_k} \boldsymbol{\phi}_k^* = \mathbf{K}^{*-1} \mathbf{M}^* \, \hat{\boldsymbol{\phi}}_k, \quad k = 1, \dots, N. \tag{4.20}$$

4.1.2 Direct frequency response

Another means of linear frequency analysis, which is also available in most FEA software, is the so-called *direct frequency response* (DFR) method for computing the steady-state response of a structure subject to harmonic loading. The method is sometimes also refered to as harmonic response analysis or simply harmonic analysis, as the external force vector is of the form

$$\mathbf{b}(t) = \mathbf{b}_c \cos \omega t + \mathbf{b}_s \sin \omega t, \quad \forall t \in [0, T], \tag{4.21}$$

where ω is the fundamental frequency of the excitation and $T = 2\pi/\omega$ the period of vibration. Then, the deformation vector is also expressed as a sum of cosine and sine functions

$$\mathbf{d}(t) = \mathbf{d}_c \cos \omega t + \mathbf{d}_s \sin \omega t, \quad \forall t \in [0, T], \tag{4.22}$$

which leads to the following form of the discretized equation of motion (4.4):

$$\begin{aligned} & \Big(-\omega^2 \, \mathbf{M} \, \mathbf{d}_c + \omega \, \mathbf{C} \, \mathbf{d}_s + \mathbf{K} \, \mathbf{d}_c - \mathbf{b}_c \Big) \cos \omega t + \\ & \Big(-\omega^2 \, \mathbf{M} \, \mathbf{d}_s - \omega \, \mathbf{C} \, \mathbf{d}_c + \mathbf{K} \, \mathbf{d}_s - \mathbf{b}_s \Big) \sin \omega t \; = \mathbf{0} \quad \forall t \in [0, T]. \end{aligned} \tag{4.23}$$

Both time-independent terms in brackets have to be zero for (4.23) to fulfilled for all $t \in [0, T]$, which leads to the following $2N$-sized system of equations:

$$\begin{pmatrix} -\omega^2 \, \mathbf{M} + \mathbf{K} & \omega \, \mathbf{C} \\ -\omega \, \mathbf{C} & -\omega^2 \, \mathbf{M} + \mathbf{K} \end{pmatrix} \begin{pmatrix} \mathbf{d}_c \\ \mathbf{d}_s \end{pmatrix} = \begin{pmatrix} \mathbf{b}_c \\ \mathbf{b}_s \end{pmatrix}. \tag{4.24}$$

Typically (4.24) is solved over a range of frequency values ω in order to obtain the frequency response curves, which show vibration amplitudes and phase at a certain evaluation point on the structure, or the values of kinetic or potential energy. For every time

$t \in [0, T]$, the kinetic and potential energy are:

$$E_{kin}(t) = \tfrac{1}{2}\, \dot{\mathbf{d}}(t)^T \mathbf{M}\, \dot{\mathbf{d}}(t), \quad E_{pot} = \tfrac{1}{2}\, \mathbf{d}(t)^T \mathbf{K}\, \mathbf{d}(t) = \tfrac{1}{2}\, \mathbf{d}(t)^T \mathbf{b}(t). \tag{4.25}$$

Integrating these expressions over the time interval $[0, T]$ leads to the total energies of one period of vibration:

$$\begin{aligned}
E_{kin} &= \frac{1}{T} \int_0^T \frac{1}{2}\, \dot{\mathbf{d}}(t)^T \mathbf{M}\, \dot{\mathbf{d}}(t)\, dt \\
&= \frac{\omega}{2\pi} \frac{\omega^2}{2} \int_0^T \left\{ \sin^2 \omega t\, \mathbf{d}_c^T \mathbf{M}\, \mathbf{d}_c + \cos^2 \omega t\, \mathbf{d}_s^T \mathbf{M}\, \mathbf{d}_s - 2 \sin \omega t \cos \omega t\, \mathbf{d}_c^T \mathbf{M}\, \mathbf{d}_s \right\} dt \\
&= \frac{\omega^2}{4} \left(\mathbf{d}_c^T \mathbf{M}\, \mathbf{d}_c + \mathbf{d}_s^T \mathbf{M}\, \mathbf{d}_s \right), \\
E_{pot} &= \frac{1}{T} \int_0^T \frac{1}{2}\, \mathbf{d}(t)^T \mathbf{K}\, \mathbf{d}(t)\, dt \\
&= \frac{\omega}{2\pi} \frac{1}{2} \int_0^T \left\{ \cos^2 \omega t\, \mathbf{d}_c^T \mathbf{K}\, \mathbf{d}_c + \sin^2 \omega t\, \mathbf{d}_s^T \mathbf{K}\, \mathbf{d}_s + 2 \cos \omega t \sin \omega t\, \mathbf{d}_c^T \mathbf{K}\, \mathbf{d}_s \right\} dt \\
&= \frac{1}{4} \left(\mathbf{d}_c^T \mathbf{K}\, \mathbf{d}_c + \mathbf{d}_s^T \mathbf{K}\, \mathbf{d}_s \right).
\end{aligned} \tag{4.26}$$

4.2 Survey of nonlinear frequency analysis methods

The solution of eigenvalue problems and direct frequency response are two standard methods in engineering practice for linear frequency and vibration analysis of structures and implemented in almost every commercial and open-source finite element software for structural analysis. However, nonlinear vibration analysis is a much more difficult and unconventional task, which is lacking efficient numerical methods and implementations for large-scale applications in structural dynamics. For a general summary of methods for nonlinear oscillation resp. frequency analysis we refer to [86, 87, 117].

To give an overview of methods for nonlinear frequency analysis methods in structural dynamics, we recall the semi-discretized equation of motion with periodicity boundary conditions

$$\begin{aligned}
\mathbf{M}\, \ddot{\mathbf{d}}(t) + \mathbf{C}\, \dot{\mathbf{d}}(t) + \mathbf{f}(\mathbf{d}(t), \dot{\mathbf{d}}(t)) = \mathbf{b}(t) \quad \forall t \in [0, T], \\
\mathbf{d}(0) = \mathbf{d}(T), \quad \dot{\mathbf{d}}(0) = \dot{\mathbf{d}}(T).
\end{aligned} \tag{4.27}$$

This is a nonlinear ordinary differential equation system, in contrast to the linear or linearized equation of motion in (4.4), which we have treated so far in Section 4.1. The system arises from the isogeometric finite element discretization of nonlinear continuum mechanics with large deformations and visco-hyperelastic material models, as we have derived it in Section 3.2, (3.45).

4.2.1 Nonlinear counterparts of eigenmodes

We review two kinds of extensions or counterparts of the concept of linear eigenmodes, which can be used to describe vibrational behavior of nonlinear systems: *tangent modes* and *nonlinear normal modes*. Both can also be employed in reduced-order modeling of nonlinear systems, see later Section 5.1.

Tangent modes

Tangent modes are the eigenmodes one obtains from the solution of an updated eigenvalue problem with the tangent stiffness for the current deformation state [96, 112]:

$$\omega_k^2 \, \mathbf{M} \, \boldsymbol{\phi}_k = \mathbf{K}_T(\boldsymbol{\phi}_k) \, \boldsymbol{\phi}_k. \tag{4.28}$$

While linear eigenmodes in (4.6) are independent of their scaling, the tangent stiffness matrix $\mathbf{K}_T(\boldsymbol{\phi}_k)$ depends on the size and scaling of the tangent mode $\boldsymbol{\phi}_k$, and thus also on the mode itself. Tangent modes $\boldsymbol{\phi}_k^\alpha$ can be computed depending on a parameter α, which could be for example the norm of the mode $\alpha = \|\boldsymbol{\phi}_k^\alpha\|$, or the value of a specific component $\alpha = \{\boldsymbol{\phi}_k^\alpha\}_i$. Defining $\boldsymbol{\phi}_k^0$ for $\alpha = 0$ as the linear eigenmode, one can set up a hysteresis for computing $\boldsymbol{\phi}_k^\alpha$ and observe the nonlinear dependency of the tangent mode on the parameter α.

We compute tangent modes for example in the numerical application of a thick cylinder in Section 4.4.2 and Figure 4.6.

Nonlinear normal modes

Another nonlinear counterpart of linear eigenmodes, which are sometimes also called linear normal modes, are *nonlinear normal modes* (NNMs). They were first introduced for single-DOF and multiple-DOF systems in [103, 108, 122]. In this context a sound theoretical foundation was established, including existence, stability and bifurcation of NNMs.

However, the concept of NNMs was restricted to weakly nonlinear systems, where the nonlinearity depends on a perturbation parameter ε. Only since 1990's NNMs have been also investigated in nonlinear structural dynamics with stronger nonlinearities [72, 92].

NNMs can be defined either as "a vibration in unison of the system (i.e., a synchronous periodic oscillation)" [92] or as "two-dimensional invariant manifold in phase space" [92], which depend on the energy of the system [103, 108] – very similar to tangent modes depending on the scaling parameter α. For systems with only few DOFs they are computed by an energy-based formulation, an invariant manifold approach using two master coordinates, the multiple scales method or a truncated Fourier series ansatz for the time domain [72, 92]. For larger systems numerical techniques must be used, such as numerical integration, also using shooting methods, the so-called asymptotic-numerical method, or the autonomous version of the harmonic balance method, see the following Section 4.3.

Tangent modes are relatively simple to compute as iterative solutions of the eigenvalue problem or using a continuation of the parameter α, but they do not account for internal resonances and can only be determined in the neighborhood of a linear eigenfrequency

resp. eigenmode. The concept of NNMs is therefore more general, but numerical algorithms for their computation are more complex. For instance, an autonomous version of harmonic balance method (see Section 4.3) can be used.

4.2.2 Steady-state response by time integration

The problem of steady-state response to harmonic loading is the nonlinear counterpart of linear DFR, see Section 4.1.2. In engineering practice it is typically solved by *time integration* of the initial value problem (4.27) [20, 54, 130], also in the IGA context [39].

A suitable time integration method, such as explicit or implicit Euler methods, Newmark, Runge-Kutta, or BDF, has to be selected [20, 113, 130]. Since all of these methods rely on the approximation of time derivatives of displacements, i.e. velocities, the time-step size Δt is a critical quantity. It has to be chosen carefully with $\Delta t \ll T = 2\pi/\omega$ in order to guarantee the accuracy of the method and be able to capture the oscillatory behavior of loads and displacements in wave propagation problems [130].

Then, time integration must be carried out over many periods T until a steady-state of motion is reached. For strongly damped systems this is the case much faster than for undamped or only lightly damped systems. This indicates that numerical damping might be needed for stability of the integration method for a conservative system, where no physical dissipation is included. But then it introduces a phase shift and inaccuracy of the solution, since angular momentum and energy might not be conserved [130].

Shooting methods can also be employed to solve (4.27) with time integration as a boundary value problem instead of an initial value problem [54, 113].

Due to the above-mentioned disadvantages of time integration methods, high computational effort due to small step size and integration over many cycles, we prefer a different method for the computation of steady-state response, namely the harmonic balance method.

4.3 The harmonic balance method

The *Harmonic Balance Method* (HBM) is a means for the approximation of solutions of periodic nonlinear ODE systems, which is based on a truncated Fourier series expansion of the solution. It was originally developed by W. Szemplińska-Stupnicka in 1960's as a semi-analytical method and applied to systems with only few DOFs [115, 116, 117]. Sometimes it is also called *multi-harmonic balance* or *describing function* method.

Nowadays it is widespread in application to electrical circuits with nonlinear components [31, 54, 55, 106], or also for electromagnetic problems [9]. In structural dynamics, it has been mainly applied to FE discretizations of lower-dimensional beam and shell models [80, 81, 87, 100, 98, 99].

HBM can be used to compute either the solution of a nonlinear, self-excited system, i.e. a nonlinear normal mode, see Section 4.2.1, or to determine steady-state response to a periodic external force, as an alternative to time integration presented in Section 4.2.2 [87].

4.3.1 Introduction of the method

Here, we apply the harmonic balance method to compute steady-state response of nonlinear mechanical systems, which are governed by large deformation visco-hyperelasticity. Starting point is the equation of motion after semi-discretization using isogeometric finite elements, which was already given in (4.27). It is a nonlinear second-order ODE for the vector of control point displacements $\mathbf{d}(t) \in \mathbb{R}^N$ with periodicity conditions:

$$\begin{aligned} \mathbf{M}\,\ddot{\mathbf{d}}(t) + \mathbf{C}\,\dot{\mathbf{d}}(t) + \mathbf{f}(\mathbf{d}(t), \dot{\mathbf{d}}(t)) = \mathbf{b}(t) \quad \forall t \in [0, T], \\ \mathbf{d}(0) = \mathbf{d}(T), \quad \dot{\mathbf{d}}(0) = \dot{\mathbf{d}}(T). \end{aligned} \tag{4.29}$$

As mentioned before, periodic external excitations of the structure are considered with a fundamental frequency ω, resp. frequency $f = \omega/(2\pi)$ or period $T = 2\pi/\omega$, which can be described as an harmonic series with finite number m^* of cosine and sine terms:

$$\mathbf{b}(\omega, t) = \tfrac{1}{2}\mathbf{b}_0 + \sum_{k=1}^{m^*} \cos(k\omega t)\,\mathbf{b}_k + \sin(k\omega t)\,\mathbf{b}_{2m^*-k+1}. \tag{4.30}$$

The response to periodic excitation is expected to be ω-periodic as well and thus the displacement vector $\mathbf{d}(t)$ of the spatial discretization $\mathbf{u}^h(\mathbf{x}, t) = \sum_{i=1}^{n} N_i^p(\mathbf{x})\,\mathbf{d}_i(t)$ (3.39), and consequently also the velocities $\dot{\mathbf{d}}$ and accelerations $\ddot{\mathbf{d}}$, are expressed as an harmonic series, or in other words as a truncated Fourier expansion, with $m \geq m^*$ harmonic terms of fundamental frequency ω and amplitudes $\mathbf{q} = \left(\mathbf{q}_0^T, \ldots, \mathbf{q}_{2m}^T\right)^T \in \mathbb{R}^{(2m+1)N}$:

$$\begin{aligned} \mathbf{d}(\mathbf{q}, \omega, t) &= \tfrac{1}{2}\mathbf{q}_0 + \sum_{k=1}^{m} \cos(k\omega t)\,\mathbf{q}_k + \sin(k\omega t)\,\mathbf{q}_{\bar{k}}, \\ \dot{\mathbf{d}}(\mathbf{q}, \omega, t) &= \sum_{k=1}^{m} -k\omega \sin(k\omega t)\,\mathbf{q}_k + k\omega \cos(k\omega t)\,\mathbf{q}_{\bar{k}}, \\ \ddot{\mathbf{d}}(\mathbf{q}, \omega, t) &= \sum_{k=1}^{m} -k^2\omega^2 \cos(k\omega t)\,\mathbf{q}_k - k^2\omega^2 \sin(k\omega t)\,\mathbf{q}_{\bar{k}}, \end{aligned} \tag{4.31}$$

using the abbreviation $\bar{k} := 2m - k + 1$.

Substitution of the ansatz for displacements from (4.31) into (4.29) results in a residual vector:

$$\mathbf{r}(\mathbf{q}, \omega, t) = \mathbf{M}\,\ddot{\mathbf{d}}(\mathbf{q}, \omega, t) + \mathbf{C}\,\dot{\mathbf{d}}(\mathbf{q}, \omega, t) + \mathbf{f}\Big(\mathbf{d}(\mathbf{q}, \omega, t), \dot{\mathbf{d}}(\mathbf{q}, \omega, t)\Big) - \mathbf{b}(\omega, t). \tag{4.32}$$

In order to compute the amplitudes $\mathbf{q}_k$, Ritz procedure is applied by projecting the residual $\mathbf{r}$ onto the basis functions of the frequency domain, which results in a Fourier expansion of the residual $\mathbf{r}$ with $2m+1$ coefficient vectors $\hat{\mathbf{r}}_j$ that have to be evaluated to $\mathbf{0}$ (*balance of the harmonics*):

$$\begin{aligned} \hat{\mathbf{r}}_j(\mathbf{q}, \omega) &= \frac{2}{T} \int_0^T \mathbf{r}(\mathbf{q}, \omega, t)\, \cos(j\omega t)\, dt \;\stackrel{!}{=}\; \mathbf{0}, \quad j = 0, \ldots, m\,, \\ \hat{\mathbf{r}}_{\bar{j}}(\mathbf{q}, \omega) &= \frac{2}{T} \int_0^T \mathbf{r}(\mathbf{q}, \omega, t)\, \sin(j\omega t)\, dt \;\stackrel{!}{=}\; \mathbf{0}, \quad j = 1, \ldots, m. \end{aligned} \tag{4.33}$$

The nonlinear system of $(2m+1)N$ equations given by (4.33), which we abbreviate as

$$\hat{\mathbf{r}}(\mathbf{q}, \omega) = \mathbf{0}, \tag{4.34}$$

has to be solved to determine the amplitudes $\mathbf{q}$ and thus obtain the steady-state frequency response of the system.

4.3.2 Implementation aspects

Fourier transform of residual

As mentioned above, the projection of the residual vector $\mathbf{r}$ onto harmonic basis functions in (4.33) equals a Fourier transform, or more precisely a Hartley transform, since it transforms the real-valued residual onto real-valued coefficients [58].

Thus the numerical evaluation of integrals in (4.33) can be performed as a discrete Hartley transform (DHT, [27]) of the residual. First the integrals are transformed onto a non-dimensional time $\tau = \omega t$, such that the domain of integration becomes $[0, 2\pi]$. Then the residual $\mathbf{r}(\mathbf{q}, \omega, \tau)$ has to be sampled at equidistant times $\tau_j = \frac{2\pi j}{2m+1}$, $j = 0, \ldots, 2m$ and it becomes:

$$\hat{\mathbf{r}}_0 = \frac{\hat{\mathbf{r}}_0^*}{2m+1}, \quad \hat{\mathbf{r}}_j = \frac{\hat{\mathbf{r}}_j^* + \hat{\mathbf{r}}_{\bar{j}}^*}{2m+1}, \quad \hat{\mathbf{r}}_{\bar{j}} = \frac{\hat{\mathbf{r}}_j^* - \hat{\mathbf{r}}_{\bar{j}}^*}{2m+1}, \quad j = 1, \ldots, m, \tag{4.35}$$

where

$$\hat{\mathbf{r}}_j^* = \mathbf{r}(\mathbf{q}, \omega, \tau_0) + \sum_{k=1}^{2m} \mathbf{r}(\mathbf{q}, \omega, \tau_k)\, \sqrt{2} \cos\left(\frac{2\pi j k}{2m+1} - \frac{\pi}{4}\right), \quad j = 0, \ldots, 2m. \tag{4.36}$$

Aliasing effects due to undersampling do not occur here, since the highest frequency of the signal, here the highest harmonic of (4.31), is m, which is smaller than half of the sampling rate, which is $2m+1$. Thus Nyquist-Shannon/WKS sampling theorem is fulfilled [26, 90].

Solution using Newton's method

For given ω, (4.34) is a nonlinear system of $(2m+1)N$ equations in $\hat{\mathbf{r}}$ for the same number of unknowns $\mathbf{q}$. Thus it can be solved using a Newton's method, just like Algorithm 1 (page 39) for the solution of the static nonlinear elasticity problem.

For that matter also the Jacobian $\hat{\mathbf{J}} \in \mathbb{R}^{(2m+1)N \times (2m+1)N}$ of residual coefficients $\hat{\mathbf{r}}_j$ with respect to amplitudes $\mathbf{q}_k$ needs to be computed:

$$\begin{aligned}
\hat{\mathbf{J}}(\mathbf{q}, \omega) &= \left(\frac{d\hat{\mathbf{r}}_j}{d\mathbf{q}_k}(\mathbf{q}, \omega)\right)_{j,k=0,\ldots,2m} : \\
\frac{d\hat{\mathbf{r}}_j}{d\mathbf{q}_k}(\mathbf{q}, \omega) &= \frac{2}{T} \int_0^T \frac{d\mathbf{r}}{d\mathbf{q}_k}(\mathbf{q}, \omega, t)\, \cos(j\omega t)\, dt, \quad j = 0, \ldots, m\,, \\
\frac{d\hat{\mathbf{r}}_{\bar{j}}}{d\mathbf{q}_k}(\mathbf{q}, \omega) &= \frac{2}{T} \int_0^T \frac{d\mathbf{r}}{d\mathbf{q}_k}(\mathbf{q}, \omega, t)\, \sin(j\omega t)\, dt, \quad j = 1, \ldots, m.
\end{aligned} \tag{4.37}$$

As described above, the integrals in (4.37) are also evaluated using DHT and are thus transformed onto $\tau = \omega t$ and sampled at times τ_j. Furthermore, also the Jacobians $\frac{d\hat{\mathbf{r}}_j}{d\mathbf{q}_k} = \mathbf{J}_k \in \mathbb{R}^{N\times N}$ of the residual vector $\mathbf{r}$ with respect to amplitude vectors $\mathbf{q}_k$ need to be computed:

$$\begin{aligned}
\mathbf{J}_k(\mathbf{q},\omega,t) = \frac{d\mathbf{r}}{d\mathbf{q}_k}(\mathbf{q},\omega,t) = &- k^2\omega^2\cos(k\omega t)\,\mathbf{M} - k\omega\sin(k\omega t)\,\mathbf{C} + \cos(k\omega t)\,\frac{d\mathbf{f}}{d\mathbf{d}}(\mathbf{q},\omega,t)\\
&- k\omega\sin(k\omega t)\,\frac{d\mathbf{f}}{d\dot{\mathbf{d}}}(\mathbf{q},\omega,t), \quad k = 0,\dots,m,\\
\mathbf{J}_k(\mathbf{q},\omega,t) = \frac{d\mathbf{r}}{d\mathbf{q}_{\bar{k}}}(\mathbf{q},\omega,t) = &- k^2\omega^2\sin(k\omega t)\,\mathbf{M} + k\omega\cos(k\omega t)\,\mathbf{C} + \sin(k\omega t)\,\frac{d\mathbf{f}}{d\mathbf{d}}(\mathbf{q},\omega,t)\\
&+ k\omega\cos(k\omega t)\,\frac{d\mathbf{f}}{d\dot{\mathbf{d}}}(\mathbf{q},\omega,t), \quad k = 1,\dots,m.
\end{aligned} \tag{4.38}$$

Here the terms $\frac{d\mathbf{f}}{d\mathbf{d}}(\mathbf{q},\omega,t)$ and $\frac{d\mathbf{f}}{d\dot{\mathbf{d}}}(\mathbf{q},\omega,t)$ refer to the tangent stiffness matrix $\mathbf{K}_T(\mathbf{d},\dot{\mathbf{d}})$, see (3.54), and a viscous tangent matrix $\mathbf{C}_T(\mathbf{d},\dot{\mathbf{d}})$, which have to be computed and evaluated for the current displacement and velocity vectors $\mathbf{d}(t)$ and $\dot{\mathbf{d}}(t)$, which depend on the amplitudes $\mathbf{q}$, frequency ω, and time t using (4.31).

Altogether, Newton's method for the solution of harmonic balance is summarized in Algorithm 3.

The effort of computing $\mathbf{q}$ for a fixed ω using Algorithm 3 is mainly the assembly of force vectors and tangent matrices for each of the $2m+1$ times τ_j of the sampling loop (line 8), which has to be repeated for each iteration step s of the Newton-Raphson loop. Furthermore, a bottle neck is the solution of the linear system of size $(2m+1)N$ in line 14, which is addressed with the reduction method proposed in Chapter 5.

Frequency response curves

Response curves (RC) are a wide-spread means of visualizing the frequency response of steady-state vibrating systems, also for linear DFR (Section 4.1.2). Typically, the total amplitude a_k and phase ϕ_k of one or more harmonics k are evaluated at a specific point on the structure for fixed ω and plotted over a certain range of frequency. They can be computed as follows:

$$a_k = \sqrt{q_k^2 + q_{\bar{k}}^2}, \qquad \phi_k = \arctan\frac{q_{\bar{k}}}{q_k}, \tag{4.39}$$

$$q_k\cos(k\omega t) + q_{\bar{k}}\sin(k\omega t) = a_k\cos(k\omega t + \phi_k). \tag{4.40}$$

The simplest method for generating response curves and functions is simply to start from a fixed ω, compute the response via HBM using Algorithm 3 or DFR, compute amplitude and phase at the evaluation point, and then increment the frequency step by step [86, 87].

However, nonlinear vibrational behavior usually also includes bifurcations with several solution branches and turning points, which makes it necessary to use homotopy resp. continuation methods [1, 57, 86, 97]. Usually an arc-length parameter $\lambda = \lambda(\mathbf{q},\omega)$ is introduced, which is incremented instead of frequency increments only, and allows a simultaneous update of amplitude vector $\mathbf{q}$ and frequency ω. Hence Algorithm 3 has to be

Algorithm 3 Newton's method for harmonic balance

Preassembly: $\mathbf{M},\ \mathbf{C}$
Tolerances: $\varepsilon_q,\ \varepsilon_r > 0$
Initial guess: $\mathbf{q}^0$
Initialization: $s \leftarrow 0$
repeat
  for $j = 0, \dots, 2m$ **do**
    Sampling time: $\tau_j = 2\pi j/(2m+1)$
    Current displacement: $\mathbf{d}(\tau_j) = \mathbf{q}_0^s/2 + \sum_{k=1}^{m} \cos(k\tau_j)\, \mathbf{q}_k^s + \sin(k\tau_j)\, \mathbf{q}_k^s$
    Assembly: $\mathbf{f}(\tau_j) \leftarrow \mathbf{f}(\mathbf{d}(\tau_j), \dot{\mathbf{d}}(\tau_j)),\ \mathbf{b}(\tau_j)$
    $\mathbf{K}_T(\tau_j) \leftarrow \mathbf{K}_T(\mathbf{d}(\tau_j), \dot{\mathbf{d}}(\tau_j)),$
    $\mathbf{C}_T(\tau_j) \leftarrow \mathbf{C}_T(\mathbf{d}(\tau_j), \dot{\mathbf{d}}(\tau_j))$
    Evaluate residual: $\mathbf{r}(\tau_j) \leftarrow \mathbf{M}\,\ddot{\mathbf{d}}(\tau_j) + \mathbf{C}\,\dot{\mathbf{d}}(\tau_j) + \mathbf{f}(\tau_j) - \mathbf{b}(\tau_j)$
    Evaluate Jacobians: $\mathbf{J}_k(\tau_j) \leftarrow$ see (4.38), $k = 0, \dots, 2m$
  end for
  DHT of residual: $\hat{\mathbf{r}}^s \leftarrow \mathrm{DHT}(\mathbf{r}(\tau_0), \dots, \mathbf{r}(\tau_{2m}))$
  DHT of Jacobians: $\hat{\mathbf{J}}_k^s \leftarrow \mathrm{DHT}(\mathbf{J}_k(\tau_0), \dots, \mathbf{J}_k(\tau_{2m})),\ k = 0, \dots, 2m$
  Compute update: $\Delta\mathbf{q}^s \leftarrow$ Solve $\hat{\mathbf{J}}^s\, \Delta\mathbf{q}^s = -\hat{\mathbf{r}}^s$
  Evaluate error: $e_q \leftarrow \frac{\|\Delta\mathbf{q}^s\|}{\|\mathbf{q}^s\|},\ e_r \leftarrow \frac{\|\hat{\mathbf{r}}^s\|}{\|\mathbf{q}^s\|}$
  Update: $\mathbf{q}^{s+1} = \mathbf{q}^s + \Delta\mathbf{q}^s$
  $s \leftarrow s + 1$
until $e_q < \varepsilon_q \ \wedge\ e_r < \varepsilon_r$
Return value: $\mathbf{q} \leftarrow \mathbf{q}^s$

modified such that an additional equation for the arc-length parameter and derivatives w.r.t. ω are introduced [106].

4.3.3 Theoretical properties

We apply the harmonic balance method for a time-discretization of the equation of motion of elasticity, which is a hyperbolic, nonlinear PDE boundary value problem and reads in the continuous form, compare (3.11):

$$\begin{aligned}
\rho_0 \ddot{\mathbf{u}}(\mathbf{x},t) - \operatorname{div}[\mathbf{F}\,\mathbf{S}](\mathbf{x},t) &= \rho_0 \mathbf{b}(\mathbf{x},t) && \forall \mathbf{x} \in \Omega, && \forall t \in [0,T], \\
\mathbf{u}(\mathbf{x},t) &= \mathbf{h}(\mathbf{x},t) && \forall \mathbf{x} \in \Gamma_u, && \forall t \in [0,T], \\
[\mathbf{F}\,\mathbf{S}\,\mathbf{n}](\mathbf{x},t) &= \mathbf{t}(\mathbf{x},t) && \forall \mathbf{x} \in \Gamma_n, && \forall t \in [0,T], \\
\mathbf{u}(\mathbf{x},0) &= \mathbf{u}(\mathbf{x},T) && \forall \mathbf{x} \in \Omega, \\
\dot{\mathbf{u}}(\mathbf{x},0) &= \dot{\mathbf{u}}(\mathbf{x},T) && \forall \mathbf{x} \in \Omega.
\end{aligned} \tag{4.41}$$

Using isogeometric finite elements for the spatial discretization (Section 3.2) and the harmonic balance method for the temporal or frequency domain discretization (Section

4.3.1), it follows that a weak solution of this problem can be expressed by separation of variables as

$$\mathbf{u}^h(\mathbf{x},t) = \sum_{i=1}^{n} N_i^p(\mathbf{x}) \left(\tfrac{1}{2}\mathbf{q}_{0,i} + \sum_{k=1}^{m} \cos(k\omega t)\, \mathbf{q}_{k,i} + \sin(k\omega t)\, \mathbf{q}_{\bar{k},i} \right). \tag{4.42}$$

Properties of the IGA-FEM discretization have already been outlined in Section 2.2.2. The harmonic balance method is a Fourier spectral method [26], i.e. a Galerkin method where the span of the basis functions is global and ranges over the whole domain. Here, Fourier basis functions cosine and sine are employed on time domain $[0, T]$, which automatically fulfill the periodicity boundary conditions.

It can be shown that the Fourier coefficients of a C^∞-continuous function decrease exponentially [26]. For spectral methods with sufficiently smooth exact solution and data, this means that the error in approximating the exact solution of a differential or integral equation is of order $\mathcal{O}(m^{-m})$, where m is the number of spectral basis functions. This so-called *exponential convergence* of spectral methods such as harmonic balance can be achieved since m is at the same time the order of the basis functions and the mesh parameter is $h = \mathcal{O}(1/m)$ [26].

However, we use a Fourier series for the approximation of the solution of a forced vibration problem in nonlinear elasticity, where an exact solution and its Fourier series expansion is in general not known. Thus the accuracy of an harmonic balance approximation may highly depend on the number of harmonics m. Nonlinear effects, such as the cubic nonlinearity of large deformation kinematics, nonlinear constitutive laws, internal resonance and coupling of modes, typically cause response in higher harmonics $m > m^*$ than the highest excited harmonic.

In the numerical examples presented in this thesis, we typically use $m \geq 2m^*$.

4.4 Computational applications

Having introduced harmonic balance as our prefered method for steady-state nonlinear frequency response analysis, we want to use some computational examples to verify the method and examine its properties numerically. In the first application in Section 4.4.1 we investigate a sub-harmonic resonance of a nonlinear Euler-Bernoulli beam. We study convergence of HBM regarding the isogeometric spatial discretization and also the influence of Fourier series length for the time domain discretization. Then we use the forced vibration of a thick cylinder as example for 3-dimensional nonlinear elasticity in Section 4.4.2. The results of HBM are verified in the comparison to linear DFR and nonlinear tangent modes.

4.4.1 Convergence studies for the nonlinear Euler-Bernoulli beam

As a first feasibility study for the use of isogeometric finite element discretizations in combination with harmonic balance method for the nonlinear analysis of forced vibrations, we have investigated the nonlinear Euler-Bernoulli beam. Since the beam is a simplified structural model with a one-dimensional parameterization and two displacement components, see Section 3.4, computational effort of a nonlinear frequency analysis is much

$$L = 1.0 \text{ m}, \quad A = 0.1 \text{ m}^2, \quad E = 0.2 \text{ MPa},$$
$$I = 0.00081 \text{ m}^{-4}, \; r = 0.09 \text{ m}, \; \rho = 2000 \text{ kg/m}^3,$$
$$p(x,t) = 20\, EI\, r/L^3 \, \sin(\pi x/L) \, \cos(\omega t),$$

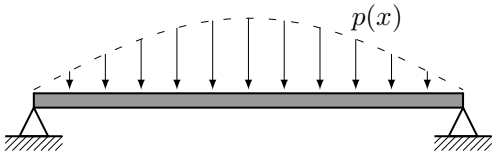

Figure 4.1: Properties of simply supported beam subject to periodic sinusoidal load

less for the beam than for a 3-dimensional continuum mechanics formulation. Hence it is especially suitable for the investigation of convergence properties of the methods, i.e. of the spatial discretization using IGA and of the time/frequency-domain discretization with harmonic balance. The results presented in this section have been obtained within the diploma thesis [126] and were published in [127].

The parameters of a simply supported beam subject to a time-periodic, sinusoidal distributed load are given in Figure 4.1. For the error calculation and convergence study we focus on the mid span of the beam, where sub-harmonic resonance in the third harmonic a_3 occurs around $\omega/\omega_1 \approx 0.34$.

In Figure 4.2 the response curves for degree $p = 3$ and $n = 8, 12$ control points around $\omega/\omega_1 \approx 0.34$ are plotted. Fourier series length is fixed at $m = 3$ and we compare the response curves for k-refinement method (IGA) and p-method (FEM). As the curves are hardly distinguishable, in all cases the sub-harmonic resonance in with rapidly growing amplitude a_3 is captured. Only for the p-method with $\ell = 8$ a difference to the other curves is visible, for the other cases the curves match optically very well.

For a more detailed convergence analysis of the spatial discretization with respect to p, $h = 1/\ell$ and continuity, Fourier series length is fixed at $m = 3$, since the contribution of higher-frequency amplitudes above a_3 is very small. The convergence plot in Figure 4.3 shows the error in the amplitude of the third harmonic $|a_3^h - a_3|$ at $\omega/\omega_1 = 0.338$ for $p = 3, 4, 5$. As reference solution a_3 we take the numerical one obtained from $p = 5$ and a sufficient number of DOFs with an accuracy of 8 digits (an error of magnitude 10^{-9} is assumed to be equal to exact solution $a_3 = 0.20568197$ m). The order of convergence is again $\mathcal{O}(h^{2(p-1)})$, at least for $p = 3$, but in general the error for the C^{p-1} k-method (IGA) is much smaller than for C^1-continuous p-method (FEM). This matches the error estimates obtained for linear modal analysis and the static deformation computation, see Section 2.2.2.

Now we take a deeper look at the m-convergence, i.e. convergence with respect to the number of harmonics or Fourier series length of the harmonic balance discretization. In Table 4.1 the amplitudes a_3 at $\omega/\omega_1 = 0.336$ are given for increasing Fourier series length m with IGA and $p = 5, \ell = 18$. Here, $\varepsilon = |a_3^{11} - a_3^m|/|a_3^{11}|$ is the relative error in a_3 compared to the value for $m = 11$, which is also plotted over m in Figure 4.4. It can be observed that the error decreases very fast with increasing m, which is a sign of the exponential convergence order m^{-m} of harmonic balance. However, not all increments in m contribute to a decrease of ε. The reason is probably that the 5th or 8th harmonic simply do not contribute to the solution due to the type of nonlinearity.

Altogether, with the nonlinear Euler-Bernoulli beam feasibility study we could show that the convergence properties of isogeometric finite elements carry over to nonlinear frequency analysis, i.e. a higher accuracy compared to Lagrangian FE, and also that there is a rapid convergence with respect to the Fourier series length m.

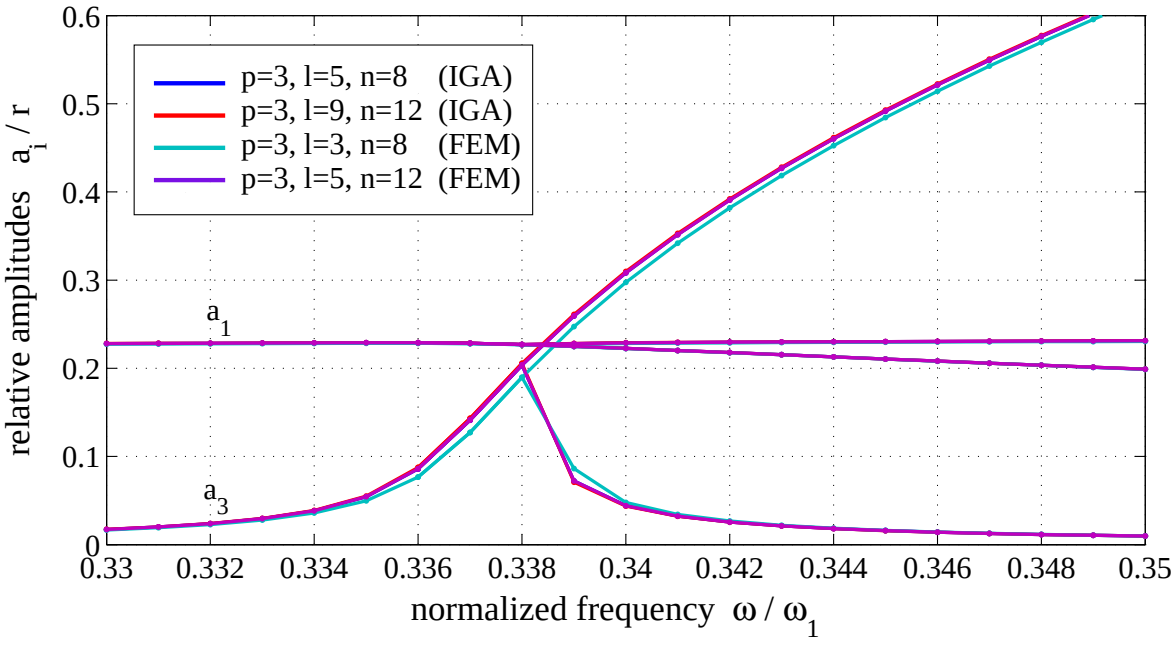

Figure 4.2: Response curves of beam for C^2- (IGA) and C^1-continuous (FEM) cubic B-Splines ($p = 3$) and $n = 8, 12$ control points. Amplitudes a_1 and a_3 are normalized by beam thickness r and shown at sub-harmonic resonance around $\omega/\omega_1 \approx 0.34$

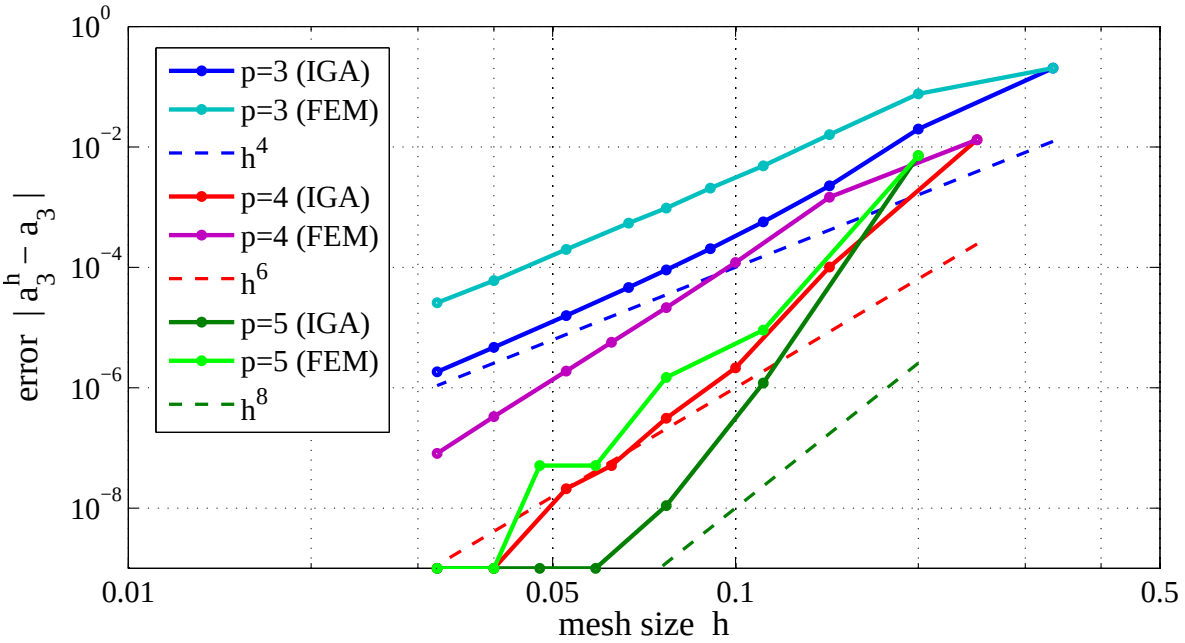

Figure 4.3: Convergence plot of the error in third harmonic amplitude a_3 at $\omega/\omega_1 = 0.338$ using k- (IGA) and p-refinement (FEM) for degrees $p = 3, 4, 5$ and different mesh sizes h

m	3	4	5	6
a_3	0.08762534	0.11654205	0.11658537	0.12138500
ε	$2.774 \cdot 10^{-1}$	$3.892 \cdot 10^{-2}$	$3.856 \cdot 10^{-2}$	$1.018 \cdot 10^{-3}$

m	7	8	9	10
a_3	0.12126404	0.12126439	0.12126145	0.12126152
ε	$2.078 \cdot 10^{-5}$	$2.367 \cdot 10^{-5}$	$5.773 \cdot 10^{-7}$	$1.000 \cdot 10^{-9}$

Table 4.1: Convergence of amplitude a_3 at $\omega/\omega_1 = 0.336$ using IGA with $p = 5, \ell = 18$ for increasing Fourier series length m. $\varepsilon = |a_3^{11} - a_3^m|/|a_3^{11}|$ is the normalized error compared to the solution with $m = 11$

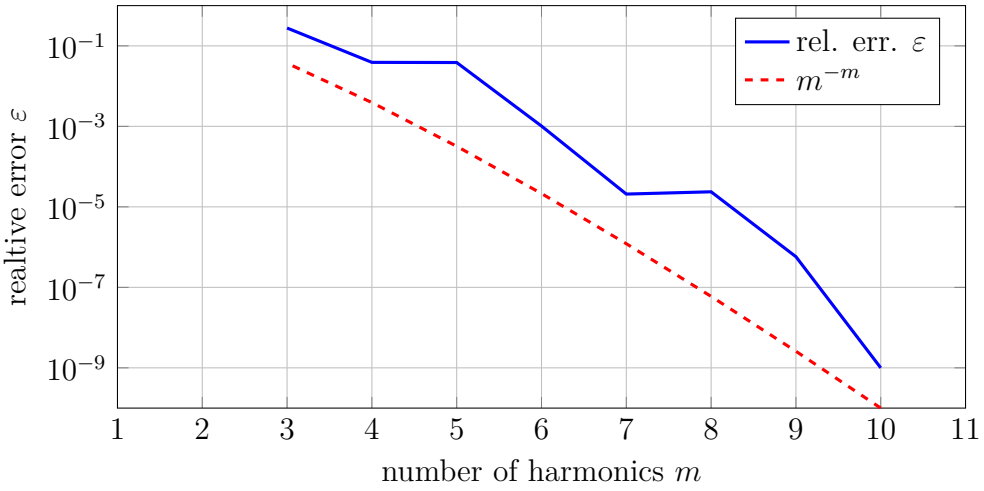

Figure 4.4: Relative error $\varepsilon = |a_3^{11} - a_3^m|/|a_3^{11}|$ of amplitude a_3 for increasing m at $\omega/\omega_1 = 0.336$ using $p = 5, \ell = 18$, compared to exponential convergence rate m^{-m}

4.4.2 Large amplitude vibration of a thick cylinder

As an example for the verification of the simulation of a nonlinear, large amplitude vibration of a 3-dimensional object, we pick up the thick cylinder application from Section 3.5.1. As before, the cylinder is described by Neo-Hookean material law and subject to symmetry boundary conditions, but now we only consider one eighth of it. The dimensions of the cylinder, material parameters and loads can be found again in Figure 4.5. The surface Neumann loads are periodic. For the isogeometric discretization we choose $p = 3, 3, 3,\ \ell = 4, 4, 1,\ n = 588$.

We compute the first linear eigenfrequency as $f_1 = 1581.9$ Hz as an initial step before the nonlinear frequency analysis. Furthermore, we also compute first tangent modes and corresponding eigenfrequencies, see Section 4.2.1, which are plotted as "NLEVP" in Figure 4.6.

Now we perform a harmonic balance frequency response analysis with $m = 3$ (HBM) near the first eigenfrequency within the frequency range of $0.85 < f/f_1 < 1.15$ and compare the results to linear direct frequency response (DFR). Figure 4.6 shows the z-

$$
\begin{aligned}
l &= 0.15 \text{ m}, \\
r &= 0.08 \text{ m}, \\
t &= 0.02 \text{ m}, \\
E &= 74.0 \text{ GPa}, \\
\nu &= 0.33, \\
\rho &= 2800 \text{ kg/m}^3 \\
p_1 &= -2.0 \cdot 10^7 \cos \omega t \text{ N/m}^2, \\
p_2 &= \ 2.0 \cdot 10^7 \cos 2\omega t \text{ N/m}^2.
\end{aligned}
$$

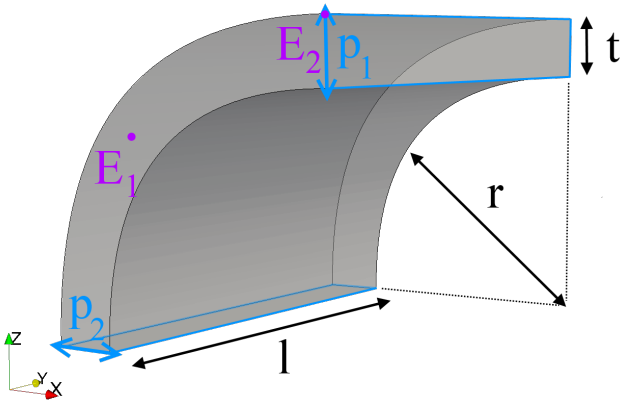

Figure 4.5: Geometry, material parameters and loads of the vibrating thick cylinder

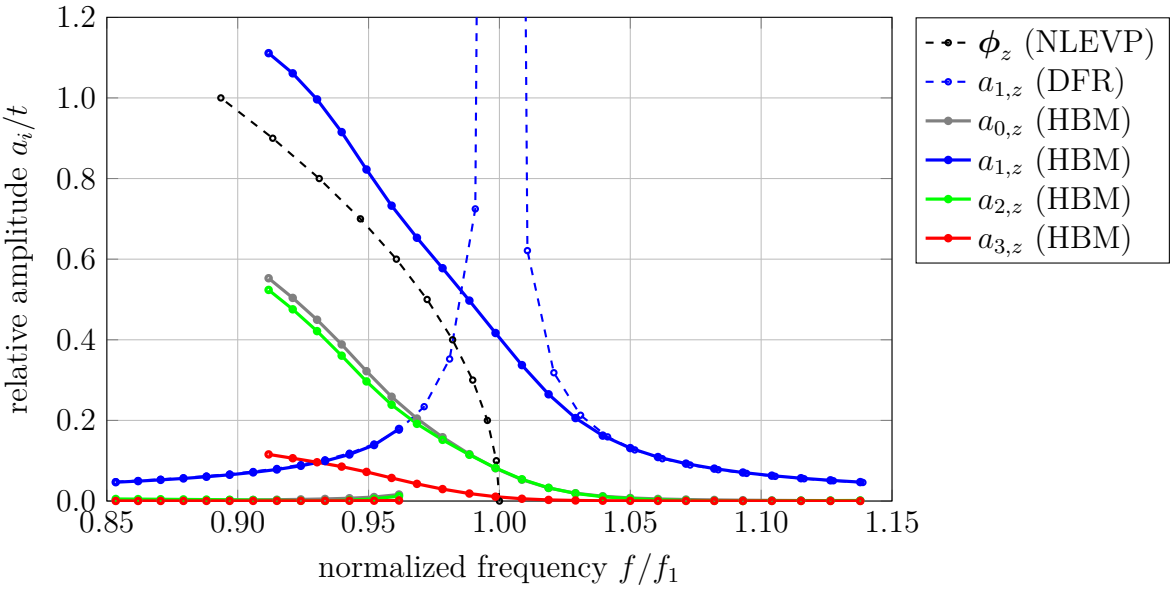

Figure 4.6: Frequency response curves of z-amplitudes of vibrating cylinder $a_{i,z}$ at evaluation point E_1. Comparison of linear DFR and nonlinear tangent mode ϕ_z with HBM validates nonlinear frequency response analysis

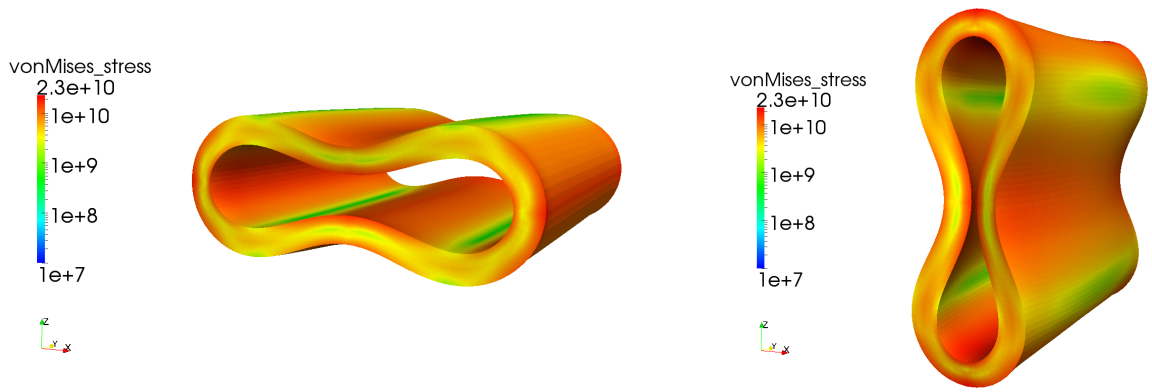

(a) $\tau = 0$ (b) $\tau = \pi$

Figure 4.7: Snapshots of maxima of large deformation of the vibrating cylinder at $\tau = 0$ (a) and $\tau = \pi$ (b) for $f/f_1^h = 0.95$, colored by von Mises stress

amplitudes evaluated at the center point of the front surface of the cylinder (E_1 in Figure 4.5), normalized by the thickness t.

We can find a typical nonlinear resonance behavior with two branches. For the left one we have no more convergence at $f/f^1 = 0.97$, probably due to a turning point that we can not detected with simple frequency increments. Around $f/f^1 \approx 1.0$, where a_1 from linear DFR tends to ∞, we can also detect strong contributions of a_0, a_2 and a_3, which show the nonlinearity of the deformation. Coming from the right, we see that the nonlinear amplitude a_1 also approaches the nonlinear tangent mode $\boldsymbol{\phi}$. Further away from the resonance amplitudes of DFR and HBM correspond quite well, which means that there is only little nonlinear influence.

Snapshots of the deformed vibrating cylinder for $f/f_1 = 0.95$ can be seen in Figure 4.7. At non-dimensional times $\tau = 0$ and $\tau = \pi$ the maxima of amplitudes occur and show a very large deformation. Nevertheless, the isogeometric harmonic balance still exhibits a good convergence behavior, with 4-5 Newton iterations per frequency step.

The correspondence of amplitudes of DFR and HBM further away from resonance, together with the HBM amplitudes approaching the tangent mode near resonance, and also the good convergence properties of the Newton's method, all testify to the validation of the implementation of the HB method.

4.5 Summary

In this chapter we have addressed nonlinear frequency analysis for mechanical applications, based on the isogeometric finite element discretizations of 3-dimensional nonlinear elasticity and the nonlinear Euler-Bernoulli beam, which we have introduced in previous Chapter 3,

First, we have surveyed different methods for free and forced vibration analysis. In the linear context, modal analysis of eigenfrequencies and eigenmodes is a standard practice, and its counterparts in the nonlinear regime are tangent modes and nonlinear normal modes (NNMs). Direct frequency response (DFR) can be used to analyze forced vibrations of linear systems and time integration is usually employed for nonlinear frequency response problems.

We set our focus onto the harmonic balance method (HBM), which can be used to compute both NNMs and forced nonlinear frequency response, where it can be much more efficient than time integrations methods. With the numerical applications that we have presented, we could validate our implementations of HBM in comparison to DFR and tangent modes. Furthermore, the benefits of nonlinear analysis became obvious, as we could compute complex sub-harmonic resonances and accuracy is higher for large amplitude vibrations than when DFR is used.

A convergence study with respect to the isogeometric finite element discretization showed that the advantages of a spatial discretization with higher continuity are also beneficial in the context of nonlinear vibrations.

5 A reduction method for nonlinear vibration analysis

As we have outlined in Section 4.3.2, the harmonic balance method for nonlinear vibration analysis requires the solution of a nonlinear system of equations (4.34):

$$\hat{\mathbf{r}}(\mathbf{q}, \omega) = \mathbf{0}. \tag{5.1}$$

This system is of size $(2m+1)N$, where N is the number of DOFs of the spatial discretization and m the number of harmonics in the Fourier expansion of each of the spatial DOFs. Thus in each step of a Newton iteration, see Algorithm 3 (page 62), a linear system of equations of size $(2m+1)N \times (2m+1)N$ has to be solved.

Furthermore, the linear system is not only $(2m+1)$-times larger than the system to be solved in a static problem, see Section 3.2.3 and Algorithm 1 (page 39), but also more densely populated, as each row of the matrix $\hat{\mathbf{J}}$ has $(2m+1)$-times the number of nonzero entries of the corresponding row of the tangent stiffness matrix $\mathbf{K}_T$. Moreover, $\hat{\mathbf{J}}$ is not symmetric anymore.

This is a severe draw-back regarding the solution process of the system using sparse linear solvers, which are mostly designed for the solution of large, symmetric systems with only few nonzero entries per row, as they arise for instance in finite element discretizations. While sampling time for Fourier transform, i.e. $(2m+1)$-times the assembly of force vector and tangent stiffness, increases linearly with m, and time for Fourier transform itself by $m \log m$, solution time and memory consumption of the system increase at least quadratically [56]. For complex engineering structures with several hundreds of thousands or even millions of DOFs in the finite element model, a harmonic balance analysis becomes even almost impossible.

A possible cure is to use solution methods for the linear system which are more sophisticated and tailored to the harmonic balance problem. For example in [10] a special adaptation of a multigrid preconditioner for iterative solvers of harmonic balance in eddy current problems was proposed. In [106] a direct solver is presented, which treats the matrix as a sparse $N \times N$ matrix with dense $(2m+1) \times (2m+1)$ blocks of Fourier coefficients of a spatial DOF instead of scalar entries.

Another approach, which is pursued in this thesis, is model order reduction (MOR). It aims at decreasing the complexity and computational effort for solving the linear system by a reduction of degrees of freedom of the spatial discretization on $r \ll N$.

In the following we first give an overview of projection methods typically used for model order reduction in Section 5.1. Subsequently, we motivate the usage of our method of choice, i.e. projection with modal derivatives, introduce it in detail and apply it to HBM in Section 5.2. In Section 5.3 we establish an analytical investigation of the properties of modal derivatives for continuous problems for a better general understanding. Finally, in Section 5.1 we show numerical results confirming the quality of the approach.

5.1 Overview of model order reduction methods

Having identified the need for model order reduction to increase the feasibility of harmonic balance frequency response analysis, we are giving a brief overview of different kinds of model reduction methods and a classification with regard to application in nonlinear structural mechanics, dynamics, and especially vibrations [62, 94, 130].

There is a wide range of projection based reduction methods, where the physical coordinate vector $\mathbf{d} \in \mathbb{R}^N$ is expressed by a linear transformation of reduced coordinates $\mathbf{p} \in \mathbb{R}^r$:

$$\mathbf{d} = \mathbf{Q}\mathbf{p}. \tag{5.2}$$

$\mathbf{Q} \in \mathbb{R}^{N \times r}$ is the transformation or projection matrix, with $\operatorname{rank}(\mathbf{Q}) = r \leq N$. In case of $r = N$ (5.2) is a basis transformation, but the intention is to chose $r \ll N$ and project onto a smaller subspace of the original solution space.

The most common projection method is *modal reduction or truncation* [62, 94], where the transformation matrix is composed from a subset of linear eigenvectors $\mathbf{Q} = \mathbf{\Phi}_r$, see Section 4.1.1. It is widely used in linear structural dynamics, since it leads to a decoupling of the equation of motion, compare (4.8). However, there is only a limited applicability to nonlinear problems, as the computational examples presented in Section 5.4 reveal.

Tangent modes, which were introduced in Section 4.2.1, are the eigenmodes one obtains from the solution of an updated eigenvalue problem with the tangent stiffness $\mathbf{K}_T(\mathbf{d})$ for the current state of deformation $\mathbf{d}$. In nonlinear time integration, an updated modal basis can be determined from these tangent modes in every time step, or after a suitable number of time steps. In [112] also a reduction method with direct update of tangent modes in each time step is described. But as we need to approximate the amplitudes for one whole period of vibration in harmonic balance, there is no specific current state of deformation in our setting and these methods seem not very applicable.

Nonlinear normal modes (NNMs), which have been introduced in Section 4.2.1, are a another nonlinear counterpart of linear eigenmodes. They have shown good results already as reduction basis in nonlinear frequency analysis in terms of self-excited vibrations [2, 77, 119, 120]. However, the computational effort of numerically determining the NNMs seems very high, as each NNM requires the solution of an autonomous harmonic balance problem for the full system.

Another possibility for generating a projection basis are *Ritz vectors* [96, 112]. They are derived from the load and displacement vectors of a current state; and in nonlinear analysis basis updates and derivatives may also be included, providing a good approximation of exact solutions [112]. However, again this method relies on a fixed current state of deformation and load, and thus seems not suitable for application in harmonic balance.

For *Proper Orthogonal Decomposition* (POD) a set of sample displacement vectors has to be generated in a preprocessing step, from which an optimal basis is created [17, 60, 112]. The method leads to good results in structural time integration, but sampling requires a priori knowledge of loads. Since unexpected resonances and states of deformation are to be found in nonlinear vibration analysis with HBM, the POD method might not be suitable here.

All of the above-mentioned methods require either continuous basis updates or precomputation using known sample states of deformation, which are both not possible in HBM, or a high cost of precomputing the basis. Thus our choice of reduction method is modal reduction resp. truncation (MR) with *modal derivatives* [68, 96, 111, 112], which has already been employed successfully for time integration of nonlinear solid dynamics [11, 12]. Modal derivatives (MD) are a second order enhancement of the modal basis and account for quadratic terms as they appear in large deformation theory and Green-Lagrange strains. They can be computed from the linear and nonlinear stiffness matrix and eigenvectors in a preprocessing step and do not require basis updates during the computation.

5.2 The modal derivative reduction method

The first part of this Section is dedicated to an introduction to and definition of modal derivatives. Then we derive and show their properties, which motivate their use as a part of a reduction basis. Finally the application of reduction to nonlinear frequency analysis and HBM is sketched.

5.2.1 Introduction to modal derivatives

In the following we are presenting an introduction to the concept of *modal derivatives*, including two different approaches for the definition resp. computation of modal derivative vectors.

Introduction of the concept

Modal derivatives were initially introduced and proposed as a reduction basis for nonlinear structural dynamics by Idelsohn and Cardona [67, 68]. Here we review their derivation and definition, using references [67, 68, 111]:

In a linear modal truncation, the displacements are expressed in terms of eigenmodes of the linear problem $\boldsymbol{\phi}_i$ and modal coordinates p_i. In our nonlinear setting, the tangent stiffness matrix $\mathbf{K}_t$ depends on displacements $\mathbf{d}$, and thus also the (tangent) modes $\boldsymbol{\phi}_i(\mathbf{d})$ depend on displacements:

$$\mathbf{d}(\mathbf{p}) = \sum_{i=1}^{N} \boldsymbol{\phi}_i(\mathbf{d})\, p_i. \tag{5.3}$$

Now $\mathbf{d}(\mathbf{p})$ is developed as second-order Taylor series around the initial configuration of

zero displacements $\mathbf{p} = \mathbf{0}$ ($\mathbf{d} = \mathbf{0}$):

$$\begin{aligned}\mathbf{d} &= \mathbf{0} + \sum_{i=1}^{N} \left(\frac{\partial \mathbf{d}}{\partial p_i}(\mathbf{p} = \mathbf{0})\, p_i + \sum_{j=1}^{N} \frac{\partial^2 \mathbf{d}}{\partial p_i \partial p_j}(\mathbf{p} = \mathbf{0})\, \frac{p_i p_j}{2} \right) \\ &= \sum_{i=1}^{N} \left(\boldsymbol{\phi}_i(\mathbf{0})\, p_i + \sum_{j=1}^{N} \left(\frac{\partial \boldsymbol{\phi}_j}{\partial p_i}(\mathbf{0}) + \frac{\partial \boldsymbol{\phi}_i}{\partial p_j}(\mathbf{0}) \right) \frac{p_i p_j}{2} \right).\end{aligned} \tag{5.4}$$

For computing the modal derivatives $\frac{\partial \boldsymbol{\phi}_j}{\partial p_i}$ one can differentiate the eigenvalue problem (4.28) with $\mathbf{K} = \mathbf{K}_T(\mathbf{0})$ w.r.t. the modal coordinates:

$$\mathbf{0} = \frac{\partial}{\partial p_i} \left[\left(\mathbf{K}_T - \omega_j^2 \mathbf{M} \right) \boldsymbol{\phi}_j \right] = \left(\mathbf{K} - \omega_j^2 \mathbf{M} \right) \frac{\partial \boldsymbol{\phi}_j}{\partial p_i} + \left(\frac{\partial \mathbf{K}_T}{\partial p_i} - \frac{\partial \omega_j^2}{\partial p_i} \mathbf{M} \right) \boldsymbol{\phi}_j. \tag{5.5}$$

In [111] three different approaches for the solution of (5.5) and the computing of modal derivatives $\frac{\partial \boldsymbol{\phi}_j}{\partial p_i}$ are presented: analytical, analytical excluding inertia effects and purely numerical using finite differences of the recomputed tangent eigenvalue problem.

Here we use the "analytical approach excluding mass consideration" [111] for computing the modal derivatives, which leads to the solution of the following linear system for $\frac{\partial \boldsymbol{\phi}_j}{\partial p_i}$:

$$\frac{\partial \boldsymbol{\phi}_j}{\partial p_i} = -\mathbf{K}^{-1} \frac{\partial \mathbf{K}_T}{\partial p_i} \boldsymbol{\phi}_j, \tag{5.6}$$

with a finite difference approximation of the directional derivatives of the tangent stiffness matrix

$$\frac{\partial \mathbf{K}_T}{\partial p_i} \simeq \frac{\mathbf{K}_T(\Delta p_i\, \boldsymbol{\phi}_i) - \mathbf{K}}{\Delta p_i}. \tag{5.7}$$

This approximation leads to symmetric modal derivatives $\frac{\partial \boldsymbol{\phi}_j}{\partial p_i} = \frac{\partial \boldsymbol{\phi}_i}{\partial p_j}$.

An alternative approach

An alternative approach for the derivation and definition of modal derivatives was introduced by Barbic [12]. The idea is picked up and explained in the following:

In linear analysis, we want to find the solution $\mathbf{d} \in \mathbb{R}^N$ of a static deformation problem where the external force is a superposition of mass-scaled eigenmodes:

$$\mathbf{K}\mathbf{d} = \mathbf{M}\boldsymbol{\Phi}\boldsymbol{\Lambda}\mathbf{p}, \tag{5.8}$$

with stiffness matrix $\mathbf{K}$, mass matrix $\mathbf{M}$, eigenmode matrix $\boldsymbol{\Phi} = (\boldsymbol{\phi}_1, \ldots, \boldsymbol{\phi}_N)$, eigenvalue matrix $\boldsymbol{\Lambda} = \mathrm{diag}(\omega_1^2, \ldots, \omega_N^2)$ and parameter vector $\mathbf{p} \in \mathbb{R}^N$ (modal participation factors). From the eigenvalue problem $\mathbf{K}\boldsymbol{\Phi} = \mathbf{M}\boldsymbol{\Phi}\boldsymbol{\Lambda}$ it follows directly that

$$\mathbf{d} = \mathbf{d}(\mathbf{p}) = \boldsymbol{\Phi}\mathbf{p}. \tag{5.9}$$

This means also that a projection basis composed from a selection of eigenmodes can exactly represent the full (non-reduced) solution of a linear problem, where the external

force is a superposition of these modes:

$$\mathbf{b} = \mathbf{M}\mathbf{\Phi}\mathbf{\Lambda}\mathbf{p} \quad \Rightarrow \quad \mathbf{p} = \mathbf{\Lambda}^{-1}\mathbf{\Phi}^T\mathbf{b}. \tag{5.10}$$

This justifies and motivates the use of modal reduction in linear (static and especially dynamic) analysis.

Now we want to find the solution $\mathbf{d} = \mathbf{d}(\mathbf{p})$ of a corresponding nonlinear problem

$$\mathbf{f}(\mathbf{d}) = \mathbf{M}\mathbf{\Phi}\mathbf{\Lambda}\mathbf{p}, \tag{5.11}$$

with $\mathbf{f}(\mathbf{0}) = \mathbf{0}$ and $\frac{d\mathbf{f}}{d\mathbf{d}} = \mathbf{K}_T(\mathbf{d})$, $\mathbf{K}_T(\mathbf{0}) = \mathbf{K}$. In general it is, of course, not possible anymore to find a closed-form solution $\mathbf{d}(\mathbf{p})$, but assuming that $\mathbf{d}$ is C^2-differentiable w.r.t. $\mathbf{p}$ and also $\mathbf{f}$ is C^2-differentiable w.r.t. $\mathbf{d}$, we can expand it into a Taylor series around $\mathbf{p} = \mathbf{0}$:

$$\mathbf{d}(\mathbf{p}) = \mathbf{0} + \frac{d\mathbf{d}}{d\mathbf{p}}(\mathbf{0})\,\mathbf{p} + \frac{1}{2}\left(\frac{d^2\mathbf{d}}{d\mathbf{p}^2}(\mathbf{0}) : \mathbf{p}\right)\mathbf{p} + \dots\ . \tag{5.12}$$

Here $\frac{d^2\mathbf{d}}{d\mathbf{p}^2}(\mathbf{0})$ is a third-order $N \times N \times N$-tensor and ":" denotes the product of the tensor with a N-vector (first order tensor), which results in a $N \times N$-matrix (second order tensor).

In order to find the derivatives in (5.12), we differentiate (5.11) w.r.t. $\mathbf{p}$:

$$\frac{d\mathbf{f}}{d\mathbf{d}}\,\frac{d\mathbf{d}}{d\mathbf{p}} = \mathbf{M}\mathbf{\Phi}\mathbf{\Lambda}. \tag{5.13}$$

Evaluation at $\mathbf{p} = \mathbf{0}$ leads to

$$\mathbf{K}\,\frac{d\mathbf{d}}{d\mathbf{p}}(\mathbf{0}) = \mathbf{M}\mathbf{\Phi}\mathbf{\Lambda}, \tag{5.14}$$

and from the linear eigenvalue problem it follows

$$\frac{d\mathbf{d}}{d\mathbf{p}}(\mathbf{0}) = \mathbf{\Phi}, \tag{5.15}$$

i.e. the first derivatives are the linear eigenmodes, as expected.

Differentiating (5.13) once again we obtain

$$\left(\frac{d^2\mathbf{f}}{d\mathbf{d}^2} : \frac{d\mathbf{d}}{d\mathbf{p}}\right)\frac{d\mathbf{d}}{d\mathbf{p}} + \frac{d\mathbf{f}}{d\mathbf{d}}\,\frac{d^2\mathbf{d}}{d\mathbf{p}^2} = \mathbf{0} \tag{5.16}$$

and evaluate at $\mathbf{p} = \mathbf{0}$:

$$\left(\frac{d^2\mathbf{f}}{d\mathbf{d}^2}(\mathbf{0}) : \mathbf{\Phi}\right)\mathbf{\Phi} + \mathbf{K}\,\frac{d^2\mathbf{d}}{d\mathbf{p}^2}(\mathbf{0}) = \mathbf{0}. \tag{5.17}$$

Thus the modal derivatives $\frac{d^2\mathbf{d}}{d\mathbf{p}^2}(\mathbf{0}) = \frac{d\mathbf{\Phi}}{d\mathbf{p}} =: \mathbf{\Psi}$ can be defined by the equation system

$$\mathbf{K}\,\mathbf{\Psi} = -\left(\mathbf{H} : \mathbf{\Phi}\right)\mathbf{\Phi}, \tag{5.18}$$

where $\mathbf{H}$ is a third-order tensor:

$$\mathbf{H} = \frac{d\mathbf{K}_T}{d\mathbf{d}}(\mathbf{0}) = \frac{d^2\mathbf{f}}{d\mathbf{d}^2}(\mathbf{0}). \tag{5.19}$$

Using the notation $\boldsymbol{\Psi} = (\boldsymbol{\psi}_{ij})_{i,j=1,\dots,N}$ and exploiting that $(\mathbf{H} : \boldsymbol{\phi}_i)$ is the directional derivative of $\mathbf{K}_T$ w.r.t. $\boldsymbol{\phi}_i$, i.e.

$$(\mathbf{H} : \boldsymbol{\phi}_i) = \lim_{\Delta p_i \to 0} \frac{1}{\Delta p_i}(\mathbf{K}_T(\Delta p_i \boldsymbol{\phi}_i) - \mathbf{K}) =: \frac{\partial \mathbf{K}_T}{\partial p_i}, \tag{5.20}$$

we can write (5.18) in index notation as

$$\mathbf{K}\,\boldsymbol{\psi}_{ij} = -\frac{\partial \mathbf{K}_T}{\partial p_i}\boldsymbol{\phi}_j, \quad i,j = 1,\dots,N, \tag{5.21}$$

and arrive at the same expression for the modal derivatives as we had already in (5.6).

Altogeher, the truncated 2nd order Taylor expansion of $\mathbf{d}(\mathbf{p})$ around $\mathbf{p} = \mathbf{0}$ can be written as:

$$\mathbf{d}(\mathbf{p}) = \boldsymbol{\Phi}\,\mathbf{p} + \frac{1}{2}\,(\boldsymbol{\Psi} : \mathbf{p})\,\mathbf{p} = \sum_{i=1}^{N} \boldsymbol{\phi}_i\, p_i + \frac{1}{2}\sum_{i=1}^{N}\sum_{j=i}^{N} \boldsymbol{\psi}_{ij} p_i p_j. \tag{5.22}$$

The definition of modal derivatives $\boldsymbol{\psi}_{ij}$ in (5.21) is not the same as in Idelsohn et al. [68] and (5.5), which is obtained by differentiating the eigenvalue problem. However, it is equivalent to the simplified approach without mass consideration, see (5.6), and leads to symmetric modal derivatives.

5.2.2 Modal derivatives as reduction basis

Based on the approach to modal derivatives used by Barbic [12], which was outlined above, we have further investigated the properties of the Taylor series expansion of the displacement vector using modal derivatives. These findings motivate the use of a reduction basis composed from eigenmodes and modal derivatives, which is also shown here.

Theorem 5.1. *The representation of displacements $\boldsymbol{d}(\boldsymbol{p})$ as quadratic Taylor series expansion*

$$\boldsymbol{d}(\boldsymbol{p}) = \boldsymbol{\Phi}\,\boldsymbol{p} + \tfrac{1}{2}\,(\boldsymbol{\Psi} : \boldsymbol{p})\,\boldsymbol{p}$$

is a 2nd order appoximation of the solution $\boldsymbol{d}$ of the problem

$$\boldsymbol{f}(\boldsymbol{d}) = \boldsymbol{M}\boldsymbol{\Phi}\boldsymbol{\Lambda}\boldsymbol{p}$$

in the neighborhood of $\boldsymbol{p} = \boldsymbol{0}$, i.e.

$$\boldsymbol{f}(\boldsymbol{d}) - \boldsymbol{f}(\boldsymbol{d}(\boldsymbol{p})) = \mathcal{O}(\|\boldsymbol{p}\|^3).$$

Proof. We develop $\mathbf{f}(\mathbf{d})$ as Taylor series around $\mathbf{d} = \mathbf{0}$ up to second order:

$$\mathbf{f}(\mathbf{d}) = \mathbf{0} + \mathbf{K}\mathbf{d} + \tfrac{1}{2}(\mathbf{H} : \mathbf{d})\mathbf{d} + \mathcal{O}(\|\mathbf{d}\|^3).$$

Now we substitute $\mathbf{d}(\mathbf{p})$:

$$\begin{aligned}\mathbf{f}(\mathbf{d}(\mathbf{p})) &= \mathbf{K}\,\mathbf{d}(\mathbf{p}) + \tfrac{1}{2}\,(\mathbf{H} : \mathbf{d}(\mathbf{p}))\,\mathbf{d}(\mathbf{p}) + \mathcal{O}(\|\mathbf{d}(\mathbf{p})\|^3)\\ &= \mathbf{K}\boldsymbol{\Phi}\mathbf{p} + \tfrac{1}{2}\mathbf{K}\,(\boldsymbol{\Psi} : \mathbf{p})\,\mathbf{p} + \tfrac{1}{2}\left(\mathbf{H} : \left(\boldsymbol{\Phi}\mathbf{p} + \mathcal{O}(\|\mathbf{p}\|^2)\right)\right)\left(\boldsymbol{\Phi}\mathbf{p} + \mathcal{O}(\|\mathbf{p}\|^2)\right) + \mathcal{O}(\|\mathbf{p}\|^3)\\ &= \mathbf{K}\boldsymbol{\Phi}\mathbf{p} + \tfrac{1}{2}\mathbf{K}\,(\boldsymbol{\Psi} : \mathbf{p})\,\mathbf{p} + \tfrac{1}{2}\,(\mathbf{H} : (\boldsymbol{\Phi}\mathbf{p}))\,\boldsymbol{\Phi}\mathbf{p} + \mathcal{O}(\|\mathbf{p}\|^3).\end{aligned}$$

Taking advantage of the definition of modal derivatives in (5.18) we continue:

$$\begin{aligned}&= \mathbf{K}\boldsymbol{\Phi}\mathbf{p} + \tfrac{1}{2}\mathbf{K}\,(\boldsymbol{\Psi} : \mathbf{p})\,\mathbf{p} - \tfrac{1}{2}\mathbf{K}\,(\boldsymbol{\Psi} : \mathbf{p})\,\mathbf{p} + \mathcal{O}(\|\mathbf{p}\|^3)\\ &= \mathbf{M}\boldsymbol{\Phi}\boldsymbol{\Lambda}\mathbf{p} + \mathcal{O}(\|\mathbf{p}\|^3)\\ &= \mathbf{f}(\mathbf{d}) + \mathcal{O}(\|\mathbf{p}\|^3).\end{aligned}$$

Thus it follows

$$\mathbf{f}(\mathbf{d}) - \mathbf{f}(\mathbf{d}(\mathbf{p})) = \mathcal{O}(\|\mathbf{p}\|^3).$$

□

Above we have shown that with the quadratic expression of displacements in terms of the parameter vector $\mathbf{p}$ as in (5.22), using the full sets of linear eigenmodes $\boldsymbol{\Phi}$ and modal derivatives $\boldsymbol{\Psi}$, it is possible to approximate the solution of the nonlinear problem (5.11) with an error of third order in $\mathbf{p}$.

Given a general right hand side $\mathbf{b}$, the parameter vector can be computed as $\mathbf{p} = \boldsymbol{\Lambda}^{-1}\boldsymbol{\Phi}^T\mathbf{b}$ to obtain an expression $\mathbf{b} = \mathbf{M}\boldsymbol{\Phi}\boldsymbol{\Lambda}\mathbf{p}$. As the eigenvalues in $\boldsymbol{\Lambda}$ are arranged in a growing order, it is assumed that there is an index r such that $|p_i| < \varepsilon\ \forall i = r+1, \dots, N$ for a certain $0 < \varepsilon < 1$. Furthermore, it is required that $\|\mathbf{p}\|_\infty < 1$ for the Taylor series to converge.

Accordingly by selecting a basis consisting of only the first r eigenmodes using $\boldsymbol{\Phi}_r = (\boldsymbol{\phi}_1, \dots, \boldsymbol{\phi}_r)$, $\mathbf{p}_r = (p_1, \dots, p_r)^T$ and $\boldsymbol{\Lambda}_r = \operatorname{diag}(\omega_1^2, \dots, \omega_r^2)$, we can compute $\mathbf{p}_r = \boldsymbol{\Lambda}_r^{-1}\boldsymbol{\Phi}_r^T\mathbf{b}$.

In a linear problem (5.8) it is then:

$$\mathbf{d} - \mathbf{d}(\mathbf{p}_r) = \mathbf{d}(\mathbf{p}) - \mathbf{d}(\mathbf{p}_r) = \boldsymbol{\Phi}\mathbf{p} - \boldsymbol{\Phi}_r\mathbf{p}_r = \sum_{i=r+1}^{N} \boldsymbol{\phi}_i p_i, \tag{5.23}$$

and

$$\|\mathbf{d} - \mathbf{d}(\mathbf{p}_r)\| = \left\| \sum_{i=r+1}^{N} \boldsymbol{\phi}_i p_i \right\| \le \sum_{i=r+1}^{N} \|\boldsymbol{\phi}_i\|\,|p_i| < (N-r)\varepsilon\delta, \tag{5.24}$$

where $\delta = \max_{i=r+1,\dots,N} \|\boldsymbol{\phi}_i\|$.

For the nonlinear problem (5.11) with the same right hand side and reduced modal derivative tensor $\boldsymbol{\Psi}_r = (\boldsymbol{\psi}_{ij})_{i,j=1,\dots,r}$ it follows:

$$\begin{aligned}\mathbf{d} - \mathbf{d}(\mathbf{p}_r) &= \mathbf{d}(\mathbf{p}) + \mathcal{O}(\|\mathbf{p}\|^3) - \mathbf{d}(\mathbf{p}_r)\\ &= \boldsymbol{\Phi}\mathbf{p} + \frac{1}{2}(\boldsymbol{\Psi} : \mathbf{p})\mathbf{p} - \boldsymbol{\Phi}_r\mathbf{p}_r - \frac{1}{2}(\boldsymbol{\Psi}_r : \mathbf{p}_r)\mathbf{p}_r + \mathcal{O}(\|\mathbf{p}\|^3)\\ &= \sum_{i=r+1}^{N} \boldsymbol{\phi}_i p_i + \frac{1}{2}\sum_{i=r+1}^{N}\sum_{j=r+1}^{N} \boldsymbol{\psi}_{ij} p_i p_j + \sum_{i=1}^{N}\sum_{j=r+1}^{N} \boldsymbol{\psi}_{ij} p_i p_j + \mathcal{O}(\|\mathbf{p}\|^3),\end{aligned} \tag{5.25}$$

and

$$\begin{aligned}\|\mathbf{d}-\mathbf{d}(\mathbf{p}_r)\| &\leq \sum_{i=r+1}^{N}\|\boldsymbol{\phi}_i\|\,|p_i| + \frac{1}{2}\sum_{i=r+1}^{N}\sum_{j=r+1}^{N}\|\boldsymbol{\psi}_{ij}\|\,|p_i|\,|p_j| \\ &\quad + \sum_{i=1}^{N}\sum_{j=r+1}^{N}\|\boldsymbol{\psi}_{ij}\|\,|p_i|\,|p_j| + \mathcal{O}(\|\mathbf{p}\|^3) \\ &< (N-r)\varepsilon\delta + \frac{1}{2}(N-r)^2\varepsilon^2\delta^* \\ &\quad + (N-r)N\varepsilon\delta^* + \mathcal{O}(\|\mathbf{p}\|^3),\end{aligned} \tag{5.26}$$

with $\delta^* = \max_{i=1,\ldots,N,\, j=r+1,\ldots,N}\|\boldsymbol{\psi}_{ij}\|$.

Thus we have an error of order ε for a reduced basis in the linear case and in the nonlinear case also order ε plus the terms of order 3 in terms of all components of $\mathbf{p}$.

This shows that a combination of linear eigenmodes and modal derivatives has very good capabilities of representing the character and solution of a nonlinear system. It motivates the use of a reduced basis composed of a selection of linear eigenmodes $\boldsymbol{\Phi}_r$ and modal derivatives $\boldsymbol{\Psi}_r$ in nonlinear analysis, since the quadratic approximation is able to provide a smiliar accuracy as modal truncation in the linear case.

The linear projection for reduction onto this basis of length $r = r_d + r_d(r_d+1)/2$ is thus given by the projection matrix:

$$\mathbf{Q} = \left(\boldsymbol{\phi}_1, \ldots, \boldsymbol{\phi}_{r_d}, \boldsymbol{\psi}_{11}, \boldsymbol{\psi}_{12}, \ldots, \boldsymbol{\psi}_{1r_d}, \ldots, \boldsymbol{\psi}_{r_d r_d}\right), \tag{5.27}$$

and the projection reads:

$$\mathbf{d} = \mathbf{Q}\mathbf{p} = \sum_{i=1}^{r_d}\boldsymbol{\phi}_i\, p_i + \sum_{i=1}^{r_d}\sum_{j=i}^{r_d}\boldsymbol{\psi}_{ij}\, p_{ij}. \tag{5.28}$$

Note that from the quadratic Taylor expansion with dependent quadratic coefficients $p_i p_j$ as in (5.4) and (5.12), we have generated a reduced linear expansion in (5.28) with independent coefficients p_{ij}. Using these additional degrees of freedom, our reduction should be at least as accurate as the quadratic expression, since we have more degrees of freedom available and $p_{ij} = p_i p_j/2$ is a possible choice for these additional DOFs.

The computational effort for computing all $r_d(r_d+1)/2$ symmetric modal derivatives by Algorithm 4 mainly consists of computing the r_d linear eigenvectors $\boldsymbol{\phi}_j$, assembling r_d-times a tangent stiffness matrix in (5.7) and then solving the linear system (5.6) $r_d(r_d+1)/2$-times. If the problem size is not too large and one can solve (5.6) by LU-decomposition of $\mathbf{K}$, the computation becomes very efficient.

5.2.3 Application of reduction to harmonic balance

Here we describe the application of the modal projection method with eigenmodes and modal derivatives, as introduced in the preceding Section 5.2.1, to the harmonic balance method, see Section 4.3. This idea was already published by the author in [128] and is presented here with slight modifications.

The displacement vector $\mathbf{d}$ in the equation of motion of harmonic balance (4.29) is

Algorithm 4 Computation of a reduction basis with modal derivatives

1: Assemble: $\mathbf{M}$, $\mathbf{K}$
2: Solve linear EVP: $\omega_j^2 \mathbf{M}\,\boldsymbol{\phi}_j = \mathbf{K}\,\boldsymbol{\phi}_j,\ j = 1, \ldots, r_d$
3: **for** $i = 1, \ldots, r_d$ **do**
4: Assemble: $\mathbf{K}_T \leftarrow \mathbf{K}_T(\Delta p_i\,\boldsymbol{\phi}_i)$
5: Compute: $\frac{\partial \mathbf{K}_T}{\partial p_i} \leftarrow (\mathbf{K}_T - \mathbf{K})/\Delta p_i$
6: **for** $j = i, \ldots, r_d$ **do**
7: Compute MD: $\frac{\partial \boldsymbol{\phi}_j}{\partial p_i} \leftarrow$ Solve $\mathbf{K}\,\frac{\partial \boldsymbol{\phi}_j}{\partial p_i} = -\frac{\partial \mathbf{K}_T}{\partial p_i}\,\boldsymbol{\phi}_j$
8: **end for**
9: **end for**
10: Return basis: $\mathbf{Q} = (\boldsymbol{\phi}_1, \ldots, \boldsymbol{\phi}_{r_d}, \frac{\partial \boldsymbol{\phi}_1}{\partial p_1}, \ldots, \frac{\partial \boldsymbol{\phi}_1}{\partial p_{r_d}}, \ldots, \frac{\partial \boldsymbol{\phi}_{r_d}}{\partial p_{r_d}})$

projected using modal coordinates $\mathbf{p}$:

$$\mathbf{d}(t) = \mathbf{Q}\mathbf{p}(t), \tag{5.29}$$

where $\mathbf{Q}$ is the projection matrix with a selection of $r \ll N$ linear eigenmodes $\boldsymbol{\phi}_i$ and corresponding modal derivatives $\frac{\partial \boldsymbol{\phi}_j}{\partial d_i}$ as columns, see (5.28).

Now the equation of motion (4.29) is projected onto modal coordinates by left-multiplication with $\mathbf{Q}^T$:

$$\mathbf{Q}^T\mathbf{M}\mathbf{Q}\,\ddot{\mathbf{p}}(t) + \mathbf{Q}^T\mathbf{C}\mathbf{Q}\,\dot{\mathbf{p}}(t) + \mathbf{Q}^T\mathbf{f}(\mathbf{d}(t), \dot{\mathbf{d}}(t)) = \mathbf{Q}^T\mathbf{b}(t). \tag{5.30}$$

This equation may be rewritten using the notations

$$\tilde{\mathbf{M}} = \mathbf{Q}^T\mathbf{M}\mathbf{Q}, \qquad \tilde{\mathbf{C}} = \mathbf{Q}^T\mathbf{C}\mathbf{Q}, \qquad \tilde{\mathbf{f}} = \mathbf{Q}^T\mathbf{f}, \qquad \tilde{\mathbf{b}} = \mathbf{Q}^T\mathbf{b}, \tag{5.31}$$

as

$$\tilde{\mathbf{M}}\,\ddot{\mathbf{p}}(t) + \tilde{\mathbf{C}}\,\dot{\mathbf{p}}(t) + \tilde{\mathbf{f}}(\mathbf{d}(t), \dot{\mathbf{d}}(t)) = \tilde{\mathbf{b}}(t). \tag{5.32}$$

The spatial discretization of the nonlinear equation system has been reduced from a sparse $N \times N$ to a dense $r \times r$ one, but note that the nonlinear term $\tilde{\mathbf{f}}(\mathbf{d}(t), \dot{\mathbf{d}}(t))$ (and also the corresponding tangent $\tilde{\mathbf{K}}_T(\mathbf{d}(t), \dot{\mathbf{d}}(t)) = \mathbf{Q}^T\mathbf{K}_T(\mathbf{d}(t), \dot{\mathbf{d}}(t))\mathbf{Q}$) still depend on the physical displacement vector $\mathbf{d}$ (and velocities $\dot{\mathbf{d}}$) and have to be assembled in the usual way without any speed-up. Complexity reduction methods such as Discrete Empirical Interpolation [34] might be applied to further decrease the computational effort.

The further procedure of applying the harmonic balance method is equivalent to the steps described in Section 4.3: Fourier expansion of reduced coordinates $\mathbf{p}$ using amplitudes $\tilde{\mathbf{q}}$, substitution into (5.32) for a residual vector $\tilde{\mathbf{r}}$, Fourier transform of the residual and its Jacobian, and solution of the equation system for $\tilde{\mathbf{q}}$, which has now size $r \cdot (2m+1)$. Physical displacements can then be recovered within each sampling or Newton step using $\mathbf{d}(t) = \mathbf{Q}\mathbf{p}(t)$.

A schematic overview of the algorithm for nonlinear frequency analysis with modal derivative reduction is presented in Algorithm 5, where the reduction basis with modal derivatives is computed using Algorithm 4.

Algorithm 5 Nonlinear frequency analysis with modal derivative reduction

Input basis: $\mathbf{Q} = (\boldsymbol{\phi}_1, \ldots, \boldsymbol{\phi}_{r_d}, \boldsymbol{\psi}_{11}, \ldots, \boldsymbol{\psi}_{1r_d}, \ldots, \boldsymbol{\psi}_{r_d r_d})$
Initial guess: $\mathbf{q}^0 \leftarrow \mathbf{Q}\tilde{\mathbf{q}}^0$
Initialization: $s \leftarrow 0$
repeat
  for $j = 0, \ldots, 2m$ **do**
    Sampling time: $\tau_j = 2\pi j/(2m+1)$
    Current displacement: $\mathbf{d}(\tau_j) = \mathbf{Q}\left(\tilde{\mathbf{q}}_0^s/2 + \sum_{k=1}^{m} \cos(k\tau_j)\, \tilde{\mathbf{q}}_k^s + \sin(k\tau_j)\, \tilde{\mathbf{q}}_k^s\right)$
    Assembly: $\mathbf{f}(\tau_j) \leftarrow \mathbf{f}(\mathbf{d}(\tau_j), \dot{\mathbf{d}}(\tau_j))$, $\mathbf{b}(\tau_j)$
    $\mathbf{K}_T(\tau_j) \leftarrow \mathbf{K}_T(\mathbf{d}(\tau_j), \dot{\mathbf{d}}(\tau_j))$,
    $\mathbf{C}_T(\tau_j) \leftarrow \mathbf{C}_T(\mathbf{d}(\tau_j), \dot{\mathbf{d}}(\tau_j))$
    Evaluate residual: $\mathbf{r}(\tau_j) \leftarrow \mathbf{M}\,\ddot{\mathbf{d}}(\tau_j) + \mathbf{C}\,\dot{\mathbf{d}}(\tau_j) + \mathbf{f}(\tau_j) - \mathbf{b}(\tau_j)$
    Evaluate Jacobians: $\mathbf{J}_k(\tau_j) \leftarrow$ see (4.38), $k = 0, \ldots, 2m$
    Reduction: $\tilde{\mathbf{r}}(\tau_j) \leftarrow \mathbf{Q}^T\mathbf{r}(\tau_j)$
    $\tilde{\mathbf{J}}_k(\tau_j) \leftarrow \mathbf{Q}^T\mathbf{J}_k(\tau_j)\mathbf{Q}$, $k = 0, \ldots, 2m$
  end for
  DHT of reduced residual: $\hat{\tilde{\mathbf{r}}}^s \leftarrow \mathrm{DHT}(\tilde{\mathbf{r}}(\tau_0), \ldots, \tilde{\mathbf{r}}(\tau_{2m}))$
  DHT of reduced Jacobians: $\hat{\tilde{\mathbf{J}}}_k^s \leftarrow \mathrm{DHT}(\tilde{\mathbf{J}}_k(\tau_0), \ldots, \tilde{\mathbf{J}}_k(\tau_{2m}))$, $k = 0, \ldots, 2m$
  Compute reduced update: $\Delta\tilde{\mathbf{q}}^s \leftarrow$ Solve $\hat{\tilde{\mathbf{J}}}^s\, \Delta\tilde{\mathbf{q}}^s = -\hat{\tilde{\mathbf{r}}}^s$
  Evaluate error: $\tilde{e}_q \leftarrow \frac{\|\Delta\tilde{\mathbf{q}}^s\|}{\|\tilde{\mathbf{q}}^s\|}$, $\tilde{e}_r \leftarrow \frac{\|\hat{\tilde{\mathbf{r}}}^s\|}{\|\tilde{\mathbf{q}}^s\|}$
  Reduced update: $\tilde{\mathbf{q}}^{s+1} = \tilde{\mathbf{q}}^s + \Delta\tilde{\mathbf{q}}^s$
  $s \leftarrow s + 1$
until $\tilde{e}_q < \varepsilon_q \ \wedge\ \tilde{e}_r < \varepsilon_r$
Return value: $\mathbf{q} \leftarrow \boldsymbol{\Phi}\tilde{\mathbf{q}}^s$

5.3 Theoretical analysis of modal derivatives

In previous Section 5.2.1 we have seen that modal derivatives can be used to obtain a second-order approximation of the solution of a discretized nonlinear problem in matrix-vector formulation, where the right hand side is a superposition of linear eigenmodes.

In the following we want to transfer the concept of modal derivatives to continuous problems of nonlinear elliptic partial differential equations and establish a more theoretical analysis and understanding. In Section 5.3.1 we derive modal derivatives also for continuous PDE operators and show that we can also obtain a second-order approximation of the solution. To illustrate these analytical results, we compute modal derivatives of a one-dimensional model problem in Section 5.3.2. We also apply the calculus of modal derivatives to the nonlinear Euler-Bernoulli beam problem in Section 5.3.2, which helps us to understand numerical observations made earlier.

5.3.1 Modal derivatives of a continuous problem

In this Section we derive the definition and calculus of modal derivatives also for boundary value problems of nonlinear PDE operators. Then we can show that a quadratic Taylor series expansion of the analytical solution of the problem can be obtained using eigenfunctions and modal derivatives.

Assumption 5.1.

$$\mathcal{N}[\cdot] : H^1(\Omega) \to L^2(\Omega)$$

is a nonlinear, compact, Fréchet-differentiable, 2nd order elliptic partial differential operator on the open domain $\Omega \subset \mathbb{R}^d$ *such that its Fréchet derivatives*

$$\mathcal{L}(u)[\cdot] := \mathcal{N}'(u) : H^1(\Omega) \to L^2(\Omega)$$

are linear, compact, Fréchet-differentiable, 2nd order elliptic partial differential operators for any $u \in H^1(\Omega)$, $\mathcal{L} := \mathcal{L}(0)$, *and*

$$\mathcal{H}(u)[\cdot,\cdot] := \mathcal{L}'(u) = \mathcal{N}''(u,u) : H^1(\Omega) \times H^1(\Omega) \to L^2(\Omega),$$

such that $\mathcal{H} := \mathcal{H}(0)$ *exists.*

Under Assumption 5.1 it follows that the linear eigenvalue problem

$$\begin{aligned} \mathcal{L}[u] &= \lambda u \quad && \text{in } \Omega, \\ u &= 0 && \text{on } \partial\Omega, \\ \|u\| &= 1 \end{aligned} \tag{5.33}$$

has nontrivial solutions $(\lambda_k, u_k)_{k\in\mathbb{N}}$ such that $\lambda_k \in \mathbb{R}$, $0 < \lambda_1 \leq \lambda_2 \leq \ldots \to \infty$ and $\{u_k\}_{k\in\mathbb{N}}$ form an orthonormal basis of $L^2(\Omega)$ and an orthogonal basis of $H_0^1(\Omega)$ [85]. Furthermore, it follows that for $p_k \in \mathbb{R}$ and $k \in \mathbb{N}$, the solution of the elliptic boundary value problem

$$\begin{aligned} \mathcal{L}[u] &= \sum_{k\in\mathbb{N}} \lambda_k u_k p_k \quad && \text{in } \Omega, \\ u &= 0 && \text{on } \partial\Omega, \end{aligned} \tag{5.34}$$

is $u = u(\mathbf{p}) = \sum_{k\in\mathbb{N}} u_k p_k$, where $\mathbf{p} = (p_1, p_2, \ldots)$ serves as a parameter resp. load factor vector.

Now we are interested in the solution of the following nonlinear problem:

Definition 5.1 (Nonlinear boundary value problem on $H^1(\Omega)$)**.** *Find* $u \in H^1(\Omega)$ *such that*

$$\begin{aligned} \mathcal{N}[u] &= f \quad && \textit{in } \Omega, \\ u &= 0 && \textit{on } \partial\Omega, \end{aligned} \tag{5.35}$$

where $f = \sum_{k\in\mathbb{N}} \lambda_k u_k p_k$ *and* $|p_k| < 1 \; \forall k \in \mathbb{N}$.

We start by developing the exact solution $u = u(\mathbf{p})$ as a Taylor series around $\mathbf{p} = \mathbf{0}$ up to second order:

$$u(\mathbf{p}) = 0 + \sum_{k\in\mathbb{N}} \frac{\partial u}{\partial p_k}\bigg|_0 p_k + \frac{1}{2} \sum_{j,k\in\mathbb{N}} \frac{\partial^2 u}{\partial p_k \partial p_j}\bigg|_0 p_k p_j + \mathcal{O}(\|\mathbf{p}\|^3). \tag{5.36}$$

Theorem 5.2. *The partial derivatives of u w.r.t. the components of the parameter vector $\boldsymbol{p}$ in the Taylor series expansion* (5.36) *are:*

$$\left.\frac{\partial u}{\partial p_k}\right|_0 = u_k, \qquad \left.\frac{\partial^2 u}{\partial p_k \partial p_j}\right|_0 = -\mathcal{L}^{-1}\left[\mathcal{H}\left[u_k, u_j\right]\right], \tag{5.37}$$

where $u_{kj} := \left.\frac{\partial^2 u}{\partial p_k \partial p_j}\right|_0$ *are called* modal derivatives *of* u.

Proof. For computing the partial derivatives of u w.r.t. the parameters we differentiate (5.35) w.r.t. the components of $\mathbf{p}$:

$$\frac{\partial \mathcal{N}}{\partial p_k} = \frac{\partial \mathcal{N}}{\partial u}\left[\frac{\partial u}{\partial p_k}\right] = \mathcal{L}(u)\left[\frac{\partial u}{\partial p_k}\right] \stackrel{!}{=} \lambda_k u_k. \tag{5.38}$$

Setting $\mathbf{p} = \mathbf{0}$, i.e $u = 0$, we obtain the linear problem

$$\begin{aligned} \mathcal{L}\left[\left.\frac{\partial u}{\partial p_k}\right|_0\right] &= \lambda_k u_k \quad && \text{in } \Omega, \\ u &= 0 && \text{on } \partial\Omega, \end{aligned} \tag{5.39}$$

and using (5.34) it follows that

$$\left.\frac{\partial u}{\partial p_k}\right|_0 = u_k. \tag{5.40}$$

We continue by differentiating (5.38) once again:

$$\frac{\partial^2 \mathcal{N}}{\partial p_k \partial p_j} = \frac{\partial^2 \mathcal{N}}{\partial u^2}\left[\frac{\partial u}{\partial p_k}, \frac{\partial u}{\partial p_j}\right] + \frac{\partial \mathcal{N}}{\partial u}\left[\frac{\partial^2 u}{\partial p_k \partial p_j}\right] = \mathcal{H}(u)\left[\frac{\partial u}{\partial p_k}, \frac{\partial u}{\partial p_j}\right] + \mathcal{L}(u)\left[\frac{\partial^2 u}{\partial p_k \partial p_j}\right] \stackrel{!}{=} 0. \tag{5.41}$$

Evaluation at $\mathbf{p} = \mathbf{0}$ yields

$$\mathcal{H}(0)\left[\left.\frac{\partial u}{\partial p_k}\right|_0, \left.\frac{\partial u}{\partial p_j}\right|_0\right] + \mathcal{L}(0)\left[\left.\frac{\partial^2 u}{\partial p_k \partial p_j}\right|_0\right] = 0, \tag{5.42}$$

and it follows that the *modal derivatives* $u_{kj} := \left.\frac{\partial^2 u}{\partial p_k \partial p_j}\right|_0$ can be obtained from the following linear problem:

$$\begin{aligned} \mathcal{L}\left[u_{kj}\right] &= -\mathcal{H}\left[u_k, u_j\right] \quad && \text{in } \Omega, \\ u &= 0 && \text{on } \partial\Omega. \end{aligned} \tag{5.43}$$

□

Theorem 5.3. *The quadratic Taylor series expansion*

$$u(\boldsymbol{p}) = \sum_{k\in\mathbb{N}} u_k p_k + \frac{1}{2}\sum_{j,k\in\mathbb{N}} u_{kj} p_k p_j, \tag{5.44}$$

with partial derivatives from Theorem 5.2, is a second-order approximation of the solution of the nonlinear boundary value problem of Definition 5.1 around $u = 0$ in terms of the parameter vector $\boldsymbol{p}$, i.e.

$$\mathcal{N}[u(\boldsymbol{p})] - \mathcal{N}[u] = \mathcal{O}(\|\boldsymbol{p}\|^3). \tag{5.45}$$

Proof. Using Taylor's theorem for Banach spaces [85], we can write the Taylor series expansion of $\mathcal{N}[u]$ around $u = 0$ as

$$\mathcal{N}[u] = 0 + \mathcal{L}(0)[u] + \frac{1}{2}\mathcal{H}(0)[u,u] + \mathcal{O}(\|u\|^3). \tag{5.46}$$

Substituting the second-order Taylor expansion from (5.44) using Theorem 5.2 we obtain:

$$\begin{aligned}\mathcal{N}[u(\mathbf{p})] &= \mathcal{L}(0)\left[u(\mathbf{p})\right] + \frac{1}{2}\mathcal{H}(0)\left[u(\mathbf{p}), u(\mathbf{p})\right] + \mathcal{O}(\|u(\mathbf{p})\|^3) \\ &= \mathcal{L}\left[\sum_{k\in\mathbb{N}} u_k p_k + \frac{1}{2}\sum_{j,k\in\mathbb{N}} u_{kj} p_k p_j\right] \\ &\quad + \frac{1}{2}\mathcal{H}\left[\sum_{k\in\mathbb{N}} u_k p_k + \frac{1}{2}\sum_{j,k\in\mathbb{N}} u_{kj} p_k p_j, \sum_{k\in\mathbb{N}} u_k p_k + \frac{1}{2}\sum_{j,k\in\mathbb{N}} u_{kj} p_k p_j\right] + \mathcal{O}(\|\mathbf{p}\|^3).\end{aligned} \tag{5.47}$$

Making use of the linearity of $\mathcal{L}$ and bilinearity of $\mathcal{H}$ in the arguments [85], we continue:

$$\begin{aligned}\mathcal{N}[u(\mathbf{p})] &= \sum_{k\in\mathbb{N}} \mathcal{L}[u_k] p_k + \frac{1}{2}\sum_{j,k\in\mathbb{N}} \mathcal{L}[u_{kj}] p_k p_j \\ &\quad + \frac{1}{2}\left(\sum_{j,k\in\mathbb{N}} \mathcal{H}[u_k, u_j] p_k p_j + \mathcal{O}(\|\mathbf{p}\|^3)\right) + \mathcal{O}(\|\mathbf{p}\|^3) \\ &= \sum_{k\in\mathbb{N}} \lambda_k u_k p_k + \frac{1}{2}\left(\sum_{j,k\in\mathbb{N}} \Big(\mathcal{L}[u_{kj}] + \mathcal{H}[u_k, u_j]\Big) p_k p_j\right) + \mathcal{O}(\|\mathbf{p}\|^3).\end{aligned} \tag{5.48}$$

Using the definition of modal derivatives (5.43), we arrive at:

$$\mathcal{N}[u(\mathbf{p})] = \sum_{k\in\mathbb{N}} \lambda_k u_k p_k + \mathcal{O}(\|\mathbf{p}\|^3). \tag{5.49}$$

□

Remark 5.1. *In the infinite-dimensional case any right-hand side f of Problem (5.35) can be written as $f = \sum_{k\in\mathbb{N}} \lambda_k u_k p_k$, since u_k are an orthonormal basis of $L^2(\Omega)$ and thus it is $p_k = (f, u_k)/\lambda_k \ \forall k \in \mathbb{N}$, where $(\cdot,\cdot)$ is the L^2-scalar product. If $f = \lambda_k u_k p_k$ for a certain $k \in \mathbb{N}$, then it follows simply that $u(\boldsymbol{p}) = u_k\, p_k + \frac{1}{2} u_{kk}\, p_k^2$.*

Remark 5.2. *These findings motivate the use of subsets of the eigenfunctions $\{u_k\}_{k\in\mathbb{N}}$ and modal derivatives $\{u_{kj}\}_{k,j\in\mathbb{N}}$ as basis functions of "reduced" resp. finite-dimensional subspaces of $H^1(\Omega)$ for the approximation of the exact solution of a nonlinear BVP such as (5.35).*

Only when the L^2-projection of the right-hand side f onto a certain linear eigenfunction u_k, i.e. $p_k = (f, u_k)/\lambda_k$, is significant, i.e. $0 < \varepsilon < |p_k| < 1$, the mode k needs to be considered for the approximation space. Thus we obtain a set $I \subset \mathbb{N}$ of modes $\{u_k\}_{k\in I}$ to be included in the approximation space and also their modal derivatives $\{u_{kj}\}_{j,k\in I}$.

5.3.2 Nonlinear model problem

Now we want to demonstrate the above presented concepts for a small model problem. The 1D problem is chosen as a nonlinear extension of Poisson's equation with a quadratic nonlinearity, which resembles the large deformation elasticity problem in 2D or 3D.

Definition 5.2 (1D nonlinear model problem)**.** *The model problem is defined by*

$$\Omega = (0, \pi)$$

and

$$\mathcal{N}[u] = -(1+u')u'' = -\left(u' + \frac{1}{2}u'^2\right)',$$

where $(\cdot)' = \frac{d}{dx}(\cdot)$.

From the definition of $\mathcal{N}$ we can compute the Fréchet derivatives:

$$\begin{aligned}
\frac{d}{du}\mathcal{N}(u)[h_1] &= \lim_{t\to 0}\frac{1}{t}\Big(\mathcal{N}[u+th_1] - \mathcal{N}[u]\Big) = -h_1'u'' - h_1''(1+u'),\\
\frac{d^2}{du^2}\mathcal{N}(u)[h_1,h_2] &= \lim_{t\to 0}\frac{1}{t}\Big(\mathcal{L}(u+th_2)[h_1] - \mathcal{L}(u)[h_1]\Big) = -h_1'h_2'' - h_1''h_2',\\
\frac{d^3}{du^3}\mathcal{N}(u)[h_1,h_2,h_3] &= \lim_{t\to 0}\frac{1}{t}\Big(\mathcal{H}(u+th_3)[h_1,h_2] - \mathcal{H}(u)[h_1,h_2]\Big) = 0,
\end{aligned} \tag{5.50}$$

and evaluate them at $u = 0$:

$$\begin{aligned}
\mathcal{L}[u] &= \frac{d}{du}\mathcal{N}(0)[u] = -u'',\\
\mathcal{H}[u,v] &= \frac{d^2}{du^2}\mathcal{N}(0)[u,v] = -(u'v'' + u''v'),\\
&\frac{d^3}{du^3}\mathcal{N}(0)[u,v,w] = 0.
\end{aligned} \tag{5.51}$$

Thus the second-order Taylor expansion of $\mathcal{N}$ around $u = 0$ gives the exact operator $\mathcal{N}$:

$$\mathcal{N}[u] = -(1+u')u'' = -u'' - u'u'' = \mathcal{L}[u] + \frac{1}{2}\mathcal{H}[u,u]. \tag{5.52}$$

The eigenfunctions and modal derivatives can be computed from:

$$\begin{aligned}
k \in \mathbb{N}: \quad & \mathcal{L}[u_k] = \lambda_k u_k && \Leftrightarrow && -u_k'' = \lambda_k u_k,\\
k,j \in \mathbb{N}: \quad & \mathcal{L}[u_{kj}] = -\mathcal{H}[u_k,u_j] && \Leftrightarrow && -u_{kj}'' = u_k'u_j'' + u_k''u_j'.
\end{aligned} \tag{5.53}$$

In order to continue with the computation of u_k and u_{kj} we need to specify the boundary conditions.

Homogeneous boundary condition

As in Section 5.3.1, we now assume homogeneous boundary conditions for u, i.e.

$$u(0) = u(\pi) = 0. \tag{5.54}$$

Obviously then the eigenvalues and eigenfunctions are for $k \in \mathbb{N}$:

$$\lambda_k = k^2, \quad u_k(x) = \sqrt{2/\pi}\, \sin(kx). \tag{5.55}$$

The modal derivatives can also be computed for $k, j \in \mathbb{N}$:

$$\begin{aligned} u_{kj} &= -\int_0^\pi \int_0^\pi u_k' u_j'' + u_k'' u_j' \, dx \, dx = -\int_0^\pi u_k' u_j' + C \, dx = \\ &= -\frac{2}{\pi} \int_0^\pi kj \cos(kx)\cos(jx) + C \, dx = -\frac{kj}{\pi} \left(\frac{\sin((k-j)x)}{k-j} + \frac{\sin((k+j)x)}{k+j} \right), \end{aligned} \tag{5.56}$$

where we have made use of the boundary conditions and for $k = j$ we define $0/0 := 0$. Here the modal derivatives u_{kj} are linear combinations of the eigenfunctions u_k! This is a result of the very special structure of the eigenfunctions in this case.

Now let us assume $f = p\sqrt{\frac{2}{\pi}} \sin x = p\lambda_1 u_1$. We choose $V_h^1 = \{u_1\}$ and thus have $u_h^1 = pu_1$. Then it is

$$\begin{aligned} \mathcal{N}[u_h^1] &= \left(1 + \sqrt{\frac{2}{\pi}} p \cos x \right) \sqrt{\frac{2}{\pi}} p \sin x = \sqrt{\frac{2}{\pi}} p \sin x + \frac{2}{\pi} p^2 \sin x \cos x \\ &= \sqrt{\frac{2}{\pi}} p \sin x + \frac{p^2}{\pi} \sin 2x. \end{aligned} \tag{5.57}$$

Thus the error of the approximation is

$$e^1 = \mathcal{N}[u_h^1] - f = \frac{p^2}{\pi} \sin 2x = \mathcal{O}(p^2). \tag{5.58}$$

Now we add the modal derivative to the approximation space, i.e. $V_h^2 = \{u_1, u_{11}\}$, where $u_{11} = -\frac{1}{2\pi} \sin 2x$, and obtain $u_h^2 = pu_1 + \frac{p^2}{2} u_{11}$:

$$\begin{aligned} \mathcal{N}[u_h^2] &= \left(1 + \sqrt{\frac{2}{\pi}} p \cos x - \frac{p^2}{2\pi} \cos 2x \right) \left(\sqrt{\frac{2}{\pi}} p \sin x - \frac{p^2}{\pi} \sin 2x \right) \\ &= \sqrt{\frac{2}{\pi}} p \sin x + \frac{2p^2}{\pi} \sin x \cos x - \frac{p^2}{\pi} \sin 2x + \mathcal{O}(p^3) = \sqrt{\frac{2}{\pi}} p \sin x + \mathcal{O}(p^3). \end{aligned} \tag{5.59}$$

Then the approximation error of the residual is, as expected, of order 3 in p:

$$e^2 = \mathcal{N}[u_h^2] - f = \mathcal{O}(p^3). \tag{5.60}$$

Inhomogeneous boundary condition

Now let us assume inhomogeneous boundary conditions for u,

$$u(0) = 0, \quad u(\pi) = p > 0. \tag{5.61}$$

Then the eigenvalues and eigenfunctions are for $k \in \mathbb{N}$:

$$\lambda_k = (k-0.5)^2, \quad u_k(x) = \sqrt{2/\pi}\,\sin((k-0.5)x). \tag{5.62}$$

Again we compute the modal derivatives from (5.53) for $k, j \in \mathbb{N}$:

$$\begin{aligned} u_{kj} &= -\int_0^\pi \int_0^\pi u_k' u_j'' + u_k'' u_j'\,dx\,dx = -\int_0^\pi u_k' u_j' + C\,dx \\ &= -\frac{2}{\pi}\int_0^\pi (k-0.5)(j-0.5)\cos((k-0.5)x)\cos((j-0.5)x) + C\,dx \\ &= -\frac{1}{\pi}(k-0.5)(j-0.5)\left(\frac{\sin((k-j)x)}{k-j} + \frac{\sin((k+j-1)x)}{k+j-1}\right) + C_0 + C_1 x, \end{aligned} \tag{5.63}$$

For the modal derivatives it should hold $u_{kj}(0) = u_{kj}(\pi) = 0$ and thus C_0 and C_1 are 0. Here the modal derivatives are no more a linear combination of the eigenfunctions! To get an impression of the modal derivatives, Figure 5.1 shows the first 4 eigenfunctions $u_1, \ldots, u_4$ and corresponding first 10 modal derivatives $u_{11}, \ldots, u_{44}$.

Again we can show that the error of an approximate solution $u_h^2 = pu_1 + \frac{p^2}{2}u_{11}$ is of order 3 in p for $f = \frac{p}{4}\sqrt{\frac{2}{\pi}}\sin\frac{x}{2} = p\lambda_1 u_1$:

$$\begin{aligned} \mathcal{N}[u_h^2] &= \left(1 + \frac{p}{2}\sqrt{\frac{2}{\pi}}\cos\frac{x}{2} - \frac{p^2}{8\pi}\cos x\right)\left(\frac{p}{4}\sqrt{\frac{2}{\pi}}\sin\frac{x}{2} - \frac{p^2}{8\pi}\sin x\right) \\ &= \frac{p}{4}\sqrt{\frac{2}{\pi}}\sin\frac{x}{2} - \frac{p^2}{8\pi}\sin x + \frac{2p^2}{8\pi}\sin\frac{x}{2}\cos\frac{x}{2} + \mathcal{O}(p^3) = \frac{p}{4}\sqrt{\frac{2}{\pi}}\sin\frac{x}{2} + \mathcal{O}(p^3). \end{aligned} \tag{5.64}$$

Thus it is

$$e^2 = \mathcal{N}[u_h^2] - f = \mathcal{O}(p^3). \tag{5.65}$$

5.3.3 Nonlinear Euler-Bernoulli beam

In the diploma thesis [126] we have already briefly numerically investigated the use of modal truncation (without modal derivatives) for nonlinear vibration analysis of Euler-Bernoulli beams, see Section 3.4.1. It turned out that a basis consisting of linear eigenmodes was good enough to approximate the nonlinear frequency response with a high accuracy.

As in the model problem above, this behavior can now be explained analytically using the concept of modal derivatives. For the nonlinear Euler-Bernoulli beam with pinned (simple) support, modal derivatives are also a linear combination of higher linear eigenmodes, which will be shown in the following. Thus it is sufficient to use a modal reduction with enough linear eigenmodes.

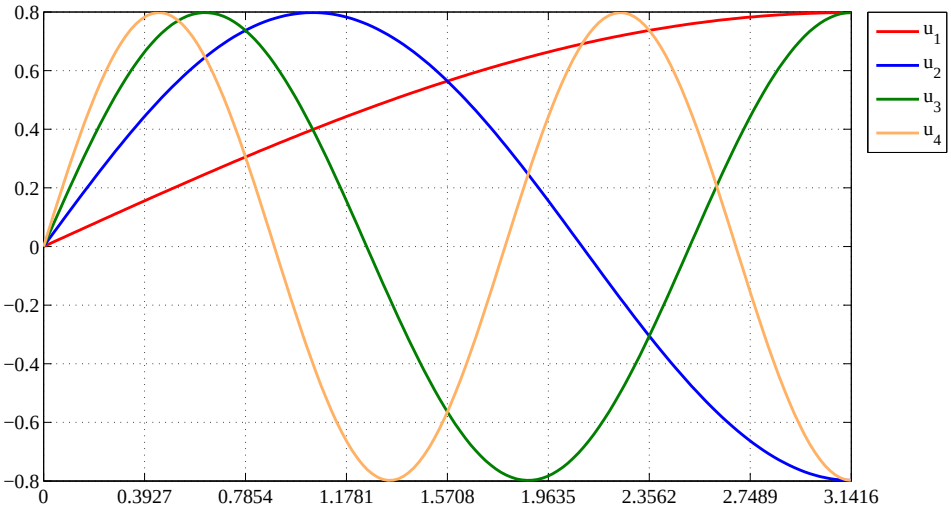

(a) First 4 eigenfunctions $u_1, \ldots, u_4$

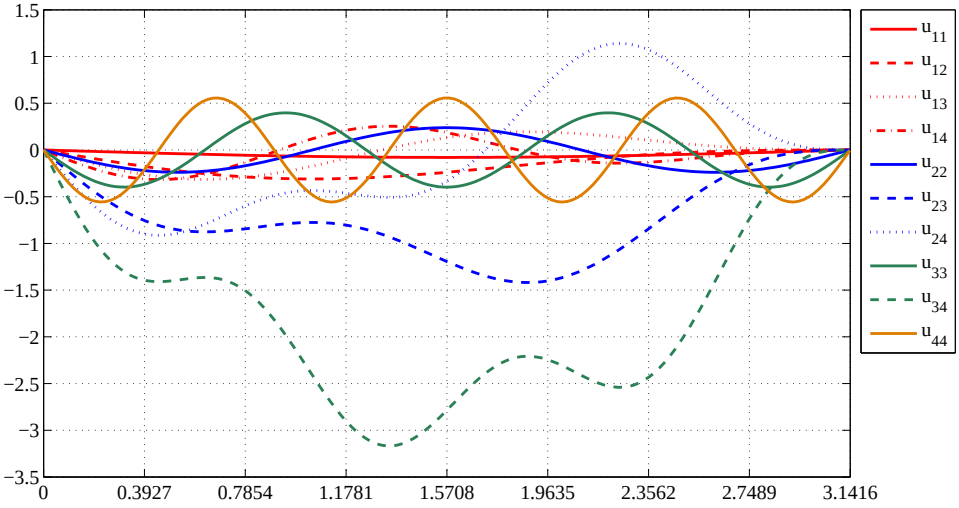

(b) First 10 modal derivatives $u_{11}, \ldots, u_{44}$

Figure 5.1: Eigenfunctions and modal derivatives of the nonlinear model problem Def. 5.2 with inhomogeneous boundary conditions

Definition 5.3. *Nonlinear Euler-Bernoulli beam model (with constants $E, A, I = 1$ and $L = \pi$):*

$$\begin{aligned} -\left(u' + \frac{1}{2}w'^2\right)' &= f \quad \text{for } x \in (0,\pi), \\ -\left[\left(u' + \frac{1}{2}w'^2\right)w'\right]' + w^{IV} &= g \quad \text{for } x \in (0,\pi), \\ u = w = w'' &= 0 \quad \text{for } x \in \{0,\pi\}. \end{aligned} \tag{5.66}$$

Then the corresponding linearized version of (5.66) is:

$$\begin{aligned} -u'' &= f \quad \text{for } x \in (0,\pi), \\ w^{IV} &= q \quad \text{for } x \in (0,\pi), \\ u = w = w'' &= 0 \quad \text{for } x \in \{0,\pi\}. \end{aligned} \tag{5.67}$$

These are the linear string and beam equations, which are decoupled, i.e. there is no more interaction of the equations involving u and w. Then the solutions of the corresponding eigenproblems are:

$$\begin{aligned} \omega_j^u &= j, \qquad \phi_j^u = \sqrt{2/\pi}\sin(jx), \qquad j = 1, 2, \dots , \\ \omega_k^w &= k^2, \qquad \phi_k^w = \sqrt{2/\pi}\sin(kx), \qquad k = 1, 2, \dots . \end{aligned} \tag{5.68}$$

Theorem 5.4. *The modal derivatives of the nonlinear Euler-Bernoulli beam problem from Def. 5.3 are linear combinations of sine-functions, i.e. of the eigenfunctions from* (5.68)*.*

Proof. The modal derivatives are computed explicitly, see Section A.2 in the Appendix. □

In Theorem 5.4 we have shown that the modal derivatives of the Euler-Bernoulli beam are linear combinations of higher linear eigenfunctions. This means that a second-order approximation of the problem is already possible using a sufficient number of eigenfunctions and explains why a reduction method with eigenmodes delivers very good results for this special problem.

5.4 Computational applications

With the computational applications presented in this Section, we want to show that the projection method with eigenmodes and modal derivatives is a powerful means of model order reduction in nonlinear static and vibration analysis. First, we carry out a detailed convergence study for the accuracy of reduction with eigenmodes and modal derivatives in static nonlinear elasticity (Section 5.4.1). Then we examine the accuracy of reduction in nonlinear frequency response analysis, using the application of the cylinder (Section 5.4.2). With the TERRIFIC Demonstrator in Section 5.4.3, we show that also larger-scale applications of nonlinear vibration analysis are now possible using the proposed MD reduction method. These results were already published in [128] and presented here with minor adaptions.

5.4.1 Convergence study of reduction in 3D nonlinear elastostatics

Before applying the modal reduction technique from Section 5.2 to nonlinear vibration analysis, we want to study the accuracy of reduction with eigenmodes and modal derivatives for nonlinear large deformation hyperelasticity in a static 3-dimensional case, i.e. projecting (3.53)

$$\mathbf{Q}^T\mathbf{f}(\mathbf{d}) = \mathbf{Q}^T\mathbf{b}, \quad \mathbf{d} = \mathbf{Q}\mathbf{p}, \quad \mathbf{Q} \in \mathbb{R}^{n\times r}, \tag{5.69}$$

and solving it using a Newton's method as in Algorithm 1.

We use a 3D geometry with no symmetries, which is parametrized as a linear B-Spline volume with 8 control points $\mathbf{v}_{ijk},\ i, j, k = 0, 1$ in lexicographical order:

$$\begin{pmatrix}0.0\\0.0\\0.0\end{pmatrix}, \begin{pmatrix}0.2\\0.0\\0.0\end{pmatrix}, \begin{pmatrix}0.0\\0.2\\0.0\end{pmatrix}, \begin{pmatrix}0.2\\0.2\\0.0\end{pmatrix}, \begin{pmatrix}0.4\\0.2\\0.3\end{pmatrix}, \begin{pmatrix}0.4\\0.2\\0.2\end{pmatrix}, \begin{pmatrix}0.4\\0.3\\0.3\end{pmatrix}, \begin{pmatrix}0.4\\0.3\\0.2\end{pmatrix} \text{ [m]}. \tag{5.70}$$

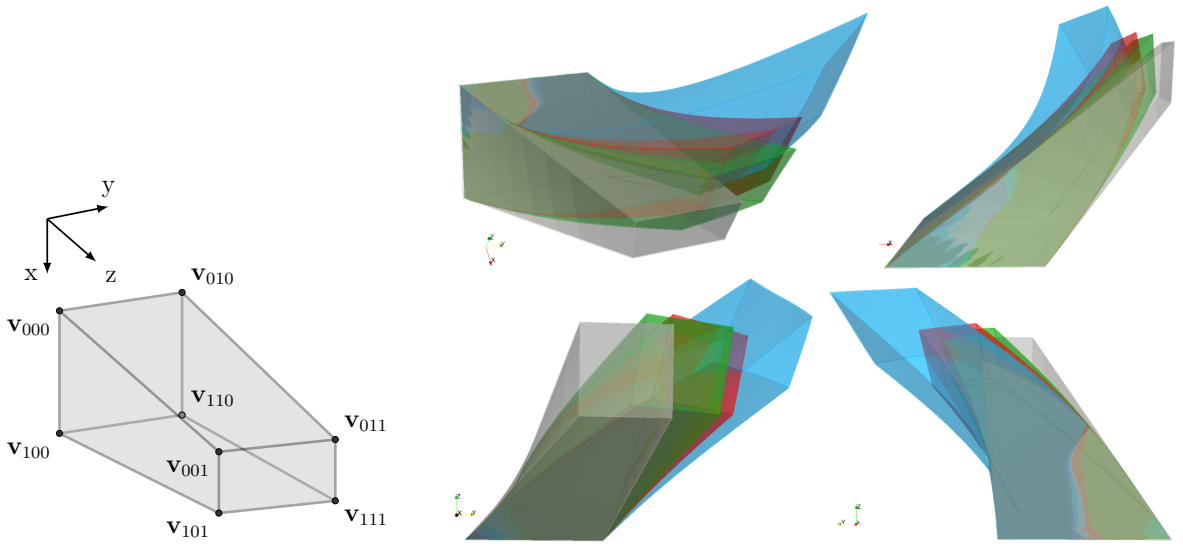

(a) Geometry as B-Spline volume with control points $\{\mathbf{v}_{ijk}\}_{i,j,k=0,1}$

(b) Static displacement: undeformed geometry (gray), linear displacement (blue), nonlinear displacement (red) and nonlinear displacement with modal reduction $r = 50$ (green). Modal derivative reduction with $r_d = 10$, $r = 65$ would be almost indistinguishable from the red plot

Figure 5.2: Geometry of 3D object in (a) and static displacement without and with reduction methods in (b)

The geometry of the object together with results of subsequent computations is visualized in Figure 5.2. Large deformations kinematics and linear St. Venant-Kirchhoff material law with material parameters

$$E = 71.72 \text{ GPa}, \quad \nu = 0.3, \quad \rho = 2800 \text{ kg/m}^3 \tag{5.71}$$

are employed. The bottom or $\{\xi_3 = 0\}$ boundary face of the object is fixed by Dirichlet boundary conditions and then eigenvalues and eigenvectors are computed for setting up the modal matrix $\mathbf{Q}$ with first r eigenmodes as columns. For reduction with modal derivatives we compute the modal derivative basis $\mathbf{Q}$ with r_d eigenmodes and corresponding modal derivatives using Algorithm 4. For static computations a Neumann boundary condition is applied to the top or $\{\xi_3 = 1\}$ face with force contributions in all 3 dimensions, $\mathbf{t} = (1.0,\ 3.0,\ 2.0)^T$ GPa. It causes a large deformation up to 100% of the object's dimensions.

For a quite coarse isogeometric discretization with $p = (2, 2, 2)$, $\ell = (2, 2, 4)$, $n = (4, 4, 6)$, $N = 288$, we compare the accuracy of modal reduction (MR) and modal reduction with derivatives (MD) with the full, unreduced nonlinear computation. In Figure 5.3 we compare the relative errors in L^2- and H^1-norms of the full and reduced solutions, e.g. $\|u^{\text{full}} - u^{\text{MD}}\|_{L^2} / \|u^{\text{full}}\|_{L^2}$, for the linear case with MR and the nonlinear case with MR and MD. While no significant improvement of accuracy with increasing basis length (number of modes) is noticeable for MR in the nonlinear case, MD provides a similar convergence behavior as MR in the linear case. Note that for $r = 240$ we are already considering the full set of displacement modes and for $r = N$ the transformation is bijective and thus must reproduce the results of the full system.

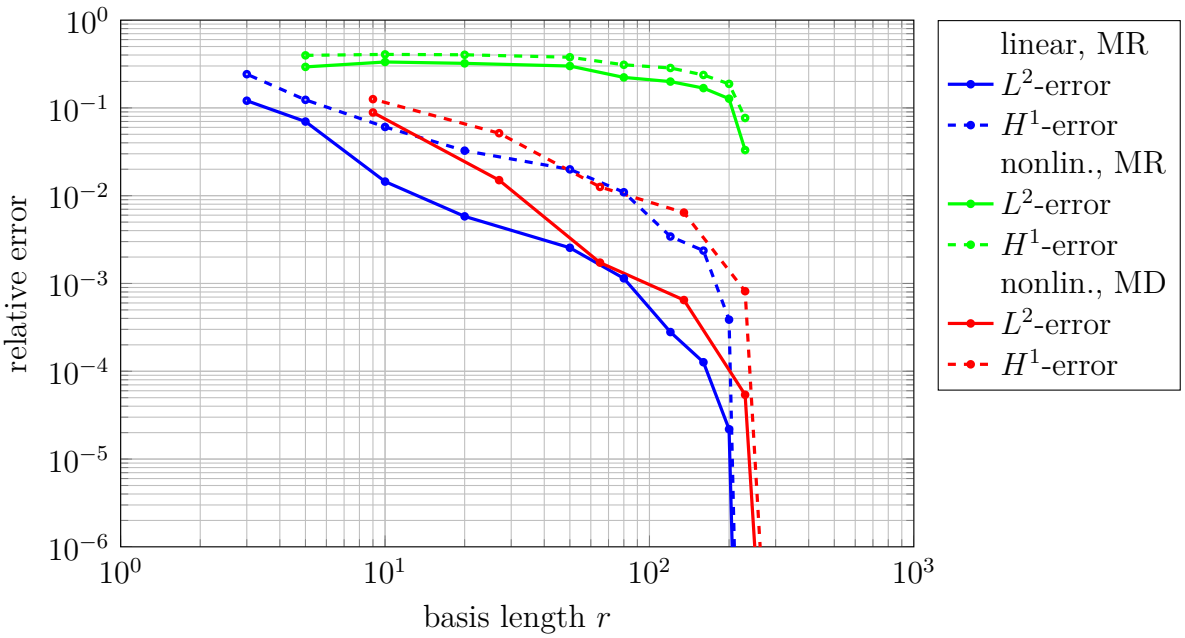

Figure 5.3: Convergence of reduction methods w.r.t. basis length r in relative L^2- and H^1-norms. Modal derivatives (MD) in nonlinear analysis (red) are as good as modal reduction (MR) in linear analysis (blue), while MR fails in nonlinear analysis (green)

Furthermore, we have also investigated the behavior of modal reduction and modal derivatives for different load factors. Figure 5.4 shows the displacement at the evaluation point for load factor 1 to 1000 (100 corresponds to the load level of previous results). In Figure 5.5 the relative errors of displacements in L^2- and H^1-norm are shown over increasing load factor. While errors for MD are small and roughly stay constant up to very large load factors and thus displacements, relative errors for MR grow fast and to a very high, completely unacceptable level.

The increasing error for MD for high load factors can be explained with the validity of the Taylor series expansions of $\mathbf{d}(\mathbf{p})$ and $\mathbf{f}(\mathbf{d})$ used in the definition of modal derivatives, since they only converge when the parameter vector $\mathbf{p}$ is small, i.e. $\|\mathbf{p}\|_\infty < 1$. Computing the parameter vector from the projection of the right hand side vector as $\mathbf{p} = \mathbf{\Lambda}^{-1}\mathbf{\Phi}^T\mathbf{b}$, compare (5.10), we notice that $\|\mathbf{p}\|_\infty > 1$ for a load factor over 300.

With this numerical study we have examined the approximation properties of our projection method for large deformations in a static setting. We can conclude that modal reduction is unsuitable for reduction of large deformation problems, while a reduction basis with eigenmodes and modal derivatives provides a high accuracy in the nonlinear static problem setting and opens a perspective for the use in nonlinear vibration analysis. In [128] we have furthermore shown that the picture stays the same when a constitutive nonlinearity is included using Neo-Hookean material.

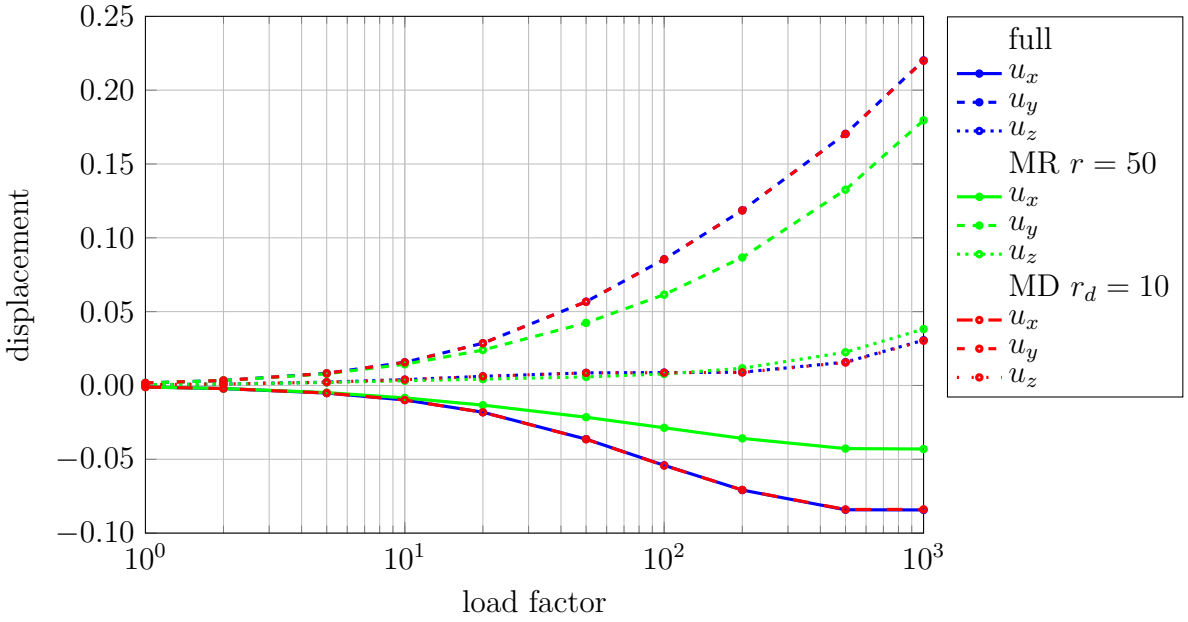

Figure 5.4: Displacement at evaluation point for full computation (full, blue), modal reduction with 50 modes (MR $r = 50$, green) and modal derivatives for 10 modes (MD $r_d = 10$, $r = 65$, red) for increasing load factor. Curves for full system and MD-reduction are optically indistinguishable

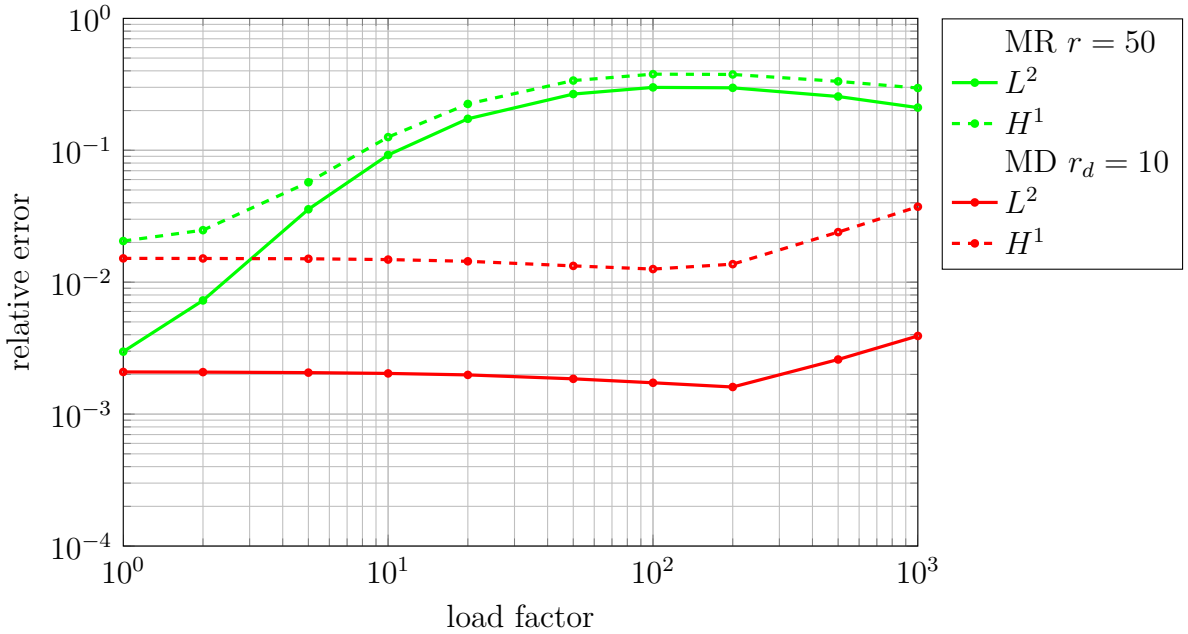

Figure 5.5: Relative error of displacements in L^2- and H^1-norm of MR ($r = 50$, green) and MD ($r_d = 10$, $r = 65$, red) w.r.t. full computation for increasing load factor. Accuracy of MD is much better than MR and up to a certain level independent from load factor

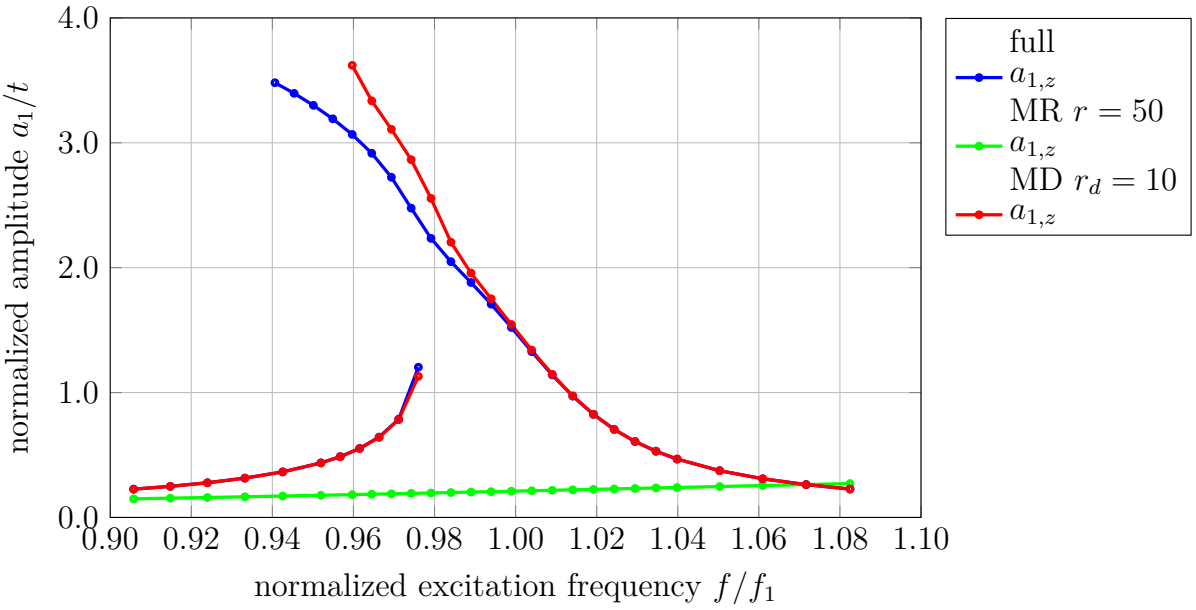

Figure 5.6: Frequency response curves of vibrating cylinder: normalized z-amplitudes of first harmonic a_1/t are plotted around $f/f_1 \approx 1.0$. While full harmonic balance (full, blue) and modal derivatives (MD, red) are almost identical, modal reduction (MR, green) completely fails to capture the resonance

5.4.2 Large amplitude vibration of a thick cylinder

In Section 4.4.2 we have already investigated a large amplitude forced vibration of a thick cylinder using the harmonic balance method. Now we want to use this application to validate the reduction approach with modal derivatives in nonlinear frequency analysis.

Geometry and parameters are the same as shown in 4.5, but for the comparison of reduction methods with the "exact" or "full" HBM solutions, we have changed the refinement of isogeometric parameterization to $p = (2, 2, 2)$, $\ell = (4, 4, 1)$, $n = (6, 6, 3)$, $N = 324$ and the evaluation point to the top right corner of the front surface E_2. The number of harmonics is $m = 3$ and thus the total number of DOFs of HBM is $N \cdot (2m + 1) = 2,268$.

We investigate the frequency response of the cylinder at resonance in the neighborhood of the first eigenfrequency, i.e. $f/f_1 \approx 1.0$. We compare full harmonic balance (full) with conventional modal reduction (MR) with $r = 50$ eigenmodes and with modal derivative reduction (MD) with $r_d = 10$ eigenmodes and corresponding modal derivatives, i.e. total basis length $r = 65$.

In Figure 5.6 we have plotted the z-amplitudes of the first harmonic a_1 at the evaluation point, normalized by the cylinder thickness t. For modal reduction we have a complete failure with no meaningful reproduction of the results of full HBM, as the resonance is not captured. In contrast to that, the extended basis with modal derivatives reproduces the amplitudes of the full harmonic balance with high accuracy up to a level where strong resonance with very large amplitudes occurs. Then for $a_1/t > 2$ deviations become visible and the reduced MD solution over-estimates the exact amplitudes.

Figure 5.7 shows the other z-amplitudes a_0, a_2, a_3, which have smaller magnitudes than a_1. Here the picture is very similar to Figure 5.6, as MD reduction can approximate the full computation very well, whereas amplitudes of MR are almost zero.

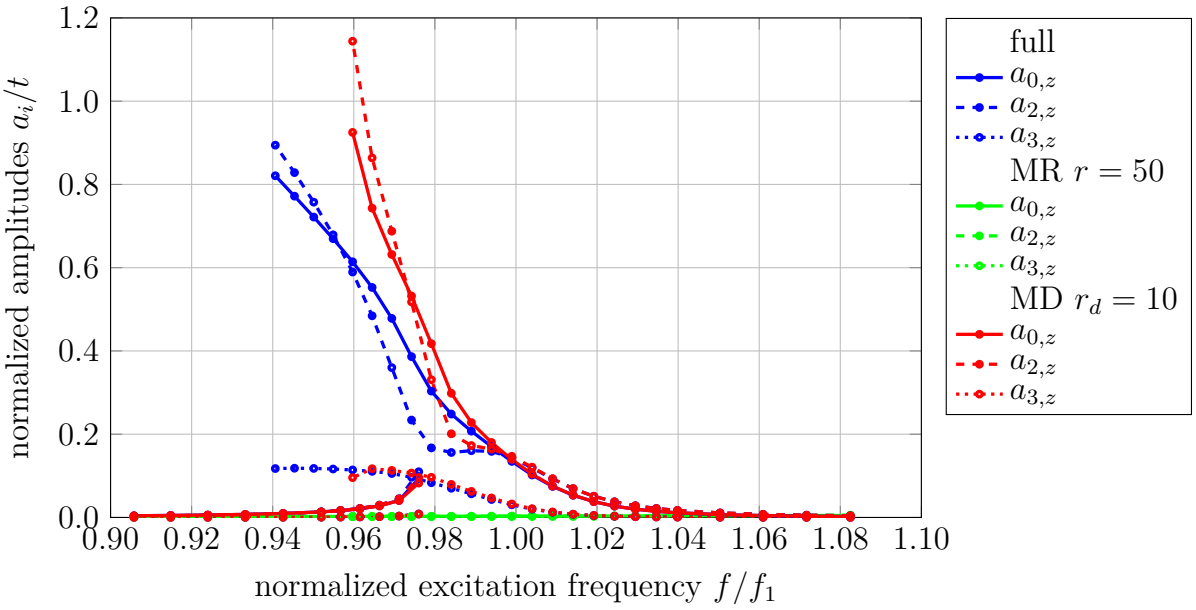

Figure 5.7: Frequency response curves of vibrating cylinder: normalized z-amplitudes a_i/t, $i = 0, 2, 3$ are plotted around $f/f_1 \approx 1.0$. While full harmonic balance (full, blue) and modal derivatives (MD, red) correspond very well, modal reduction (MR, green) completely fails with zero amplitudes

As explained already in the preceding example, the reason for the lower accuracy of MD at resonance is probably that very large deformations occur, compare Figure 4.7, which exceed the range of validity of the quadratic Taylor series approximation provided by the modal derivative approach.

Using the reduction methods, the problem size of HBM could be lowered from 2,268 (full) to 455 (MD) resp. 350 (MR) degrees of freedom. Regarding the solution time of the linear system using a direct solver, which is not the main focus here as the full system is quite small anyway, a reduction from around 4.0 seconds (full) to less than 0.05 seconds (MD & MR) could be achieved.

Altogether, with this application we have shown that reduction with modal derivatives is vey well capable of reproducing the nonlinear frequency response behavior, as long as deformations are not too large and the nonlinear effects are moderate. On the contrary, ordinary modal reduction with only eigenmodes cannot be used at all.

5.4.3 TERRIFIC Demonstrator as large-scale application

In Section 3.5.2 we have already introduced the "TERRIFIC Demonstrator" as a realistic component, which has to be parameterized for isogeometric analysis as a multi-patch model, see Figure 3.8.

As mentioned before, the volume parameterization consists of 15 patches with a total of 19,422 DOFs. Enforcing interface constraints on the patches with Lagrangian multipliers, the isogeometric finite element discretization of the model has 22,914 DOFs. Taking a Fourier series length of $m = 3$, the problem size of a harmonic balance nonlinear frequency analysis grows in this case to a total of 160,398 DOFs and due to its low sparsity the linearized equation system is not solvable on a personal computer. Hence we need to

	full	$r_d = 5$ ($r = 15$)		$r_d = 10$ ($r = 65$)	
	abs. val.	abs. val.	rel. err.	abs. val.	rel. err.
u_x	$1.42{\cdot}10^{-2}$	$1.33{\cdot}10^{-2}$	5.7%	$1.41{\cdot}10^{-2}$	0.04%
u_y	$6.57{\cdot}10^{-3}$	$5.85{\cdot}10^{-3}$	11.0%	$6.59{\cdot}10^{-3}$	0.27%
u_z	$1.05{\cdot}10^{-3}$	$2.69{\cdot}10^{-3}$	155.8%	$1.05{\cdot}10^{-3}$	0.48%
L^2	$1.53{\cdot}10^{-4}$	$1.45{\cdot}10^{-4}$	11.8%	$1.53{\cdot}10^{-4}$	0.24%
H^1	$1.47{\cdot}10^{-3}$	$1.40{\cdot}10^{-3}$	8.4%	$1.47{\cdot}10^{-3}$	0.80%

Table 5.1: Nonlinear static analysis of TERRIFIC Demonstrator. Accuracy of reduction with modal derivatives in comparison to full problem. MD reduction with $r_d = 10$ provides an acceptable error of less than 1.0%

apply model reduction to make the problem resp. the linear system solvable.

For a frequency analysis, the material parameters and boundary conditions remain the same as in (3.82) and (3.83), only the load is now time-dependent and multiplied by an harmonic factor $\cos \omega t$.

We start the computational analysis procedure by computing the first four eigenfrequencies ($f_i = 2\pi/\omega_i$) of the part:

$$\begin{aligned} f_1 &= 223.66 \text{ Hz}, \qquad f_2 = \ 358.05 \text{ Hz}, \\ f_3 &= 740.78 \text{ Hz}, \qquad f_4 = 1233.54 \text{ Hz}. \end{aligned} \tag{5.72}$$

Then a frequency response analysis of the part around the first two eigenfrequencies, i.e. in the range of 150 Hz $< f <$ 450 Hz shall be carried out. As the surface tractions cause a large deformation of the demonstrator, we expect a significant difference between the results of a linear DFR and the nonlinear HBM with reduction.

As part of preprocessing we use the results of Section 3.5.2, where the nonlinear static displacement caused by a static load of the same magnitude was computed. Then we use Algorithm 4 to set up a reduction basis with 5 resp. 10 linear eigenmodes and all corresponding modal derivatives, and solve the reduced versions of the nonlinear static problem. The comparison of absolute values and relative errors of displacements at evaluation point E, L^2- and H^1-norms in Table 5.1 reveals that $r_d = 5$ is not sufficient to capture the nonlinear displacement behavior, whereas $r_d = 10$ provides a sufficient accuracy of $\|u_{full} - u_{r_d}\|_{L^2} / \|u_{full}\|_{L^2} < 1.0\%$.

We proceed with the harmonic balance frequency response analysis in conjunction with modal derivative reduction with $r_d = 10$, i.e. the first 10 linear eigenmodes and the $r_d(r_d+1)/2 = 55$ corresponding modal derivatives. The HBM-MD problem size is now 455 DOFs, compared to 160,398 DOFs of full HBM.

In Figure 5.8 we have plotted the frequency response curves of x-, y- and z-amplitudes evaluated at evaluation point E for the frequency range 150 Hz $< f <$ 450 Hz, together with corresponding amplitudes computed from linear DFR. Around $f = 179.0$ Hz $= 0.5 f_2$ there is a remarkable sub-harmonic response in a_2, which can not be determined with linear frequency analysis. In the vicinity of the first eigenfrequency $f_1 = 223.7$ Hz we

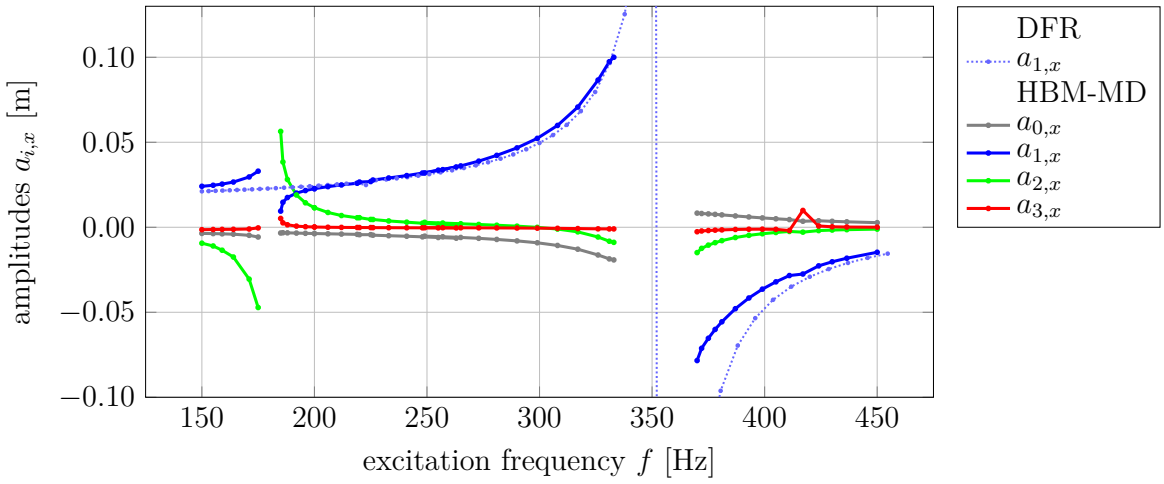

(a) x-amplitudes

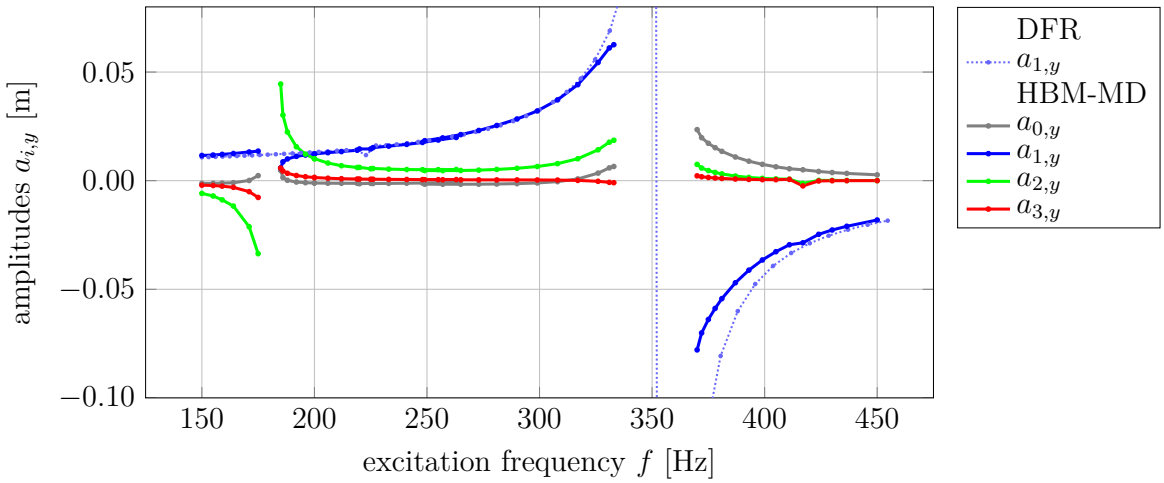

(b) y-amplitudes

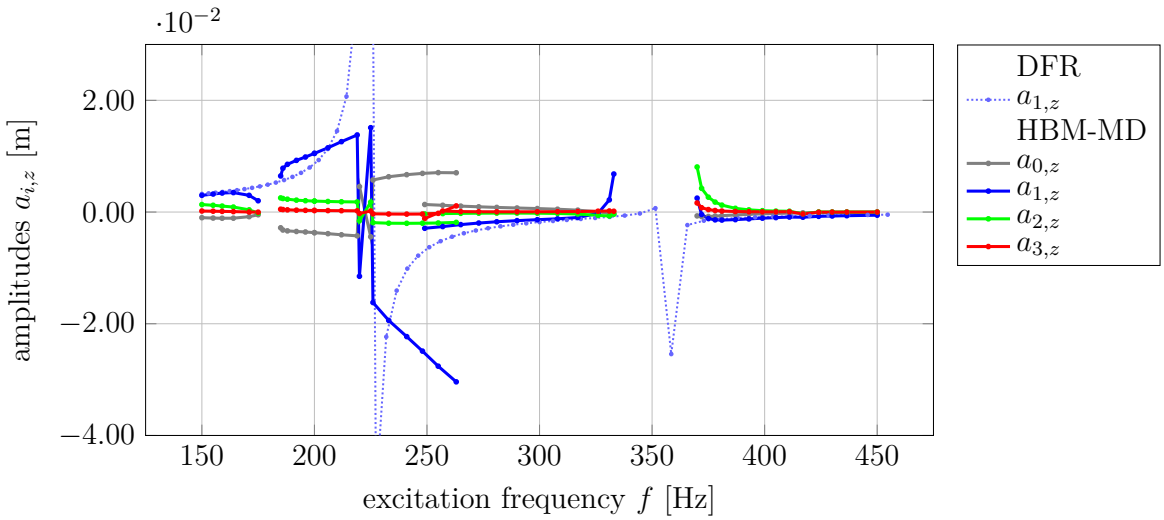

(c) z-amplitudes

Figure 5.8: Frequency response curves of amplitudes of vibrating TERRIFIC Demonstrator for DFR (dashed lines) and HBM with MD reduction (solid lines). HBM-MD shows strong nonlinear contributions of higher harmonics at $f \approx 358$ Hz and can also detect a sub-harmonic resonance at $f \approx 179$ Hz

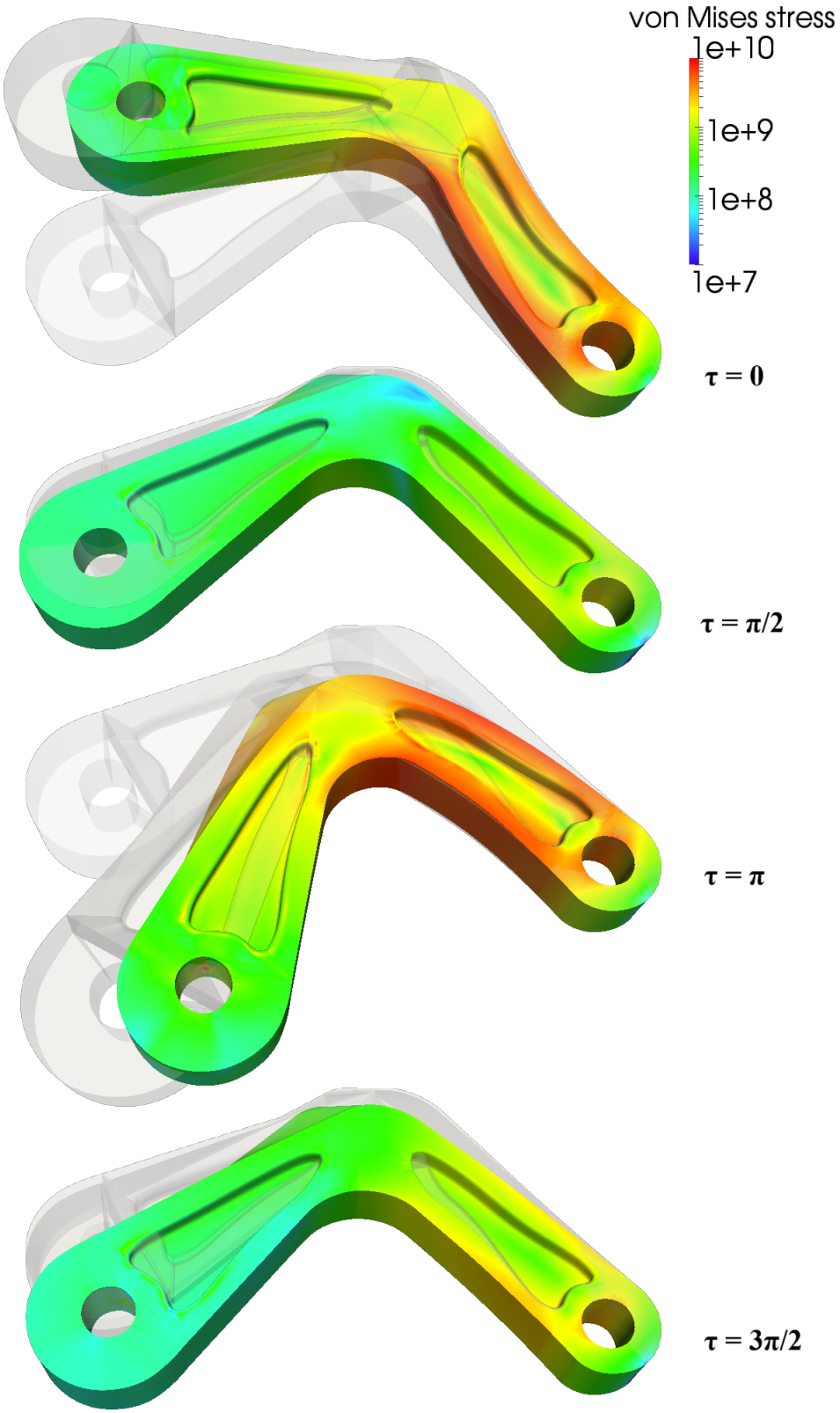

Figure 5.9: Snapshots of vibrating TERRIFIC Demonstrator for $f = 331.3$ Hz at non-dimensional times $\tau = 0,\ \pi/2,\ \pi,\ 3\pi/2$. Significant deviations between non-linear deformation from HBM-MD (colored by von Mises stress in Pa), and linear DFR deformation (in gray) are visible. Undeformed configuration is also shown in gray

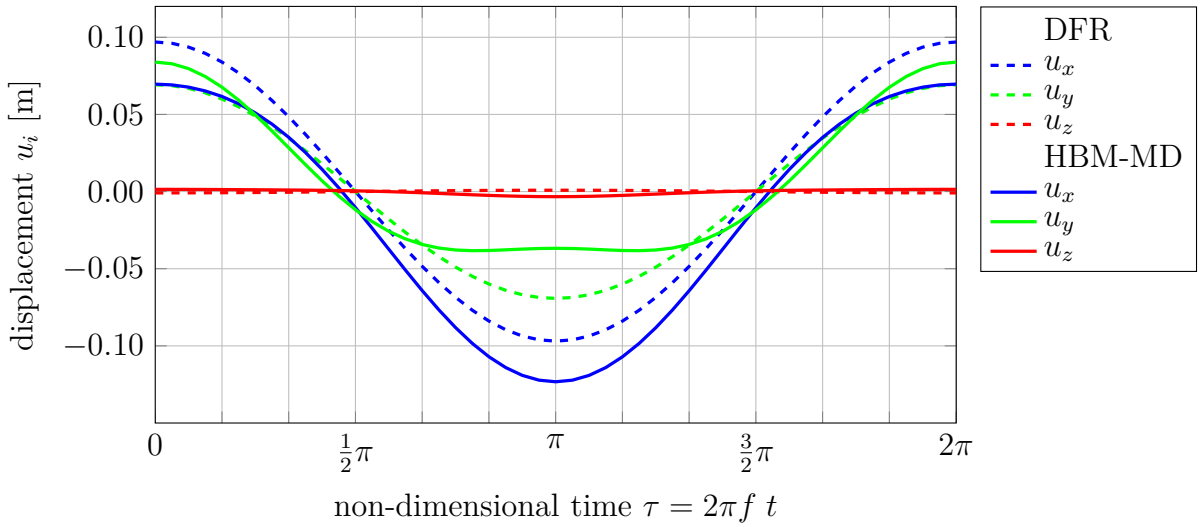

Figure 5.10: Displacement of evaluation point on TERRIFIC Demonstrator over one period of vibration for $f = 331.3$ Hz for HBM-MD (solid lines) and DFR (dashed lines). Significant deviations due to nonlinear effects are visible

notice that the nonlinear response behavior in z-amplitudes is different from the linear one obtained from DFR, but with our simple frequency stepping method we cannot follow complex solution paths here. The resonance behavior around $f_2 = 358.0$ Hz is very strong and we have convergence problems with our method for 335 Hz $< f <$ 355 Hz. There are strong contributions from higher harmonics here, which lead to much more realistic deformations as we discuss in more detail below. Rapidly growing z-amplitudes at resonance indicate that there might by turning points in the frequency response curves here, which we could only follow using continuation methods.

Figure 5.9 shows the vibrating structure at a frequency of $f = 331.3$ Hz, i.e. near the first eigenfrequency of $f_1 = 358.1$ Hz, where resonance with very large deformation occurs. The four snapshots are taken at times $\tau = 0,\ \pi/2,\ \pi,\ 3\pi/2$ display the deformed structure from the HBM-MD computation colored by von Mises stress in Pa. As references the deformed structure from DFR linear frequency analysis and undeformed structure both also shown in gray. It is obvious that the nonlinear results lead to a much better prediction of the small volume change of the structure and thus much more realistic states of deformation than linear DFR. Furthermore, it is interesting that the bending of the structure is stronger in the nonlinear case than in the linear case for $\tau = \pi$.

These findings can also be observed in Figure 5.10, where we have plotted the x-, y- and z-displacement at the evaluation point over one vibration period of $\tau \in [0, 2\pi]$ for $f = 331.3$ Hz for both HBM-MD and DFR. Significant differences are visible between the nonlinear deformation from HBM-MD (solid lines) and the linear deformation from DFR (dashed lines).

Altogether, the results presented here for the "TERRIFIC Demonstrator" show that a reduction with modal derivatives makes harmonic balance nonlinear frequency response analysis feasible for larger scale applications. Although we do not have the solutions of a full, unreduced nonlinear frequency analysis here as reference, the results could be validated in comparison to linear DFR. It could be shown that HBM-MD is able to capture nonlinear effects such as sub-harmonic resonance and provide much more realistic results than DFR for large amplitude vibrations.

5.5 Summary

The harmonic balance method, as we have introduced it in Chapter 4, is a powerful means for nonlinear steady-state frequency analysis. However, its major drawback is the size of the resulting linear system to be solved, which makes HBM unfeasible for large problems. In this chapter we have addressed this issue and proposed a model order reduction method for the spatial discretization, which reduces the problem size significantly and enables large-scale applications.

After a review of commonly used projection methods for model order reduction, we have decided to use a modal projection basis, which is enhanced with modal derivatives (MD). We have introduced the concept of modal derivatives and shown that modal derivatives can be used to obtain a second-order approximation of displacements. This motivated the use of MD for model reduction in nonlinear frequency analysis and HBM.

In order to gain a better understanding of the concept, we have established a more theoretical framework by transferring the idea of modal derivatives to the continuous formulation of PDE problems. Using a model problem and the nonlinear Euler-Bernoulli beam as examples, we could show that MDs can be analytically computed and used to approximate the exact solutions.

With computational examples we could demonstrate that reduction with modal derivatives is very accurate for moderate nonlinearities. Also the application in nonlinear frequency response analysis was successful and HBM-MD could approximate the results of full HBM very well. It provides a substantial reduction of the total number of DOFs, but is at the same time still able to reproduce the main characteristics of nonlinear vibrations, such as sub-harmonic resonances. With the TERRIFIC Demonstrator we have shown that a larger scale nonlinear frequency analysis is now feasible with HBM-MD.

6 Isogeometric mixed methods for near incompressible vibrations

An important practical application of the method for nonlinear vibration analysis using isogeometric finite elements, harmonic balance, and modal derivative reduction, which we have developed over the preceding chapters, is the simulation of rubber and elastomer components. These are described using incompressible and near incompressible visco-hyperelastic materials laws, which have a Poisson's ratio ν equal or very close to 0.5. In this situation, finite element methods used without particular care can lead to locking phenomena, and consequently unreliable numerical simulations [23].

In the following we discuss the phenomenon of *volumetric locking* and review possible cures in Section 6.1. To avoid locking in near incompressible elasticity, we present isogeometric mixed finite element methods in Section 6.2. We integrate these mixed methods also into our framework for nonlinear frequency analysis, i.e. the harmonic balance method, in Section 6.3 and study their performance for application in nonlinear static and frequency response analysis numerically in Section 6.4.

6.1 Near incompressibility and locking

Locking phenomena can be observed for all kinds of physical problems subject to constraints, such as fluid mechanics with incompressible Stokes and Navier-Stokes equations, continuum mechanics with near incompressible elasticity and plasticity (volumetric locking), and structural elements such as thin plates, shells and beams (shear and membrane locking) [23, 130]. The term *locking* means that a finite element formulation underestimates the true or analytical solution of a problem, i.e. it shows an unphysically stiff behavior and only converges very slowly, as can be seen in later presented numerical examples in Section 6.4.

In elasticity, the constitutive equation dependends on the two parameters μ and λ, the so-called Lamé constants, compare Section 3.1.3. When Poisson's ratio $\nu \to 0.5$, it follows that

$$\mu \to \frac{E}{3}, \quad \lambda \to \infty, \tag{6.1}$$

which leads for near incompressible problems to an ill-conditioning of the stiffness matrix and thus volumetric locking, and for full incompressiblity conventional methods cannot be used at all.

The incompressibility condition, which is div $\mathbf{u} = 0$ in linear and $J = 1$ in nonlinear elasticity, acts as an additional constraint for the deformation control points or nodes. For example, a linear triangular finite element can completely lock in incompressible 2D plain strain problems and allows no deformation at all for a whole mesh [39].

For higher-order finite elements, such as p-FEM and isogeometric methods, volumetric locking effects are alleviated or even totally disappearing for very high degree p. However, it is not always desireable to use very high orders due to limited regularity of the exact solution and lower sparsity of resulting stiffness matrices [130], which applies for both p-FEM and IGA.

A number of alternative methods have been developed for locking-free finite element discretizations and many of them have been adapted to the context of isogeometric analysis already: Mixed formulations for the incompressible Stokes problem in 2D where investigated in [30] and mixed three-field formulations based on the Hu-Washizu functional for (near) incompressible linear and nonlinear elasticity and plasticity in [84, 118]. A stream function formulation, where the divergence-free constraint is directly imposed on the discretization space, was studied for plain elasticity problems in [4]. The same class of problems was treated by $\bar{B}$- and $\bar{F}$-projection methods in [48]. Furthermore, the assumed natural strain (ANS) method for shells [32] and descrete shear gap (DSG) and reduced integration methods for Timoshenko beams [24, 47] were investigated.

6.2 Isogeometric mixed finite element discretizations

In order to cure volumetric locking and be able to accurately solve near and fully incompressible elasticity problems, we employ a mixed method. In a mixed method applied to a certain formulation, such as the elasticity equations, different variables are discretized independently from each other. In [33] we have already described the isogeometric finite element discretization of mixed formulations and their implementation using `igatools` software library [91]. Here we review the derivation of mixed formulations for near and fully incompressible, linear and nonlinear elasticity based on references [6, 7, 23, 109, 130], and outline the discretization using different kinds of mixed isogeometric elements.

6.2.1 Formulation for linear (near) incompressibility

To describe the mixed methods, we begin with the static linear elasticity equation and the corresponding energy functional, which was already introduced in Section 3.3 as (3.62), and is only displacement-based:

$$\psi_d(\mathbf{u}) = \mu \operatorname{tr}(\boldsymbol{\varepsilon}^2(\mathbf{u})) + \frac{\lambda}{2} \operatorname{tr}(\boldsymbol{\varepsilon}(\mathbf{u}))^2. \tag{6.2}$$

Now we introduce the pressure-like scalar variable $p = \lambda \operatorname{tr}(\boldsymbol{\varepsilon}(\mathbf{u}))$ and rewrite the strain energy functional in a mixed form depending on both $\mathbf{u}$ and p [6]:

$$\psi_m(\mathbf{u}, p) = \mu \operatorname{tr}(\boldsymbol{\varepsilon}^2(\mathbf{u})) + p \operatorname{tr}(\boldsymbol{\varepsilon}(\mathbf{u})) - \frac{1}{2\lambda} p^2. \tag{6.3}$$

Differentiation of the mixed energy functional ψ_m w.r.t. both variables leads to the expression for the stress and the equation of the incompressibility constraint:

$$\begin{aligned} \boldsymbol{\sigma}(\mathbf{u},p) = \frac{d\psi_m}{d\mathbf{u}} &= 2\mu\boldsymbol{\varepsilon}(\mathbf{u}) + p\mathbf{I} \qquad &&= \mu(\nabla\mathbf{u} + \nabla\mathbf{u}^T) + p\mathbf{I}, \\ \frac{d\psi_m}{dp} &= \operatorname{tr}(\boldsymbol{\varepsilon}(\mathbf{u})) - \frac{1}{\lambda}p \quad &&= \operatorname{div}\mathbf{u} - \frac{1}{\lambda}p \end{aligned} \tag{6.4}$$

This leads to the strong form of the near incompressible linear elasticity problem in mixed formulation:

$$\begin{cases} -\operatorname{div}\boldsymbol{\sigma}(\mathbf{u},p) &= \rho_0\mathbf{b} \quad \text{in } \Omega, \\ \operatorname{div}\mathbf{u} - \frac{1}{\lambda}p &= 0 \quad \text{in } \Omega, \\ \mathbf{u} &= \mathbf{h} \quad \text{on } \Gamma_u, \\ \boldsymbol{\sigma}(\mathbf{u},p)\,\mathbf{n} &= \mathbf{t} \quad \text{on } \Gamma_n. \end{cases} \tag{6.5}$$

For the isogeometric finite element discretization the weak form of (6.5) is needed and as usually derived using integration by parts of the momentum equation:

$$\begin{aligned} \int_\Omega 2\mu\,\delta\boldsymbol{\varepsilon}\cdot\boldsymbol{\varepsilon}(\mathbf{u}) + p\operatorname{div}\delta\mathbf{u}\,d\mathbf{x} &= \int_\Omega \rho_0\,\delta\mathbf{u}^T\mathbf{b}\,d\mathbf{x} + \int_{\Gamma_n}\delta\mathbf{u}^T\mathbf{t}\,d\Gamma \qquad \forall\delta\mathbf{u}\in\mathcal{V}, \\ \int_\Omega q\operatorname{div}\mathbf{u} - \frac{1}{\lambda}qp\,d\mathbf{x} &= 0 \qquad \forall q\in\mathcal{Q}. \end{aligned} \tag{6.6}$$

For a fully incompressible material, i.e. where $\nu = 0.5$ and thus $\lambda \to \infty$, all terms with a factor $\frac{1}{\lambda}$ in the above-stated equations (6.3)-(6.6) vanish and the incompressibility constraint becomes

$$\operatorname{div}\mathbf{u} = 0. \tag{6.7}$$

6.2.2 Formulation for nonlinear (near) incompressibility

The nonlinear elasticity problem was in detail introduced in the displacement-based formulation in Section 3.1. For the derivation of the mixed formulation we proceed in the same fashion as for the linear case. Starting point is again the strain energy function for the Neo-Hookean material (3.22):

$$\psi_d(\mathbf{C}) = \frac{\mu}{2}\,(\operatorname{tr}(\mathbf{C}) - 3) - \mu\,\ln J + \frac{\lambda}{2}\,(\ln J)^2. \tag{6.8}$$

Now the new pressure-like variable is introduced as $p = \lambda \ln J$ and inserted for the mixed form of the strain energy function [6]:

$$\psi_m(\mathbf{C},p) = \frac{\mu}{2}\,(\operatorname{tr}(\mathbf{C}) - 3) - \mu\,\ln J + p\ln J - \frac{1}{2\lambda}p^2. \tag{6.9}$$

Differentiation yields the 2nd Piola-Kirchhoff stress and the constraint equation:

$$\begin{aligned} \mathbf{S}(\mathbf{u},p) = 2\frac{d\psi_m}{d\mathbf{C}} &= \mu(\mathbf{I} - \mathbf{C}^{-1}) + p\,\mathbf{C}^{-1}, \\ \frac{d\psi_m}{dp} &= \ln J - \frac{1}{\lambda}p. \end{aligned} \tag{6.10}$$

It follows the strong form of the near incompressible nonlinear hyperelasticity problem in mixed formulation:

$$\begin{cases} -\operatorname{div}\left(\mathbf{F}\,\mathbf{S}(\mathbf{u},p)\right) &= \rho_0\mathbf{b} & \text{in } \Omega, \\ \ln J - \frac{1}{\lambda}p &= 0 & \text{in } \Omega, \\ \mathbf{u} &= \mathbf{h} & \text{on } \Gamma_u, \\ \mathbf{F}\,\mathbf{S}(\mathbf{u},p)\,\mathbf{n} &= \mathbf{t} & \text{on } \Gamma_n. \end{cases} \tag{6.11}$$

As in Section 3.2.1, the weak form of (6.11) is be derived before a mixed finite element discretization can be applied:

$$\begin{aligned} &\int_\Omega \delta\mathbf{E}\cdot\mathbf{S}(\mathbf{u},p)\,d\mathbf{x} = \int_\Omega \rho_0\delta\mathbf{u}^T\mathbf{b}\,d\mathbf{x} + \int_{\Gamma_n}\delta\mathbf{u}^T\mathbf{g}\,d\Gamma \qquad && \forall\delta\mathbf{u}\in\mathcal{V}, \\ &\int_\Omega q\,\ln J - \frac{1}{\lambda}qp\,d\mathbf{x} = 0 && \forall q\in\mathcal{Q}. \end{aligned} \tag{6.12}$$

In the case of a fully incompressible material with $\lambda\to\infty$, again all terms with a factor $\frac{1}{\lambda}$ vanish and the incompressibility constraint becomes

$$\ln J = 0, \tag{6.13}$$

which is equal to the earlier mentioned constrained $J = \det\mathbf{F} = 1$. Depending on the nonlinear material law, different incompressibility constraints may be chosen as alternatives to (6.13). Commonly used are also J^2-1, $J-1$ and $1-1/J$ [7, 130].

6.2.3 Mixed isogeometric elements

Having derived the weak forms of the (near) incompressible elasticity problem in the linear and nonlinear setting as mixed formulations with (6.6) and (6.12), the next step in the solution of these equations is the discretization of spaces $\mathcal{V}\subset H^1(\Omega)^3$ and $\mathcal{Q}\subset L^2(\Omega)$. In our setting we certainly choose the discrete spaces $\mathcal{V}_h\subset\mathcal{V}$ and $\mathcal{Q}_h\subset\mathcal{Q}$ as (refinements of) the push-forward of spline function spaces on the domain Ω.

For the linear problem, this results in a symmetric, block-structured system of equations of size $N_u + N_p$:

$$\begin{pmatrix}\mathbf{K} & \mathbf{B}^T\\ \mathbf{B} & \mathbf{Q}\end{pmatrix}\begin{pmatrix}\mathbf{d}\\ \boldsymbol{\lambda}\end{pmatrix} = \begin{pmatrix}\mathbf{b}\\ \mathbf{0}\end{pmatrix}, \tag{6.14}$$

with $\mathbf{d}\in\mathbb{R}^{N_u}$ and $\boldsymbol{\lambda}\in\mathbb{R}^{N_p}$.

In the incompressible case the matrix $\mathbf{Q}$ is zero and in the near-incompressible it is almost zero due to the factor $\frac{1}{\lambda}$. The pressure like variable p, which is discretized using the coefficient vector $\boldsymbol{\lambda}$, acts as a Lagrangian multiplier for the incompressibility constraint and this means that (6.14) is a (perturbed) saddle point problem. In Section 2.3.3 we have already encountered saddle point problems arising from multi-patch discretizations and seen that the rank of the sub-matrix $\mathbf{B}$ is crucial for the solvability of the system.

In the context of a mixed discretization, $\mathbf{B}$ arises from the assembly of the term $b(\mathbf{v},q) = \int_\Omega q\operatorname{div}\mathbf{v}\,d\mathbf{x}$, where both discretization spaces are mixed since $\mathbf{v}_h\in\mathcal{V}_h$ and $q_h\in\mathcal{Q}_h$. The full-rank condition for $\mathbf{B}$ then leads to the well-known *Babuška-Brezzi* or *inf-sup condition*

for $\mathcal{V}_h$ and $\mathcal{Q}_h$ [7, 23, 35]:

$$\inf_{q\in\mathcal{Q}_h, q\neq 0} \sup_{\mathbf{v}\in\mathcal{V}_h, \mathbf{v}\neq\mathbf{0}} \frac{b(\mathbf{v}, q)}{\|q\|_{L^2}\|\mathbf{v}\|_{H^1}} \geq \varepsilon > 0. \tag{6.15}$$

Furthermore, as for the displacement-based case, the following coercivity condition must hold for the bilinear form $a(\mathbf{v}, \mathbf{u}) = \int_\Omega 2\mu\, \boldsymbol{\varepsilon}(\mathbf{v}) \cdot \boldsymbol{\varepsilon}(\mathbf{u})\, d\mathbf{x}$ [7, 23, 35]:

$$\inf_{\substack{\mathbf{v}\in\mathcal{V}_h, \mathbf{v}\neq\mathbf{0}, \\ \operatorname{div}\mathbf{v}=0}} \frac{a(\mathbf{v}, \mathbf{v})}{\|\mathbf{v}\|^2_{H^1}} \geq \varepsilon > 0. \tag{6.16}$$

Thus the choice of a combination of spaces for the discretization of displacement and pressure, i.e. the choice of a *mixed element* $\mathcal{V}_h/\mathcal{Q}_h$, is crucial for the stability of the method [7]. For the linear Stokes problem a mathematical analysis of mixed isogeometric finite element types based on NURBS discretizations has been carried out in [28], and the two proposed inf-sup-stable element types are presented in the following.

In the nonlinear case, the discretization of (6.12) leads to a nonlinear system of the form

$$\begin{pmatrix} \mathbf{f}(\mathbf{d}, \boldsymbol{\lambda}) \\ \mathbf{c}(\mathbf{d}, \boldsymbol{\lambda}) \end{pmatrix} = \begin{pmatrix} \mathbf{b} \\ \mathbf{0} \end{pmatrix}. \tag{6.17}$$

For an iterative solution of this nonlinear system of equations, compare the Newton's method for the displacement-based formulation presented in Algorithm 1, the linearization of (6.17) is needed and leads to a linear system with the very same block structure as (6.14).

Taylor-Hood elements

Taylor-Hood elements (TH) are well-established in classical finite element analysis and their isogeometric counterparts have already been employed in [14] for incompressible elasticity. Isogeometric TH elements are denoted by $\mathcal{S}^r_{p+1}/\mathcal{S}^r_p$ and based on the same mesh $\mathcal{T}_h(\Omega)$ for the discretization of displacements and pressure, but the degree of $\mathcal{V}_h$ is one higher than of $\mathcal{Q}_h$:

$$\mathcal{Q}_h = \mathcal{S}^r_p\big(\mathcal{T}_h(\Omega)\big), \qquad \mathcal{V}_h = \Big(\mathcal{S}^r_{p+1}\big(\mathcal{T}_h(\Omega)\big)\Big)^d. \tag{6.18}$$

This means that $\mathcal{V}_h$ is obtained from $\mathcal{Q}_h$ by one step of p-refinement, i.e. an order elevation that maintains the regularity $r < p$ of the pressure space also for the displacement space. In [28] it is proven that the isogeometric Taylor-Hood elements $\mathcal{S}^r_{p+1}/\mathcal{S}^r_p$ are inf-sup stable for $p \geq 1$.

As introduced before in Section 2.1, the notation $\mathcal{S}^r_p\big(\mathcal{T}_h(\Omega)\big)$ refers to a tensor product spline space, which is defined as push-forward of spline functions on the physical domain Ω, based on the mesh $\mathcal{T}_h(\Omega)$.

Example 6.1 (Isogeometric Taylor-Hood element $\mathcal{S}^1_3/\mathcal{S}^1_2$)**.** *Figure 6.1 shows the B-Spline basis functions of a one-dimensional isogeometric Taylor-Hood element $\mathcal{S}^1_3/\mathcal{S}^1_2$ with the*

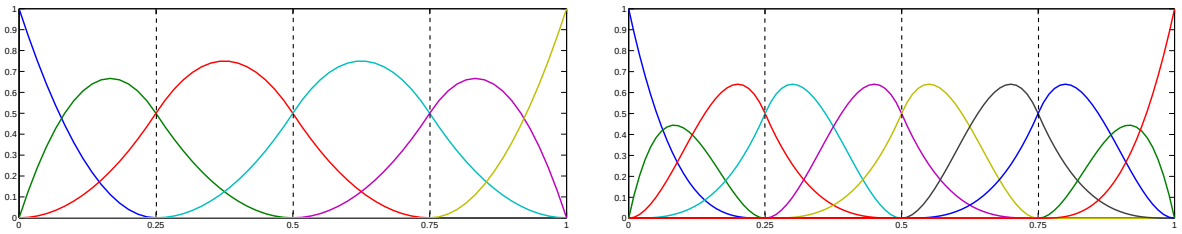

(a) Pressure space $\mathcal{Q}_h = \mathcal{S}_2^1$ (b) Displacement space $\mathcal{V}_h = \mathcal{S}_3^1$

Figure 6.1: B-Spline spaces of isogeometric Taylor-Hood element $\mathcal{S}_3^1/\mathcal{S}_2^1$ from Ex. 6.1

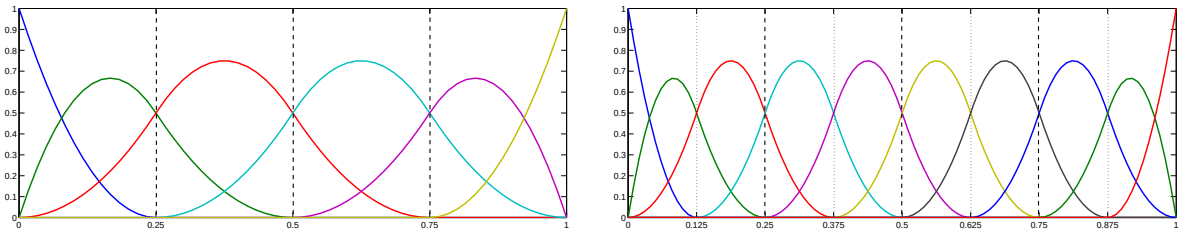

(a) Pressure space $\mathcal{Q}_h = \mathcal{S}_2^1(h)$ (b) Displacement space $\mathcal{V}_h = \mathcal{S}_2^1(h/2)$

Figure 6.2: B-Spline spaces of isogeometric subgrid element $\mathcal{S}_2^1(h/2)/\mathcal{S}_2^1(h)$ from Ex. 6.2

following parameters:

$$\begin{aligned} &p_p = 2, \quad r_p = 1, \quad n_p = 6, \quad m_p = 9, \quad \Xi_p = \left\{0,0,0,\tfrac{1}{4},\tfrac{1}{2},\tfrac{3}{4},1,1,1\right\}, \\ &p_u = 3, \quad r_u = 1, \quad n_u = 10, \quad m_u = 14, \quad \Xi_u = \left\{0,0,0,0,\tfrac{1}{4},\tfrac{1}{4},\tfrac{1}{2},\tfrac{1}{2},\tfrac{3}{4},\tfrac{3}{4},1,1,1,1\right\}. \end{aligned} \tag{6.19}$$

Remark 6.1. *In [48] the corresponding spline spaces for isogeometric $\bar{B}$- and $\bar{F}$-projection are chosen as S_p^{p-1}/S_{p-1}^{p-2}. This is a similar, but not the same choice as TH-spaces, since the pressure space is generated from the displacement space by an order reduction, which keeps the multiplicity of inner knots constant, except when they have multiplicity p. These spaces seem to work well in most cases, but are not proven theoretically to be inf-sup stable.*

Subgrid elements

For subgrid elements (SG) the displacement space is based on a refinement or subdivision $\mathcal{T}_{h/2}(\Omega)$ of the mesh of the pressure space $\mathcal{T}_h(\Omega)$:

$$\mathcal{Q}_h = \mathcal{S}_p^r\big(\mathcal{T}_h(\Omega)\big), \qquad \mathcal{V}_h = \Big(\mathcal{S}_p^r\big(\mathcal{T}_{h/2}(\Omega)\big)\Big)^d. \tag{6.20}$$

These elements are particularily interesting in the context of isogeometric analysis, since the generation of the subgrid $\mathcal{T}_{h/2}(\Omega)$ with 2^d elements for every element of the original mesh $\mathcal{T}_h(\Omega)$ can be easily realized with one step of uniform h-refinement.

In [28] it was also shown that these elements are inf-sup stable for $p \geq 1$, and even further that also a k- instead of h-refinement can be applied, which results in a displacement space $\mathcal{V}_h = \Big(\mathcal{S}_{p+1}^r\big(\mathcal{T}_{h/2}(\Omega)\big)\Big)^d$ with maximal C^p-continuity at the new knots of the

subgrid and C^r-continuity at existing inner knots.

Example 6.2 (Isogeometric subgrid element $\mathcal{S}_2^1(h)/\mathcal{S}_2^1(h/2)$)**.** *Figure 6.2 shows the B-Spline basis functions of a one-dimensional isogeometric subgrid element* $\mathcal{S}_2^1(h)/\mathcal{S}_2^1(h/2)$ *with the following parameters:*

$$\begin{aligned} &p_p = 2, \quad r_p = 1, \quad n_p = 6, \quad m_p = 9, \quad \Xi_p = \left\{0,0,0,\tfrac{1}{4},\tfrac{1}{2},\tfrac{3}{4},1,1,1\right\}, \\ &p_u = 2, \quad r_u = 1, \quad n_u = 10, \quad m_u = 13, \quad \Xi_u = \left\{0,0,0,\tfrac{1}{8},\tfrac{1}{4},\tfrac{3}{8},\tfrac{1}{2},\tfrac{5}{8},\tfrac{3}{4},\tfrac{7}{8},1,1,1\right\}. \end{aligned} \tag{6.21}$$

6.3 Application to nonlinear vibration analysis

For a nonlinear frequency response analysis involving near incompressible materials such as rubber, we have to integrate the spatial semi-discretization using mixed elements into the harmonic balance framework, which was introduced in Section 4.3.

Starting point is again the semi-discretized dynamic equation of motion, which is now also involving the degrees of freedom of the pressure-like Lagrangian multipliers:

$$\begin{pmatrix} \mathbf{M} & \mathbf{0} \\ \mathbf{0} & \mathbf{0} \end{pmatrix} \begin{pmatrix} \ddot{\mathbf{d}}(t) \\ \ddot{\boldsymbol{\lambda}}(t) \end{pmatrix} + \begin{pmatrix} \mathbf{C} & \mathbf{0} \\ \mathbf{0} & \mathbf{0} \end{pmatrix} \begin{pmatrix} \dot{\mathbf{d}}(t) \\ \dot{\boldsymbol{\lambda}}(t) \end{pmatrix} + \begin{pmatrix} \mathbf{f}(\mathbf{d}(t), \dot{\mathbf{d}}(t), \boldsymbol{\lambda}(t)) \\ \mathbf{c}(\mathbf{d}(t), \boldsymbol{\lambda}(t)) \end{pmatrix} = \begin{pmatrix} \mathbf{b}(t) \\ \mathbf{0} \end{pmatrix}. \tag{6.22}$$

It is a differential-algebraic equation (DAE) with DAE-index 3 in-case of incompressible material and index 1 for near incompressibility [109], which is very important in case a time integration method is used for the solution.

Before applying harmonic balance method to (6.22), we rewrite it using the notation $\mathbf{d}^* = \left(\mathbf{d}^T, \boldsymbol{\lambda}^T\right)^T \in \mathbb{R}^{N_u+N_p}$:

$$\mathbf{M}^* \, \ddot{\mathbf{d}}^*(t) + \mathbf{C}^* \, \dot{\mathbf{d}}^*(t) + \mathbf{f}^*(\mathbf{d}^*(t), \dot{\mathbf{d}}^*(t)) = \mathbf{b}^*(t). \tag{6.23}$$

In this formulation the equation has the same structure as we had it in (4.29) for the introduction of the harmonic balance method. Thus the integration of mixed methods into harmonic balance is straight-forward and follows the routine described in Section 4.3:

- Truncated Fourier series expansion of $\mathbf{d}^*$ using $2m+1$ amplitude vectors $\mathbf{q}_k^*$.
- Substitution into (6.23) for a residual vector $\mathbf{r}^*(\mathbf{q}^*, \omega, t)$.
- Fourier transform of the residual onto $2m+1$ coefficient vectors $\hat{\mathbf{r}^*}_j$.
- Solution of the nonlinear system of equations $\hat{\mathbf{r}^*}(\mathbf{q}^*, \omega) = \mathbf{0}$.

This means that Algorithm 3 can be reused just by replacing the vectors and matrices of the displacement-based formulation with the mixed formulation.

The mass matrix $\mathbf{M}^*$ and damping matrix $\mathbf{C}^*$ are singular, but this is also the case for a multi-patch parameterization using Lagrangian multipliers as in Section 2.3.2. It does not cause any problems in harmonic balance, since we only have to evaluate the residual $\mathbf{r}^*$ of (6.23) and its Jacobian $\mathbf{K}_T^*$, which is non-singular when appropriate mixed element spaces are used, as discussed in Section 6.2.

Near incompressible, visco-hyperelastic materials

In (6.22) we have stated that the internal force vector $\mathbf{f}(\mathbf{d}(t), \dot{\mathbf{d}}(t), \boldsymbol{\lambda}(t))$ may also depend on the velocities, as it is the case for visco-hyperelastic materials (Section 3.1.4), but so far in the derivation of nonlinear near incompressible elasticity in Section 6.2.2 this wasn't considered yet.

Hence we now introduce a near incompressible, visco-hyperelastic constitutive relation by augmenting the 2nd Piola-Kirchhoff stress term of the near incompressible Neo-Hookean material model from (6.10) with the viscous stress term from (3.31):

$$\mathbf{S}(\mathbf{u}, \dot{\mathbf{u}}, p) = \mathbf{S}_e(\mathbf{u}, p) + \mathbf{S}_v(\mathbf{u}, \dot{\mathbf{u}}) = \mu(\mathbf{I} - \mathbf{C}^{-1}) + p\,\mathbf{C}^{-1} + 2\eta\mu\dot{\mathbf{E}}. \tag{6.24}$$

6.4 Computational applications

In the following computational examples we want to study the performance of different isogeometric mixed finite element formulations, i.e. Taylor-Hood and subgrid elements, in application to nonlinear near incompressible elasticity and compare the to purely displacement based formulations. Furthermore, the use of mixed formulations within the nonlinear frequency response analysis framework is investigated.

6.4.1 Cook's membrane as benchmark problem

A popular test problem for validation and benchmarking of locking-free finite element discretizations is Cook's membrane problem [38]. It has also been used in the context of isogeometric methods [48, 84], and we have employed it in [33] to validate our implementation using `igatools` library [91].

Cook's membrane is a 2D panel, clamped on the left side and subject to a shear load on the right side, causing combined bending and shear deformation. Geometry, dimensions and values of parameters can be found in Figure 6.3(a). Large deformation kinematics and the nonlinear, near incompressible Neo-Hookean constitutive law are employed. The quantity of interest is the horizontal deformation of the top right corner of the panel u_y, which is used to study p/k- and h-convergence and locking-free behavior of mixed elements. An example for a large deformation of the panel is visualized in Figure 6.3(b).

First, the convergence behavior of isogeometric finite element formulations is studied for near incompressibility with $\nu \to 0.5$ and summarized in Table 6.1 and Figure 6.4. The mixed Taylor-Hood element $S_3^1(h)/S_2^1(h)$ and mixed subgrid element $S_2^1(h/2)/S_2^1(h)$ are compared to the displacement-based element $S_3^2(h)$ for ν being increased from 0.4 to 0.5.

For increasing incompressibility, i.e. $\nu \to 0.5$ and $\lambda/\mu = \frac{2\nu}{1-2\nu} \to \infty$, it can be seen that the accuracy of the displacement-based element S_3^2 decreases due to volumetric locking, while the mixed methods converge. Furthermore, for the mixed elements the number of iterations for convergence of the Newton's method is independent of ν, while it increases also for the non-mixed element and even load-stepping has to be applied to ensure convergence in the very near incompressible regime, which is another indicator of locking.

In Figure 6.5 convergence behavior of u_y with respect to the number of elements per side ($\ell \sim 1/h$) of the discretization of the panel is shown. We compare the isogeometric Taylor-Hood and subgrid elements with pure displacement formulations for a fixed

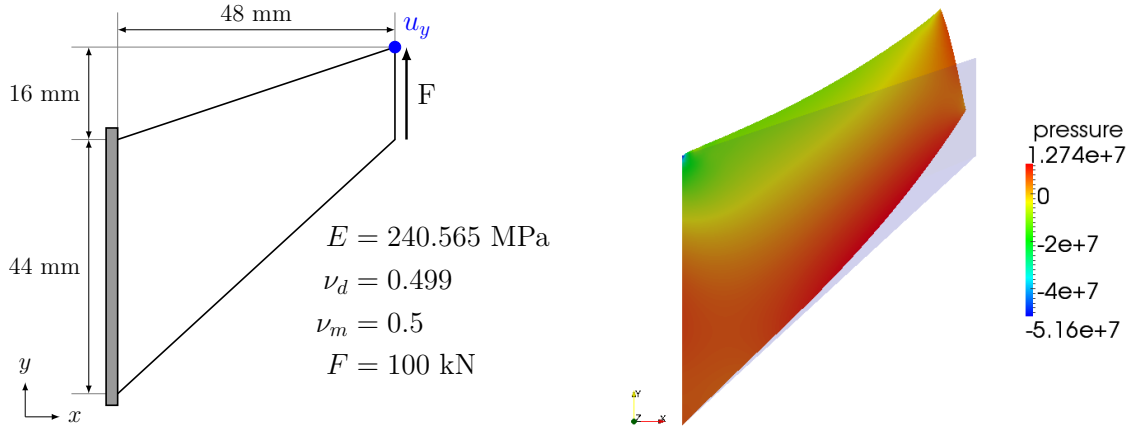

(a) Geometry and parameters of Cook's membrane problem

(b) Deformed Cook's membrane colored by pressure in Pa

Figure 6.3: Problem setting of Cook's membrane and deformation plot

		TH S_3^1/S_2^1		SG S_2^1/S_2^1		displ. S_3^2	
ν	λ/μ	u_y	it.	u_y	it.	u_y	it.
0.4	4	7.4045	5	7.3955	5	7.3324	5
0.45	9	7.1660	5	7.1551	5	7.0572	6
0.49	49	6.9393	5	6.9262	5	6.7398	9
0.495	99	6.9085	5	6.8951	5	6.6627	8
0.499	499	6.8834	5	6.8698	5	6.5089	8
0.4999	4999	6.8778	5	6.8640	5	6.3179	$2 \cdot 8$
0.49999	49999	6.8772	5	6.8635	5	6.0424	$4 \cdot 9$
0.499999	499999	6.8771	5	6.8634	5	5.7274	$10 \cdot 8$

Table 6.1: Convergence study of Cook's membrane for near incompressibility with Poisson's ratio $\nu \to 0.5$, comparison of u_y in mm and number of Newton iterations

Poisson's ratio $\nu = 0.499$. The classical displacement-based S_p^{p-1} elements show a rather slow convergence behavior due to locking, while both mixed elements, Taylor-Hood and subgrid, converge quickly for p/k- and h-refinement. These results also match very well with the ones obtained by [48], where an isogeometric $\bar{F}$-method was used instead of a mixed formulation. The accuracy of Taylor-Hood elements $S_{p+1}^{p-1}(h)/S_p^{p-1}(h)$ is a bit higher than of subgrid elements $S_p^{p-1}(h/2)/S_p^{p-1}(h)$. For same degree p both elements have the same number of degrees of freedom, since the increase in DOFs is the same for p- and h-refinement, but the benefit of a higher degree is larger than the one of a finer mesh.

Even though the purely displacement formulation also converges toward the correct value of u_y for higher polynomial degree and number of degrees of freedom, the approximation of stresses exhibits spurious oscillations, which are typical for locking phenomena. In Figure 6.6 we plot the stress component σ_{xx}. The non-mixed elements show a highly oscillatory behavior of volumetric stress components – a typical sign of volumetric locking

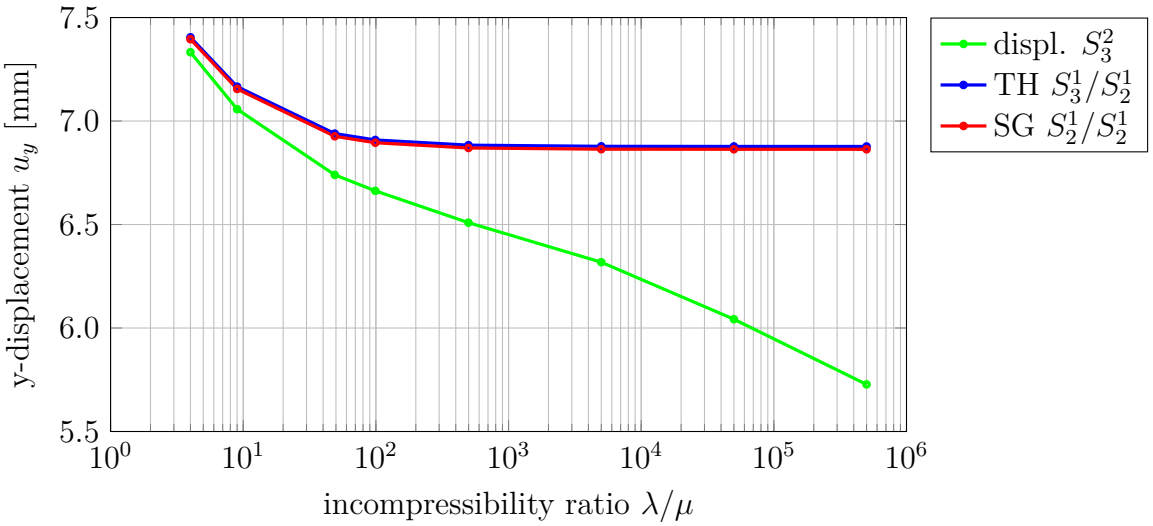

Figure 6.4: Convergence of displacement u_y of Cook's membrane over incompressibility ratio λ/μ for near incompressibility as Poisson's ratio $\nu \to 0.5$

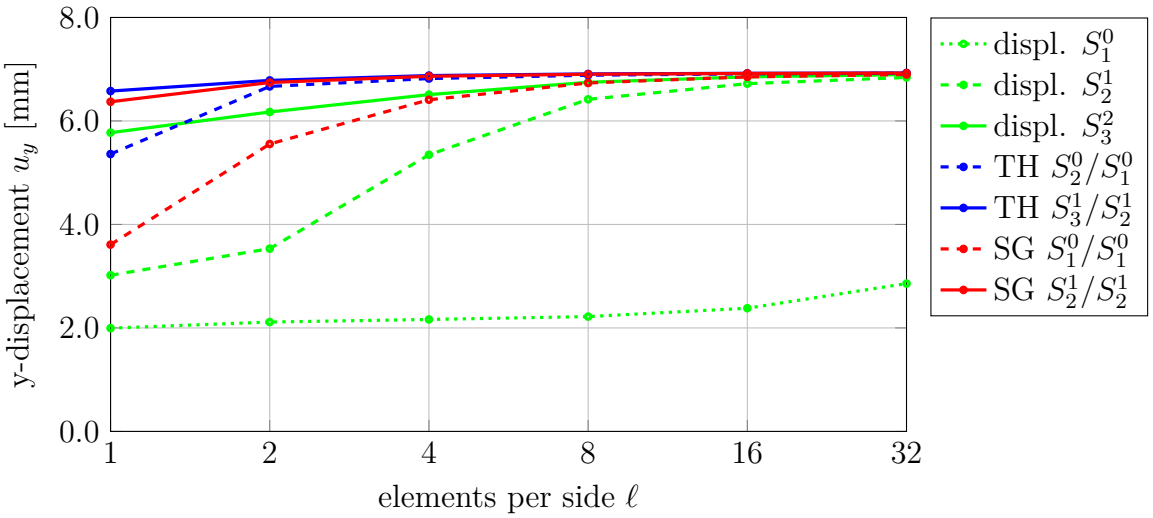

Figure 6.5: $p/h/k$-convergence of y-displacement u_y of Cook's membrane over number of elements per side ℓ for displacement-based and mixed formulations

– while the stress distributions for mixed Taylor-Hood elements are smooth.

Altogether, we have demonstrated the signs of locking of purely-displacement based elements in the near incompressible regime, which are a deterioration of convergence and stress oscillations, and we have seen numerically that mixed methods can resolve this problem.

6.4.2 Nonlinear vibration of a thick rubber cylinder

Having studied the convergence of mixed elements, we now want to move to nonlinear vibration analysis. As an application we choose a thick rubber cylinder with the same geometry, dimensions and symmetry boundary conditions as the one used in Section 3.5.1, Figure 3.6(a).

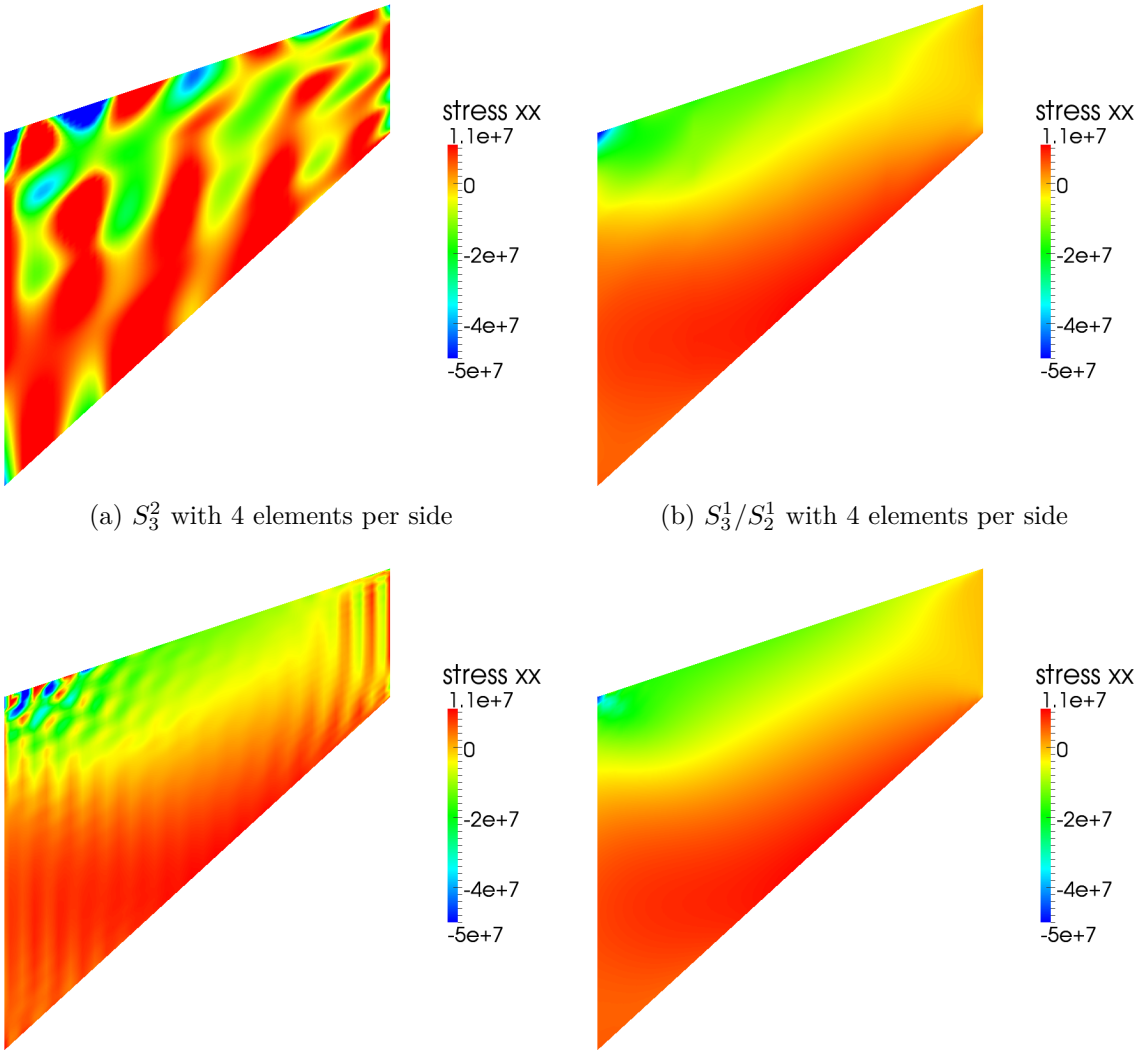

(a) S_3^2 with 4 elements per side

(b) S_3^1/S_2^1 with 4 elements per side

(c) S_3^2 with 16 elements per side

(d) S_3^1/S_2^1 with 16 elements per side

Figure 6.6: Comparison of stress component σ_{xx} for displacement-based S_3^2 and mixed S_3^1/S_2^1 Taylor-Hood element for 4 (top) resp. 16 (bottom) elements per side at $\nu = 0.499$. Displacement-based elements exhibit strong oscillations of stresses

Convergence for static displacement and eigenfrequencies

First we want to check the accuracy and convergence of the mixed and displacement-based formulations and elements for static nonlinear deformation and eigenfrequencies. The results are summarized in Figure 6.7. S_2^1 and S_3^2 refer to displacement-based elements, with $p = 2, 3$ in all three parameter directions, h-refined such that at maximal mesh size parameter h was obtained, and C^1- resp. C^2-continuous at inner knots, since the original geometry did not contain any inner knots. S_2^0/S_1^0 and S_3^1/S_2^1 refer to mixed Taylor-Hood elements, where the displacement space is obtained from the pressure space by p-refinement, with preceding h-refinement to obtain maximal mesh size parameter h. A summary of number of degrees of freedom for these discretizations is given in Table 6.2.

For static nonlinear deformation we assume a vertically directed surface load (Neumann boundary condition) on the outer shell of the cylinder with magnitude -3.0 kN, a constant

h	S_2^1		S_3^2		S_2^0/S_1^0			S_3^1/S_2^1		
	n_u	N	n_u	N	n_u	n_p	N	n_u	n_p	N
0.08	48	144	100	300	48	18	162	144	48	480
0.04	108	324	196	588	108	50	374	400	108	1308
0.02	300	900	484	1452	300	162	1062	1296	300	4188
0.01	1296	3888	1805	5415	1296	867	4755	6936	1296	22104

Table 6.2: Number of control points and degrees of freedom of spline spaces for mixed and displacement-based elements for thick rubber cylinder

Young's modulus $E = 2.432$ MPa and constant, nearly incompressible Poisson's ratio $\nu = 0.495$. The mass density of the rubber material is $\rho = 1905.7$ kg/m^3.

Figure 6.7(a) shows the z-displacement at evaluation point E_2 and Figure 6.7(b) the L^2-norm of displacements for h/k-refinement. With $u_z = -1.78$ cm, the magnitude of the displacement is about the thickness of the cylinder, which is $t = 2.0$ cm. We can observe a very slow convergence of S_2^1 and a faster convergence of other elements, which is in accordance with previous results. Especially the mixed element S_3^1/S_2^1 is very accurate already for the coarsest mesh.

The performance of mixed and displacement-based elements exhibits also a huge difference regarding the convergence behavior of the Newton's method, see Algorithm 1. For displacement-based elements we have to apply load stepping, otherwise the tangent stiffness matrix might become singular within the initial few steps of the Newton algorithm. This behavior seems to become worse with increasing degree p and smaller h, and makes the S_p-elements unreliable. For mixed elements we do not observe any convergence issues.

Furthermore, we also examine the first eigenfrequency f_1 and its frequency-dependent counterpart $f_1(f)$, which is obtained using frequency-dependent Young's modulus $E(f)$ and constant $\nu = 0.495$. The results in Figure 6.8 reveal a very similar convergence behavior as for the static nonlinear displacement. The values converge to $f_1 = 10.79$ Hz and $f_1(f) = 20.85$ Hz.

Nonlinear frequency response

Now we can compare the mixed and displacement-based elements in a nonlinear frequency response analysis with harmonic balance method. We use a visco-hyperelastic Neo-Hookean material and consider the full frequency-dependency of $E(f)$, $\nu(f)$ and also the loss factor $\eta(f)$, see Figure 3.3.

We compute the response amplitudes within the range $10.0 \text{ Hz} \leq f \leq 30.0$ Hz, i.e. around the first frequency-dependent eigenfrequency $f_1(f)$. The magnitude of the surface load is increased on -10.0 kN, since $E(f) \approx 3E(0)$ in the frequency range of interest, and the load is now harmonic in time with a factor $\cos \omega t$.

For the isogeometric discretization we use the elements S_3^2 and S_3^1/S_2^1 for $h = 0.08$, which was the coarsest mesh of our preceding convergence analysis, but already lead to sufficiently accurate results, especially for the mixed method. In the Fourier series ansatz of harmonic balance we include the first two harmonics, i.e. $m = 2$.

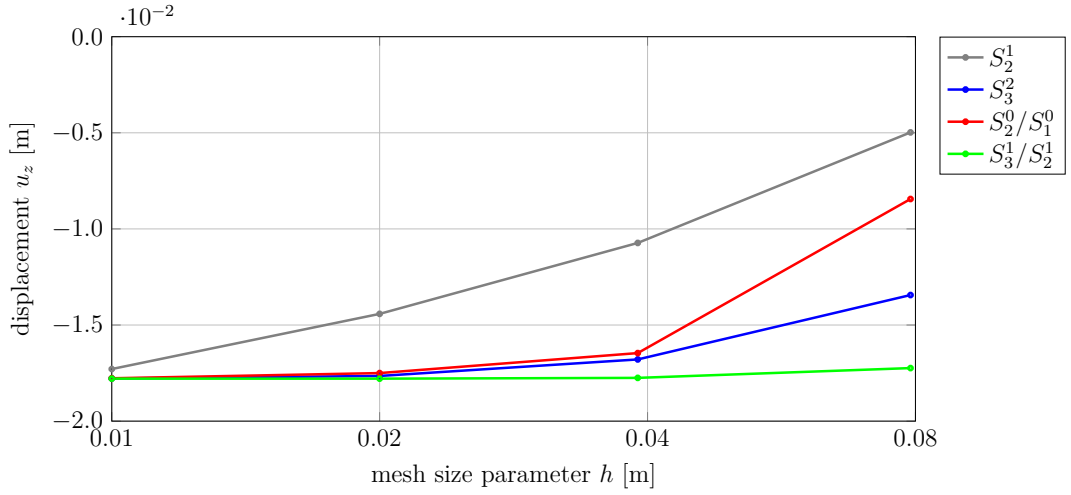

(a) z-displacement at evaluation point

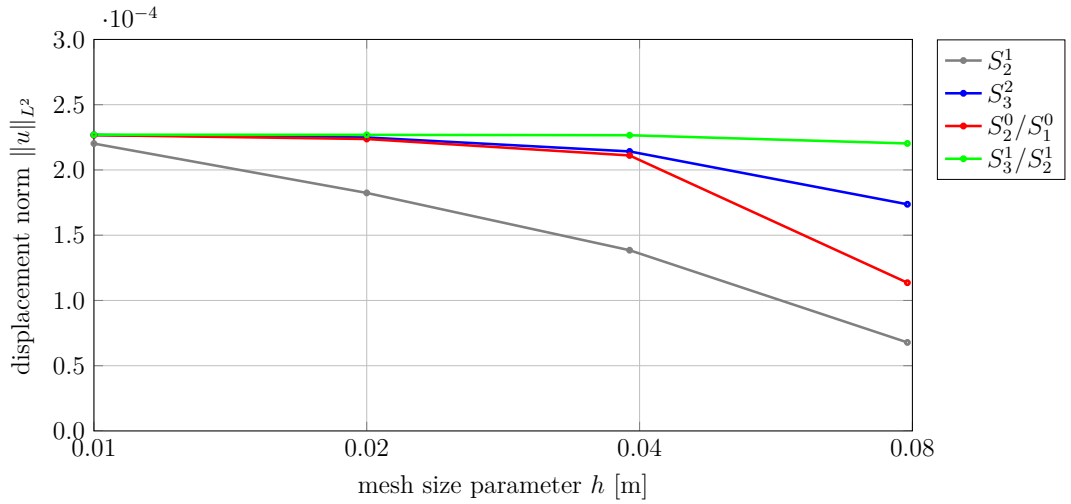

(b) L^2-norm of displacement

Figure 6.7: Convergence of nonlinear displacement for mixed S_{p+1}^{p-1}/S_p^{p-1}- and displacement-based S_p^{p-1}-elements for thick rubber cylinder

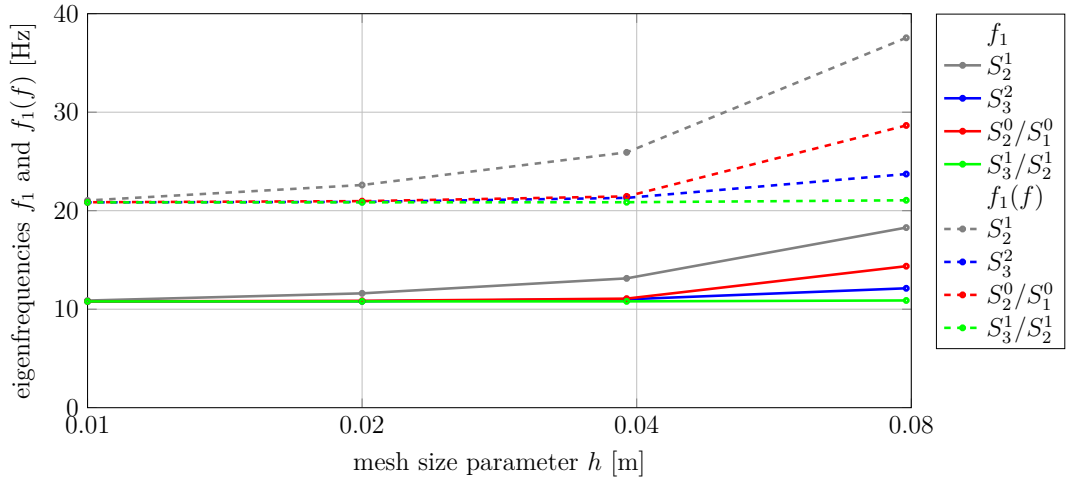

Figure 6.8: Convergence of first eigenfrequency f_1 and freq.-dept. eigenfrequency $f_1(f)$ for mixed and displacement-based elements for thick rubber cylinder

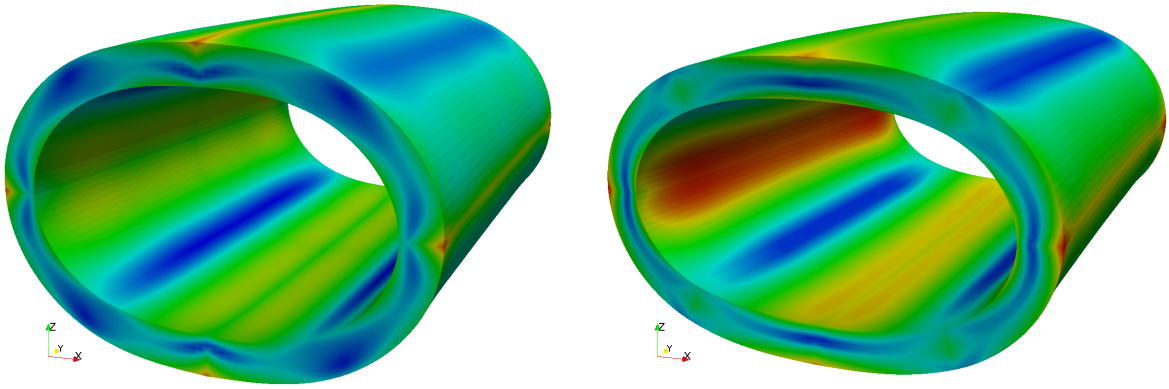

(a) displacement-based S_3^2 element (b) mixed S_3^1/S_2^1 element

Figure 6.9: Deformed rubber cylinder at $f = 20.23$ Hz and non-dimensional time $\tau = \frac{\pi}{2}$, colored by von Mises stress

The frequency response curves of z-amplitudes a_i and -phases ϕ_i at the evaluation point E_2 are plotted in Figure 6.10. Due to the increasing stiffness and strong damping of the viscoelastic material, the amplitude is in general only moderately growing at resonance. However, for the dominating first harmonic, a remarkable difference occurs between the curves of the S_3^1/S_2^1 (solid lines) and the S_3^2 (dashed lines) element. Taking into account the results of the nonlinear static and eigenfrequency analysis, it can be seen that the relative difference between the maxima of the two curves is very similar to the static deformation results, and that the resonance peaks occur at the corresponding frequency-dependent first eigenfrequencies. Thus the approximation errors of displacements and eigenfrequencies are carried over to the results of frequency response analysis. Deviations are also evident for the constant amplitude a_0 and the second harmonic a_2, which reflect the nonlinearity of the deformation resp. vibration, as well as the phases ϕ_1 and ϕ_2.

Figure 6.9 shows the deformed rubber cylinder during a vibration at $f = 20.23$ Hz, i.e. at peak of resonance, at non-dimensional time $\tau = \frac{\pi}{2}$. Comparison of the displacement-based and mixed element visualizes a difference in amplitudes and thus also von Mises stresses, which was already indicated in Figure 6.10.

Also here convergence of the Newton's method of an harmonic balance step, see Algorithm 3, is more critical for the displacement-based method than for the mixed method. Especially the initial frequency step for large amplitude vibrations might fail, as we have already observed it above for the static displacements.

Furthermore, we have also tried the modal derivative reduction method in combination with the mixed method in a first shot. Figure 6.10 includes the results for a reduction with $r_d = 10$ eigenmodes and corresponding modal derivatives ($r = 65$) as dotted lines. In the response curves the correspondence of amplitudes a_0, a_1 and a_2 and phases ϕ_1 and ϕ_2 with the ones obtained from the full solution is in general very good for all harmonics and over the whole frequency range.

Altogether, with this example we have demonstrated that mixed methods can be easily implemented inside the harmonic balance framework. We have shown that isogeometric mixed methods provide much more accurate and reliable results for nonlinear frequency

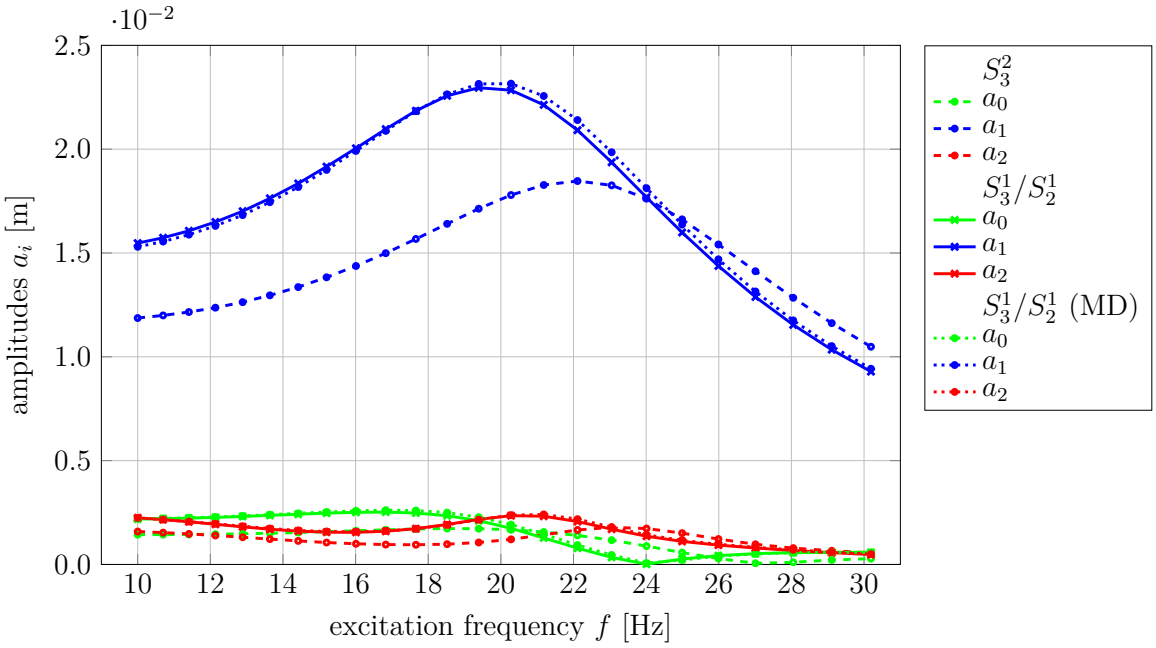

(a) Amplitudes a_i over excitation frequency f

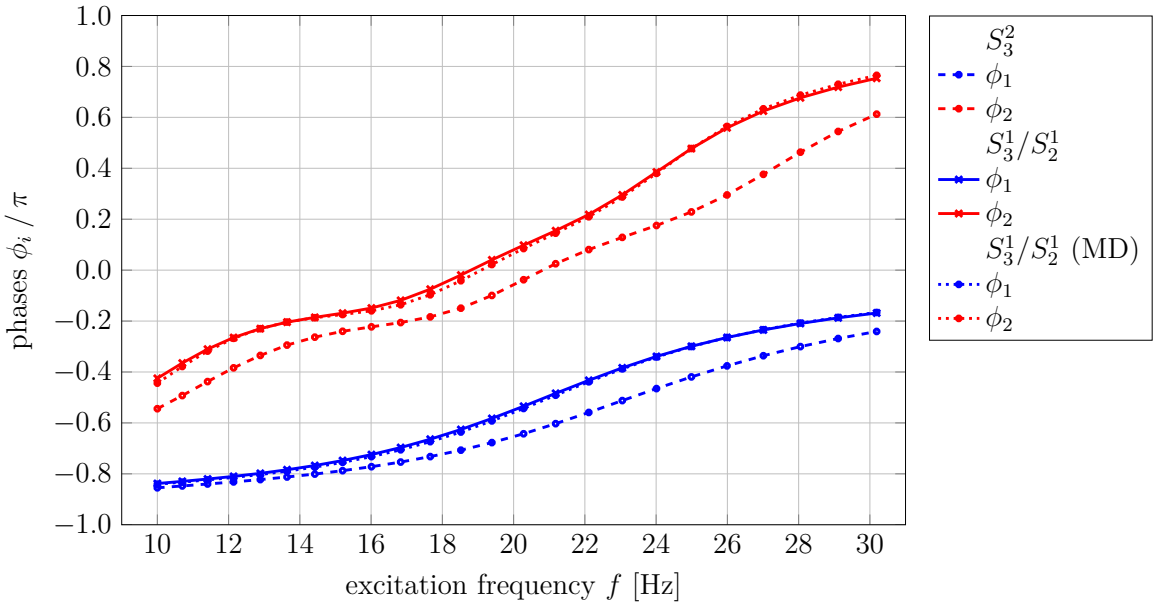

(b) Phases ϕ_i over excitation frequency f

Figure 6.10: Nonlinear frequency response curves for thick rubber cylinder. Amplitudes and phases of harmonics at evaluation point for displacement-based S_3^2-element (dashed), mixed S_3^1/S_2^1-formulation (solid line), and mixed formulation with reduction with $r_d = 10,\ r = 65$ (MD, dotted line)

response analysis with nearly incompressible materials than displacement-based methods. Reduction with modal derivatives seems to work well in the setting of mixed elements and visco-hyperelasticity, too, but as amplitudes are still moderate here due to damping effects, this has to be investigated in more detail in the future.

6.5 Summary

Rubber components are an important application of the nonlinear frequency analysis method developed over preceding chapters, as they can undergo large amplitude vibrations.

However, rubber is a nearly incompressible material and to avoid inaccuracy of numerical simulations the phenomenon of volumetric locking has to be considered. Thus we have first described and explained volumetric locking and reviewed possible cures.

In the context of isogeometric analysis, mixed finite element methods are an auspicious method for preventing locking in both linear and nonlinear near incompressible elasticity. We have outlined the use of two particular isogeometric mixed element types, namely Taylor-Hood and subgrid elements. Both are based on a two-field approach with independent discretizations of displacement field and a pressure-like variable.

Then we have presented the successful integration of these mixed formulations for near incompressible, visco-hyperelastic materials into HBM.

Using computational examples, we could demonstrate that Taylor-Hood and subgrid elements both perform well also in the nonlinear near incompressible regime. In contrast to purely displacement-based formulations, they prevent locking and exhibit a fast convergence behavior without stress oscillations. We could also confirm that the advantages of mixed methods carry over to nonlinear vibration analysis, where frequency response curves are captured much more accurately using the mixed methods. Finally, we have also tested the modal derivative reduction method and it indicated to be very accurate also for near incompressible applications.

7 Conclusion

7.1 Summary

In this thesis we have developed a novel method for the computational analysis of nonlinear steady-state frequency response, which is capable of simulating vibrational behavior of large-scale applications in solid mechanics. It is mainly based on three pillars: a spatial semi-discretization of the nonlinear elastodynamic partial differential equation using isogeometric finite elements; model order reduction of the resulting ordinary differential equation system using a projection method with so-called modal derivatives; and a frequency-domain solution of the reduced nonlinear ODE system using the method of harmonic balance.

Isogeometric finite elements based on splines have proven to be advantageous compared to classical finite elements with Lagrange polynomials due to their higher inter-element continuity, especially in linear vibration analysis and computation of eigenfrequencies. Using the nonlinear-Euler Bernoulli beam structural model, we could show that these properties also carry over to nonlinear frequency analysis. Although IGA claims to close the gap between computer-aided design and computational simulation, it is necessary to generate analysis-suitable volume models from CAD surface models. For complex, real-life engineering geometries this leads to multi-patch volume parameterizations. Many techniques for implementation and coupling of multi-patch parameterizations have been established already, but here we deal with them for the first time in the setting of 3-dimensional nonlinear continuum mechanics, with large deformations, visco-hyperelastic materials, and larger scale applications.

The harmonic balance method can be used for nonlinear modal and frequency response analysis of nonlinear ODE and DAE systems. It is based on a transformation from the time to the frequency domain and approximates the solution as a truncated Fourier series. Here we apply it successfully for nonlinear steady-state frequency response analysis of the discretized equation of motion coming from an isogeometric finite element discretization of nonlinear visco-hyperelasticity. With our numerical examples we could highlight the benefits of nonlinear frequency analysis and the differences to linear results. Furthermore, we could observe exponential convergence of this spectral method with respect to the number of Fourier harmonic terms.

However, the Fourier series expansion of each spatial DOF within the harmonic balance method leads to a blow-up of degrees of freedom of the final nonlinear equation system to be solved iteratively. As the resulting linear systems are not only large, but also of low

sparsity, this is a very limiting factor for the applicability of the method for large-scale problems. Thus we have introduced a model order reduction method into the nonlinear frequency analysis framework, which is based on a linear projection onto a subspace spanned by linear eigenmodes and modal derivatives, providing a second-order enhancement of the projection basis. We have extended the motivation and theoretical foundation of the concept of modal derivatives and could show that it can also be applied to continuous problems. Numerical results revealed that the vibrational behavior, i.e. resonance frequencies and response amplitudes, can be very well reproduced for moderately large amplitudes and nonlinearities. Nonlinear frequency analysis becomes even feasible for realistic applications with large spatial discretizations, as the effort for numerical solution of the harmonic balance equation system is significantly reduced.

As mixed finite element methods are a means for solving incompressible elasticity problems and a cure of volumetric locking in the near incompressible setting, which is particularly important for the simulation of rubber components, we have also included them into our nonlinear frequency analysis framework. We have investigated the usage and convergence properties of two isogeometric element types, Taylor-Hood and subgrid, in nonlinear incompressible elasticity. We could show that these mixed elements can be easily implemented also into the harmonic balance method for nonlinear frequency analysis and provide much higher accuracy for near incompressible vibrations.

7.2 Outlook

We have applied the isogeometric discretization and harmonic balance frequency analysis method to two mechanical models, namely the nonlinear Euler-Bernoulli beam and 3-dimensional nonlinear continuum mechanics. As isogeometric methods have shown to be advantageous also for application to other structural models, the framework could be extended to Timoshenko beams, Cosserat rods, Kirchhoff-Love shells and Reissner-Mindlin plates [18, 73]. This might open the scope to many more interesting engineering applications of our nonlinear frequency analysis framework.

In realistic applications with large amplitude vibrations of rubber components self-contact might occur, which is a field where the benefits of isogeometric methods have been explored already and could be implemented to extend the usability of the method.

An interesting feature of isogeometric methods is also the combination with shape optimization, where the consistent geometry representation allows a direct optimization of the spline control points. Shape optimization methods could be developed, which take the characteristics of nonlinear frequency analysis, such as resonance frequencies, amplitudes, stress maxima or vibration energy, as objective functions or constraints.

From the algorithmic point of view, a continuation method could be added to harmonic balance in order to be able to find more complex solution paths with turning points and bifurcations. Then the solution of homogeneous problems without external excitation for nonlinear normal modes and self-excitation resonance frequencies would be possible as well.

The proposed reduction method makes nonlinear frequency response analysis feasible for 3-dimensional structural problems, but it still remains a time-consuming task. Especially for very large spatial discretizations, a speed-up of the sampling process is necessary, since currently the full residual vector and tangent matrix have to be assembled for every

sample. A complexity reduction might be achieved by methods such as Discrete Empirical Interpolation [34]. It might also be possible to develop a complexity reduction method based on the modal derivative concept.

We also see a great potential for the application of the reduction method using modal derivatives for other applications, such as DAE systems in multi-body dynamics or simulation of networks and electric circuits.

A Appendix

A.1 Frequency-dependent eigenvalue problem

In Section 4.1.1 we have introduced an iterative eigenvalue problem for computing eigenfrequencies of structures with frequency-dependent material properties.

Now we want to explore the properties of this eigenvalue problem for the special case of a quasi-linear frequency-depedency of the stiffness matrix:

$$\mathbf{K}(\omega) = \frac{E(\omega)}{E_0}\mathbf{K}_0 \ ,$$

where $E_0 = E(0)$ and $\mathbf{K}_0 = \mathbf{K}(0)$.

Assumption A.1. *The frequency-dependent Young's modulus $E(\omega)$ is a nonlinear function of ω with the following properties:*

$$\begin{gathered} E : [0,\infty) \to (0,\infty) \ , \\ \frac{dE}{d\omega}(\omega) \geq 0 \ , \\ \inf_{\omega} E(\omega) = E(0) = E_0 \ , \\ \sup_{\omega} E(\omega) = \lim_{\omega\to\infty} E(\omega) = E_\infty \ . \end{gathered}$$

Theorem A.1. *When Assumption A.1 holds, the solutions $\hat{\omega}_k,\ \hat{\boldsymbol{\phi}}_k,\ k = 1,\ldots,N$ of the frequency-dependent eigenvalue problem* (4.13) *are*

$$\hat{\boldsymbol{\phi}}_k = \boldsymbol{\phi}_k \quad \wedge \quad \hat{\omega}_k^2 = \omega_k^2 \, \frac{E(\hat{\omega}_k)}{E_0} \ . \tag{A.1}$$

Proof. From the linear eigenvalue problem for eigenfrequencies ω_k and eigenmodes $\boldsymbol{\phi}_k$:

$$\omega_k^2 \, \mathbf{M} \, \boldsymbol{\phi}_k = \mathbf{K}_0 \, \boldsymbol{\phi}_k \ ,$$

we get by scalar multiplication with $\frac{E(\omega)}{E_0}$ for arbitrary ω:

$$\omega_k^2 \, \frac{E(\omega)}{E_0} \, \mathbf{M} \, \boldsymbol{\phi}_k = \mathbf{K}(\omega) \, \boldsymbol{\phi}_k \ . \tag{A.2}$$

In (4.13) we want to find $\hat{\omega}_k$ and $\hat{\boldsymbol{\phi}}_k$ such that:

$$\hat{\omega}_k^2 \, \mathbf{M} \, \hat{\boldsymbol{\phi}}_k = \mathbf{K}(\hat{\omega}_k) \, \hat{\boldsymbol{\phi}}_k \; ,$$

i.e. $\hat{\omega}_k$ shall be an eigenfrequency for the eigenvalue problem with $\mathbf{M}$ and $\mathbf{K}(\hat{\omega}_k)$ with eigenmode $\hat{\boldsymbol{\phi}}_k$, and comparison with (A.2) shows that it must hold:

$$\hat{\boldsymbol{\phi}}_k = \boldsymbol{\phi}_k \quad \wedge \quad \hat{\omega}_k^2 = \omega_k^2 \, \frac{E(\hat{\omega}_k)}{E_0} \; .$$

□

Thus with (A.1) we have found a scalar nonlinear equation for the frequency-dependent eigenfrequency $\hat{\omega}_k$, which is already a fixed-point equation, and can solve this (much more simpler) problem compared to the iterative eigenvalue problem (4.13).

Theorem A.2. *There exists a unique solution* $\hat{\omega}_k, \; k = 1, \ldots, N$ *of*

$$\hat{\omega}_k = \omega_k \sqrt{\frac{E(\hat{\omega}_k)}{E_0}} \tag{A.3}$$

for $\omega_k < \frac{2\,E_0}{\lambda_E}$ *with* $\lambda_E = \sup_\omega \frac{dE}{d\omega}$.

Proof. The existence and uniqueness of $\hat{\omega}_k$ is given by the Banach fixed-point theorem once we can show that the map $T_k(\omega) = \omega_k \sqrt{\frac{E(\omega)}{E_0}}$ defined by (A.3) is a contraction:

$$\begin{aligned}
|T_k(\omega_1) - T_k(\omega_2)| &= \left| \omega_k \sqrt{\frac{E(\omega_1)}{E_0}} - \omega_k \sqrt{\frac{E(\omega_2)}{E_0}} \right| \\
&= \frac{\omega_k}{\sqrt{E_0}} \left| \sqrt{E(\omega_1)} - \sqrt{E(\omega_2)} \right| \\
&= \frac{\omega_k}{\sqrt{E_0}} \frac{1}{\sqrt{E(\omega_1)} + \sqrt{E(\omega_2)}} \, |E(\omega_1) - E(\omega_2)| \\
&\leq \frac{\omega_k}{2\,E_0} \, |E(\omega_1) - E(\omega_2)| \\
&\leq \frac{\omega_k}{2\,E_0} \, \lambda_E \; |\omega_1 - \omega_2| \; .
\end{aligned}$$

For $T_k(\omega)$ to be a contraction it must hold:

$$\frac{\omega_k}{2\,E_0} \, \lambda_E < 1 \quad \Leftrightarrow \quad \omega_k < \frac{2\,E_0}{\lambda_E} \; .$$

Thus the solution is guaranteed by Banach fixed-point theorem for sufficiently small k resp. ω_k. □

Theorem A.3. *Properties of* $\hat{\omega}_k, \; k = 1, \ldots, N$*:*

$$\begin{aligned}
&\hat{\omega}_k > \omega_k \; , \\
&\hat{\omega}_{k+1} \geq \hat{\omega}_k \;\; \textit{for} \;\; \omega_{k+1} \geq \omega_k \; .
\end{aligned} \tag{A.4}$$

Proof. From the Banach fixed-point theorem it follows that for arbitrary $\hat{\omega}_k^0$ the sequence $\hat{\omega}_k^s = T_k(\hat{\omega}_k^{s-1})$ converges $\hat{\omega}_k^s \to \hat{\omega}_k$, when the contraction criterium $\omega_k < \frac{2\,E_0}{\lambda_E}$ is fulfilled.

When we use $\hat{\omega}_k^0 = \omega_k$, it follows

$$\hat{\omega}_k^1 = \omega_k \sqrt{\frac{E(\hat{\omega}_k^0)}{E_0}} = \omega_k \sqrt{\frac{E(\omega_k)}{E_0}} > \omega_k = \hat{\omega}_k^0 \ ,$$

since $\omega_k > 0$ and inductively that

$$\hat{\omega}_k^{s+1} > \hat{\omega}_k^s > \omega_k \ .$$

For the first inequality we then have

$$\hat{\omega}_k = \lim_{s\to\infty} \hat{\omega}_k^s = \lim_{s\to\infty} \omega_k \sqrt{\frac{E(\hat{\omega}_k^{s-1})}{E_0}} > \omega_k \ ,$$

since $E(\hat{\omega}_k^{s-1}) > E_0 = E(0)$.

For the second inequality we use induction starting with

$$\hat{\omega}_{k+1}^0 = \omega_{k+1} \geq \omega_k = \hat{\omega}_k^0 \ .$$

It follows for $s \to s+1$:

$$\frac{\hat{\omega}_{k+1}^{s+1}}{\hat{\omega}_k^{s+1}} = \sqrt{\frac{E(\hat{\omega}_{k+1}^s)}{E(\hat{\omega}_k^s)}} \geq 1 \ ,$$

since the induction assumption is $\hat{\omega}_{k+1}^s \geq \hat{\omega}_k^s$ and $E(\omega)$ is montonously increasing. Thus we have

$$\frac{\hat{\omega}_{k+1}}{\hat{\omega}_k} = \lim_{s\to\infty} \frac{\hat{\omega}_{k+1}^s}{\hat{\omega}_k^s} \geq 1 \ .$$

□

Remark A.1 (Computing $\hat{\omega}_k$)**.** *$\hat{\omega}_k$ can be compute from* (A.1) *using the fixed-point iteration as in the proof above with linear convergence, or also use a Newton's method with quadratic convergence:*

$$\begin{aligned} r(\omega) &= \omega - \omega_k \sqrt{\frac{E(\omega)}{E_0}} \ , \\ \frac{dr}{d\omega}(\omega) &= 1 - \omega_k \frac{1}{2\,E_0} \sqrt{\frac{E_0}{E(\omega)}} \frac{dE}{d\omega}(\omega) \ . \end{aligned} \tag{A.5}$$

A.2 Modal derivatives of nonlinear Euler-Bernoulli beam

Here we present the proof of Theorem 5.4 of Section 5.3.3.

Proof. We derive the modal derivatives of Problem 5.3 by the procedure presented in (5.2.1):

The external forces f and g are expressed in terms of the solution of the eigenvalue problem (5.68):

$$\begin{aligned} f = f(\mathbf{p}) &= \sum_j \omega_j^{u2}\, \phi_j^u\, p_j &&= \sum_j j^2\, \sqrt{2/\pi}\, \sin(jx)\, p_j, \\ g = g(\mathbf{q}) &= \sum_k \omega_k^{w2}\, \phi_k^w\, q_k &&= \sum_k k^4\, \sqrt{2/\pi}\, \sin(kx)\, q_k. \end{aligned} \tag{A.6}$$

Thus it is $u = u(\mathbf{p}, \mathbf{q}),\ w = w(\mathbf{p}, \mathbf{q})$ for the exact solutions of (5.66).

From the first equation in (5.66) it follows by $\frac{\partial}{\partial p_j}$:

$$-\left(\frac{\partial u''}{\partial p_j} + \frac{\partial w'}{\partial p_j} w'' + \frac{\partial w''}{\partial p_j} w'\right) = j^2\, \sqrt{2/\pi}\, \sin(jx) \tag{A.7}$$

and evaluation at $\mathbf{p} = \mathbf{q} = \mathbf{0}$ yields:

$$-\left.\frac{\partial u''}{\partial p_j}\right|_0 = j^2\, \sqrt{2/\pi}\, \sin(jx) \tag{A.8}$$

and it follows by integration w.r.t. x:

$$\left.\frac{\partial u}{\partial p_j}\right|_0 = \sqrt{2/\pi}\, \sin(jx) = \phi_j^u. \tag{A.9}$$

Note that here and in the following integration constants vanish due to the boundary conditions for u and w (third equation in (5.66)).

From the first equation in (5.66) it follows by $\frac{\partial}{\partial q_k}$:

$$-\left(\frac{\partial u''}{\partial q_k} + \frac{\partial w'}{\partial q_k} w'' + \frac{\partial w''}{\partial q_k} w'\right) = 0 \tag{A.10}$$

and evaluation at $\mathbf{p} = \mathbf{q} = \mathbf{0}$ yields:

$$-\left.\frac{\partial u''}{\partial q_k}\right|_0 = 0 \tag{A.11}$$

and it follows by integration w.r.t. x:

$$\left.\frac{\partial u}{\partial q_k}\right|_0 = 0. \tag{A.12}$$

From the second equation in (5.66) it follows by $\frac{\partial}{\partial p_j}$:

$$\begin{aligned} -\left(\frac{\partial u'}{\partial p_j}+\frac{\partial w'}{\partial p_j}w'\right)w''-\left(u'+\frac{1}{2}w'^2\right)\frac{\partial w''}{\partial p_j} \\ -\left(\frac{\partial u''}{\partial p_j}+\frac{\partial w'}{\partial p_j}w''+\frac{\partial w''}{\partial p_j}w'\right)w'-\left(u''+w'w''\right)\frac{\partial w'}{\partial p_j} \\ +\frac{\partial w^{IV}}{\partial p_j}=0 \end{aligned} \tag{A.13}$$

and evaluation at $\mathbf{p}=\mathbf{q}=\mathbf{0}$ yields:

$$\left.\frac{\partial w^{IV}}{\partial p_j}\right|_0=0 \tag{A.14}$$

and it follows by integration w.r.t. x:

$$\left.\frac{\partial w}{\partial p_j}\right|_0=0. \tag{A.15}$$

From the second equation in (5.66) it follows by $\frac{\partial}{\partial q_k}$:

$$\begin{aligned} -\left(\frac{\partial u'}{\partial q_k}+\frac{\partial w'}{\partial q_k}w'\right)w''-\left(u'+\frac{1}{2}w'^2\right)\frac{\partial w''}{\partial q_k} \\ -\left(\frac{\partial u''}{\partial q_k}+\frac{\partial w'}{\partial q_k}w''+\frac{\partial w''}{\partial q_k}w'\right)w'-\left(u''+w'w''\right)\frac{\partial w'}{\partial q_k} \\ +\frac{\partial w^{IV}}{\partial q_k}=k^4\sqrt{2/\pi}\,\sin(kx) \end{aligned} \tag{A.16}$$

and evaluation at $\mathbf{p}=\mathbf{q}=\mathbf{0}$ yields:

$$\left.\frac{\partial w^{IV}}{\partial q_k}\right|_0=k^4\sqrt{2/\pi}\,\sin(kx) \tag{A.17}$$

and it follows by integration w.r.t. x:

$$\left.\frac{\partial w}{\partial q_k}\right|_0=\sqrt{2/\pi}\,\sin(kx)=\phi_k^w. \tag{A.18}$$

As expected, we have so far the results that the derivatives of the solutions w.r.t. the modal participation factors correspond to the linear eigenfunctions:

$$\left.\frac{\partial u}{\partial p_j}\right|_0=\phi_j^u,\quad \left.\frac{\partial u}{\partial q_k}\right|_0=0,\quad \left.\frac{\partial w}{\partial p_j}\right|_0=0,\quad \left.\frac{\partial w}{\partial q_k}\right|_0=\phi_k^w. \tag{A.19}$$

Now we continue with the second derivatives of (5.66) in order to determine the modal derivatives:

We apply $\frac{\partial}{\partial p_r}$ to (A.7):

$$\frac{\partial^2 u''}{\partial p_j \partial p_r} + \frac{\partial^2 w'}{\partial p_j \partial p_r} w'' + \frac{\partial w'}{\partial p_j}\frac{\partial w''}{\partial p_r} + \frac{\partial^2 w''}{\partial p_j \partial p_r} w' + \frac{\partial w''}{\partial p_j}\frac{\partial w'}{\partial p_r} = 0 \tag{A.20}$$

Evaluation at $\mathbf{p} = \mathbf{q} = \mathbf{0}$ yields:

$$\left.\frac{\partial^2 u''}{\partial p_j \partial p_r}\right|_0 = 0 \tag{A.21}$$

and it follows by integration w.r.t. x:

$$\left.\frac{\partial^2 u}{\partial p_j \partial p_r}\right|_0 = 0. \tag{A.22}$$

We apply $\frac{\partial}{\partial q_s}$ to (A.7):

$$\frac{\partial^2 u''}{\partial p_j \partial q_s} + \frac{\partial^2 w'}{\partial p_j \partial q_s} w'' + \frac{\partial w'}{\partial p_j}\frac{\partial w''}{\partial q_s} + \frac{\partial^2 w''}{\partial p_j \partial q_s} w' + \frac{\partial w''}{\partial p_j}\frac{\partial w'}{\partial q_s} = 0 \tag{A.23}$$

Evaluation at $\mathbf{p} = \mathbf{q} = \mathbf{0}$ yields:

$$\left.\frac{\partial^2 u''}{\partial p_j \partial q_s}\right|_0 = 0 \tag{A.24}$$

and it follows by integration w.r.t. x:

$$\left.\frac{\partial^2 u}{\partial p_j \partial q_s}\right|_0 = 0. \tag{A.25}$$

We apply $\frac{\partial}{\partial q_s}$ to (A.10):

$$\frac{\partial^2 u''}{\partial q_k \partial q_s} + \frac{\partial^2 w'}{\partial q_k \partial q_s} w'' + \frac{\partial w'}{\partial q_k}\frac{\partial w''}{\partial q_s} + \frac{\partial^2 w''}{\partial q_k \partial q_s} w' + \frac{\partial w''}{\partial q_k}\frac{\partial w'}{\partial q_s} = 0 \tag{A.26}$$

Evaluation at $\mathbf{p} = \mathbf{q} = \mathbf{0}$ yields:

$$\begin{aligned} &\left.\frac{\partial^2 u''}{\partial q_k \partial q_s}\right|_0 + \left.\frac{\partial w'}{\partial q_k}\frac{\partial w''}{\partial q_s}\right|_0 + \left.\frac{\partial w''}{\partial q_k}\frac{\partial w'}{\partial q_s}\right|_0 = 0 \\ &\qquad \Leftrightarrow \qquad \left.\frac{\partial^2 u''}{\partial q_k \partial q_s}\right|_0 = \frac{2}{\pi}\left(ks^2\cos(kx)\sin(sx) + k^2 s\sin(kx)\cos(sx)\right) \end{aligned} \tag{A.27}$$

and it follows by integration w.r.t. x:

$$\left.\frac{\partial^2 u}{\partial q_k \partial q_s}\right|_0 = -\frac{ks}{\pi}\left(\frac{\sin((k-s)x)}{k-s} + \frac{\sin((k+s)x)}{k+s}\right). \tag{A.28}$$

We apply $\frac{\partial}{\partial p_r}$ to (A.13):

$$\begin{aligned}
&-\left(\frac{\partial^2 u''}{\partial p_j \partial p_r}+\frac{\partial w'}{\partial p_j}\frac{\partial w'}{\partial p_r}+\frac{\partial^2 w'}{\partial p_j \partial p_r}w'\right)w''-\left(\frac{\partial u'}{\partial p_j}+\frac{\partial w'}{\partial p_j}w'\right)\frac{\partial w''}{\partial p_r}\\
&\qquad-\left(\frac{\partial u'}{\partial p_r}+\frac{\partial w'}{\partial p_r}w'\right)\frac{\partial w''}{\partial p_j}-\left(u'+\frac{1}{2}w'^2\right)\frac{\partial^2 w''}{\partial p_j \partial p_r}\\
&-\left(\frac{\partial^2 u''}{\partial p_j \partial p_r}+\frac{\partial^2 w'}{\partial p_j \partial p_r}w''+\frac{\partial w'}{\partial p_j}\frac{\partial w''}{\partial p_r}+\frac{\partial^2 w''}{\partial p_j \partial p_r}w'+\frac{\partial w''}{\partial p_j}\frac{\partial w'}{\partial p_r}\right)w'\\
&\qquad-\left(\frac{\partial u''}{\partial p_j}+\frac{\partial w'}{\partial p_j}w''+\frac{\partial w''}{\partial p_j}w'\right)\frac{\partial w'}{\partial p_r}\\
&\qquad-\left(\frac{\partial u''}{\partial p_r}+\frac{\partial w'}{\partial p_r}w''+\frac{\partial w''}{\partial p_r}w'\right)\frac{\partial w'}{\partial p_j}-\left(u''+w'w''\right)\frac{\partial^2 w'}{\partial p_j \partial p_r}\\
&\qquad+\frac{\partial^2 w^{IV}}{\partial p_j \partial p_r}=0.
\end{aligned}\tag{A.29}$$

Evaluation at $\mathbf{p}=\mathbf{q}=\mathbf{0}$ yields:

$$\left.\frac{\partial^2 w^{IV}}{\partial p_j \partial p_r}\right|_0=0 \tag{A.30}$$

and it follows by integration w.r.t. x:

$$\left.\frac{\partial^2 w}{\partial p_j \partial p_r}\right|_0=0. \tag{A.31}$$

We apply $\frac{\partial}{\partial q_s}$ to (A.13):

$$\begin{aligned}
&-\left(\frac{\partial^2 u''}{\partial p_j \partial q_s}+\frac{\partial w'}{\partial p_j}\frac{\partial w'}{\partial q_s}+\frac{\partial^2 w'}{\partial p_j \partial q_s}w'\right)w''-\left(\frac{\partial u'}{\partial p_j}+\frac{\partial w'}{\partial p_j}w'\right)\frac{\partial w''}{\partial q_s}\\
&\qquad-\left(\frac{\partial u'}{\partial q_s}+\frac{\partial w'}{\partial q_s}w'\right)\frac{\partial w''}{\partial p_j}-\left(u'+\frac{1}{2}w'^2\right)\frac{\partial^2 w''}{\partial p_j \partial q_s}\\
&-\left(\frac{\partial^2 u''}{\partial p_j \partial q_s}+\frac{\partial^2 w'}{\partial p_j \partial q_s}w''+\frac{\partial w'}{\partial p_j}\frac{\partial w''}{\partial q_s}+\frac{\partial^2 w''}{\partial p_j \partial q_s}w'+\frac{\partial w''}{\partial p_j}\frac{\partial w'}{\partial q_s}\right)w'\\
&\qquad-\left(\frac{\partial u''}{\partial p_j}+\frac{\partial w'}{\partial p_j}w''+\frac{\partial w''}{\partial p_j}w'\right)\frac{\partial w'}{\partial q_s}\\
&\qquad-\left(\frac{\partial u''}{\partial q_s}+\frac{\partial w'}{\partial q_s}w''+\frac{\partial w''}{\partial q_s}w'\right)\frac{\partial w'}{\partial p_j}-\left(u''+w'w''\right)\frac{\partial^2 w'}{\partial p_j \partial q_s}\\
&\qquad+\frac{\partial^2 w^{IV}}{\partial p_j \partial q_s}=0.
\end{aligned}\tag{A.32}$$

Evaluation at $\mathbf{p} = \mathbf{q} = \mathbf{0}$ yields:

$$-\left.\frac{\partial u'}{\partial p_j}\frac{\partial w''}{\partial q_s}\right|_0 - \left.\frac{\partial u''}{\partial p_j}\frac{\partial w'}{\partial q_s}\right|_0 + \left.\frac{\partial^2 w^{IV}}{\partial p_j \partial q_s}\right|_0 = 0 \tag{A.33}$$

$$\Leftrightarrow \qquad \left.\frac{\partial^2 w^{IV}}{\partial p_j \partial q_s}\right|_0 = -\frac{2}{\pi}\left(js^2\cos(jx)\sin(sx) + j^2 s\sin(jx)\cos(x)\right) \tag{A.34}$$

and it follows by integration w.r.t. x:

$$\left.\frac{\partial^2 w}{\partial p_j \partial q_s}\right|_0 = \frac{js}{\pi}\left(\frac{\sin((j-s)x)}{j-s} + \frac{\sin((j+s)x)}{j+s}\right). \tag{A.35}$$

We apply $\frac{\partial}{\partial q_s}$ to (A.16):

$$\begin{aligned}
&-\left(\frac{\partial^2 u''}{\partial q_k \partial q_s} + \frac{\partial w'}{\partial q_k}\frac{\partial w'}{\partial q_s} + \frac{\partial^2 w'}{\partial q_k \partial q_s}w'\right)w'' - \left(\frac{\partial u'}{\partial q_k} + \frac{\partial w'}{\partial q_k}w'\right)\frac{\partial w''}{\partial q_s} \\
&\qquad - \left(\frac{\partial u'}{\partial q_s} + \frac{\partial w'}{\partial q_s}w'\right)\frac{\partial w''}{\partial q_k} - \left(u' + \frac{1}{2}w'^2\right)\frac{\partial^2 w''}{\partial q_k \partial q_s} \\
&-\left(\frac{\partial^2 u''}{\partial q_k \partial q_s} + \frac{\partial^2 w'}{\partial q_k \partial q_s}w'' + \frac{\partial w'}{\partial q_k}\frac{\partial w''}{\partial q_s} + \frac{\partial^2 w''}{\partial q_k \partial q_s}w' + \frac{\partial w''}{\partial q_k}\frac{\partial w'}{\partial q_s}\right)w' \\
&\qquad - \left(\frac{\partial u''}{\partial q_k} + \frac{\partial w'}{\partial q_k}w'' + \frac{\partial w''}{\partial q_k}w'\right)\frac{\partial w'}{\partial q_s} \\
&\qquad - \left(\frac{\partial u''}{\partial q_s} + \frac{\partial w'}{\partial q_s}w'' + \frac{\partial w''}{\partial q_s}w'\right)\frac{\partial w'}{\partial q_k} - (u'' + w'w'')\frac{\partial^2 w'}{\partial q_k \partial q_s} \\
&\qquad + \frac{\partial^2 w^{IV}}{\partial q_k \partial q_s} = 0.
\end{aligned} \tag{A.36}$$

Evaluation at $\mathbf{p} = \mathbf{q} = \mathbf{0}$ yields:

$$\left.\frac{\partial^2 w^{IV}}{\partial q_k \partial q_s}\right|_0 = 0 \tag{A.37}$$

and it follows by integration w.r.t. x:

$$\left.\frac{\partial^2 w}{\partial q_k \partial q_s}\right|_0 = 0. \tag{A.38}$$

All in all we have:

$$
\begin{aligned}
\frac{\partial \phi_j^u}{\partial p_r} &= \left.\frac{\partial^2 u}{\partial p_j \partial p_r}\right|_0 = 0, \\
\frac{\partial \phi_j^u}{\partial q_s} &= \left.\frac{\partial^2 u}{\partial p_j \partial q_s}\right|_0 = 0, \\
&\left.\frac{\partial^2 u}{\partial q_k \partial p_r}\right|_0 = 0, \\
&\left.\frac{\partial^2 u}{\partial q_k \partial q_s}\right|_0 = -\frac{ks}{\sqrt{2\pi}}\left(\frac{1}{k-s}\phi_{k-s}^w + \frac{1}{k+s}\phi_{k+s}^w\right), \\
&\left.\frac{\partial^2 w}{\partial p_j \partial p_r}\right|_0 = 0, \\
&\left.\frac{\partial^2 w}{\partial p_j \partial q_s}\right|_0 = \frac{js}{\sqrt{2\pi}}\left(\frac{1}{j-s}\phi_{j-s}^w + \frac{1}{j+s}\phi_{j+s}^w\right) \\
\frac{\partial \phi_k^w}{\partial p_r} &= \left.\frac{\partial^2 w}{\partial q_k \partial p_r}\right|_0 = \frac{kr}{\sqrt{2\pi}}\left(\frac{1}{k-r}\phi_{k-r}^w + \frac{1}{k+r}\phi_{k+r}^w\right), \\
\frac{\partial \phi_k^w}{\partial q_s} &= \left.\frac{\partial^2 w}{\partial q_k \partial q_s}\right|_0 = 0.
\end{aligned}
\tag{A.39}
$$

□

List of Algorithms

List of Figures

List of Tables

Bibliography

[1] E. L. Allgower and K. Georg. *Introduction to Numerical Continuation Methods*. Colorado State University, 1990.

[2] P. Apiwattanalunggarn, S. W. Shaw, C. Pierre, and D. Jiang. Finite-element-based nonlinear modal reduction of a rotating beam with large-amplitude motion. *Journal of Vibration and Control*, 9:235–263, 2003.

[3] A. Apostolatos, R. Schmidt, R. Wüchner, and K.-U. Bletzinger. A Nitsche-type formulation and comparison of the most common domain decomposition methods in isogeometric analysis. *International Journal for Numerical Methods in Engineering*, 97:473–504, 2014.

[4] F. Auricchio, L. Beirão da Veiga, A. Buffa, C. Lovadina, A. Reali, and G. Sangalli. A fully "locking-free" isogeometric approach for plane linear elasticity problems: A stream function formulation. *Computer Methods in Applied Mechanics and Engineering*, 197:160–172, 2007.

[5] F. Auricchio, L. Beirão da Veiga, T. J. R. Hughes, A. Reali, and G. Sangalli. Isogeometric collocation methods. *Mathematical Models and Methods in Applied Sciences*, 20(11):2075–2107, 2010.

[6] F. Auricchio, L. Beirão da Veiga, C. Lovadina, and A. Reali. The importance of the exact satisfaction of the incompressibility constraint in nonlinear elasticity: mixed FEMs versus NURBS-based approximations. *Computer Methods in Applied Mechanics and Engineering*, 199:314–323, 2010.

[7] F. Auricchio, L. Beirão da Veiga, C. Lovadina, A. Reali, R. Taylor, and P. Wriggers. Approximation of incompressible large deformation elastic problems: some unresolved issues. *Computational Mechanics*, 52(5):1153–1167, 2013.

[8] F. Auricchio, F. Calabrò, T. J. R. Hughes, A. Reali, and G. Sangalli. A simple algorithm for obtaining nearly optimal quadrature rules for NURBS-based isogeometric analysis. *Computer Methods in Applied Mechanics and Engineering*, 249-252:15–27, 2012.

[9] F. Bachinger, U. Langer, and J. Schöberl. Numerical analysis of nonlinear multiharmonic eddy current problems. *Numerische Mathematik*, 100(4):593–616, 2005.

[10] F. Bachinger, U. Langer, and J. Schöberl. Efficient solvers for nonlinear time-periodic eddy current problems. *Computing and Visualization in Science*, 9(4):197–207, 2006.

[11] J. Barbic. *Real-time Reduced Large-Deformation Models and Distributed Contact*

for Computer Graphics and Haptics. PhD thesis, Carnegie Mellon University, 2007.

[12] J. Barbic. FEM Simulation of 3D Deformable Solids: A practitionerś guide to theory, discretization and model reduction. Part 2: Model Reduction. In *SIGGRAPH 2012 Course Notes*, 2012.

[13] K.-J. Bathe and E. L. Wilson. Solution methods for eigenvalue problems in structural mechanics. *International Journal for Numerical Methods in Engineering*, 6:213–226, 1973.

[14] Y. Bazilevs, L. Beirão da Veiga, J. Cottrell, T. J. R. Hughes, and G. Sangalli. Isogeometric analysis: Approximation, stability and error estimates for h-refined meshes. *Mathematical Methods and Models in Applied Sciences*, 16:1031–1090, 2006.

[15] Y. Bazilevs, V. M. Calo, J. A. Cottrell, J. A. Evans, T. J. R. Hughes, S. Lipton, M. A. Scott, and T. W. Sederberg. Isogeometric analysis using t-splines. *Computer Methods in Applied Mechanics and Engineering*, 199:229–263, 2010.

[16] Y. Bazilevs, V. M. Calo, T. J. R. Hughes, and Y. Zhang. Isogeometric fluid-structure interaction: theory, algorithms, and computations. *Computational Mechanics*, 43(1):3–37, 2008.

[17] U. Becker. *Efficient time integration and nonlinear model reduction for incompressible hyperelastic materials*. PhD thesis, TU Kaiserslautern, 2012.

[18] L. Beirão da Veiga, A. Buffa, C. Lovadina, M. Martinelli, and G. Sangalli. An isogeometric method for the Reissner-Mindlin plate bending problem. *Computer Methods in Applied Mechanics and Engineering*, 209:45–53, Feb. 2012.

[19] L. Beirão da Veiga, A. Buffa, G. Sangalli, and R. Vázquez. Mathematical analysis of variational isogeometric methods. *Acta Numerica*, 23:157–287, 2014.

[20] T. Belytschko, W. K. Liu, and B. Moran. *Nonlinear Finite Elements for Continua and Structures*. John Wiley & Sons, 2000.

[21] D. J. Benson, Y. Bazilevs, M. C. Hsu, and T. J. R. Hughes. Isogeometric shell analysis: The reissner-mindlin shell. *Computer Methods in Applied Mechanics and Engineering*, 199:276–289, 2010.

[22] M. Benzi, G. H. Golub, and J. Liesen. Numerical solution of saddle point problems. *Acta Numerica*, 14:1–137, 2005.

[23] D. Boffi, F. Brezzi, and M. Fortin. *Mixed Finite Element Methods and Applications*. Springer Series in Computational Mathematics 44. Springer, 2013.

[24] R. Bouclier, T. Elguedj, and A. Combescure. Locking free isogeometric formulations of curved thick beams. *Computer Methods in Applied Mechanics and Engineering*, 245–246:144–162, 2012.

[25] A. F. Bower. *Applied Mechanics of Solids*. CRC Press, 2009.

[26] J. Boyd. *Chebyshev and Fourier Spectral Methods: Second Revised Edition*. Dover books on mathematics. Dover Publications, 2 edition, 2001.

[27] R. N. Bracewell. Discrete Hartley transform. *Journal of the Optical Society of America*, 73(12):1832–1835, 1983.

[28] A. Bressan and G. Sangalli. Isogeometric discretizations of the stokes problem: stability analysis by the macroelement technique. *IMA Journal of Numerical Analysis*, 33:629–651, 2013.

[29] E. Brivadis, A. Buffa, B. Wohlmuth, and L. Wunderlich. Isogeometric mortar meth-

ods. *submitted to Computer Methods in Applied Mechanics and Engineering*, 2014.

[30] A. Buffa, C. de Falco, and G. Sangalli. IsoGeometric Analysis: Stable elements for the 2D Stokes equation. *International Journal for Numerical Methods in Fluids*, 65(11-12):1407–1422, 2011.

[31] Cadence Design Systems Inc. RF Analysis in Virtuoso Spectre Circuit Simulator XL Datasheet. Technical report, 2007.

[32] J. F. Caseiro, R. A. F. Valente, A. Reali, J. Kiendl, F. Auricchio, and R. J. Alves de Sousa. On the Assumed Natural Strain method to alleviate locking in solid-shell NURBS-based finite elements. *Computational Mechanics*, 53(6):1341–1353, 2014.

[33] N. Cavallini, O. Weeger, M. S. Pauletti, M. Martinelli, and P. Antolín. Effective integration of sophisticated operators in isogeometric analysis with igatools. In B. Jüttler and B. Simeon, editors, *submitted to Isogeometric Analysis and Applications - IGAA 2014*, Lecture Notes in Computational Science and Engineering. Springer International Publishing, 2015.

[34] S. Chaturantabut and D. C. Sorensen. Nonlinear model reduction via discrete empirical interpolation. *SIAM Journal on Scientific Computing*, 32(5):2737–2764, 2010.

[35] P. G. Ciarlet. *Mathematical elasticity*, volume Volume 1: 3-dimensional elasticity. North-Holland, 1988.

[36] N. Collier, L. Dalcin, D. Pardo, and V. M. Calo. The cost of continuity: Performance of iterative solvers on isogeometric finite elements. *SIAM Journal on Scientific Computing*, 35(2):A767–A784, 2013.

[37] Computer History Museum. 1965 – "Moore's Law" Predicts the Future of Integrated Circuits, `http://www.computerhistory.org/semiconductor/timeline/1965-Moore.html`, 2007.

[38] R. D. Cook. Improved two-dimensional finite element. *Journal of the Structural Division*, 100:1851–1863, 1974.

[39] J. A. Cottrell, T. J. R. Hughes, and Y. Bazilevs. *Isogeometric Analysis: Toward Integration of CAD and FEA*. John Wiley & Sons, Ltd, 2009.

[40] J. A. Cottrell, T. J. R. Hughes, and A. Reali. Studies of refinement and continuity in isogeometric structural analysis. *Computer Methods in Applied Mechanics and Engineering*, 196:4160–4183, 2007.

[41] J. A. Cottrell, T. J. R. Hughes, A. Reali, and G. Sangalli. Isogeometric discretizations in structural dynamics and wave propagation. In *ECCOMAS Thematic Conference on Computational Methods in Structural Dynamics and Earthquake Engineering*, Rethymno, Crete, Greece, 13-16 June 2007, June 2007.

[42] J. A. Cottrell, A. Reali, Y. Bazilevs, and T. J. R. Hughes. Isogeometric analysis of structural vibrations. *Computer Methods in Applied Mechanics and Engineering*, 195(41–43):5257–5296, 2006.

[43] M. Dittmann, M. Franke, I. Temizer, and C. Hesch. Isogeometric analysis and thermomechanical mortar contact problems. *Computer Methods in Applied Mechanics and Engineering*, 274:192–212, 2014.

[44] T. Dokken, T. Lyche, and K. F. Pettersen. Polynomial splines over locally refined box-partitions. *Computer Aided Geometric Design*, 30:331–356, 2013.

[45] T. Dokken, E. Quak, and V. Skytt. Requirements from isogeometric analysis for

changes in product design ontologies. In *Focus K3D Conference on Semantic 3D media and content*, 2010.

[46] A. D. Drozdov. *Viscoelastic Structures: Mechanics of Growth and Aging*. Academic Press, 1998.

[47] R. Echter and M. Bischoff. Numerical efficiency, locking and unlocking of NURBS finite elements. *Computer Methods in Applied Mechanics and Engineering*, 199:374–382, Jan. 2010.

[48] T. Elguedj, Y. Bazilevs, V. M. Calo, and T. J. R. Hughes. B-bar and F-bar projection methods for nearly incompressible linear and non-linear elasticity and plasticity based on higher-order NURBS elements. *Computer Methods in Applied Mechanics and Engineering*, 197:2732–2762, 2008.

[49] T. Elguedj and T. J. R. Hughes. Isogeometric analysis of nearly incompressible large strain plasticity. Technical report, ICES Report 11-35, 2011.

[50] J. A. Evans, Y. Bazilevs, I. Babuška, and T. J. R. Hughes. n-widths, sup-infs, and optimality ratios for the k-version of the isogeometric finite element method. *Computer Methods in Applied Mechanics and Engineering*, 198(21–26):1726 – 1741, 2009.

[51] G. E. Farin. *Curves and Surfaces for CAGD: A Practical Guide*. The Morgan Kaufmann Series in Computer Graphics and Geometric Modeling. Morgan Kaufmann, 2002.

[52] D. Forsey and R. Bartels. Hierarchical b-spline refinement. *Computer Graphics*, 22:205–212, 1988.

[53] E. U. FP7-project. Towards Enhanced Integration of Design and Production in the Factory of the Future through Isogeometric Technologies (TERRIFIC), 2011-2014.

[54] R. J. Gilmore and M. B. Steer. Nonlinear circuit analysis using the method of harmonic balance–a review of the art. part i. introductory concepts. *International Journal of Microwave and Millimeter-Wave Computer-Aided Engineering*, 1(1):22–37, 1991.

[55] R. J. Gilmore and M. B. Steer. Nonlinear circuit analysis using the method of harmonic balance–a review of the art. part ii. advanced concepts. *International Journal of Microwave and Millimeter-Wave Computer-Aided Engineering*, 1(2):159–180, 1991.

[56] G. Golub and C. V. Loan. *Matrix Computations*. Johns Hopkins University Press, 3rd edition edition, 1996.

[57] W. E. Haisler, J. A. Stricklin, and J. E. Key. Displacement incrementation in nonlinear structural analysis by the self-correcting method. *International Journal for Numerical Methods in Engineering*, 11(1):3–10, 1977.

[58] R. V. L. Hartley. A more symmetrical Fourier analysis applied to transmission problems. *Proceedings of the IRE*, 30(3):144–150, 1942.

[59] C. Heinrich, B. Simeon, and S. Boschert. A finite volume method on NURBS geometries and its application in isogeometric fluid–structure interaction. *Mathematics and Computers in Simulation*, 82(9):1645–1666, 2012.

[60] S. Herkt. *Model Reduction of Nonlinear Problems in Structural Mechanics: Towards a Finite Element Tyre Model for Multibody Simulation*. PhD thesis, TU Kaiserslautern, 2008.

[61] C. Hesch and P. Betsch. Isogeometric analysis and domain decomposition methods. *Computer Methods in Applied Mechanics and Engineering*, 213-216:104–112, 2012.

[62] T. J. R. Hughes. *The Finite Element Method: Linear Static and Dynamic Finite Element Analysis*. Dover Publications, Mineola, New York, 2000.

[63] T. J. R. Hughes, J. A. Cottrell, and Y. Bazilevs. Isogeometric analysis: CAD, finite elements, NURBS, exact geometry and mesh refinement. *Computer Methods in Applied Mechanics and Engineering*, 194(39–41):4135–4195, 2005.

[64] T. J. R. Hughes, J. A. Evans, and A. Reali. Finite element and NURBS approximations of eigenvalue, boundary-value, and initial-value problems. *Computer Methods in Applied Mechanics and Engineering*, 272:290–320, 2014.

[65] T. J. R. Hughes, A. Reali, and G. Sangalli. Duality and unified analysis of discrete approximations in structural dynamics and wave propagation: Comparison of p-method finite elements with k-method NURBS. *Computer Methods in Applied Mechanics and Engineering*, 197(49–50):4104 – 4124, 2008.

[66] T. J. R. Hughes, A. Reali, and G. Sangalli. Efficient quadrature for NURBS-based isogeometric analysis. *Computer Methods in Applied Mechanics and Engineering*, 199(5-8):301 – 313, 2010.

[67] S. R. Idelsohn and A. Cardona. A load-dependent basis for reduced nonlinear structural dynamics. *Computers & Structures*, 20:203–210, 1985.

[68] S. R. Idelsohn and A. Cardona. A reduction method for nonlinear structural dynamics analysis. *Computer Methods in Applied Mechanics and Engineering*, 49:253–279, 1985.

[69] K. A. Johannessen, T. Kvamsdal, and T. Dokken. Isogeometric analysis using LR B-splines. *Computer Methods in Applied Mechanics and Engineering*, 269:471–514, 2013.

[70] B. Jüttler, M. Kapl, D.-M. Nguyen, Q. Pan, and M. Pauley. Isogeometric segmentation: The case of contractible solids without non-convex edges. *Computer-Aided Design*, 57:74–90, 2014.

[71] A. Karatarakis, P. Karakitsios, and M. Papadrakakis. GPU accelerated computation of the isogeometric analysis stiffness matrix. *Computer Methods in Applied Mechanics and Engineering*, 269:334–355, 2014.

[72] G. Kerschen, M. Peeters, J. C. Golinval, and A. F. Vakakis. Nonlinear normal modes, part i: A useful framework for the structural dynamicist. *Mechanical Systems and Signal Processing*, 23:170–194, 2009.

[73] J. Kiendl, K.-U. Bletzinger, J. Linhard, and R. Wüchner. Isogeometric shell analysis with Kirchhoff-Love elements. *Computer Methods in Applied Mechanics and Engineering*, 198(49–52):3902–3914, 2009.

[74] G. Kiss, C. Giannelli, U. Zore, B. Jüttler, D. Großmann, and J. Barner. Adaptive CAD model (re-)construction with THB-splines. *Graphical Models*, 76:273–288, 2014.

[75] S. Kleiss, C. Pechstein, B. Jüttler, and S. Tomar. IETI - isogeometric tearing and interconnecting. *Computer Methods in Applied Mechanics and Engineering*, 247-248:201–215, 2012.

[76] R. Kolman. Isogeometric free vibration of an elastic block. *Engineering Mechanics*, 19(4):279–291, 2012.

[77] M. Krack, L. P. von Scheidt, and J. Wallaschek. A method for nonlinear modal analysis and synthesis: Application to harmonically forced and self-excited mechanical systems. *Journal of Sound and Vibration*, 332(25):6798–6814, 2013.

[78] R. Lakes. *Viscoelastic Materials*. Cambridge University Press, 2009.

[79] G. Lallement and D. J. Inman. A tutorial on complex eigenvalues. In *SPIE - the international society for optical engineering*, pages 490–495, 1995.

[80] R. Lewandowski. Non-linear, steady-state vibration of structures by harmonic balance/finite element method. *Computers & Structures*, 44(1-2):287–296, 1992.

[81] R. Lewandowski. Computational formulation for periodic vibration of geometrically nonlinear structures, part 1: Theoretical background; part 2: Numerical strategy and examples. *International Journal of Solids and Structures*, 34(15):1925–1964, 1997.

[82] A. Mantzaflaris and B. Jüttler. Exploring matrix generation strategies in isogeometric analysis. In M.-L. Mazure et al. (Eds.), editor, *Mathematical Methods for Curves and Surfaces*, pages 1–19, 2013.

[83] J. Marsden and T. J. R. Hughes. *Mathematical foundations of elasticity*. Dover Publications, Inc. , New York, 1983.

[84] K. M. Mathisen, K. M. Okstad, T. Kvamsdal, and S. B. Raknes. Isogeometric analysis of finite deformation nearly incompressible solids. *Rakenteiden Mekaniikka (Journal of Structural Mechanics)*, 44(3):260–278, 2011.

[85] R. E. Moore and M. J. Cloud. *Computational Functional Analysis*. Horwood Publishing, 2007.

[86] A. H. Nayfeh and B. Balachandran. *Applied Nonlinear Dynamics: Analytical Computational, and Experimental Methods*. Wiley Series in Nonlinear Science. John Wiley & Sons, 1995.

[87] A. H. Nayfeh and D. T. Mook. *Nonlinear Oscillations*. Wiley Classics Library. John Wiley & Sons, 1995.

[88] D.-M. Nguyen, A. Evgrafov, and J. Gravesen. Isogeometric shape optimization for electromagnetic scattering problems. *Progress in Electromagnetic Research B*, 45:117–146, 2012.

[89] D.-M. Nguyen, M. Pauley, D. Mayer, J. Špeh, O. Weeger, and B. Jüttler. The isogeometric segmentation pipeline. In B. Jüttler and B. Simeon, editors, *submitted to Isogeometric Analysis and Applications - IGAA 2014*, Lecture Notes in Computational Science and Engineering. Springer International Publishing, 2015.

[90] N. Nyquist. Certain topics in telegraph transmission theory. *Proceedings of the IEEE*, 90(2):280–305, 2002.

[91] M. S. Pauletti, M. Martinelli, N. Cavallini, and P. Antolín. Igatools: An isogeometric analysis library. *I.M.A.T.I.-C.N.R. Technical Report*, 3PV14/1/0:1–27, 2014.

[92] M. Peeters, R. Viguié, G. S'erandour, G. Kerschen, and J.-C.Golinval. Nonlinear normal modes, part ii: Toward a practical computation using numerical continuation techniques. *Mechanical Systems and Signal Processing*, 23:195–216, 2009.

[93] L. A. Piegl and W. Tiller. *The NURBS Book*. Monographs in Visual Communication. Springer, 1997.

[94] Z.-Q. Qu. *Model Order Reduction Techniques with Applications in Finite Element Analysis*. Springer, 2004.

[95] J. N. Reddy. *An Introduction to Nonlinear Finite Elements*. Oxford University Press, New York, 2004.

[96] J. Remke and H. Rothert. Eine modale Reduktionsmethode zur geometrisch nichtlinearen statischen und dynamischen Finite-Element-Berechnung. *Archive of Applied Mechanics*, 63(2):101 – 115, 1993.

[97] W. Rheinboldt. *Methods for Solving Systems of Nonlinear Equations*. CBMS-NSF Regional Conference Series in Applied Mathematics. Society for Industrial and Applied Mathematics, 1998.

[98] P. Ribeiro. Hierarchical finite element analyses of geometrically non-linear vibration of beams and plane frames. *Journal of Sound and Vibration*, 246(2):225–244, 2001.

[99] P. Ribeiro. Non-linear forced vibrations of thin/thick beams and plates by the finite element and shooting methods. *Computers and Structures*, 82(17-19):1413–1423, 2004.

[100] P. Ribeiro and M. Petyt. Non-linear vibration of beams with internal resonance by the hierarchical finite element method. *Journal of Sound and Vibration*, 224(15):591–624, 1999.

[101] O. Roderick, M. Anitescu, and P. Fischer. Polynomial regression approaches using derivative information for uncertainty quantification. *Nuclear Science and Engineering*, 164(2):122–139, 2010.

[102] D. F. Rogers. *An Introduction to NURBS With Historical Perspective*. Academic Press, San Diego, CA, USA, 2001.

[103] R. M. Rosenberg. On nonlinear vibrations of systems with many degrees of freedom. *Advances in Applied Mechanics*, 9:155–242, 1966.

[104] M. Ruess, D. Schillinger, A. I. Özcan, and E. Rank. Weak coupling for isogeometric analysis of non-matching and trimmed multi-patch geometries. *Computer Methods in Applied Mechanics and Engineering*, 269:46–71, 2014.

[105] D. Schillinger, J. A. Evans, A. Reali, M. A. Scott, and T. J. R. Hughes. Isogeometric collocation: Cost comparison with Galerkin methods and extension to adaptive hierarchical NURBS discretizations. *Computer Methods in Applied Mechanics and Engineering*, 267:170–232, 2013.

[106] M. Schneider, U. Wever, and Q. Zheng. Parallel harmonic balance. *VLSI 93, Proceedings of the IFIP TC10/WG 10.5 International Conference on Very Large Scale Integration, Grenoble, France, 7-10 September, 1993*, pages 251–260, 1993.

[107] T. Sederberg, J. Zheng, A. Bakenov, and A. Nasri. T-Splines and T-NURCCs. *ACM Transactions on Graphics (SIGGRAPH 2003)*, 22:477–484, 2003.

[108] S. W. Shaw and C. Pierre. Normal modes for non-linear vibratory systems. *Journal of Sound and Vibration*, 164:85–124, 1993.

[109] B. Simeon, R. Serban, and L. Petzold. A model of macroscale deformation and microvibration in skeletal muscle tissue. *ESAIM: Mathematical Modelling and Numerical Analysis*, 43(4):805–823, 2009.

[110] R. N. Simpson, S. P. A. Bordas, J. Trevelyan, and T. Rabczuk. A two-dimensional isogeometric boundary element method for elastostatic analysis. *Computer Methods in Applied Mechanics and Engineering*, 209-212:87–100, 2012.

[111] P. M. A. Slaats, J. de Jongh, and A. A. H. J. Sauren. Model reduction tools for nonlinear structural dynamics. *Computers & Structures*, 54(6):1155–1171, 1995.

[112] H. Spiess. *Reduction Methods in Finite Element Analysis of Nonlinear Structural Dynamics*. PhD thesis, Universität Hannover, 2005.

[113] J. Stoer, R. Bulirsch, R. Bartels, W. Gautschi, and C. Witzgall. *Introduction to Numerical Analysis*. Texts in Applied Mathematics. Springer, 2002.

[114] G. Strang and G. Fix. *An analysis of the finite element method*. Wellesley-Cambridge Press, 1997.

[115] W. Szemplińska-Stupnicka. Higher harmonic oscillations in heteronomous nonlinear systems with one degree of freedom. *International Journal of Non-Linear Mechanics*, 3(1):17 – 30, 1968.

[116] W. Szemplińska-Stupnicka. The generalized harmonic balance method for determining the combination resonance in the parametric dynamic systems. *Journal of Sound and Vibration*, 58(3):347 – 361, 1978.

[117] W. Szemplińska-Stupnicka. *The Behaviour of Nonlinear Vibrating Systems*. Kluwer Academic Publishers, Dordrecht Boston London, 1990.

[118] R. L. Taylor. Isogeometric analysis of nearly incompressible solids. *International Journal for Numerical Methods in Engineering*, 87(1-5):273–288, 2010.

[119] C. Touzé and M. Amabili. Nonlinear normal modes for damped geometrically nonlinear systems: Application to reduced-order modelling of harmonically forced structures. *Journal of Sound and Vibration*, 298:958–981, 2006.

[120] C. Touzé, M. Amabili, and O. Thomas. Reduced-order models for large-amplitude vibrations of shells including in-plane inertia. *Computer Methods in Applied Mechanics and Engineering*, 197:2030–2045, 2008.

[121] TU Kaiserslautern, Group Differential-Algebraic Systems. IGASolvers 2.0, `http://www.mathematik.uni-kl.de/en/das/research/aktuelle-projekte/terrific/`, Sept. 2014.

[122] A. F. Vakakis, L. I. Manevitch, Y. V. Mikhlin, V. N. Pilipchuk, and A. A. Zevin. *Normal modes and localization in nonlinear systems*. Wiley Series in Nonlinear Science. John Wiley & Sons, New York, 1996.

[123] C. M. A. Vasques, R. A. S. Moreira, and J. Dias Rodrigues. Viscoelastic damping technologies–part i: Modeling and finite element implementation. *Journal of Advanced Research in Mechanical Engineering*, 1:76–95, 2010.

[124] C. Vömel, R. G. Veprek, U. Weber, and P. Arbenz. Iterative solution of generalized eigenvalue problems from optoelectronics with trilinos. Technical report, Eidgenössische Technische Hochschule Zürich, Institute of Computational Science, 2012.

[125] A.-V. Vuong, C. Giannelli, B. Jüttler, and B. Simeon. A hierarchical approach to adaptive local refinement in isogeometric analysis. *Computer Methods in Applied Mechanics and Engineering*, 200:3554–3567, 2011.

[126] O. Weeger. Berechnung nichtlinearer Strukturvibrationen mit isogeometrischen Finiten Elementen. Master's thesis, TU München, 2011.

[127] O. Weeger, U. Wever, and B. Simeon. Isogeometric analysis of nonlinear Euler-Bernoulli beam vibrations. *Nonlinear Dynamics*, 72(4):813–835, 2013.

[128] O. Weeger, U. Wever, and B. Simeon. Nonlinear frequency response analysis of structural vibrations. *Computational Mechanics*, 54(6):1477–1495, 2014.

[129] D. B. West. *Introduction to Graph Theory (2nd Edition)*. Prentice Hall, 2001.

[130] P. Wriggers. *Nonlinear Finite Element Methods*. Springer, 2008.

Wissenschaftlicher Werdegang

Oliver Manuel Weeger

06/2005	Abitur am Simon-Marius-Gymnasium, Gunzenhausen
10/2006–11/2011	Studium Diplom-Technomathematik, TU München
01/2012–12/2014	Doktorand bei Siemens AG, Corporate Technology, München
01/2012–04/2015	Promotion in Mathematik, TU Kaiserslautern
01/2015–04/2015	Wiss. Mitarbeiter am FB Mathematik, TU Kaiserslautern

Scientific career

Oliver Manuel Weeger

06/2005	Abitur at Simon-Marius-Gymnasium, Gunzenhausen
10/2006–11/2011	Studying Diploma Techno-Mathematics, TU Munich
01/2012–12/2014	PhD student at Siemens AG, Corporate Technology, Munich
01/2012–04/2015	Doctorate in mathematics, TU Kaiserslautern
01/2015–04/2015	Research assistant at dept. of Mathematics, TU Kaiserslautern